



Thesis Title:

**Structural plasticity of active zones in mouse hippocampal mossy
fiber synapses**

**Strukturelle Plastizität aktiver Zonen in Maus hippocampalen
Moosfasersynapsen**

Doctoral thesis for a doctoral degree
at the Graduate School of Life Sciences,
Julius-Maximilians-Universität Würzburg,
Section Neuroscience

submitted by

Marzieh Sharifi

from

Abadeh, Iran

Würzburg

2021



Submitted

on:

.....

Office stamp

Members of the Thesis Committee

Chairperson: Prof. Dr. Carmen Villmann

Primary Supervisor Prof. Dr. med. Anna-Leena Sirén

Supervisor (Second): Prof. Dr. Markus Sauer

Supervisor (Third): Prof. Manfred Heckmann

Date of Public Defence:

Date of Receipt of Certificates:

.....

Parts of this thesis are published in the following articles:

Pauli, M., Paul, M. M., Proppert, S., Mrestani, A., Sharifi, M., Repp, F., ... Sirén, A. L. (2021). Targeted volumetric single-molecule localization microscopy of defined presynaptic structures in brain sections. *Communications Biology*, 4(1), 1–13. <https://doi.org/10.1038/s42003-021-01939-z>

Contents

| | | |
|----------|--|-----------|
| 1 | Summary | 2 |
| 2 | Introduction | 1 |
| 2.1 | <i>Chemical synapses</i> | 1 |
| 2.1.1 | Electrical and chemical signal transduction at synapses | 1 |
| 2.1.2 | The vesicular release | 2 |
| 2.1.3 | The presynaptic active zone | 3 |
| 2.1.4 | Synaptic plasticity and memory | 15 |
| 2.2 | <i>Hippocampal formation</i> | 22 |
| 2.2.1 | Patient HM | 22 |
| 2.2.2 | Hippocampal synaptic plasticity | 22 |
| 2.2.3 | Mossy fiber boutons | 23 |
| 2.3 | <i>Microscopy</i> | 27 |
| 2.3.1 | Optical light microscopy; Diffraction-Barrier and Its Impact | 27 |
| 2.3.2 | Super-resolution microscopy | 31 |
| 2.4 | <i>The motivation of the study</i> | 38 |
| 3 | Material and methods | 39 |
| 3.1 | <i>Animals</i> | 39 |
| 3.2 | <i>Material</i> | 39 |
| 3.2.1 | Acute Brain Slice Preparation | 39 |
| 3.2.2 | cLTP | 40 |
| 3.2.3 | Fixation and cryosectioning | 41 |
| 3.2.4 | Cryosectioning equipment | 41 |
| 3.2.5 | Calibration bead slide set and Silan-coated coverslips | 41 |
| 3.2.6 | Immunofluorescence | 42 |
| 3.3 | <i>Reagents</i> | 43 |
| 3.3.1 | Reagent setup; Chemicals, Buffering, Fixing and Dyeing Solutions | 44 |
| 3.3.2 | Reagent for imaging setup | 46 |
| 3.4 | <i>Devices and software</i> | 47 |
| 3.4.1 | Devices for acute brain slices and cryotome sectioning | 47 |
| 3.4.2 | SR imaging setup devices | 47 |
| 3.5 | <i>Methods and procedure</i> | 48 |
| 3.5.1 | Sample Preparation and the setup | 48 |
| 3.5.2 | Acute brain slices | 51 |
| 3.5.3 | Induction of chemical plasticity | 53 |
| 3.5.4 | Fixation, flat-mounting, and cryosectioning | 54 |
| 3.5.5 | Super-resolution imaging | 56 |
| 4 | Statistics and analysis | 63 |
| 5 | Results and Discussion | 64 |
| 5.1 | <i>Super-resolving Microscopy of hippocampus mossy fiber active zones</i> | 64 |
| 5.2 | <i>Summarized setup workflow</i> | 64 |
| 5.3 | <i>SIM</i> | 65 |
| 5.3.1 | Alignment accuracy in multi-color data | 66 |
| 5.3.2 | Imaging synaptic contacts of hippocampal mossy fiber; Application of SIM to MFB | 69 |
| 5.3.3 | Surface analysis; Reconstruction of MF and AZ proteins in SIM images | 72 |
| 5.3.4 | Quantification of EGFP/MFB volume in SIM images | 74 |
| 5.3.5 | Quantification of Bassoon, Munc 13-1 and Tomosyn protein intensity in SIM images | 77 |

| | | |
|-----------|---|------------|
| 5.3.6 | Influence of Forskolin | 82 |
| 5.4 | <i>dSTORM</i> data | 100 |
| 5.4.1 | Application of <i>dSTORM</i> to the brain slices | 100 |
| 5.4.2 | Surface analysis; Reconstruction of MF and AZ protein Bsn in <i>dSTORM</i> images | 101 |
| 5.4.3 | Forskolin effect in hippocampal MFBs using <i>dSTORM</i> | 102 |
| 5.5 | <i>Morphology of Bassoon protein in SIM and dSTORM imaging techniques</i> | 104 |
| 6 | Conclusion and outlook | 106 |
| 7 | References | 107 |
| 8 | Abbreviation | 132 |
| 9 | List of figures | 135 |
| 10 | List of Tables | 137 |

Declaration of Authorship

Affidavit

I hereby declare that my thesis entitled: “Structural plasticity of active zones in mouse hippocampal mossy fiber synapses” is the result of my own work. I did not receive any help or support from commercial consultants. All sources and/or materials applied are listed and specified in the thesis.

Furthermore, I verify that the thesis has not been submitted as part of another examination process, neither in identical nor in a similar form.

Eidesstattliche Erklärung

Hiermit erkläre ich an Eides statt, die Dissertation: „Strukturelle Plastizität aktiver Zonen in Maus hippocampalen Moosfasersynapsen“, eigenständig, d. h. insbesondere selbständig und ohne Hilfe eines kommerziellen Promotionsberaters, angefertigt und keine anderen, als die von mir angegebenen Quellen und Hilfsmittel verwendet zu haben.

Ich erkläre außerdem, dass die Dissertation weder in gleicher noch in ähnlicher Form bereits in einem anderen Prüfungsverfahren vorgelegen hat.

Signed:

Date:

Acknowledgements

"Shoot for the moon. Even if you miss, you'll land among the stars."

Les Brown

I'd like to express my gratitude to everyone who has supported me over the last few years.

From the bottom of my heart, I would like to say a special thank you to my supervisor, Professor Anna-Leena Sirén for giving me the opportunity to work in her group. Her support and guidance have encouraged me in my academic research and daily life. *Olen oppinut paljon, kiitos!*

I'd like to thank Professor Markus Sauer for his competence, enthusiasm, and understanding.

I would also like to thank Professor Manfred Heckmann for accepting to be my third referee and for assisting me with neuroscience-related questions.

I'd like to thank all the colleagues who supported me throughout the project, in particular Dr. Martin Pauli for his guidance and methodological support.

Last but not least, I would like to thank my family, my parents, and my sisters for their unconditional support, encouragement, and love, and without which I would not have come this far.

1 Summary

Chemical synapses are a physically and functionally varied type of cell-cell contact specialized in conducting communication between neurons. They are the smallest "computational" unit of the brain and are often classified as electrical and chemical, and they can be distinguished based on their transmission mechanism. These categories could be further broken into many kinds, each having a specific structure-function repertoire that is hypothesized to provide neural networks with distinct computational capabilities. Heterogeneity refers to the variety of structures and functions present in a particular category of synapses. Contributing factors for this heterogeneity may be the synaptic vesicles, the active zone (AZ), the synaptic cleft, the postsynaptic density, and the glial processes associated with the synaptic contacts. Each of these five structural modules has its own set of functions, and their combination determines the spectrum of functional heterogeneity at mammalian excitatory synapses. This work focused on the changes in AZ protein expression after chemical induction of plasticity with forskolin in synaptic contacts of the hippocampal mossy fibers. With the nanoscopic resolution provided by *d*STORM, along with the multicolor SIM imaging capabilities, changes in expression of key presynaptic AZ components were analyzed. Using SIM imaging along with a standardized stimulation protocol in acute brain slices from male 16-week old Thy1-mEGFP (*Lsi1*) mice, the changes of the key AZ proteins Bassoon, Munc 13-1 and Tomosyn were investigated 30 min after stimulation with forskolin (50 μ M for 30 min). Forskolin induced changes in these proteins largely in small synaptic contacts whereas no clear changes were detected in large mossy fiber boutons. However, due to the high variability it cannot be ruled out that forskolin may differentially modify AZ protein composition depending on experimental circumstances such as age and gender of mice or the time point and duration of forskolin stimulation.

The *d*STORM data demonstrated feasibility to perform single molecule 3D imaging of hippocampal presynaptic AZs and allowed quantitative mapping of molecular changes in AZ proteins after induction of plasticity. The findings suggest high heterogeneity in mossy fiber synaptic contacts that may have an impact on the function of neural networks. These imaging approaches may now be used to identify potential differences in functional molecular rearrangements of synaptic proteins in healthy and diseased brain (e.g. after induction of traumatic brain injury).

1. Zusammenfassung

Chemische Synapsen sind eine physikalisch und funktionell vielfältige Art von Zell-Zell-Kontakten, die auf die Kommunikation zwischen Neuronen spezialisiert sind. Sie sind die kleinste "computational" Einheit des Gehirns und werden oft als elektrisch und chemisch klassifiziert, und sie können auf der Grundlage ihres Übertragungsmechanismus unterschieden werden. Diese Kategorien lassen sich weiter in viele Arten unterteilen, die jeweils ein spezifisches Struktur-Funktions-Repertoire aufweisen, von dem angenommen wird, dass es neuronale Netze mit unterschiedlichen Berechnungsfähigkeiten ausstattet. Heterogenität bezieht sich auf die Vielfalt der Strukturen und Funktionen, die in einer bestimmten Kategorie von Synapsen vorhanden sind. Die wichtigsten Gründe für diese Heterogenität sind molekulare und strukturelle Unterschiede in synaptischen Vesikeln, der aktiven Zone (AZ), synaptischem Spalt, postsynaptischer Dichte und der mit der Synapse verbundenen glialen Prozesse. Jedes dieser fünf strukturellen Module hat seine eigenen Funktionen, und ihre Kombination bestimmt das Spektrum der funktionellen Heterogenität an exzitatorischen Synapsen von Säugetieren. Diese Arbeit konzentrierte sich auf Änderungen der AZ Proteine nach chemischer Induktion von Plastizität an hippocampalen Moosfasersynapsen mittels superhochauflösende Fluoreszenzmikroskopie. Mit der nanoskopischen Auflösung von *d*STORM und der Mehrfarben-SIM-Bildgebung könnten Proteine in der präsynaptischen AZ abgebildet werden. Mithilfe der SIM-Bildgebung wurden Veränderungen in der Expression von AZ-Proteinen Bassoon, Munc 13-1 und Tomosyn nach der Induktion von Plastizität mit Forskolin an akuten Hirnschnitten von 16-Wochen alten männlichen Thy1-mEGFP (Lsi1) Mäusen analysiert. Forskolin reduzierte die Expression von Bassoon, Munc-13-1 und Tomosyn hauptsächlich in kleinen Moosfasersynapsen. Aufgrund der hohen Variabilität kann jedoch nicht ausgeschlossen werden, dass Forskolin die Expression der AZ-Proteine abhängig von den experimentellen Bedingungen, wie z.B. dem Alter oder dem Geschlecht der Mäuse oder der Zeitpunkt und der Dauer der Forskolin-Stimulation unterschiedlich verändern könnte.

Die *d*STORM-Daten zeigten, dass es möglich ist, eine Einzelmolekül-3D-Bildgebung präsynaptischer aktiver Zonen in Hippocampus durchzuführen. Die Methode ermöglichte eine quantitative Analyse der molekularen Veränderungen in AZ-Proteinen nach Induktion von Plastizität. Die Ergebnisse deuten auf eine große Heterogenität der Moosfasersynapsen, die einen Einfluss auf die Funktion neuronaler Netzwerke haben könnte. Diese bildgebenden Verfahren können nun eingesetzt werden, um potenzielle Unterschiede in den funktionellen molekularen Änderungen synaptischer Proteine im gesunden und pathologischen Gehirn (z. B. nach einer traumatischen Schädelverletzung) zu untersuchen.

2 Introduction

2.1 Chemical synapses

2.1.1 Electrical and chemical signal transduction at synapses

The fast and precise information transfer in the brain, from acute initiation of movement to higher cognitive functions such as memory and emotions, occurs at synapses, the specialized intercellular contact sites between neurons and their target cells. The synapse concept originated from considerations of how muscles are contracted and so locomotion affected over a period of 2400 years, from the time of Plato and Aristotle in the 4th century BC to the early part of the 20th century (Bennett 1999). However, just over one hundred years ago, in 1897, Charles Sherrington, in the edition of Sir Michael Foster's Text-book of physiology, introduced the term synapse – from the Greek *synapsis* (συνάψις), meaning “conjunction” – as the sites of communication between neurons. Although there are many kinds of synapses within the human brain, two different types of synapses—electrical and chemical—can be distinguished based on their transmission mechanism. This work will focus on the chemical synapse first propounded by Santiago Ramón y Cajal (S. Cajal 1888). Initially, it was considered that all trans-synaptic signaling is based on electrical transmission. Electrical synapses do convey inter-neuronal communication electrically via so-called gap junctions that allow the fast, direct and passive flow of ions and small molecules from one neuron to the next (Walter, Böhme, and Sigrist 2018). At the beginning of the 1920s, the notion that the transducing signal is of chemical rather than electrical was the subject of intense debate. At the time, Otto Loewi performed an essential experiment with frog hearts, where he electrically stimulated the vagus nerve, which decelerates the heart rate. Loewi collected the fluid surrounding the heart shortly after this stimulation. When he applied this fluid to the second heart, it led to a deceleration of the heart's rate, as if its vagus nerve had been stimulated as well. He concluded that the fluid itself has a chemical substance and named it “*Vagusstoff*.” This was the first verification of chemical neurotransmission, a clear demonstration that neurotransmitters (NTs) are released from neurons and affect the connected tissue the first (Loewi 1921). Presynaptic release and postsynaptic detection of neurotransmitter molecules are required for chemical synapses to function. In addition to signal amplification, this enables synapses to perform as small computational elements capable of

2. Introduction

modifying signals in an activity-dependent way, thereby affecting synaptic strength (Südhof 2012). Chemical synapses can be structurally described by asymmetric organization with a bouton -the presynaptic nerve terminal- consisting of synaptic vesicles, a synaptic cleft, and a postsynaptic neurotransmitter reception, the postsynaptic density (PSD) (Schoch and Gundelfinger 2006).

Chemical synapses are essential regulators of neuronal information and the focus of this work. Transmission at chemical synapses is based on the elaborate sequence of events. Information at these synapses in the form of an action potential arrives at a presynaptic terminal (Katz 1969). The depolarization in the membrane potential leads to the opening of voltage-gated calcium channels in the presynaptic membrane. Elevation of the presynaptic Ca^{2+} concentration triggers secretory organelles - synaptic vesicles (SVs) - to fuse with the presynaptic membrane. Before SVs can fuse with the plasma membrane to release their neurotransmitter molecules into the synaptic cleft, they have to be recruited to and docked at the highly specialized area of the presynaptic plasma membrane, the active zone (AZ), followed by “priming,” a maturation process, that makes them fusion-competent (reviewed in [(Südhof 2013)]). Following exocytosis, specific postsynaptic receptor ion channels activate and enable current flow to convey the neuronal signal. In this way, information is transmitted from one neuron to another (Kaeser and Regehr 2014; Südhof 2012; Schoch and Gundelfinger 2006). The focal point of this work is this complex protein meshwork within the presynaptic terminal, AZs.

2.1.2 The vesicular release

The synaptic vesicular release process triggered by the influx of calcium ions is controlled in a speedy and precise manner. The time course of pre and postsynaptic currents at the squid giant synapse was first measured by Rodolfo Llinás and colleagues in the 1980s. Their research showed a time gap of 200 μ s between voltage-dependent calcium influx and transmitter release (Llinás, Steinberg, and Walton 1981). The temporally ultrafast neurotransmitter release requires the positioning of SVs directly near the AZ and calcium channels. For this spatial conformation, particular interactions between molecules located at the SVs, AZs, and cytomatrix are essential. It has long been assumed that the macromolecules of the presynaptic release sites perform this role. However, the

2. Introduction

investigation of active zone material due to its small size and complex structure has been problematic (Limbach et al. 2011; Pulido and Marty 2017).

Nevertheless, new advancements of super-resolution microscopy, and the developments of electron microscopy (EM) methods, including high-pressure cryofixation and EM tomography, have provided high-quality and precise images of the active zone material at many synapses. These new improvements are reviewed next. This work investigates the ultrastructure of the active zone using super-resolution light microscopic techniques.

2.1.3 The presynaptic active zone

The fusion of SVs with the presynaptic plasma membrane is controlled spatially and temporally highly precisely. AZs, with their protein-rich cytomatrix (cytomatrix associated with the AZ; CAZ), build a structural platform for molecular interactions, guiding vesicle exocytosis and synaptic neurotransmission (Zhai and Bellen 2004). CAST (Cytomatrix at the Active zone-associated Structural protein) is a 120 kilo Dalton (kDa) protein that was first isolated from rat brain (Ohtsuka et al. 2002) and afterward identified as the Rab3-interacting molecule (RIM)-binding protein, ERC2, through yeast two-hybrid screening (Xiaolu Wang et al. 2009). After electron microscopy was applied to synaptic structures, it was apparent that synaptic vesicles closely surround specialized, thickened portions of the presynaptic membrane Figure 1; (Gray 1963).

It was postulated that these specializations were sites of neurotransmitter release. However, for more than a decade after the proposal of the ‘vesicular hypothesis,’ definitive proof that exocytosis occurred at these sites remained elusive (Birks, Huxley, and Katz 1960; Gray 1963). Finally, in 1970, Couteaux and Pecot-Dechavassine captured images of specialized parts of the nerve terminal, facing folds of the postsynaptic membrane, where the synaptic vesicle (SV) exocytosis takes place. They called these areas “active zones” and proposed that these were the sites of nerve-evoked exocytosis of synaptic vesicles (Couteaux, R., and Pecot-Dechavassine 1970; Tsuji 2006).

AZs dense projections morphology has been studied in different types of synapses in various species. AZs in a variety of organisms exhibit conserved morphological features despite their size, location, or types of neurons and their target cells. AZs are characterized by an electron-dense protein network, the CAZ, and an exact alignment with the PSD.

2. Introduction

The presynaptic active zones are integrally involved in achieving the high spatial and temporal precision of synaptic vesicle exocytosis and neurotransmitter release with the requisite speed and plasticity needed for a synapse's information transfer and computational function in five critical functions.

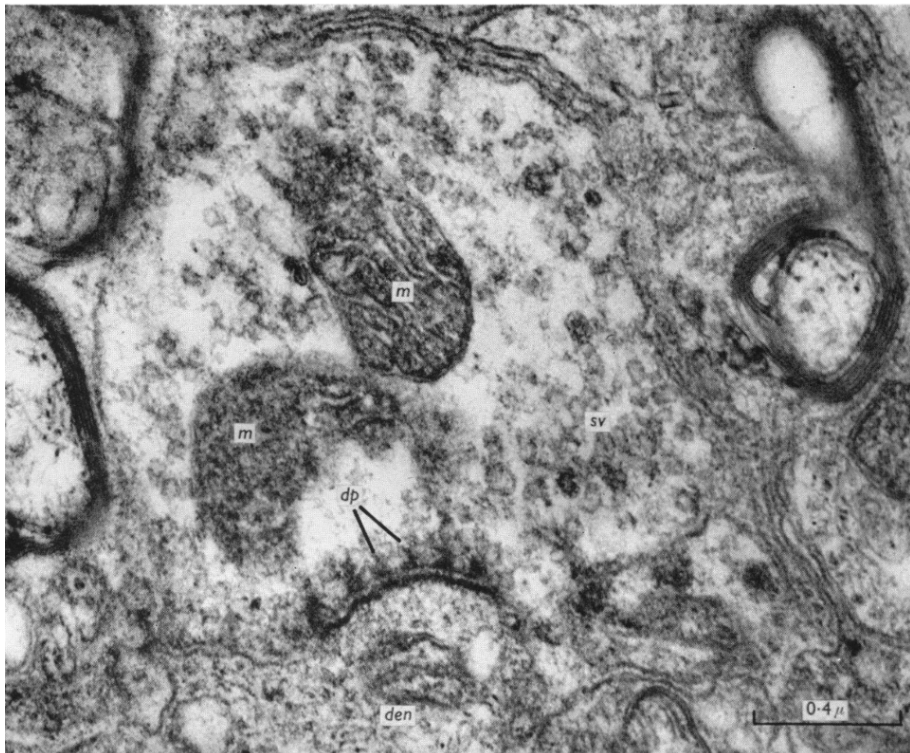


Figure 1. Spinal cord synapses with dense projections in presynaptic processes. [modified from (Gray 1963)]

First, they dock and prime synaptic vesicles. Before SVs can fuse with the plasma, they have to be recruited and docked at the AZ, followed by the priming maturation process (Südhof 2013). Second, AZs organize the exact opposition of the pre and postsynaptic specializations by particular trans-synaptic cell adhesion molecules. Third, to grant the fast-synchronous excitation/release coupling, AZs components play a role in recruiting voltage-gated Ca^{2+} channels (VGCCs). Fourth, AZ is involved in the sorting of SV proteins to the endocytic machinery. Finally, AZs either directly respond to second messengers such as Ca^{2+} or diacylglycerol whose production leads to plasticity or indirectly through recruitment of other plasticity-related proteins mediate much of the activity-induced presynaptic short- and long-term plasticity (Michel et al. 2015; Südhof

2. Introduction

2012). So that finally, SVs cluster, tether, and fuse at the AZs (Zhai and Bellen 2004; Michel et al. 2015; Heuser and Reese 1973).

Despite notable progress, there are still many open questions regarding the active zones. This work focuses on novel insights into the correlation between ultrastructure and function at the AZs.

2.1.3.1 Structural organization and diversity of AZs

Considerable diversity of the AZ's structure has been observed between different neuron types, synapses of the same neuron innervating different postsynaptic cells, and even between individual synapses formed by the same partner neurons. This heterogeneity and differentiation likely occur in response to specific physiological requirements. In Figure 2, electron micrographs and schematic models of the active zone structures found in different synapses of various organisms are shown.

A. Frog Neuromuscular Junction

It has been suggested that at the frog neuromuscular junction (NMJ), docking and exocytosis of SVs take place at particular locations outside intramembrane particles arranged in two lines, which are assumed to represent VGCCs (Heuser et al. 1979; Pulido and Marty 2017). Over the last 20 years, studies of this structure using electron tomography revealed an array-like and elongated structure, reaching on the order of 1 μm in length, composed of a network of macromolecules, which can be categorized in three layers (Harlow et al. 2001; Szule, Jung, and McMahan 2015).

B. *Drosophila* Neuromuscular Junction

Electron microscopy and super-resolution optical microscopy have provided detailed images of the *Drosophila* NMJ structure. In Figure 2, a model of *Drosophila* NMJ AZ obtained with these methods is shown (Ehmann, Oswald, and Kittel 2017; Pulido and Marty 2017). In electron microscopy, the *Drosophila* NMJ AZ meshwork has been given the name “T-bars,” reflecting a conspicuous thick meshwork of filaments overlying a pedestal. T- bar spans approximately 100–200 nm from the membrane into the cytoplasm (Jiao et al. 2010; Wichmann, C.Sigrist 2010; Ehmann, Oswald, and Kittel 2017).

2. Introduction

The protein *Bruchpilot* (BRP) has been considered to be a vital element of this structure and essential for its formation. Along with BRP, T-bars contain RIM, Dunc13, RBP, and Fife (Graf et al. 2012).

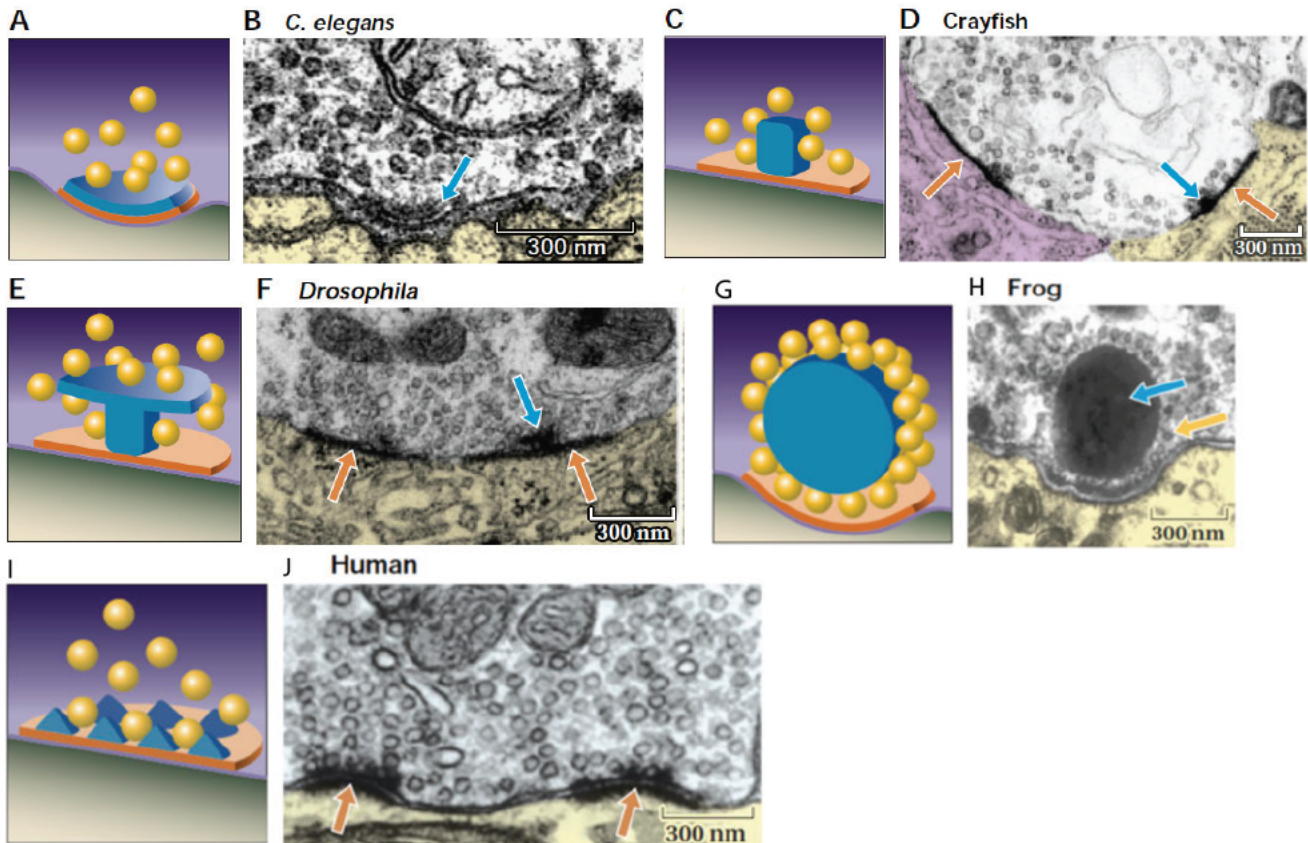


Figure 2. AZ ultrastructures. (A-J) Schematics of AZ structures in different organisms Modified from (Zhai and Bellen 2004).

A, C, E, H, K, M, and O are diagrams of the active zone structure in the synaptic terminal electron micrographs shown to their right. B) neuromuscular junction (NMJ) terminal in *Caenorhabditis elegans* (Hallam et al. 2002). D) NMJ terminal in crayfish (Govind, Quigley, and Pearce 2001). F) dense projection called T bar in an NMJ terminal in *Drosophila* (Meinertzhagen et al. 1998). I) a synaptic terminal in the human hippocampus shows the compact projection as part of the presynaptic particle web (Dresbach et al. 2001) with two active zones (red arrows).

C. Mammalian Neuromuscular Junction

The AZs material of mammalian NMJ contains common components such as beams, ribs, and pegs, but with a different arrangement, in which at mouse NMJ, the SVs are positioned at the center of AZs and beams are located peripherally (Nagwaney et al. 2009). These studies show that even with common molecular

2. Introduction

components, notable structural differences have been found (Pulido and Marty 2017).

D. Central Mammalian Synapses

Giant central synapses are complex structures consisting of many components functioning in parallel, similar to the mammalian neuromuscular junction (Pulido and Marty 2017). EM studies in mammalian central nervous systems by Bloom and Aghajanian and subsequently by Pfenninger and colleagues showed that the CAZ is a hexagonal grid of electron-dense projection (Bloom and Aghajanian 1968; Pfenninger et al. 1972; Phillips et al. 2001; Michel et al. 2015). In central synapses of vertebrates, active zones are characterized by disc-like structures with a 0.2–0.5 μm diameter, surrounded by a perisynaptic zone (Brodin and Shupliakov 2006; Südhof 2012).

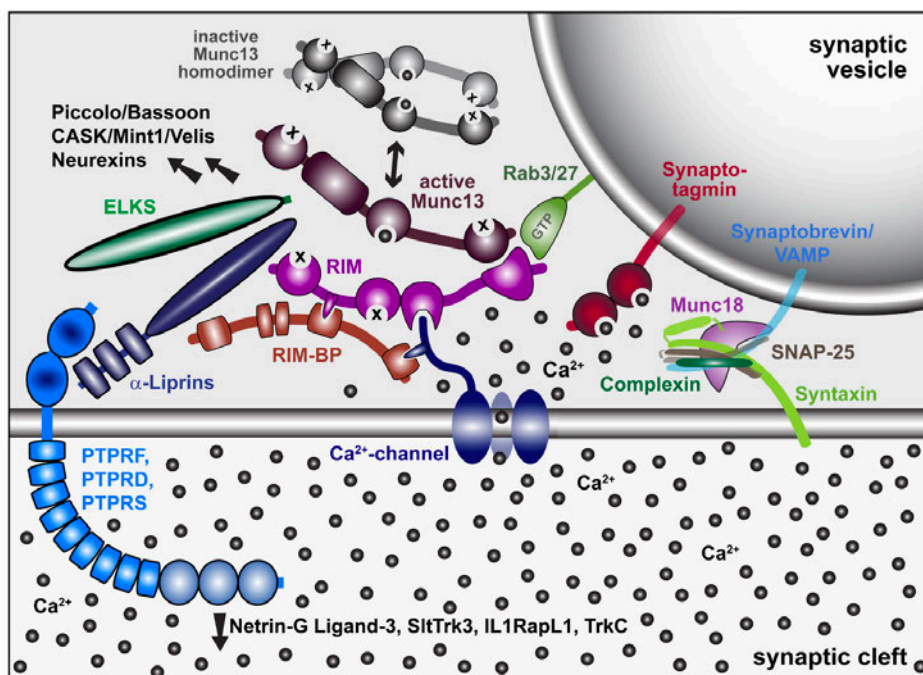


Figure 3 Molecular Model of main players at the presynaptic AZ. An SV (grey) is shown schematically with the numerous active zone proteins and their interconnections.

The AZ core protein complex, which includes RIM, RBP, Munc13, Liprin-, and the CAZ-associated protein CAST/ERC/ELKS, as well as an AZ Ca^{2+} channel, can be seen on the left and middle. On the right is the core fusion machinery, which contains the SNARE proteins, Munc18, and Complexin. [An adaptation of the originally published in (Südhof 2012)].

2. Introduction

Nonetheless, all AZs share crucial fundamental characteristics. Their variations in size and shape appear to have developed to meet the kinetic demands of transmitter release at particular synapse sites.

2.1.3.2 Molecular architecture of the AZ

After recruiting the SVS to the AZ, they need to be ready for fusion. Although many SVs may be localized at the presynaptic membrane, just a few SVs contribute to the fusion process. This thought to be based on their exact positioning and molecular state (Walter, Böhme, and Sigrist 2018). The unique proteome of the AZ governs the basis for efficient and accurate neurotransmission, synaptic contact, and the short and long-term structural and functional dynamics (Rosenmund, Rettig, and Brose 2003). To understand the regulation and modulation of chemical signaling, it is vital to identify AZ's proteinaceous inventory (Weingarten et al. 2014). Due to the complexity of acquiring relatively pure preparations, the composition of the CAZ has remained not well defined (Michel et al. 2015).

Although the core AZ proteins are strongly enriched at the specialized area of the presynaptic plasma membrane, they are not just only localized to the AZs but can be partially expressed also in neuroendocrine and or even non-neuronal cells (Weingarten et al. 2014). The AZ proteins are not only restricted to their localization to the CAZ but also are of large molecular size and contain multiple interaction sites.

So far, a variety of CAZ-related proteins have been discovered. (1) SV fusion proteins, such as syntaxin, SNAP-25 (Synaptosomal-associated protein), and Munc18; (2) actin, tubulin, myosin, spectrin, and β -catenin as cytoskeletal proteins (3) scaffolding proteins, including CASK, Mint, SAP97, and velis/MALS; (4) voltage-gated calcium channels; and (5) cell adhesion molecules, including neurexins (Nrx), cadherins and integrins [for review see (Dresbach et al. 2001; E D Gundelfinger and tom Dieck 2000; Rosenmund, Rettig, and Brose 2003; Ziv and Garner 2004)].

Studies have revealed five evolutionarily conserved proteins at the core of the AZ, namely RIM (Rab3-interacting molecule), Munc13 [mammalian homologue of the nematode *C. elegans* Unc13 (uncoordinated) protein], ELKS/CAST (glutamic acid (E), leucine (L), lysine (K), and serine (S)-rich protein; CAZ-associated structural proteins), α -Liprin/Syd-2 (synapse-defective 2), and RIM-BP (RIM-binding protein), that are highly enriched at and form the core of the cytomatrix at the active zone (CAZ). Two additional large homologous proteins, Bassoon and Piccolo/Aczonin are associated with AZs, which initially were thought to be vertebrate-specific (Tom Dieck et al. 1998; Garner, Kindler, and Gundelfinger 2000; Schoch and Gundelfinger 2006; Limbach et al. 2011). However, structurally more distant family equivalents, such as Fife and Bruchpilot, have been discovered in invertebrates (Wagh et al. 2006; Sigrist and Schmitz 2011;

2. Introduction

Bruckner et al. 2012; Ackermann, Waites, and Garner 2015), which may have a similar significance in the CAZ (Eckart D. Gundelfinger, Reissner, and Garner 2016).

Through physical interactions, these proteins construct a scaffold in the active zone for the assembly of dense projections or the whole presynaptic particle web and contribute to coordinating SV release and retrieval, as well as modulating release changes in both short-term and long-term synaptic plasticity (Limbach et al. 2011; Schoch and Gundelfinger 2006).

The interconnected network formation of a large protein structure from these AZ proteins that are linked to SVs, cytoskeletal proteins, and calcium channels facilitates the efficient docking and priming of SVs, recruiting Ca²⁺ channels to the docked and primed vesicles, tethering the vesicles and Ca²⁺ channels to synaptic cell-adhesion molecules, and mediates synaptic plasticity (Südhof 2012). In contrast, the plasma membrane SNARE (soluble N-ethylmaleimide-sensitive factor attachment receptor)-proteins such as syntaxin and SNAP-25 and the SM (Sec1/Munc18-like)-protein Munc18 are not enriched in active zones and distributed all over the plasma membrane (Südhof 2012) and are also involved in the SV fusion machinery for exocytosis (Südhof and Rothman 2009; Südhof 2013). Moreover, proteins related to *C. elegans* SYD-1 (synapse defective-1) could be identified to play a crucial role in assembling invertebrate AZs (Owald et al. 2010).

SNARE and SM proteins go through a series of assembly and disassembly. In a manner that during priming vesicular SNARE protein synaptobrevin assembles into a trans-SNARE complex with the plasma membrane SNARE proteins syntaxin-1 and SNAP-25 (Söllner et al. 1993), to form a helically coiled complex that brings the SV membrane and the presynaptic plasma membrane in close proximity. Before SNARE complex assembly, syntaxin-1 is in a closed conformation, and Munc18-1 is linked with monomeric syntaxin-1 in a way that syntaxin-1 cannot engage in SNARE complex formation; to proceed, syntaxin-1 has to open for SNARE complex assembly (Misura, Scheller, and Weis 2000; Dulubova et al. 1999; Hata, Slaughter, and Südhof 1993). As a result of Munc18-1 connection to assembling trans-SNARE via interacting with the syntaxin-1 N-peptide during SNARE complex assembly, Munc18-1 changes its binding form to syntaxin-1. By the time that SNARE complexes are partially assembled, Complexin binds to further their priming (Dulubova et al. 2007).

The SNARE/SM complex remains in the plasma membrane following vesicle fusion and neurotransmitter release. To allow repeated fusion cycles NSF (N-ethylmaleimide-sensitive factor) and SNAPs (soluble NSF attachment proteins) must disassemble this complex (Wojcik and Brose 2007; Südhof 2013; Jahn and Fasshauer 2012). Munc18, Munc13, synaptotagmin, and complexin represent essential components of SNARE-mediated vesicle fusions. Excitation-secretion coupling, or the conversion of an electrical stimulus into neurotransmitter release

2. Introduction

after neuronal depolarization, requires all of these proteins (Wojcik and Brose 2007; Schneggenburger and Neher 2005).

Table 1 *The principal roles of some vertebrate active zone protein*

| Protein | MW (kDa) | Function |
|----------------|-----------------|--|
| Bassoon | 420 | Main scaffolding protein of ribbon synapses (Tom Dieck et al. 1998; Khimich et al. 2005; Regus-Leidig, tom Dieck, and Brandstätter 2010) |
| | | Transport adapter for PTVs (Fejtova et al. 2009; Shapira et al. 2003) |
| | | Modulation of synaptic ubiquitination and proteostasis (Waites et al. 2013; Reimer et al. 2017) |
| | | Clustering of calcium channels (Davydova et al. 2014; Frank et al. 2010) |
| | | Involvement in the interaction between synaptic activity and gene expression (Ivanova et al. 2015) |
| Munc13 | 200 | SV priming and fusion (C. Ma et al. 2011; Betz et al. 2001; Xiaolu Wang et al. 2009) |
| | | Presynaptic plasticity (Junge et al. 2004; Dulubova et al. 2005) |
| Tomosyn | 130 | Regulating SV and dense-core vesicle (DCV) secretion (Geerts et al. 2017) |
| RIM | 190 | SV priming (Y. Wang et al. 1997) Calcium channel recruitment to AZ (Ko et al. 2003; Kaeser et al. 2011) |

The four components required for rapid and accurate excitation-secretion coupling are vesicle docking, priming, Ca²⁺ triggering, and vesicle fusion (Wojcik and Brose 2007). According to a popular concept, vesicle docking involves the attachment SVs to the presynaptic plasma membrane, where they develop to become fusion competent (priming), which results in the formation of an RRP (readily releasable pool) of SVs that can be released speedily in response to Ca²⁺ flux into the cell (Südhof 2013). A substantial protein complex comprised of RIM, RBP, and Munc13 ensures the docking and priming of SV and the recruitment of Ca²⁺ channels in mammalian AZs (Kaeser et al. 2011; Südhof 2013).

The association of RIM with the tiny vesicular GTP (guanosine triphosphate)-binding proteins Rab3 and Rab27 docks SVs (Gracheva et al. 2008; Kaeser et al. 2011; Han et al. 2011; Fernández-Busnadiego et al. 2013) while activation of Munc13 by RIM results in SV priming through the SNARE complex formation (Brose et al. 1995; Augustin et al. 1999; Betz et al. 2001; Richmond, Weimer, and

2. Introduction

Jorgensen 2001; Deng et al. 2011; C. Ma et al. 2013). SVs and Ca²⁺ channels are closely accompanied in order to respond rapidly to changes in AZ Ca²⁺ concentrations. Such precise proximity is established via the interplay of RIM and RBP, which cooperate to recruit Ca²⁺ channels towards fusion sites (Hibino et al. 2002; Han et al. 2011; Kaeser et al. 2011; Liu et al. 2011).

Some of the molecular and functional characteristics of individual components of the AZ are described in further depth below.

A. Munc13 Proteins:

The Munc13 protein family in vertebrates consists of Munc13-1, Munc13-2, Munc13-3, and Munc13-4 (Koch, Hofmann, and Brose 2000). Alternative splicing of the Munc13-2 gene results in the production of two isoforms, one of which is ubiquitously expressed (ubMunc13-2) and the other of which is produced exclusively in the brain (bMunc13-2) (Betz et al. 2001).

In terms of their central and C-terminal regions, all Munc13 isoforms have a highly homologous structure that includes a C1-domain which can connect the second messenger diacyl-glycerol (DAG) and β -phorbol esters (β -PE) (Koch, Hofmann, and Brose 2000), a central Munc homology domain (MUN) (Basu et al. 2005) surrounded by two C2-domains, a central C2B-domain, and a C-terminal C2C-domain (Schoch and Gundelfinger 2006).

According to its functional characteristics, Munc13 is crucial for synaptic vesicle priming. It has been reported that Munc13-1-deficient mice do not feed and could be recognized from wild-type mice soon after birth due to a lack of milk in their stomachs, fragility, and a decreased respiratory rate. Just a few hours after birth, mutant mice die due to their abnormalities. The overall shape and cytoarchitecture of mutant brains and the arrangement of synaptic markers (synaptotagmin, synapsin) were indistinguishable from those of wild-type controls in newborn offspring from heterozygous interbreeding. Electrophysiological analysis of cultured single hippocampal neurons from wild-type and mutant hippocampi showed no significant differences in overall morphology or cell density. Whole-cell patch-clamp examination, on the other hand, indicated a significant phenotypic shift in Munc13-1-deficient cells. Although wild-type and heterozygous hippocampus neurons elicited comparable robust excitatory postsynaptic responses. (Augustin et al. 1999).

Munc13-1's activity is closely coordinated by Ca²⁺ (through the C2B-domain, diacylglycerol synthesis, and calmodulin) and RIM (Südhof and Rizo 2011; Deng et al. 2011). The Munc13-RIM interaction is regarded as the beginning point of priming since it has been discovered that Munc13 can exist in the form of a self-inhibited homodimer, which must be transformed into an active RIM/Munc13 heterodimer by interaction with RIM (Deng et al. 2011; Dulubova et al. 2005).

It has been identified through genetic studies in *C. elegans* (Richmond, Davis, and Jorgensen 1999), *Drosophila* (Aravamudan et al. 1999), and mice (Augustin et al.

2. Introduction

1999; Varoqueaux et al. 2002) that Munc13 proteins are required for the maturation/priming of synaptic vesicles in order for them to acquire the competent fusion state, as well as for the generation and maintenance of the readily releasable pool of synaptic vesicles.

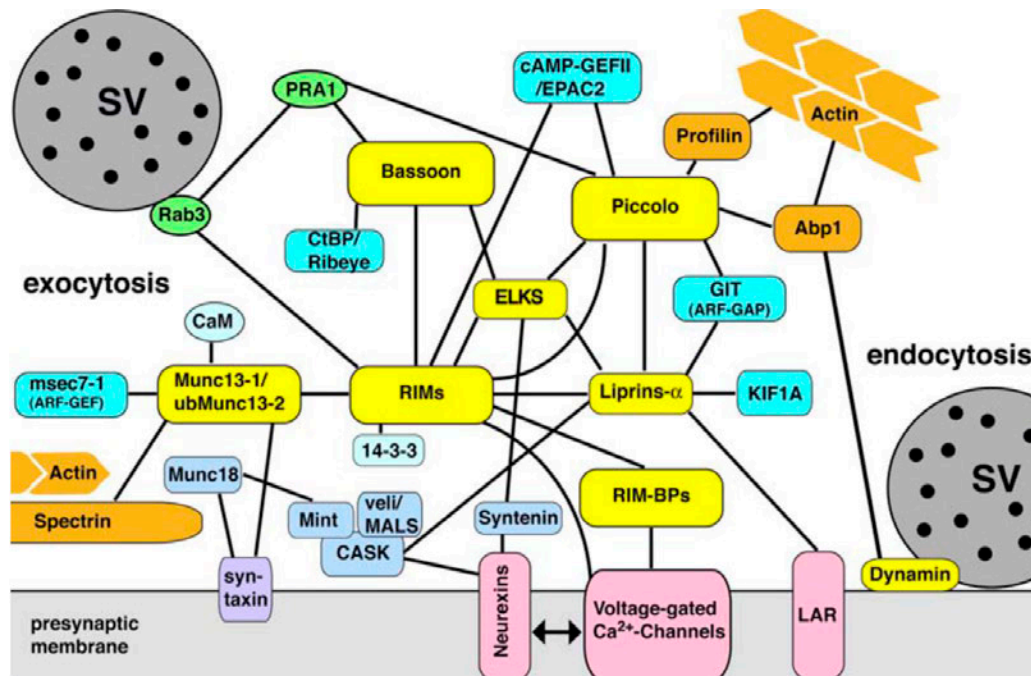


Figure 4. Schematic diagram illustrates how the CAZ proteins interact to form a network that regulates the active zone. for abbreviations, see Abbreviation Table) (Eckart D. Gundelfinger and Fejtova 2012)

Neurotransmitter release in short-term synaptic plasticity is significantly facilitated by Munc13s (Rosenmund et al. 2002). Notably, Munc13-1-expressing synapses exclusively exhibit short depression during a train of action potentials; however, ubMunc13-2-expressing neurons show short-term augmentation (Schoch and Gundelfinger 2006).

B. Rab3-interacting molecule 1 (RIM) and RIM-Binding Protein (RIM-BP):

RIM1 was initially discovered as a potential Rab3 effector and is plentiful in synaptic vesicles (Y. Wang et al. 1997). RIM1 is a member of a broad family of proteins that are expressed by four genes that provide over 200 variations because of alternative splicing (Y. Wang and Südhof 2003). Not only the long isoforms (RIM1 α and RIM2 α) but also the short isoforms (RIM3 γ and RIM4 γ) of RIM have been shown to influence voltage-gated calcium (Ca_v) channels (Kiyonaka et al. 2007; Uriu et al. 2010; Kaeser et al. 2011). Kaeser et al. observed that a direct connection between the RIM PDZ-domain and the Ca_v2.1 or Ca_v2.2 C termini is essential for anchoring Ca_v2 channels to active zones since genetic deletion of

2. Introduction

RIM influences the coupling between Ca^{2+} and neurotransmitter release (Kaeser et al. 2011). RIMs interacting with various synaptic proteins (Figure 4) have been identified. *C. elegans* and mice genetic Studies revealed that RIM is necessary for synaptic vesicle docking (Koushika et al. 2001; Schoch et al. 2002; Gracheva et al. 2008; Han et al. 2011) and the recruitment of Ca^{2+} channels to AZs (Kaeser et al. 2012) and short-term plasticity (Schoch et al. 2002). RIM may tether Ca^{2+} channels (voltage-dependent calcium channel) to active zones through three main pathways (a) via interaction with the $\text{Ca}_v\beta$ subunit, (b) with association with the $\text{Ca}_v\alpha1$ subunit, and (c) through indirect interaction with RIM-BP (Acuna et al. 2015).

C. Bassoon and Piccolo:

Bassoon and Piccolo were found in a screen intended to detect structural components of rat synaptic connections (Cases-Langhoff et al. 1996; Langnaese et al. 1996). According to their molecular characterization, they are structurally similar multi-domain proteins that contain ten highly conserved areas, known as Piccolo-Bassoon homology domains (Tom Dieck et al. 1998; X Wang et al. 1999; Fenster et al. 2000). Bassoon is composed of two zinc finger domains at the N-terminus, three coiled-coil domains, and glutamine repeats at the C-terminus (Tom Dieck et al. 1998). In contrast to Piccolo, Bassoon does not directly engage in F-actin dynamic (Torres and Inestrosa 2017). Bassoon and Piccolo have a role in the organization of the neurotransmitter release mechanism, particularly the tethering of SVs and priming of SVs at AZs. Thus, both proteins contribute to the development of the CAZ core complex, which attracts components required for SV tethering and priming, such as Munc13s and RIM1/2 α -isoforms. Additionally, Bassoon's C-terminus has the potential to interact with Munc13's N-terminal C2A domain (Xiaolu Wang et al. 2009). Bassoon, Piccolo, and Munc13-1 are closely linked with CAST's center coiled area (Takao-Rikitsu et al. 2004; Xiaolu Wang et al. 2009; Hida and Ohtsuka 2010).

Interestingly, the disruption of binding between CAST and Bassoon does not have any impact on synaptic localization of CAST and Bassoon at nerve terminals, contrasting to the disruption of the binding between CAST and RIM1 (Takao-Rikitsu et al. 2004). However, when excitatory postsynaptic potentials (EPSPs) are recorded from cultured superior cervical ganglion neurons (SCGNs), the disruption is shown to substantially decrease neurotransmission (Takao-Rikitsu et al. 2004).

Notably, the absence of Bassoon at central synapses results in a fewer fusion competent SV and a reduction in the RRP pool size of vesicles at glutamatergic synapses, as well as an increase in short-term depression and a significant percentage of silent synapses (Altrock et al. 2003; Fejtova et al. 2010). Additionally, the loss of Bassoon from both ribbon-type (Frank et al. 2010; Jing et al. 2013) and *Calyx* of Held synapses (a huge synapse in the mammalian

2. Introduction

auditory CNS) (Mendoza Schulz et al. 2014) results in a reduction in SV replenishment and the size of RRP, indicating that Bassoon plays an essential role in the plasticity of neurotransmitter release (Hamada and Ohtsuka 2017; Torres and Inestrosa 2017).

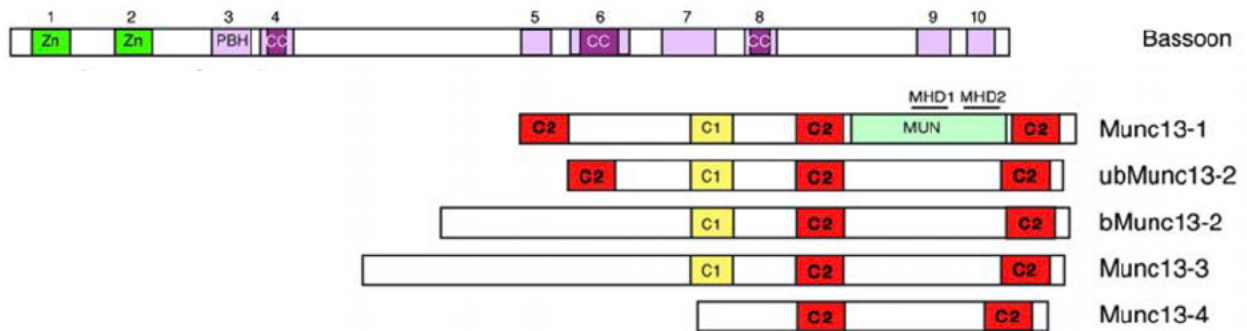


Figure 5. Domain structure of CAZ protein Munc13s and Bassoon. [modified from (Schoch and Gundelfinger 2006)]

Munc13s are composed of two or three C2-domains and one C1-domain that are engaged in the binding to diacyl-glycerol and phorbol esters. The bassoon is formed by two zinc-finger domains (ZN1, ZN2), three CC coiled-coil domains, multiple Q proline and ten, ofhomology, so-called Piccolo Bassoon homology, areas.

D. Tomosyn:

Tomosyn, also referred to as syntaxin-binding protein, is a 130-kDa cytosolic protein that inhibits synaptic transmission and vesicle release probability (Fujita et al. 1998; Yizhar et al. 2004; Baba et al. 2005; Gracheva et al. 2006; Ashery 2009). Tomosyn is transcribed in mammals by two genes: tomosyn1 and tomosyn2, which collectively create seven isoforms: tomosyn1 splice s, b, and tomosyn2 splice s, m, b, and xb (Groffen et al. 2005). The distribution of tomosyn1 mRNA transcripts in the mouse hippocampus implies that it is distributed uniformly in the dentate gyrus (DG) granular cell bodies and at a slightly reduced but comparable level in CA3 and CA1 pyramidal cell bodies (Groffen et al. 2005).

Tomosyn-1/STXBP5 protein was first isolated from the brain. S-Tomosyn and mtomosyn, two isoforms of Tomosyn-1/STXBP5, are selectively expressed at the neural synapse (Yokoyama et al. 1999). In the mouse hippocampus, evidence indicates that tomosyn-1/STXBP5 is strongly expressed in glutamatergic synapses, with variable expression within these synapses in various anatomical areas of the mouse hippocampus (Yokoyama et al. 1999; Barak et al. 2010). In particular, new data reveals that tomosyn-1/STXBP5 is concentrated in hippocampus mossy fiber-to-CA3 synapses and that lack of this protein significantly decreases long-term potentiation (Ben-Simon et al. 2015). Tomosyn-1/STXBP5 does seem to have a functional impact on the priming of vesicles prior to membrane fusion (Batten et al. 2016). Tomosyn2 mRNA levels, on the other

2. Introduction

hand, are more expressed in the CA2 pyramidal cell bodies and relatively equally distributed in the granular cell bodies of the dentate gyrus and CA1 pyramidal cell bodies (Barak et al. 2010).

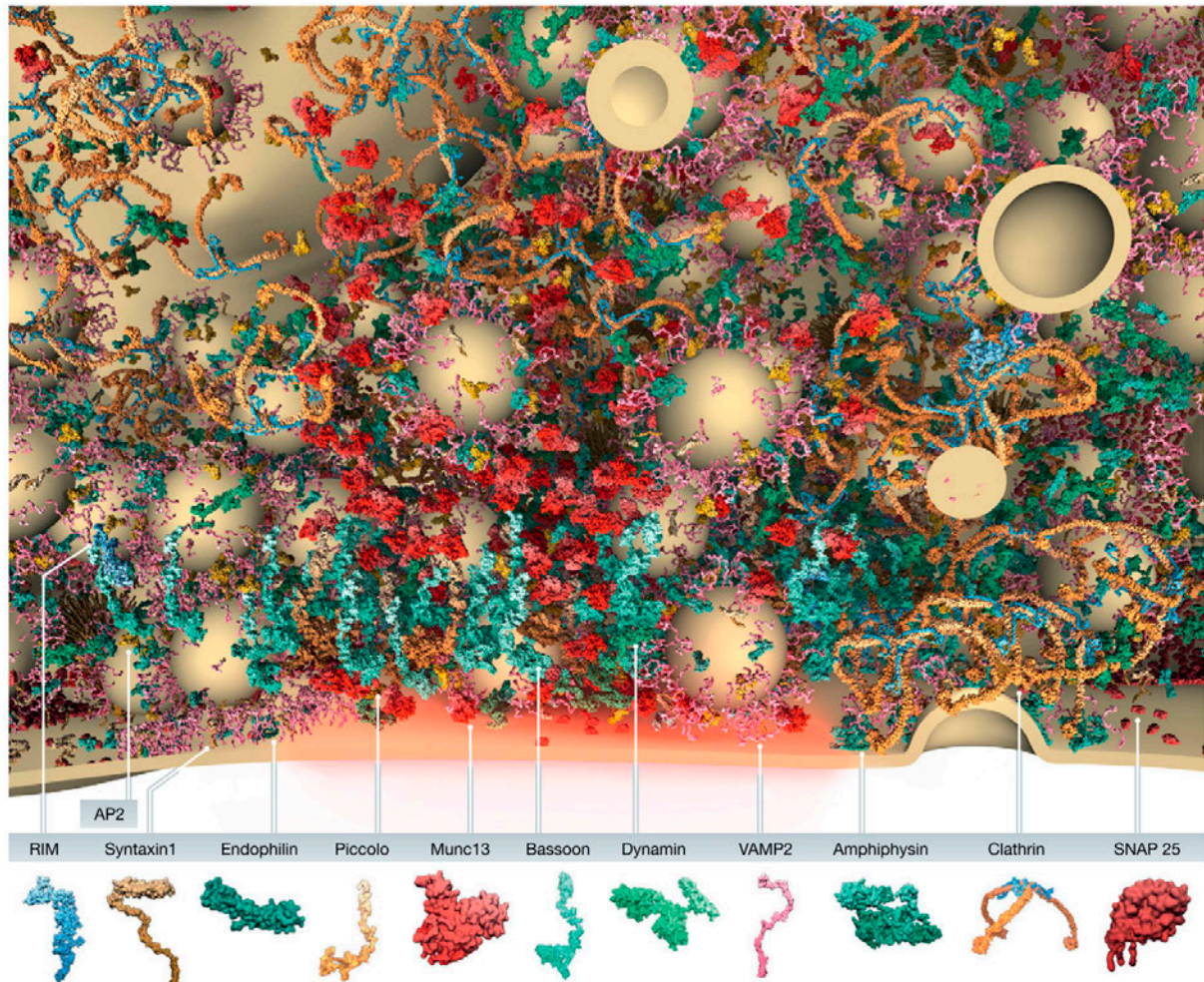


Figure 6. Schematic model of the presynaptic bouton and the composition of the active zone proteins.

A segment across a vertebrate synapse's active and endocytic zones illustrating the spatial distribution and copy quantity of presynaptic proteins. The bottom panel has a graphical caption describing the estimated structures of the model's presynaptic proteins. The SVs on view have a diameter of 42 nm. Burkhard Rammner of the Rizzoli Laboratory graciously created the illustration (Ackermann, Waites, and Garner 2015; Wilhelm et al. 2014).

2.1.4 Synaptic plasticity and memory

The basic concept that learning is associated with changes in synaptic strength was proposed by Ramón y Cajal and later refined by Donald Hebb (Hebb DO

2. Introduction

1949). Donald Hebb hypothesized in the late 1940s that synaptic transmission is a dynamic phenomenon, and associative memories are generated in the brain through a synaptic remodeling process that reinforces connections when presynaptic activity corresponds to postsynaptic firing (Hebb DO 1949). Until the early 1970s, experimental evidence for such long-lasting, activity-dependent changes in synaptic strength was lacking until Bliss and colleagues revealed that repetitive stimulation of excitatory synapses in the hippocampus led to potentiation of synaptic strength (Bliss and Lomo 1973; Bliss and Gardner-Medwin 1973).

The Latin “*plasticus*” ultimately derives from the Greek “*plastikós*” or “*plastos*,” which initially meant “moulded, formed.” Synaptic plasticity, an important element of learning and memory, is now known to be the adjustment of synaptic components based on activity, prompting extensive research in both the invertebrate and vertebrate systems (Eric R Kandel 1976; E R Kandel 2001; Bliss and Lomo 1973; Bliss and Collingridge 1993).

Synaptic plasticity was subsequently assigned to either presynaptic modifications in neurotransmitter release effectiveness (Bear and Malenka 1994; Bliss and Collingridge 1993; Enoki et al. 2009; Lisman 2003) or postsynaptic changes in receptor biophysical parameters such as conductivity or receptive probability (Banke et al. 2000; Derkach, Barria, and Soderling 1999; Scannevin and Hugarir 2000). Activity may either increase or depress synaptic transmission. These changes can occur over a wide range of time scales, from milliseconds to hours, days, and, probably, much more extended periods of time (Citri and Malenka 2008). Synaptic plasticity can be expressed in the mammalian brain in a variety of different ways at the same time. Traditionally, various forms of synaptic plasticity have been classified according to the time scale on which they occur and may be generally described as short-term and long-term plasticity (García-Junco-Clemente, Linares-Clemente, and Fernández-Chacón 2005).

2.1.4.1 Short-term synaptic plasticity

Short-term synaptic plasticity alterations manifest themselves as potentiation (STP) or depression (STD) of synaptic reactions, and they may last from around a few hundred microseconds to a few minutes. Short-term improvements are classified as facilitation, augmentation, or post-tetanic potentiation depending on the length and kinetics of their effects. These alterations are transient, as they do not necessitate long-lasting changes to the signaling mechanism, such as membrane protein expression. STP’s cellular mechanisms, which are mainly

2. Introduction

presynaptic, are relatively well characterized. Short-term plasticity is often described by direct presynaptic impacts such as residual increases in intracellular Ca^{2+} concentration, accelerating changes, or reducing some pool of readily releasable vesicles, in the case of depression [reviewed in (Zucker and Regehr 2002)].

2.1.4.2 Long-term synaptic plasticity

The determination of whether the experimental paradigm of long-term potentiation (LTP), a model for synaptic plasticity, is a model that accurately describes memory encoding has been and continues to be a key reason for performing research into synaptic plasticity throughout years (Bailey, Bartsch, and Kandel 1996; Baudry and Lynch 2001; Bliss and Collingridge 1993; Kirkwood, Rioult, and Bear 1996; Martin, Grimwood, and Morris 2000; R A Nicoll and Malenka 1999; Squire 1992; Squire, Knowlton, and Musen 1993; K. M. Harris 2020; Smolen, Baxter, and Byrne 2020). As a matter of fact, numerous earlier studies have tried to establish a direct connection between LTP and memory encoding; however, most of the data points to indirect associations (Smolen, Baxter, and Byrne 2020). Furthermore, the application of pharmacological LTP-inhibitors resulted in learning failure or impairment of memory retention in animal models (R. G. Morris 1989). Currently, LTP is the primary candidate of the *curreea* process, which links activity-based plasticity with learning and memory in the central nervous system (CNS) at many synapses (Alkadhi 2021), and learning, memory, and behavioral adaptability essentially rely on it (Citri and Malenka 2008).

In comparison to STP, long-term plasticity changes occur over hours to weeks. Long-term plasticity changes manifest as either an increase in synaptic strength, LTP, or a decrease in synaptic strength, known as long-term depression (LTD) (García-Junco-Clemente, Linares-Clemente, and Fernández-Chacón 2005).

Traditionally, LTP has been addressed by substituting high-frequency electrical stimulation of a neuronal pathway or repetitive pairings of presynaptic and postsynaptic cell firing for the learning event. Theoretically, LTP is generated when presynaptic activity precedes postsynaptic activity within a temporal window, while LTD is formed when the pairing is reversed. Overall, LTP will improve synaptic effectiveness by allowing more cations to reach the postsynaptic terminals. Yet, based on the experimental protocols used and the brain region being investigated, the actual plasticity results may vary considerably (Abraham, Jones, and Glanzman 2019).

2.1.4.3 Early-LTP and late-LTP

LTP may manifest itself in two distinct forms: early-LTP and late-LTP, distinguished by the length of time they last. In the case of early-LTP, the potentiated state will last roughly 1 to 2 hours and gradually fade over time, reverting to pre-stimulation levels due to homeostatic processes (Vitureira and Goda 2013). This drop happens mainly due to the trafficking of AMPARs, which diminishes the elevated synaptic strength to the level of pre-stimulation (Shepherd et al. 2006; Dong et al. 2015). As early-LTP fades with time, late-LTP has been reported to remain and last from a few weeks (Staubli and Lynch 1987) to months (Abraham et al. 2002) *in vivo*, even perhaps as long as the memory lasts. This endurance is linked to the engagement of several signaling cascades and molecular components such as calcium-dependent enzymes including Ca²⁺/calmodulin-dependent protein kinase II (CaMKII) (Lisman, Yasuda, and Raghavachari 2012; Silva et al. 1992) and CaMKIV (Ho et al. 2000), protein kinase C zeta PKM ζ (Sacktor et al. 1993), and protein kinase A (PKA) (Abel et al. 1997). Taken together, early-LTP and late-LTP operate primarily as cellular determinants of short- and long-term memory, respectively (Bin Ibrahim, Benoy, and Sajikumar 2021).

A significant amount of evidence suggests that N-methyl-D-aspartate glutamate receptors (NMDARs) are critical mediators of information storage during the formation of long-term memory (R. G. M. Morris 2013). Although LTP and LTD mediated by NMDARs are the best-known types of long-term synaptic plasticity, they are not the only physiological processes that modulate synaptic strength consistently. mGluRs are a broad group of glutamate receptors that stimulate adenylate cyclase or release calcium from intracellular storage through IP₃-mediated influx and regulate second messenger levels (Cartmell et al. 1994; Kemp et al. 1994; Pin and Acher 2002). Even when NMDARs are inhibited, activation of mGluRs may induce both LTP (Bortolotto and Collingridge 1993) and LTD (Palmer et al. 1997). It is proven that both presynaptic and postsynaptic pathways could produce long-term increases and reductions in synaptic strength. Aside from mGluR-dependent LTP and LTD that are triggered and produced postsynaptically, there are non-NMDAR variants of long-term plasticity exhibited in presynaptic terminals of glutamatergic synapses (Vose and Stanton 2017).

Moreover, activity-dependent synaptic plasticity, such as LTP, has been linked to a variety of disorders, including neuropathic pain (Zimmermann 2001), stroke (Di Filippo et al. 2008), traumatic brain injury (Shohami and Biegon 2014), and

2. Introduction

epilepsy (Meador 2007). Nonetheless, contemporary neuroscience's concepts of plasticity have yet to be completely defined. For understanding the neurological foundation of many aspects of normal and abnormal brain function, properly grasping the processes behind synaptic plasticity is essential. This work attempts to provide an overview of the structural changes associated with LTP, the most prominent type of plasticity seen in the mouse brain (García-Junco-Clemente, Linares-Clemente, and Fernández-Chacón 2005).

2.1.4.4 Plasticity of AZs

The docked and primed SV position has traditionally been thought to be fixed and irreversible; nevertheless, emerging findings have revealed proof that the docked and primed SV state may be labile and highly dynamic even while at rest. This plasticity of AZ states is both a developmental and mature nervous system event, occurring in reaction to variations in synaptic activity. It is known that synaptic plasticity mechanisms alter the structure and function of the presynaptic terminal and/or the postsynaptic system (Kittel and Heckmann 2016).

When it comes to information processing in a neural circuit, the number, size, and localization of active zones significantly impact how the circuit adjusts in response to various internal and external stimuli. Despite the fact that AZs play a particularly important role in synaptic transmission, it is still difficult to ascertain, how the number and density of active zones within a presynaptic terminal are regulated during the development and maturation of synapses or changes related to synaptic plasticity (Clarke, Chen, and Nishimune 2012).

The assessment of the density of AZs inside an axon that constitutes *en passant* synapses in *C. elegans* uncovered critical biological processes underlying active zone formation. During stimulus-dependent alterations in synaptic effectiveness, active zone density changes in the central nervous system (Jin 2005).

This work aims to investigate the structural and functional relationship of the active zone, including AZs density and number within a single synaptic terminal or a synaptic bouton, and the molecular mechanisms that contribute to the density alteration of active zones during synaptic plasticity.

2.1.4.4.1 Active zones detection with different analysis methods

A broad range of techniques has been developed to appraise active zones, each of which yields a somewhat different appearance. The ultrastructural analysis techniques (discussed in detail in the microscopy chapter) have been used to delineate the active zone and demonstrate its high-resolution structure. Notwithstanding, an investigation of the distribution pattern of all active zones within a single presynaptic terminal is challenging to obtain by utilizing freeze-fracture and tomography methods. Additionally, it is incredibly time-consuming

2. Introduction

to reconstruct serially sectioned transmission electron micrographs of repeatedly sectioned transmission electron micrographs. The relatively recent use of the presynaptic cytosolic protein Bassoon as a marker for active zones has enabled the identification of active zones in the central and peripheral nervous system's synapses via fluorescent immunohistochemistry (Nishimune, Sanes, and Carlson 2004; Dondzillo et al. 2010; Bednarek and Caroni 2011; Chen, Billings, and Nishimune 2011).

2.1.4.5 Induction protocols for LTP

A. High-frequency potentiation

For electrophysiological studies, diverse patterns of electrical stimulation have been utilized in different induction protocols. Conventionally, high-frequency stimulation (HFS) can be applied in which a train or burst of 100 pulses is given for 1 second (100 Hz) (Bliss and Lomo 1973; Bliss and Collingridge 1993; Malenka and Bear 2004). Notably, conventional HFS patterns now seem to be fundamentally distinct from naturally occurring neuronal firing patterns. For instance, it is questionable if hippocampus neurons fire at 100 Hz for a whole second in a live animal, casting doubt on conventional HFS methods. A typical firing burst of three to four spikes from *cornu ammonis* (CA)1 hippocampal pyramidal cells lasts just 30–40 milliseconds (Feder and Ranck 1973; KANDEL and SPENCER 1961; KANDEL, SPENCER, and BRINLEY 1961).

B. Theta burst potentiation

Other scientists chose Theta-burst stimulation (TBS) since it has been proven to be a more physiologically relevant method in free-moving animals than theta stimulation. In 1995, in an experiment by Huerta and Lisman, a single burst of four pulses at 100 Hz was designed to evaluate and determine its efficacy in inducing long-term potentiation (Huerta and Lisman 1995). A single TBS train consists of 5 pulses at 100 Hz with an intertrain break of around 200 ms (Sajikumar and Korte 2011; Park et al. 2019), though the number of trains varies among studies. To produce either early-LTP or late-LTP, the quantity of stimulation can be modified. Differential influences of particular circumstances and pharmacological substances in occluding or amplifying either type of LTP will be investigated via these induction techniques (Park et al. 2019; Y Y Huang and Kandel 1994).

C. Primed burst potentiation

Primed burst (PB) potentiation is another experimental approach used in the CA1 to strengthen the synaptic transmission (Diamond, Dunwiddie, and Rose 1988;

2. Introduction

Rose and Dunwiddie 1986). Commonly, five pulses are utilized in this protocol, with the first pulse taking place 170 milliseconds before the last four pulses (occurring at 100 Hz). Rose and Dunwiddie's article from 1986 was one of the first to demonstrate that the PB stimulation technique elevated the amplitude of population spike (PS), comparable to HFS, indicating that both protocols contributed to the induction of long-term potentiation (LTP) (i.e., PB-PS 243 percent baseline; HFS- PS 331 percent baseline) (Rose and Dunwiddie 1986). Further investigation has revealed that PB is as effective as or more beneficial than HFS and that a small time frame containing particular intervals (140–200 ms), which coincidentally corresponds to 6–7 Hz (i.e., theta range), produces long-lasting modifications (LTP) (Moore, Browning, and Rose 1993; Diamond, Dunwiddie, and Rose 1988; Pavlides et al. 1988).

D. Chemical-Induced LTP

It is also feasible to chemically induce LTP by administering substances such as forskolin (FSK), an adenylyl cyclase stimulator that boosts intracellular cyclic AMP (cAMP) concentrations (Otmakhov 2004; Yan You Huang, Li, and Kandel 1994; Maccaferri, Tóth, and McBain 1998), or through activation of dopaminergic receptors (Navakkode, Sajikumar, and Frey 2007; Navakkode et al. 2010, 2012; Shetty and Sajikumar 2017).

For several reasons, there has been significant interest in establishing LTP chemically rather than electrically. First and foremost, the fact that direct chemical stimulation of particular biochemical processes causes potentiation offers notable support for the participation of these processes in long-term potentiation. Second, to conduct biochemical and morphological investigations of LTP, it is preferable to expand the number of synapses subjected to the plasticity alterations as much as achievable. In order to accomplish this, conventional induction methods, wherein LTP is triggered by electrical stimulation of a small percentage of synaptic inputs to a pyramidal cell, as is usually the case, are insufficient. Synaptic stimulation occurs at random locations throughout the dendritic tree, making it challenging to define the synapses that have been excited. On the other hand, the exposure of stimulants that directly activate biochemical LTP pathways to synapses on a significant proportion of the cells in the preparation offers the potential of modifying a majority of the synapses on a large fraction (Otmakhov 2004).

For some purposes, however, this bath application does not have the precision input that electrical stimulation of separate pathways may provide. In spite of this, it is effective in assessing possible molecular players participating in LTP induction and expression.

Bath application of chemicals that elevate cAMP levels is a commonly utilized procedure for inducing cLTP. It is hypothesized that this method directly activates transcription and translation pathways, leading to the formation of

2. Introduction

protein synthesis reliant late stages of LTP (Otmakhov 2004). This protocol is primarily suitable for N-methyl-D-aspartate (NMDA) independent LTP, where we can observe in mossy fiber (MF) synapse onto CA3 pyramidal neurons (see below) (Wiera and Mozrzymas 2015).

2.2 Hippocampal formation

2.2.1 Patient HM

In 1953, a bilateral mesial temporal lobe resection including “*the anterior two-thirds of the hippocampus and hippocampal gyrus bilaterally, as well as the uncus and the amygdala.*” was done on patient Henry Molaison (also known as patient HM) by neurosurgeon William Beecher Scoville. Molaison had been suffering from epilepsy at the time. Following the operation, Molaison suffered severe amnesia. Scoville and Milner argued in 1957 in a seminal article that structures in the mesial temporal lobe, especially the hippocampi, were critical for the development of recent memories (Dossani, Missios, and Nanda 2015).



Figure 7. Henry Molaison in Hartford, Connecticut, USA, in 1975. (Photograph courtesy of Dr. Suzanne Corkin (Dossani, Missios, and Nanda 2015))

Since then, the hippocampus formation has received a great deal of interest, resulting in a significant number of researchers studying the signals processed by the hippocampal formation, supplying insights into potential roles of mossy fiber synapses within the neural network (Dossani, Missios, and Nanda 2015; Tsanov and O’Mara 2015). This offers a unique opportunity to investigate higher brain features at several levels, spanning from biophysical to behavioral.

2.2.2 Hippocampal synaptic plasticity

In the hippocampus, mossy fiber-CA3 synapses exhibit presynaptic LTP regulated by calcium inflow through voltage-dependent calcium channels, which results in the generation of the second messenger cyclic AMP (Zalutsky and Nicoll 1990; Maccaferri, Tóth, and McBain 1998; Yan You Huang, Li, and Kandel 1994).

2.2.3 Mossy fiber boutons

2.2.3.1 Anatomy and physiology of mossy fiber

Over a century ago, advances in tissue staining and microscopy facilitated a considerable improvement in the morphological description of the vertebrate nervous system. Golgi, Sala, and Schaffer referred to nerve fibers precisely characterized by the Spanish anatomist Ramón y Cajal (S. Cajal 1888; Ramon y Cajal 1894; Ramón y Cajal 1909). With their many distinctive varicosities and filopodial extrusions along their axons, these fibers reminded Ramón y Cajal of moss, and he gave them the name of “*fibers moussues*” (Palay and Chan-Palay 2012; S. R. Y. Cajal 1894).

Unmyelinated mossy fibers in the hippocampus originate from granule cells in the dentate gyrus and demonstrate collateralization in the hilar (Claiborne, Amaral, and Cowan 1986).

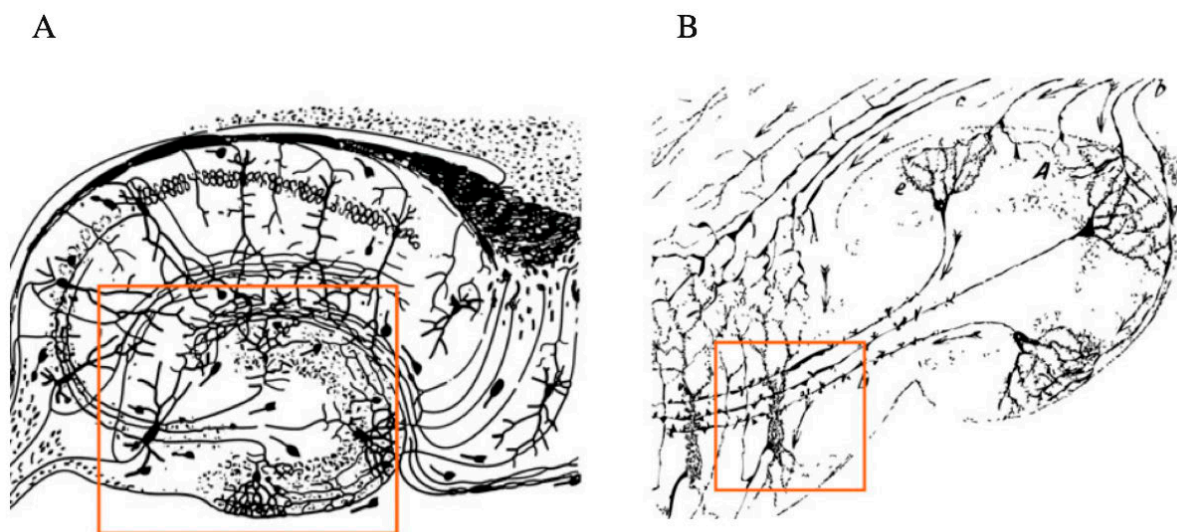


Figure 8. Anatomical component drawings of a hippocampus A, B (Ramón y Cajal), microscopic illustration of mossy fibers and their postsynaptic target cells.

The dentate gyrus granule cells produce mossy fiber axons that pass further into CA area of the hippocampus (Ramon y Cajal 1894; Ruediger et al. 2011).

This mossy morphology is owing to the fact that, unlike axons of other cortical fundamental neurons, granule cell axons have more than one ending form: in addition to massive mossy fiber boutons (MFBs), these boutons also include tiny filopodial extensions (Roger A. Nicoll and Schmitz 2005). Granule cells of the hippocampus dentate gyrus are the brain’s most peculiar neuronal population.

2. Introduction

They are constantly produced throughout one's life, which is a feature that may be linked to their function in the formation of memories (Seress and Frotscher 1990).

Granule cells acquire completely separated cortical and hippocampus internal input. Tracing of nonmyelinated axons of granule cells demonstrated that throughout passing thru the hilus, each MF provides existence to several branching collaterals, which interact with a multitude of hilar neurons, whereas the primary axons proceed forward into the pyramidal cell layer of the hippocampus CA3 region. In the CA3 region, MFs do not generate collaterals, they are laminar-organized along with the pyramid cell layer, and their projection is confined to the *stratum lucidum* (Evstratova and Tóth 2014).

2.2.3.2 The mossy fiber synapse onto CA3 pyramidal neurons

One of the most extensively investigated synapses in the CNS is the dentate mossy fiber (MF) input onto hippocampal CA3 pyramidal cells.

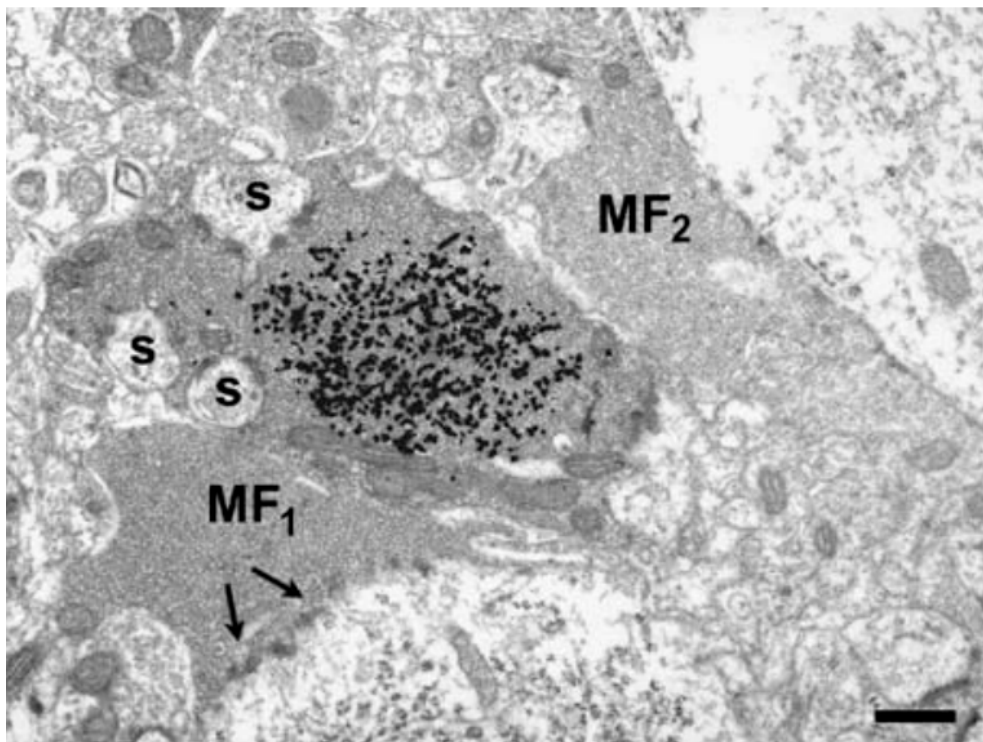


Figure 9. characterization of hippocampal mossy fibre synapses using Golgi impregnation and electron microscopy (Frotscher, Jonas, and Sloviter 2006).

Two giant mossy fiber boutons (MF1, MF2) were observed utilizing Golgi impregnation and gold toning in the light microscope. Gold grains are distributed throughout MF1 but do not obscure the vast number of synaptic vesicles. The bouton generates multiple non - symmetric connections between neurons with invagination of the presynaptic terminal by CA3 pyramidal cell spines (s). (Puncta adhaerentia on a proximal dendritic shaft are as seen by the arrows.)

2. Introduction

Despite the enormous amount of data about the structure and function of this synapse, we are still a long way from fully comprehending this complex structure. MFs are distinctive in their function in transforming incoming cortical signals and ensuring the accurate delivery of the resultant code to the CA3 region. The dentate gyrus is the primary mediator in the cortico-hippocampal circuit. It is responsible for translating tightly coded cortical impulses into sparse and particular hippocampus coding, which is crucial for hippocampal memory formation (Acsády and Káli 2007). These unique synaptic terminal features were discovered by slim sectioning of a Golgi-impregnated gold-toned terminal expansion of a mossy fiber axon for electron microscopy.

In comparison to other forms of presynaptic cortical boutons, the gold-labeled detected bouton is significantly larger. It is tightly packed with transparent synaptic vesicles, plus mixed with a few dense-core vesicles. As seen in Figure 9, several asymmetric synaptic connections are formed with the extremely complicated spines of the postsynaptic pyramidal cell projecting deeply into the presynaptic bouton (Chicurel and Harris 1992; Sätzler et al. 2002; Frotscher, Jonas, and Sloviter 2006).

Table 2 Links between DG–CA3 synaptic plasticity and memory

| | |
|------------------------------------|---|
| Suggested roles | Facilitate the encoding of memory in the CA3–CA3 network. |
| | Contribution to pattern separation DG cell sparse firing activity is impacted as a consequence (Rebola, Carta, and Mulle 2017) |
| Indications via experiments | Differential outcomes on pattern separation and completion have been observed when the output of adult DG neurons is Transgenic inactivated compared to the output of developmentally born DG neurons (Nakashiba et al. 2012) |
| | Novel contextual representation is altered by pharmacological disruption of DG–CA3 transmission (Lassalle, Bataille, and Halley 2000; Daumas et al. 2009) |
| | The impaired mossy fiber LTP in mice leads to an incremental learning deficiency (Otto et al. 2001) |
| | Electrically induced plasticity is regulated by exposure to new circumstances (Hagena and Manahan-Vaughan 2011) |
| | Remodeling of the structural properties of mossy fibers CA3 boutons occur as a result of learning (Routtenberg 2010; Holahan et al. 2006; Ruediger et al. 2011) |

Unlike most other synapses in the central nervous system, the hippocampal mossy fiber synapse onto CA3 pyramidal neurons has high paired-pulse facilitation

2. Introduction

(PPF), with a ratio >3 in the majority of situations (Salin et al. 1996). Additionally, LTP in the hippocampus's mossy fiber pathway exhibits the expected time pattern of enhanced post-synaptic reactions. In contrast to other excitatory hippocampus synapses, MFBs express LTP presynaptically (Goussakov et al. 2000). In the CA3 region, a single granule cell axon generates 15 giant MFBs, and one CA3 pyramidal neuron gets input from 50 MF axons (Amaral, Ishizuka, and Claiborne 1990). Hence, the morphological features of the MF synaptic connection are aligned with the notion that it forms a strong but sparse synaptic connection (Astrid Rollenhagen and Lübke 2010).

The high synaptic effectiveness and plasticity observed at the MFB-CA3 pyramidal neuron synapses may be partly related to the structure of the pool of synaptic vesicles in the giant MFBs. According to Rollenhagen et al., Mossy fiber boutons are extremely varied in form and size, with cross diameters ranging from 2 to 5 microns, surface areas ranging from 40 to 110 microns, and volumes ranging from 2 to 13 μm^3 (Astrid Rollenhagen and Lübke 2010). As mentioned previously, the number, size, and distribution of AZs inside a particular synapse are among the most important structural parameters of synaptic transmission and long- and short-term plasticity in the brain. The pre- and postsynaptic densities at MFBs produced zones of an electron-dense blurry component. According to the observations of Rollenhagen et al. at each MFBs, two types of AZs were identified: the significant number (approximately 80 percent) had pre- and postsynaptic densities that were most often disrupted, leading to the appearance of perforated structures, whereas the remaining AZs either had indentations in the pre- or postsynaptic densities or were non-perforated (A. Rollenhagen et al. 2007). Although much progress has been made, there are still many open questions, which need to be addressed in the future.

This study aims to gain a better quantitative comprehension of the structural and functional plasticity of hippocampus mossy fiber active zones. It is on the foundation of these quantitative structural data on the MFB that numerical measurements and accurate models of MF transmission can be discovered.

2.3 Microscopy

2.3.1 Optical light microscopy; Diffraction-Barrier and Its Impact

The relationship between the structure and function of objects is a fundamental topic in neuroscience. Imaging technologies serve as the principal platform and pave the way for fundamental research in nearly all fields throughout the life sciences. Since the earliest explorations of biological structures in the 17th century by early pioneers of microscopy such as Robert Hooke and Antoni van Leeuwenhoek, technological advancements and superior manufacturing have resulted in significantly improved picture quality but have ultimately been limited by the optical resolution (Schermelleh, Heintzmann, and Leonhardt 2010).

The term “resolution” is often used to refer to the farthest distance at which the image of two point-like elements seems to merge. In the late nineteenth century, Ernst Abbe and Lord Rayleigh described and formalized this diffraction-limited resolution based on experimental data and fundamental physics principles (Abbe 1873; Rayleigh 1903). For more than a century, the Abbe diffraction limit was described as $\lambda/2NA$, where λ indicates the wavelength and NA represents the numerical aperture of the microscope objective lens (Abbe 1873).

The conventional light microscopy resolution range is about 250 nm in the direction x and y and approximately $> 450\text{--}700$ nm in the direction of z. This limit, also known as the point-spread function (PSF), is the defined size of the propagation of a single point of light diffracted through a microscope; it also measures the minor point source or item size a microscope can resolve. Objects tinier than the PSF in the microscope come out to be of the same size as the PSF, and elements closer to one another than the breadth of the PSF cannot be differentiated separately (Abbe 1873; Ryan et al. 2017).

During the past few decades, confocal microscopy has been the standard fluorescent imaging technique for studying neural tissue in the field of neuroscience (Conchello and Lichtman 2005). In fixed neural preparations, laser-scanning confocal microscopy obtains three-dimensional and multi-color illustrations, which can be differentiated down to the level of single-cell and dendritic architecture. Complementary details on the neuronal and sub-compartmental ultrastructure and connectivity assessment are obtained in the brain utilizing electron microscopy (EM) (Koster and Klumperman 2003; Lichtman and Denk 2011). The application of EM is particularly beneficial for the structural investigation of neural synapses and vesicles, cell organelles, and

2. Introduction

membrane conformation. However, EM-based detection of proteins and particular electron density signatures is restricted due to technical limitations of target-specific labeling.

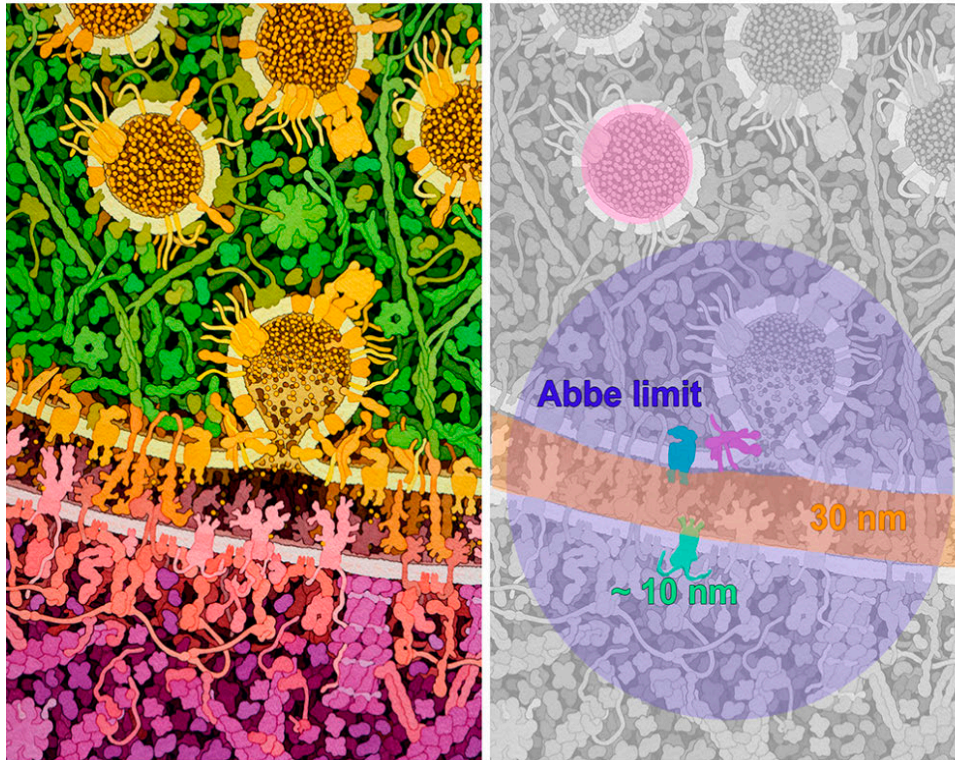


Figure 10. Illustration of pivotal synaptic components and the optical resolution limit imposed by the diffraction limit in light microscopy.

Left: A mesoscale representation of an excitatory synaptic bouton. Presynaptic compartments include synaptic vesicles with a diameter of 40–50 nm (Schikorski and Stevens 1997), and presynaptic calcium channels (dark yellow) are found at synaptic release sites. Vesicle fusion at the synaptic active zone is regulated by the formation of a SNARE complex seen between the synaptic vesicle and the plasma membrane (magenta). Observation of the narrow connecting distance of the SNARE complex at the presynaptic AZ and adjacent calcium channels (cyan). The α -amino-3-hydroxy-5-methyl-4-isoxazolepropionic acid (AMPA) and N-Methyl-D-aspartate (NMDA) receptors are located nearby the presynaptic discharge area in the post-synaptic membrane. Right: The grayscale blueprint of the main illustration on the left captures exemplary aspects of synaptic vesicles (40–50 nm), AMPA-R (10 nm), the synaptic cleft (20–30 nm), and the diffraction-limited spot (200 nm) in pale blue, symbolizes the Abbe limit of light microscopy (Werner, Sauer, and Geis 2021). Acknowledgment: Illustration by David S. Goodsell. DOI: 10.2210/rcsb_pdb/goodsell-gallery-016

2. Introduction

As a step forward in our understanding of neuronal functionality, the development of several new fluorescent dyes, functional probes, and fluorescent proteins, as well as optogenetic methods and optical actuators such as caged compounds, have facilitated not only the characterization but also the manipulation of neurons and their interactions at all levels of the nervous system, from the single-molecule level to the entire nervous system (Conchello and Lichtman 2005; Tønnesen and Nägerl 2013). In parallel, the development of various intravital video microscopy applications, including 2-photon microscopy, has permitted live-cell imaging of neuronal cell cultures, organotypic slice cultures, and intravital imaging in animal models as a component toward gaining a further comprehending neural functioning (Werner, Sauer, and Geis 2021).

However, even with excellent lenses, perfect alignment, and high numerical apertures, light microscopy's optical resolution was restricted to roughly half of the wavelength of the light utilized (Egner and Hell 2005; Galbraith and Galbraith 2011a). In practice, this implied that the light microscopy could resolve only cellular structures and objects with only a separation of at least 200 to 350 nm. For instance, the diameter of synaptic active zones is commonly between 300 and 150 nm in diameter (Ribault, Sekimoto, and Triller 2011). Synaptic vesicles, which are essential for transporting and releasing transmitter cargo, are considerably smaller, with a 40-50 nm diameter, a tenfold reduction in size (K. m. Harris and Sultan 1995). Postsynaptic receptors are bound by transmitters, which are released into the synaptic cleft with a breadth of 20–50 nm (Dittman and Ryan 2009; Takamori et al. 2006).

Therefore, in traditional light microscopy, the exocytosis machinery and trans-synaptic interaction structure remain widely concealed, necessitating an improvement in resolving power of approximately ten times (Figure 10).

A further problem arises from the enormous number of distinct molecules involved in synaptic signaling that should therefore be contained inside the tiny size of synaptic compartments, resulting in molecular density distributions that are difficult to investigate by microscopic techniques.

Even though fluorescence microscopy is the preferred technique for selectively visualizing biomolecules with a high signal-to-background ratio (Lichtman and Conchello 2005), investigation of organizational principles at the molecular scale is beyond the reach of standard light microscopy.

2.3.1.1 Methods for improving light microscopy resolution

Since the late 1800s, scientists in pursuit of scientific data have pushed the limits of optical resolution. Generally, several factors influence the resolution obtained in practice, and only under optimal circumstances does it reach the theoretical limit. To attain the highest feasible resolution described by the diffraction limit, the environment must be homogeneous in refractive index, providing a high signal intensity, and having minimum background signals (Stelzer 1998).

Background or noise may be introduced by optical aberrations in the specimen, along with parameters including microscope alignment and immersion incompatibility, which degrade contrast and diminish effective resolution. In other words, optical aberrations and out-of-focus blur reduce the signal-to-noise ratio and effectively attainable resolution, particularly in the case of complex biological samples. Fluorescence emanating beyond the intended focus plane is a significant noise source, mainly in the imaging of moderately thick biological materials. As a corollary, one popular approach for boosting resolution is to minimize the out-of-focus fluorescence. This may be accomplished computationally, as in image deconvolution, by either preventing detection of out-of-focus light, as in a confocal pinhole, or by limiting fluorophore excitation to a narrower volume (David A Agard and Sedat 1983; D A Agard et al. 1989; Wallace, Schaefer, and Swedlow 2001).

Additional previous information, namely the positive nature of the emitted signal, empowers deconvolution algorithms to “predict” aspects beyond Abbe’s limit. However, the enhancement obtained is object-dependent, with the most significant outcomes achieved for sparse objects such as filaments or vesicles (Heintzmann 2007) and minimal improvement obtained for other structures (Schermelleh, Heintzmann, and Leonhardt 2010).

New methods for bypassing the diffraction barrier were discovered in the late twentieth century, using physical or chemical means to differentiate the emission of distinct fluorophores or reducing the number of concurrently fluorescing molecules to decrease image blurring.

A modified optical path and specialized hardware are used in confocal laser scanning microscopy (CLSM). A narrowly concentrated point of laser light is applied to scan the three-dimensional specimen, and a tiny aperture (or pinhole) in the light path’s confocal imaging plane permits only light coming from the nominal focus to pass (Cremer and Cremer 1978; C. J. Sheppard and Wilson 1981; Brakenhoff et al. 1985). The objective lens collects the emission from this focal volume, as it would normally. However, instead of being captured by the

2. Introduction

human eye or a camera, it is transmitted to a light-sensitive point detector such as a photomultiplier tube (PMT) or an even more precise avalanche photodiode detector (APD). CLSM has a theoretical advantage over wide-field (WF) fluorescence microscopy in terms of resolution.

Numerous modifications to the basic confocal design have been developed over time, including the spinning disc confocal microscope and non-linear confocal imaging techniques such as two-photon imaging. Nevertheless, a comprehensive review of all of these variants is beyond the scope and purpose of this thesis.

2.3.2 Super-resolution microscopy

2.3.2.1 Breaking the diffraction barrier

The super-resolution method was awarded the 2014 Nobel Prize in Chemistry with its potential to break the diffraction barrier (“Nobel Prizes for Super-Resolution Imaging” 2014). The latest technological breakthrough of super-resolution microscopy has reduced the optical resolution limit from ~250 nm to ~10 nm (Vangindertael et al. 2018). The development of different super-resolution imaging techniques and customized fluorescent probes has provided clear visibility into the neural structure and protein configurations in cellular sub-compartments at a level of resolution previously unattainable. Individual molecules can now be observed in their dynamic interactions. Super-resolution microscopy provides scientists with intriguing possibilities to address questions regarding the cell's inner workings that were previously unavailable. As commercial super-resolution microscopes become accessible, the significance of super-resolution microscopy is speedily increasing. Nonetheless, super-resolution microscopes are not based on a single innovation, and the dissimilarities between the technologies may influence how each method is suitable for dealing with a definite biological cell challenge (Werner, Sauer, and Geis 2021; Schermelleh et al. 2019; Nosov, Kahms, and Klingauf 2020).

Super-resolution (SR) techniques can be classified into near-field and far-field methods, with subdivisions depending on the underlying fundamental principles that offer a sub-diffraction resolution. One can distinguish near-field from far-field techniques conceptually and determine if the sub-diffraction resolution is dependent on a linear or non-linear reaction of the sample to its locally illuminating (exciting or depleting) irradiance.

2. Introduction

It should be emphasized that each of the novel imaging techniques has its unique signal-to-noise consideration, which differs based on a variety of parameters (Schermelleh, Heintzmann, and Leonhardt 2010; Schermelleh et al. 2019). The fundamental principles behind these techniques are briefly discussed and described below.

2.3.2.2 Near-field methods

In order to visualize the structures near the membrane, near-field scanning optical microscopy (NSOM) (Lewis et al. 2003) and total internal reflection microscopy (TIRF) (Axelrod 2001) can be applied. Near-field scanning optical microscopy (SNOM, NSOM) is a complex near-field technique that scans samples using an extremely small physical aperture, much smaller than the wavelength of light, such as positioned at the end of tapered glass fiber, instead of employing objective lenses. In this case, the evanescent wave is limited laterally and axially, thus bypassing the diffraction limit in all three dimensions of space, bringing the resolution to below 20 nm (Lewis et al. 2003; Eric Betzig and Trautman 1992). However, the fundamental limitation remains since only surface components may be visualized (de Lange et al. 2001; Höppener et al. 2005; van Zanten et al. 2009). TIRF only improves axial resolution to below the diffraction limit ($\sim 100\text{nm}$). The exponential decay of the evanescent field illumination intensity in this method confines excitation to a thin region of 100–200 nm under the cover glass surface. The signal-to-noise ratio in the TIRF method is enhanced compared to any computational approach of out-of-focus blur reduction since there is virtually no signal from out-of-focus areas. Even though TIRF microscopy (TIRFM) has become a proper and relatively straightforward standard technique in those domains of cell biology which deal with structural features and dynamics (e.g., exo- and endocytosis in the plasma membrane, adhesion, and cytoskeleton), much of the cell interior remains inaccessible (Axelrod 2001; Ryan et al. 2017).

2.3.2.3 Far-field methods

In addition to these rather relatively specialized near-field methods, three more broadly practicable far-field techniques have been developed, including structured illumination microscopy (SIM) (M G L Gustafsson 2000), stimulated emission depletion (STED) (S W Hell and Wichmann 1994; Klar et al. 2000; Donnert et al. 2006; Willig et al. 2006; Göttfert et al. 2013), and single-molecule

2. Introduction

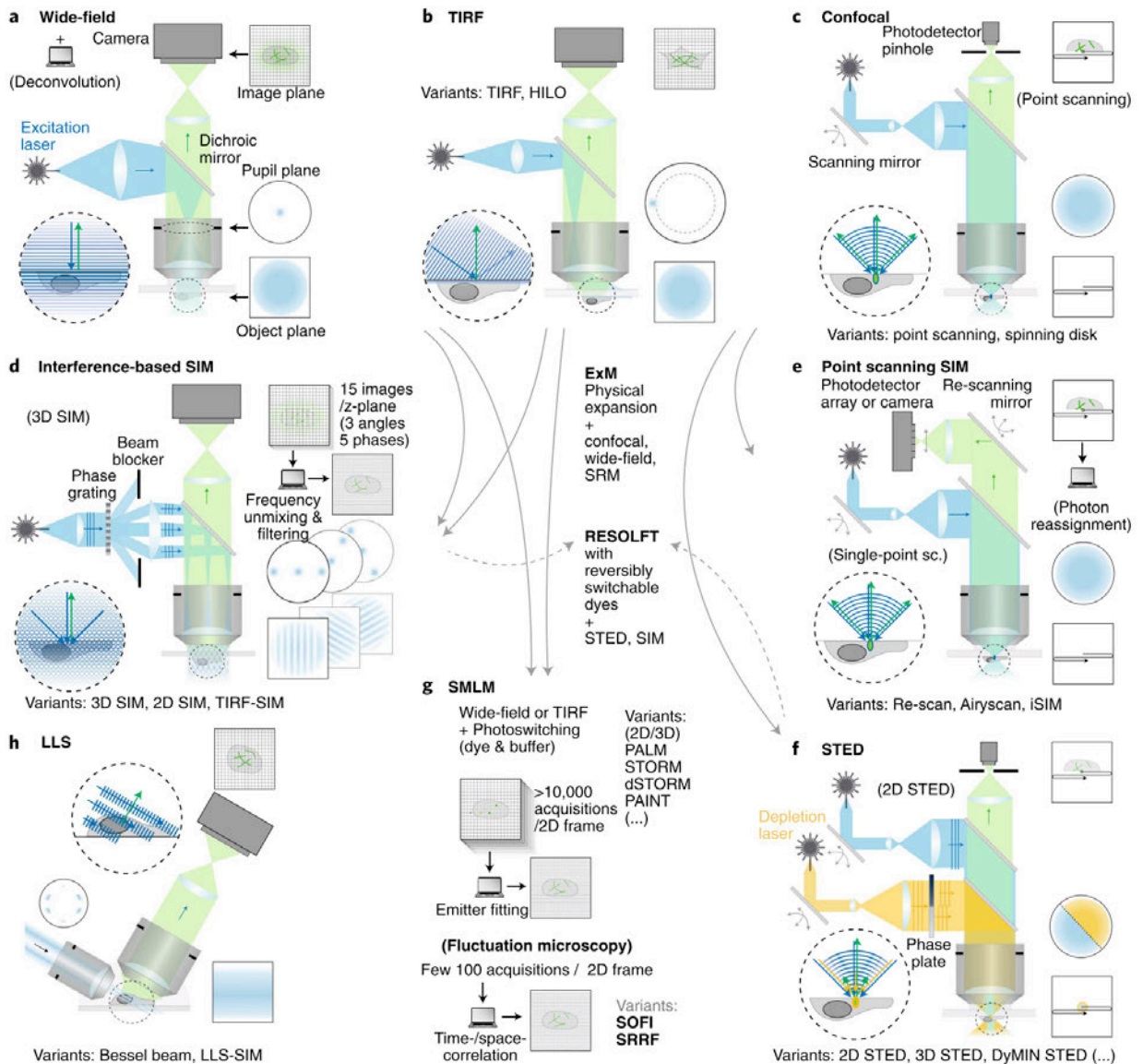


Figure 11. Fundamental principles of super-resolution microscopy.

Light pathways of common conventional (a–c) and SR (d–h) microscopy methods. a) The excitation light is focused to a single spot in the pupil plane to generate wide-field illumination. b) In TIRF microscopy, the excitation beam is angled to be fully reflected at the coverslip–sample/solution contact, resulting in a fast fading evanescent wave near to the coverslip surface. c) The pupil plane is filled in confocal microscopy, producing a focused point on the image plane that may be scanned throughout the field-of-view. Therefore, the emitted light is detected with either concurrently via a camera or through point by point photo detection. d–h) Dashed arrows signifies potential combinations of advanced methods. Advanced imaging techniques are formed as the center grey arrows demonstrate from conventional setups. Round illustration magnifications depict excitation wavefronts (blue lines and arrows) and emission wavefronts (green arrows). modified from (Schermelleh et al. 2019).

2. Introduction

based localization microscopy methods such as photoactivated localization microscopy (PALM), and direct stochastic optical reconstruction microscopy (dSTORM). These methods bypass the diffraction barrier by temporally isolating the fluorescence emission of distinct fluorophores in a deterministic (SIM, STED) or stochastic (PALM, *d*STORM) manner. Fundamental principles underlying some of these techniques are illustrated in Figure 11.

A. STED

In Coordinate-targeted nanoscopy methods, including STED and reversible saturable/switchable optical linear (fluorescence) transitions (RESOLFT) (Hofmann et al. 2005; Brakemann et al. 2011; Grotjohann et al. 2011) microscopy, using a focused excitation laser and a and a second overlaid doughnut-shaped laser, light is employed to cause transitions between two states and to turn on and off fluorophores at specified spatial coordinates.

The light in this manner features intensity minima (one, several, or many), optimally with zero intensity, where there is no off-switching, and fluorophores in the on state may fluoresce. Furthermore, the opposite situation, namely, on-switching everywhere except at the minima, can be achieved. In these two method point-scanning implementations in two dimensional (2D), the minimum is located in the center of a doughnut-shaped light focal point. This technique shrinks the size of the excitation spot and enables resolutions of 40 nm and less to be obtained (S W Hell and Wichmann 1994). STED has been modified to provide multi-color and three-dimensional imaging, and configurations that reduce acquisition time and laser intensity have formed STED a potential choice for live imaging (Stefan W Hell 2007; Nägerl et al. 2008; Schermelleh, Heintzmann, and Leonhardt 2010; Tønnesen et al. 2014).

B. STORM

STORM or photo-activated localization microscopy (PALM) relay on stochastic photoactivation, photoconversion, or photoswitching of fluorophores to detect single emitters. At the moment, the majority of implementations of the PALM/STORM principle depend on fluorophore blinking in the presence of excitation light, as in the ground state depletion with individual molecule return method (Bock et al. 2007; Egner et al. 2007; Fölling et al. 2008), also referred to as *direct* STORM (*d*STORM) (Heilemann et al. 2008). Substantially, in order to determine the exact position of these molecules, the intensity profiles of single emitters are fitted (coordinate- stochastic nanoscopy) using, for example, a 2D Gaussian function.

2. Introduction

Following imaging various subsets of fluorescent molecules repeatedly, super-resolution images are rebuilt by assembling all of the localized points.

The detection and localization of all fluorophores defining the structure of interest must occur at least once throughout the image acquisition process in order for these techniques to function properly (E Betzig et al. 2006; Hess, Girirajan, and Mason 2006; Heilemann et al. 2008; Rust, Bates, and Zhuang 2006).

For the on-off states of the fluorophore, PALM employs photoactivatable probes that are expressed genetically (E Betzig et al. 2006; Hess, Girirajan, and Mason 2006). STORM necessitates pairs of cyanine (Cy) dyes, which are usually linked to antibodies up to 15 nm in length, to serve as reporter and activator pairs to shift many times between the dark and light states (Bates, Blosser, and Zhuang 2005; Heilemann et al. 2005). Several stand-alone synthetic dyes, such as Alexa-Fluor dyes, may also be employed in a blinking mode in direct STORM (*d*STORM) to get super-resolution images. The list of (*d*)STORM dyes has been significantly increased in recent years to include rhodamine and oxazine dyes in addition to cyanine dyes (Dempsey et al. 2011; Heilemann et al. 2009; van de Linde et al. 2011).

Despite the technical differences between these techniques, based on the quantity of photons detected per molecule, a localization accuracy of up to 10 nm is obtainable (E Betzig et al. 2006; Hess, Girirajan, and Mason 2006; Bates et al. 2007). With precise single-molecule sensitivity, localization microscopy techniques have the potential to provide quantitative data on molecular distributions, ultimately revealing the absolute quantities of proteins present in subcellular compartments (Sauer 2013).

C. SIM

A subgroup of SRM methods is referred to as super-resolution structured illumination microscopy (SR-SIM) [reviewed in (Heintzmann and Huser 2017; Wu and Shroff 2018)]. SR-SIM is one of the most widely used optical super-resolution methods, and it can be applied to address a broad range of biological questions. The primary advantage of SR-SIM is that it may be applied directly to samples prepared for conventional fluorescence microscopy without needing considerable additional sample preparation effort. Furthermore, SR-SIM may be visualized and implemented on up to four distinct color channels. The fluorophores employed for sample labeling in SIM have no particular additional requirement except that they have to be sufficiently resistant to photobleaching. Structured illumination microscopy has been applied via various schemes (M G L Gustafsson 2000; Heintzmann and Cremer 1999). Consequently, a range of

2. Introduction

terms have been coined to characterize its various implementations, such as conventional interference-based linear 2D-and three dimensional (3D) -SIM approaches (Schermelleh et al. 2008; Kner et al. 2009; Mats G L Gustafsson et al. 2008), total internal reflection fluorescence SIM (TIRF-SIM) (C. J. R. Sheppard, Mehta, and Heintzmann 2013), coherent SIM (Brown et al. 2020), standing wave illumination (Access 2021) as well as more recently presented point scanning SIM techniques (Müller and Enderlein 2010; York et al. 2012; Schulz et al. 2013; York et al. 2013).

While surpassing the ‘traditional’ Abbe resolution limit, SR-SIM methods are still fundamentally constrained by the laws of diffraction, maximum doubling spatial resolution in the lateral (x, y) and axial (z) directions, which is equal to an 8-fold enhancement in volumetric (Schermelleh et al. 2019). Utilizing standard high numerical aperture (NA) objectives, traditional interference-based SIM achieves 100 nm lateral and 300 nm axial resolution via frequency shifting upon patterned wide-field illumination and computational reconstruction (Heintzmann and Cremer 1999; M G L Gustafsson 2000). Since this method relies on sensitive and accurate camera detection, it is highly photon-efficient, enables common imaging with several dyes and conventional fluorophores, and is ideally suited for volumetric live-cell imaging (Shao et al. 2011; Fiolka et al. 2012). However, classic interference-based SIM necessitates mathematical post-processing and a meticulously aligned and adjusted, and calibrated microscope setup, which tends to increase the probability of reconstruction artifacts, where it takes substantial knowledge to detect and counteract (Demmerle et al. 2017).

2.3.2.4 Application in the neuroscience

Though preliminary analyses of small diameter synaptic vesicles were limited to chemically fixed neurons utilizing EM, with the arrival of SRM, the movement of synaptic vesicles in presynaptic components could also be observed by immunotagging the calcium sensor synaptotagmin 1 (Syt 1) on synaptic vesicles and employing video-rate STED microscopy (Westphal et al. 2008). STED microscopy further provided comprehensive information on the distribution of the vesicular calcium sensor synaptotagmin after exocytosis in one of its earliest biological applications (Willig et al. 2006; Wienisch and Klingauf 2006).

Bassoon promotes vesicle release since its absence leads to significantly decreased synaptic vesicle quantities and synaptic depression at cerebellar mossy fiber-granule cell synapses (Davydova et al. 2014; Fejtova et al. 2010). STED microscopy of Bassoon and Piccolo revealed a sandwich configuration with

2. Introduction

Piccolo on either side and Bassoon in the middle (Nishimune et al. 2016), and STORM imaging in brain slices using distance measurements tracked Bassoon's orientation relative to other relevant synaptic proteins in the presynaptic and postsynaptic compartments (Dani et al. 2010).

Tomosyn, a SNARE-binding protein, was recognized by using *d*STORM to be confined to syntaxin clusters, and its β -propeller domain mutation was found to be requisite for complex formation with SNAP-25 (Bielopolski et al. 2014). Moreover, Tomosyn competes with the v-SNARE synaptobrevin to form complexes with syntaxin and SNAP-25, and it has been hypothesized that Tomosyn functions in down-regulating exocytosis (Hatsuzawa et al. 2003).

Unc-13's mammalian orthologue, Munc-13, is another critical component in priming synaptic vesicles for release. Munc-13-3 was demonstrated to attract calcium channels to active zones. 3D-STORM imaging indicated that munc-13-1 clusters at synaptic release sites and interacts with syntaxin molecules (Kusch et al. 2018; Sakamoto et al. 2018). Additionally, STED microscopy in hippocampal slices revealed that RBP2 exerts a significant control on vesicle priming and release probability at mossy fiber synapses through the placement of munc-13-1 (Brockmann et al. 2019).

Single-molecule localization microscopy (SMLM) has been effectively used to investigate cultured hippocampus synapses up to this time (Dani et al. 2010; E Betzig et al. 2006; Tang et al. 2016; Venkataramani et al. 2018; Sauer and Heilemann 2017). Furthermore, utilizing oil-immersion objectives, 3D-SMLM imaging was implemented in brain slices to evaluate the dispersion of synaptic proteins in a layer a few micrometers just above coverslip (Dani et al. 2010; Venkataramani et al. 2018). Recent advances in self-interference three-dimensional super-resolution microscopy and active point-spread function shaping in tandem with adaptive optics have permitted 3D localization to emit in tissue with a depth of approximately $50\ \mu\text{m}$ (Mlodzianoski et al. 2018; Bon et al. 2018). Nevertheless, nanoscale imaging of well-defined larger areas of interest, such as all active zones (AZs) in a whole mossy fiber (MF) bouton, has not yet been performed. Visualizing whole boutons is essential in order to comprehend the plasticity that occurs between individual boutons truly, and it would be a welcome addition to recent advances established using other techniques (Maus et al. 2020; Vandael et al. 2020a).

2.4 The motivation of the study

Despite the expanding comprehensive database of proteins, it is not understood how the molecular arrangement of AZ proteins results in neurotransmission and how their molecular assembly is modified after induction of synaptic plasticity. In this thesis, the chemical induction of plasticity was combined with the spatial accuracy of *d*STORM and SIM to analyze the plasticity-induced changes in key AZ components in hippocampal mossy fiber boutons.

3 Material and methods

3.1 Animals

Initial experiments to establish immunofluorescent stainings were performed on hippocampal tissue of male Thy1-EGFP (M) mice but male Thy1-mEGFP(Lsi1) (Deguchi et al. 2011) mice on C57/ BL6 background were used for all further experiments in this work since they express membrane-bound EGFP in hippocampal mossy fibers to obtain the desirable visualization of individual boutons surfaces (see the Results section). All animal procedures were approved and performed following the guidelines of institutional and regulatory authorities (Permit number RUF-55.2.2-2532-2-572-16 of the district government of Lower Franconia), the EU Directive 2010/63/EU, and the United States Public Health Service's Policy.

3.2 Material

3.2.1 Acute Brain Slice Preparation

I) General items

1. Gloves.
2. Eye protection.
3. Lab Coat

II) For the “nest beaker”/ Maintenance chamber

1. Nylon tights
2. Instant superglue (such as Scotch Super Glue, 3M, catalog number: AD124)
3. 15 ml tubes (such as VWR, catalog number: 89039-670 US, 525-0450 Europe)
4. Disposable 6 cm diameter plastic Petri dish (such as Thermo Fisher Scientific, Thermo Scientific™, catalog number: 123TS1)
5. Or instead of all above a Multi-slice incubation chamber: Brain Slice Keeper-4 (BSK- 4, AutoMate Scientific) or a comparable customized design for multi-slice incubation chambers

III) For dissection and obtaining the brain slice

1. Large heavy-duty kitchen scissors or guillotine for decapitation

3. Material and methods

2. Straight fine scissors for cutting through the skull (such as Fine Science Tools, catalog number: 14060-11)
3. Forceps (Fine Science Tools, catalog number: 11506-12)
4. Curved spatula (such as Fine Science Tools, catalog number: 10092-12)
5. Scalpel (such as Fine Science Tools, catalog number: 91003-12)
6. Scalpel handle (Fine Science Tools, catalog number: 10003-12)
7. Scalpel blades #15 (Fine Science Tools, catalog number: 10015-00)
8. Dry Ice
9. Endurium ceramic injector style blades EF-INZ10 (Cadence/Specialty Blades). These extremely durable blades surpass stainless steel and carbon steel feather blades in terms of cutting performance are the best choice for cutting through densely myelinated areas of the adult brain.
10. Glass disposable Pasteur pipet (such as Fisher Scientific, FisherBrand, catalog number: 13-678-6A)
11. Microspatula (Thermo Fisher Scientific, catalog number: 21-401-10)
12. Petri dishes for dissection surface (100 mm × 15 mm) (Sigma-Aldrich, catalog number: CLS3160101)
13. Transfer pipettes (Thermo Fisher Scientific, catalog number: 13-711-7M)
14. Nuclease-free microtubes (1.5–1.7 ml)
15. Dropper bulb (such as Fisher Scientific, FisherBrand, catalog number: 03-448-25)
16. Plastic container, about 2.5 cm high and 150 ml, such as the lid of a pipet tip box or a large glass Petri dish (Cole-Parmer Instrument, catalog number: EW-34551-06)
17. 1 L bottle (Sigma-Aldrich, catalog number: CLS13951L)
18. Plastic spoon
19. Whatman paper (GE Healthcare, Whatman, catalog number: 1001-090)
20. Filter paper (11 cm) (Thermo Fisher Scientific, catalog number: 09-795D)
21. Disposable Razor blade/ Single edge razor blades (such as Personna Double Edge Razor Blades [Amazon, PERSONNA, catalog number: BP9020])
22. Biohazard waste bags
23. Dissection needles (1-ml syringe + bent 0.4-mm injection needle) to detach each slice from the next tissue block by cutting through the subiculum
24. Stock artificial cerebrospinal fluid (ACSF) solution (see Recipes)
25. Ice-cold Slicing ACSF solution for dissection and physiological temperature ACSF for storage/
26. High-quality water (Millipore)

3.2.2 cLTP

Forskolin (Sigma-Aldrich, catalog number: F3917)

Dimethyl sulfoxide (DMSO) (Sigma-Aldrich, catalog number: 67-68-5)

3. Material and methods

3.2.3 Fixation and cryosectioning

1. Fixative: 4% paraformaldehyde in phosphate buffer
2. Optimal cutting temperature (OCT) compound: cryogel (Cryo-Gel 39475237, Leica)
3. Fresh tissue sample: acute brain slices
4. 3-aminopropyl- triethoxysilane (Sigma 440140, Sigma-Aldrich, Schnelldorf) 2% v/v in methanol
5. Methanol 100%
6. custom-made mounting device

3.2.4 Cryosectioning equipment

1. Brush (camel hair)
2. Container for storage of tissue sample
3. Plastic or metal tissue mold

3.2.5 Calibration bead slide set and Silan-coated coverslips

1. Ultrasonic water bath sonicator (e.g., VWR Ultrasonic Bath)
2. Custom-made comb-like polytetrafluoroethylene (PTFE) holder
3. Round shaped, 18 mm diameter, high precision cover- slips (Marienfeld No 1.5H, Lauda-Königshofen, catalog number 0107032)
4. Rectangle shaped, 24 x 60 mm diameter, high precision cover- slips (Marienfeld No 1.5H, Lauda-Königshofen, catalog number 0107242)
5. High-quality water (Millipore)
6. Chloroform (Sigma-Aldrich, catalog number 132950)
7. Hydrochloric acid (37% (vol/vol); Sigma-Aldrich, catalog number 258148)
8. Hydrogen chloride 1M (Sigma-Aldrich, catalog number: 295426)
9. Ethanol absolute (100% (vol/vol); Merck Millipore, catalog number 100983)
10. Pipette and tips (Finnpipette™ Focus Fixed Volume Pipettes, Thermo Fisher Scientific, catalog number: 4601110)
11. Lens-cleaning tissues (e.g., Whatman; GE Healthcare, catalog number. WHA2105862)
12. Soft task wipes (e.g., Kimwipe; Kimberly-Clark Professional, catalog number: 34155)

3. Material and methods

13. Cotton-tipped swabs for optical cleanup (Edmund Optics, catalog number: 56-926)
14. Glycerol (>99.5% (vol/vol); Sigma-Aldrich, catalog number 49770)
15. 1.5-ml Eppendorf tubes (Thermo Fisher Scientific, catalog number: 69715)
16. Quick-drying nail polish, Nail varnish (Amazon, Essie Nail Varnish Base Coat transparent)
17. Delicate task wipers (Kimberly-Clark, KIMWIPES SMALL. BX.280)
18. Ultra-fine forceps (Fine Science Tools, Tip Dimensions:0.01 x 0.005mm, catalog number: 11370-42)
19. Slide holder (DWK Life Sciences Wheaton™ 30-Slide Rack, Thermo Fisher Scientific, catalog number: 02927094)
7. Coplin jar (Fisherbrand™ Glass Staining Dishes for 16 Slides, Thermo Fisher Scientific, catalog number: 08817)
8. Slide storage boxes (Pelco, catalog number: 2106)
9. FluoSpheres carboxylate-modified microspheres, 0.1 μm , blue fluorescent (350/440; Thermo Fisher Scientific, catalog number: F8797)
10. FluoSpheres®, 0.2 μm , orange fluorescent (540/560) (Thermo Fisher Scientific, catalog number: T7280)
11. FluoSpheres carboxylate-modified microspheres, 0.1 μm , yellow–green fluorescent (505/515; Thermo Fisher Scientific, catalog number: F8803)
12. FluoSpheres carboxylate-modified microspheres, 0.1 μm , red fluorescent (580/605; Thermo Fisher Scientific, catalog number: F8801), blue (360/440) and deep-red (633/660) PS-Speck beads, 0.17 μm diameter (PS-Speck Microscope Point Source Kit, Thermo Fisher Scientific, catalog number: P7220)
13. TetraSpeck™ Microspheres, 0.1 μm , fluorescent blue/green/orange/dark red (Thermo Fisher Scientific, Darmstadt, catalog number: T7279).

3.2.6 Immunofluorescence

I. Primary antibodies:

1. Mouse monoclonal antibody (mAb) anti- α -Bassoon (Enzo Sap7F407, Enzo Life Sciences, Lörrach, Germany)
2. Rabbit monoclonal antibody (mAb) anti- α -Munc (Enzo Life Sciences, Lörrach, Germany)
3. Rabbit polyclonal antibody (mAb) anti- α -Tomosyn (Synaptic Systems GmbH, Göttingen, Germany)
4. Rabbit polyclonal and mAb anti-Zinc transporter 3 (ZnT3) (Synaptic Systems 197002 and 197011)
5. Anti-GFP nanobodies (GFP-Trap® (uncoupled protein), ChromoTek, Munich, Germany, custom conjugation with Alexa64747)

3. Material and methods

II. Secondary antibodies:

(Thermo Fisher, Darmstadt, Germany)

1. Alexa 647 conjugated goat α -mouse antigen-binding fragment (Fab2)
2. Alexa 532 conjugated goat α -mouse Fab
3. Alexa 647 conjugated goat α -rabbit Fab
4. Alexa 568 conjugated α -mouse
5. Alexa 532 conjugated goat α -rabbit Fab
6. ATTO 647 conjugated α -rabbit

III. Staining solutions:

1. 0.02 M glycine (Sigma)
2. 0.3% Triton X-100 (Sigma)
3. Blocking solution consisting of 1 % bovine serum albumin (BSA) (Sigma) and 5% normal goat serum (NGS) (Seralab, West Sussex, UK) in 0.3% PBT (1xPBS containing 0.3% Triton X-100, Sigma)
4. Imaging buffer (100 (100 mM mercaptoethylamine (MEA, Sigma) in PBS, buffered at pH 7.8–7.9)

3.3 Reagents

◆ High-purity chemicals

1. Glucose (Sigma-Aldrich, catalog number: G7021)
2. Sodium chloride (NaCl) (Sigma-Aldrich, catalog number: S7653)
3. Sodium phosphate monobasic anhydrous (NaH_2PO_4) (VWR, catalog number: 470302-666)
Manufacturer: ALDON, catalog number: SS0756-500GR.
4. Sodium bicarbonate (NaHCO_3) (Sigma-Aldrich, catalog number: S5761)
5. Potassium chloride (KCl) (Sigma-Aldrich, catalog number: P9333)
6. Magnesium chloride MgCl_2 solution (1M) (Sigma-Aldrich, catalog number: 63069)
7. Calcium chloride solution (1 M) (Sigma-Aldrich, catalog number: 21115)
8. Triton X100 (Sigma Aldrich catalog number: T9284)

3. Material and methods

3.3.1 Reagent setup; Chemicals, Buffering, Fixing and Dyeing Solutions

3.3.1.1 Preparing ice-cold oxygenated Artificial Cerebrospinal Fluid (ACSF)

1. Stock artificial cerebrospinal fluid (ACSF) solution (see Recipes)
 2. Ice-cold Slicing ACSF solution for dissection and physiological temperature
 3. High-quality water (Millipore)
- Through a variety of pro-oxidative impacts, trace metals in distilled or tap water may lead to poor slice quality. All solutions must be prepared using ultrapure water, such as those obtained via a Milli-Q water system. Each glassware used to store ACSF should be cleaned meticulously either in an autoclave or washed with dilute (0.1 M) nitric acid followed by generous amounts of Milli-Q water.
 - All ACSF solutions must be saturated with carbogen (95 percent O₂/5 percent CO₂) to maintain consistent pH buffering and proper oxygenation ahead of use.
 - It is advised that solutions be prepared fresh for each experiment daily.

-
- *Stock artificial cerebrospinal fluid (ACSF) solution for during experiments (1 L, store at four °C)*
-

Glucose 25 mM

Sodium chloride 125 mM

Sodium phosphate monobasic anhydrous 1.25 mM

Potassium chloride 2.5 mM

Sodium bicarbonate 25 mM

Calcium chloride 2 mM

Magnesium chloride 1 mM

pH was adjusted to 7.3 and osmolarity to 290-300 mOsm

Fill up to 1 L with distilled H₂O

-
- *Ice-cold slicing ACSF solution*
-

Glucose 25 mM

sucrose 75 mM

Sodium chloride 64 mM

Sodium phosphate monobasic anhydrous 1,25 mM

3. Material and methods

Potassium chloride 2.5 mM
Sodium bicarbonate 25 mM
Calcium chloride 0.5 mM
Magnesium chloride 7 mM

pH was adjusted to 7.3 and osmolarity to 290-300 mOsm
Make up to 300 ml with distilled H₂O

3.3.1.2 Reagents used for fixing and staining

- *Phosphate-Buffered Saline (PBS)*

Sodium chloride 137 mM
Potassium chloride 2.7 mM
sodium hydrogen phosphate 8 mM
potassium dihydrogen phosphate 2 mM

pH was adjusted to 7.4 using 1 Mol sodium hydroxide or 1 Mol hydrogen chloride
For PBT, add appropriate volume (0.05 %) of Triton X100 (T9284, Sigma Aldrich).

- *4% Formaldehyde solution in PBS*

Caution: Formaldehyde is toxic; this should be done in a fume chamber with gloves, safety glasses, and a face mask.

Preparation of 1000 ml of 4% paraformaldehyde solution in PBS

Sodium Hydroxide 1M
Hydrochloric acid 1M
1x phosphate-buffered saline (PBS)
paraformaldehyde

1. In a vented hood, add 800 mL of 1X PBS to a glass beaker on a stir plate. Heat to about 60 °C while stirring. Keep an eye on the solution to ensure it does not boil.
2. To the heated PBS solution, add 40 g of paraformaldehyde powder.
3. The powder will not dissolve quickly into the solution. Raising the pH gradually by adding 1 N sodium hydroxide (NaOH) dropwise from a pipette until the solution becomes clear
4. After dissolving the paraformaldehyde, the solution should be cooled and filtered.
5. With 1X PBS, dilute the solution to 1 L.

3. Material and methods

6. Recheck the pH and adjust it to about 6.9 with tiny quantities of dilute hydrogen chloride (HCl).
7. Aliquoted portions of the solution may be frozen or kept at 2-8 °C for up to one month.

- *PBS/glycine 0.02 M*

1. Pour 10 mlx PBS in a 100 ml Erlenmeyer
2. Add 0.15 g glycine
3. Swirl till glycine is dissolved
4. Add H₂O till 100 ml

- *30% Sucrose for cryoprotection*

500ml sterile 1x phosphate-buffered saline (PBS)
150 g sucrose

1. Mix above and stir solutions until sucrose is completely dissolved.
2. Filter sterilize with a disposable Nalgene filtration unit type S (0.45 micron).
3. Label the bottle with “30% Sucrose in 0.1M Phosphate Buffer”, the date on which it was prepared and your initials.
4. Store the 30% Sucrose solution at 4°C.

3.3.2 Reagent for imaging setup

- *1 M Hydrogen chloride*

In a 250-mL volume of ddH₂O, add 7 milliliters of concentrated HCl. Storage at room temperature will keep the solution stable for several months.

- *70% (vol/vol) ethanol*

15 ml ddH₂O and 35 ml ethanol absolute are combined in a 50-ml self-standing Falcon tube or other appropriate dispensers to create a solution for cleaning microscope slides. This solution is stable for several months at room temperature.

-
- *Chloroform*
-

Aliquots should be prepared in 50-ml Duran glass bottles; this solution is used to clean microscope slides and objectives. It is stable for many months when kept at room temperature.

3.4 Devices and software

3.4.1 Devices for acute brain slices and cryotome sectioning

1. 50 ml Pyrex beaker (such as VWR, catalog number: 10754-952)
2. Straight spring scissors (such as Fine Science Tools, catalog number: 15018-10)
3. Curved fine forceps (such as Fine Science Tools, catalog number: 11152-10)
4. 600 ml Pyrex beaker (such as VWR, catalog number: 10754-956)
5. Pressurized oxygen tank (95% O₂/5% CO₂) with tubing (such as AirGas, catalog number: Z02OX9522000043)
6. Vibratome (Various models are commercially available, we used Leica, model: Leica VT 1200 S, catalog number: 14048142066)
7. Bath heater with a thermometer (such as Thermo Fisher Scientific, Thermo Scientific, model: Precision 180, catalog number: 51221073)
8. Mechanically stable upright microscope (e.g., Zeiss Axioskop 2 FS)
9. pH meter: standard model
10. Vapor pressure osmometer: It is essential to calibrate the osmometer regularly and clean the thermocouple periodically to ensure optimum functioning.
11. Mixer for homogenization of partially frozen ACSF
12. Blade alignment mechanism
13. Cryotome

3.4.2 SR imaging setup devices

For SIM

1. commercial ELYRA S.1 structured illumination microscope (Zeiss AG).
2. 405 nm diode (50 mW) laser
3. 488 nm OPSL (100 mW) laser
4. 561 nm OPSL (100 mW) laser
5. 642 nm diode (150 mW) laser

3. Material and methods

6. Plan-Apochromat 63x/1.40 immersion-oil objective (Zeiss AG).
7. program 'Zen' (black edition, Zeiss AG)
8. SIMcheck plugin13 for ImageJ/Fiji (<https://github.com/MicronOxford/SIMcheck>).

for dSTORM:

1. Mercaptoethylamine (MEA, Sigma)
2. Inverted microscope (Olympus IX-71, Olympus, Hamburg, Germany, with Olympus APON60XOTIRF 60×, NA 1.45, oil immersion or Zeiss LD C-Apochromat, Zeiss, Jena, Germany, 63×, NA 1.15 water immersion objective)
3. Nosepiece-stage (IX2-NPS, Olympus).
4. 644 nm laser (iBEAM- SMART-640-S, Toptica, Gräfelfing, Germany)
5. 532 nm laser (Qioptiq Nano 250-532, Qioptiq; Asslar, Germany)
6. Clean-up filter (Brightline HC 642/10, Semrock, and ZET 532/10, Chroma, AHF Analysetechnik, Tübingen, Germany, respectively)
7. Dichroic mirrors (Laser-MUX BS 514–543 and HC-quadband BP, Semrock)
8. Quadband-filter (HC-quadband 446/523/600/677, Semrock)
9. Camera (iXon Ultra DU-897-U, Andor, Acal BFi, Grubenzell, Germany)
10. Dichroic mirror (HC-BS 640 imaging, Semrock)
11. Longpass-filter (Edge Basic 635, Semrock)
12. Bandpass-filter (Brightline HC 582/75, Semrock)
13. RapidSTORM (10 nm /pixel sub-pixel binning)
14. Piezo z-stage (P-736. ZR 2, Physik Instrumente, Karlsruhe, Germany)

3.5 Methods and procedure

For the SIM imaging, eighteen acute hippocampal slices (6 ACSF, 6 DMSO and 6 Forskolin) from nine 16-week-old mice and for the *dSTORM* experiment, six acute hippocampal slices from eight-week-old, male Thy1 mEGFP (*Lsi1*) mice were prepared as described in (Hallermann et al. 2003) and explained in detail below.

3.5.1 Sample Preparation and the setup

Before starting:

Ideally, the slice chamber should include a slightly submerged netting for the slices to settle on, a thin gas diffuser stone for infusion of carbogen into the ACSF, and some moderate continuous flow to circulate solution surrounding and through

3. Material and methods

the slices. A variety of holding chambers are also commercially available (e.g., Warner Instruments manufactures a submersion-style "Pre-Chamber #BSC-PC) that should be appropriate for use in aging, and transgenic mice slice experiments. For this work, a cost-friendly holding chamber was prepared. Assembly is straightforward: putting together the “nest beaker” (Edwards et al. 1989; Stuart, Dodt, and Sakmann 1993; Papouin and Haydon 2018) (Figure 12) and a modifying Pasteur pipet dropper.

1. The “nest beaker” was used to incubate slices before and after recovery, was made from nylon tights, superglue, a 6 cm plastic Petri dish, a 15 ml tube, and a 250 ml beaker. We cut it out or just opened it with kitchen scissors.
2. In order to create a strong mesh foundation for the Petri dish, the nylon was wrapped around the opening and fastened by either tying it or using elastic bands. Following that, the nylon was bonded to the exterior of the Petri dish's outer wall. We did not use excessive amounts of glue, considering this may be harmful to the slices and impede appropriate drying from taking place properly. These were allowed to air dry for 24 hours.
3. A scalpel or delicate scissors were used to cut away any extra nylon fabric. We rinsed thoroughly and soaked in clear water overnight (we encountered cases when ‘fresh’ glue turned out to be toxic to the slices). The conical end of the 15 ml tube was cut off and discarded, and a rectangular opening was cut out at the bottom end of the tube.
4. We put together all three components as illustrated [modified from (Papouin and Haydon 2018)]. To ensure proper pH and oxygenation, plastic tubing from the 95 % CO₂/5 % O₂ tank has been lowered into the 15 ml tube.



Figure 12. Nest beaker. For incubating acute brain slices both before and after recovery, modified from (Papouin and Haydon 2018).

3. Material and methods

Setting up:

1. On the experiment day, the solution enclosing 300 ml of ice-cold slicing ACSF (see Recipes) was made and placed in a 600 ml Pyrex beaker and put in a -20 °C freezer for approximately 20-30 min or until a thin coating of ice on the walls of the beaker and at the surface formed. We agitated the ice extensively in order to break it down into a homogenous frosty solution. Excessive freezing is avoided since it will radically change the solution's osmolarity and decrease the quality of the slices. Nevertheless, the quantity of ice needed to maintain a 0-1 degrees Celsius temperature during the slicing process should be sufficient. As this is suggested, we have not placed the ACSF slicing beaker inside the -80 °C freezer.
2. While the ice-cold slicing ACSF was freezing, we prepared 150 ml of recovery ACSF in the "nest beaker." Before starting, the heated bath was preheated to 33 °C and oxygenated with 95 percent O₂/5 percent CO₂ for at least 25 minutes.
3. The vibratome was prepared by filling the tray around the slicing chamber with ice and water and allowing it to sit for a couple of minutes to adjust to the suitable temperature.
4. During the intubation, we ensured that oxygen bubbles did not physically agitate the slices.
5. In order to arrange the setup, a container of ACSF Cutting Solution was placed in an ice bucket filled with ice, and around 15 mL of the solution was transferred into a 20 mL beaker similarly placed on wet ice.
6. Prior to starting, the solutions in both the bottle and the beaker were gotten at least 20 minutes of oxygenation.
7. The bench was encircled with cloth diapers, and a biohazard waste bag was conveniently located near the setup.
8. Except for the razor blades and scalpel, all dissection instruments were set in a 600 mL beaker filled with sterilized water and WypAll or KimWipe cloths immersed in the water.
9. In a bucket containing dry ice, labeled microtubes were positioned. Similarly, one petri dish piece was put on dry ice and allowed to cool. Under the microscope, a tiny ice bucket containing ice was placed.
10. One ice bucket was filled with ice, and the other half of the petri dish was placed on top of it, with the edges pointing down. On the dish, one piece of filter paper was placed.
11. A sufficient volume of ACSF cutting solution was transferred from the 20 ml beaker to the filter paper and evenly spread just before starting.
12. Before each dissection, a new cotton diaper was placed on the bench.

3. Material and methods

3.5.2 Acute brain slices

Brain Removal:

The animals were anesthetized with fluothane, checked for the absence of reflex upon tail or paw pinching, and killed by fast decapitation.

1. Small scissors were used for decapitation. The cut was made immediately behind the head, not too much posterior since extra tissue might occlude the foramen magnum.
2. The scalp skin was cut from the rodent's eyes down the midline with a razor blade as the scalp was gently pulled to the lateral sides.
3. The head was immediately immersed in ice-cold oxygenated slicing ACSF and left for 10 seconds to chill. We made sure the head stayed submerged entirely at all times.
4. One tip of the fine scissors was inserted into the foramen magnum; a cut was made laterally into the skull, and the procedure was repeated on the other side.
5. Another incision has been done from the foramen magnum along the midline towards the nose while keeping the end of the scissors as superficial as possible not to damage the brain.
6. Minor cuts were performed laterally from the midline incision near the eyes. With forceps, gentle tangential and lateral pressure was given to either of the freshly generated skull flaps. If force is appropriately applied, the skull should be entirely removed and the brain exposed.
7. Meanwhile, we used the curved spatula to reach under the brain and gently scoop out the brain without yanking it out.
8. In order to completely liberate the brain, we had to cut the optic nerve on the ventral side and the cranial nerves on the caudal side with fine scissors or directly with the spatula in some cases.
9. We also used the longer micro spatula to tear the cranial nerve fibers near the base of the brain and carefully transfer the brain to the 20 ml beaker of oxygenated ACSF cutting solution.

Isolation of the area of interest

1. The razor blade was used to remove the unwanted parts of the brain, rostral and caudal, to the region of interest (approximately 10–20% of the total brain volume). We flipped the brain onto its ventral side to isolate the hippocampus, found the superior colliculi, performed a transverse cut, and eliminated the caudal region (cerebellum). We ensured that the cut was

3. Material and methods

perpendicular to the rostrocaudal axis, as this part will be glued to the vibratome's cutting plate.

2. The brain was then flipped over so that the ventral side was facing up, the optic chiasma was identified, and a transverse cut was made. This exposed the fornix's fimbria, which is immediately rostral to the hippocampus (i.e., the hippocampus lies under it). On the dry cutting plate, a small amount of glue was spread.
3. The curved spatula was used to pick up the brain with the rostral side facing us and the ventral side facing away from us. The spatula's bottom was gently put on a paper towel to allow extra ACSF to drain by capillary action without touching the brain. The spatula was positioned directly above the glue, and the brain was carefully transferred onto the glue in a single motion by pushing it off the spatula with a finger.

Obtaining brain slices

Since metal ions are very toxic to neurons in slices, we tried to prevent them as much as possible; in particular, we were very cautious to prevent rust contamination. The solution temperature in the buffer tray during cutting was around 0-1° C with an adequate percentage of the frozen solution.

1. The plate was immediately placed in the slicing chamber, with the ventral area facing us and the dorsal part (i.e., the cortex surface) facing the vibratome's back.
2. Once the hemisphere has adhered to the bottom plate, a few drops of ice-cold physiological saline were placed over the hemisphere using a wide-lumen pipette, followed by the remaining ice-cold oxygenated slicing ACSF, which was gently poured and it was avoided to drop pieces of ice onto the brain.
3. Bubbling of the physiological saline in the buffer tray with O₂-CO₂ gas mixture was continually maintained.
4. The blade was lowered into the solution without pressing and putting pressure on the brain, and we obtained 300 μm brain transversal slices. Thinner slices would have increased visibility but degraded the quality of the slices.
5. For cutting to be effective, the angle between the blade and horizontal plane was adjusted to approximately 17°.
6. It is critical for presynaptic investigations that the slicer produces the smallest amount of vertical vibrations of the cutting blade possible. The finest slicers can achieve vertical vibrations of less than 0.1 m μm for a horizontal oscillation amplitude of 1.5 mm. The use of vertical vibrations of up to one millimeter is adequate for presynaptic observations. In order

3. Material and methods

to reduce vertical vibrations, a blade alignment mechanism was used to align the edge of the cutting blade with the main axis of the oscillation.

Optimal settings are as follows:

Blade oscillation amplitudes of 1.1–1.8 mm

Blade forward movement velocities of 3–6 mm min⁻¹

Oscillation frequencies of roughly 100 Hz

7. Once the first slice was cut, we paused the vibration and the blade's forward progress. The slice was detached from the tissue block by cutting through the subiculum with a dissection needle with no force applied to the blade.
8. The slices were cut into right and left hemisphere. For SIM experiment we just used the right hemisphere.
9. Subsequently, using the Pasteur pipet dropper (a wide-lumen pipette), the slices were transferred into the maintenance chamber/nest beaker containing the recovery ACSF (see Recipes). In contrast to the original orientation during the slicing procedure, the slices were turned upside down.
10. During maintenance, slices were first kept at 35 °C for about 30 minutes before being brought to room temperature to rest. A 30-minute recovery period at 35 degrees Celsius is adequate. This has been shown to be the most effective method of tissue preservation in our experience. Slices were in this step ready to be used chemical induction of plasticity.
11. cLTP should begin practically immediately after the slicing phase is completed.
12. The quality of the slices (particularly hippocampus slices) has been evaluated visually using a 5x objective microscope. Usually, healthy slices exhibit sharp contrasts and distinct color differences across layers and areas of the slice.

3.5.3 Induction of chemical plasticity

cLTP may be performed at either room temperature (22–24° C) or near-physiological temperature (32–34° C). We performed the cLTP at room temperature.

1. Forskolin (F6886, Sigma) was prepared as a stock solution (50 mM, in DMSO) and stored at –80°C until used at a final concentration of 50 µM in the bath ACSF. Rolipram (Sigma) stock solution (0.1 mM in DMSO) was stored at -80°C until used at a final concentration of 0.5 µM.
2. To induce plasticity, the slices were exposed for 30 minutes at room temperature to 50 µM forskolin in 0.5 percent DMSO/ACSF or to 0.5

3. Material and methods

percent or 50 μM in carbogenated ACSF. This concentration was selected since it has been found to be the most effective for facilitating LTP induction (Barad et al. 1998).

3. Following that, the slices were placed into separate maintenance chambers with carbogenated ACSF and allowed to rest at room temperature for 30 minutes before the fixation step.

3.5.4 Fixation, flat-mounting, and cryosectioning

◆ cryopreservation

1. The brain slices were washed three times briefly (each time for 5 min) with PBS.
2. Before sucrose cryopreservation, tissues should be thoroughly fixed using a formaldehyde-based fixative. If tissues are not fully fixed, they will shrink since sucrose solutions over 10% are hypertonic and will cause the intracellular solution to escape from cells. To fix the 300-micrometer thick brain slices, we used 1 ml of cold and fresh (<1wk old) 4 percent paraformaldehyde in phosphate buffer for 2 hours.
3. The slices were placed into sucrose (30%) PBS overnight (until tissue sinks)

Note: Some laboratories may utilize 20% sucrose rather than 30% sucrose for very fragile tissues and GFP visualization.

4. Following flat mounting on specimen holders with cryogel using a custom-designed mounting device, the slices were stored at -80°C for 12 hours before sectioning.

◆ Cryosectioning

Prior to the sectioning, the prepared tissue block was placed within the cryostat chamber for 30-60 minutes to allow the tissue to acclimate to -20°C . Using a cryotome, each 300 μm thick brain slice was subsequently sliced into 25 μm thick slices for *d*STORM imaging and three to four 25 μm thick sections for SIM imaging. In order to achieve a consistent cutting angle for horizontal brain slices, slices were placed on aluminium carriers with the dorsal cortical surface pointing down to provide a uniform cutting angle. The brains were trimmed until the lateral ventricles were opened and the distinctive double C-shape of the hippocampus could be initially recognized on both sides, using the bottom margins of both

3. Material and methods

cortices and the pons as markers to align the specimen to the blade. The bottom margins of both cortices and the pons were used as markers to align the specimen to the blade, and the brains were trimmed until the lateral ventricles were opened and the distinctive double C-shape of the hippocampus could be visually recognized. To match the cutting level across various animals on the same hippocampus structure, we used images from a Nissl stained horizontal brain atlas [brainmaps.org, (Mikula et al. 2007)] and aligned the sections according to the morphology of the dentate gyrus.

The following points are to be considered:

1. Correct height to the knife-edge
2. Correct angle to the knife
3. It is recommended that all instruments used in cryosectioning, including the trimming razor blade, be prechilled in the cryostat chamber before use.
4. By adjusting the glass slide on top of the platform, the rolling of the sections can also be minimized to a certain extent.
5. If the frozen tissue is not sliced evenly and smoothly, the knife may even get dull.

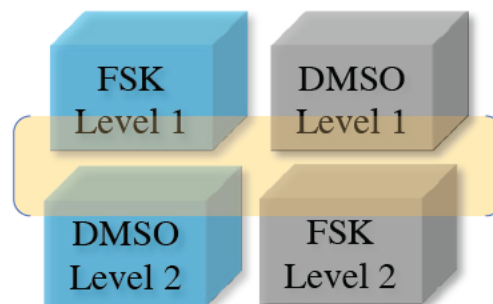


Figure 13. Treatment design for SIM experiments

Cryosections from forskolin and DMSO treated slices were cut at a defined level of the dorsal hippocampus (the yellow box) to minimize the height difference across each cryosection to 150 μm .

3. Material and methods

Table 3. Treatment design using acute hippocampal (HC) slices.

| <i>Experiment</i> | <i>Animal Number</i> | <i>Age (weeks)</i> | <i>HC/Right Level 1</i> | <i>HC/Right Level 2</i> | <i>HC/Left Level 1</i> | <i>HC/Left Level 2</i> | |
|-------------------|------------------------|--------------------|-------------------------|-------------------------|------------------------|------------------------|--|
| <i>SIM</i> | <i>FSK Experiment</i> | 1 | 16 | DMSO | Forskolin | | |
| | | 2 | 16 | Forskolin | DMSO | | |
| | | 3 | 16 | Forskolin | DMSO | | |
| | | 4 | 16 | DMSO | Forskolin | | |
| | | 5 | 16 | Forskolin | DMSO | | |
| | | 6 | 16 | Forskolin | DMSO | | |
| | <i>ACSF Experiment</i> | 1 | 16 | ACSF | ACSF | | |
| | | 2 | 16 | ACSF | ACSF | | |
| | | 3 | 16 | ACSF | ACSF | | |
| <i>dSTORM</i> | 1 | 8 | Forskolin | DMSO | DMSO | Forskolin | |
| | 2 | 8 | DMSO | Forskolin | Forskolin | DMSO | |
| | 3 | 8 | Forskolin | DMSO | DMSO | Forskolin | |

3.5.5 Super-resolution imaging

3.5.5.1 Structured illumination microscope

Trained service engineers have properly aligned and calibrated the SIM system. An example of channel alignment has been prepared. To prevent mechanical drift, fluctuation in camera output, and variations in the RI of immersion oil and samples, we kept the imaging room and surroundings at a specific temperature (23.5 °C, with 0.5 °C fluctuations per hour).

3.5.5.2 Silan-coated coverslips preparation

For *dSTORM* imaging, a set of high precision coverslips was placed vertically in a custom-made comb-like polytetrafluoroethylene (PTFE) holder and submerged in 3-aminopropyl-triethoxysilane 2 percent v/v in methanol for 2 minutes before being rinsed with methanol 100 percent and distilled water and dried.

For super-resolution SIM imaging, the coverslips must be thoroughly cleaned before calibration bead slides can be prepared. The high-precision coverslips were placed in a mini-rack and pre-cleaned for 30 minutes in a gently shaking beaker of 1 M HCl before being transferred to a Coplin jar. Slices were washed twice in ddH₂O and transferred to a beaker (a Coplin jar for slides) containing 100 percent (vol/vol) EtOH. The beaker was then covered with Parafilm for storage.

Slides and coverslips were dried vertically to prevent dust accumulation. Precleaned coverslips may be stored in 100% (vol/vol) EtOH for many months in a suitably sealed container (e.g., Petri dish covered with Parafilm), ideally at four °C to avoid evaporation.

3. Material and methods

3.5.5.3 PSF calibration slide

In order to create a 100- μ l prestock solution, 1 μ l each of 0.1 μ l 505/515 (green–yellow) and 580/605 (red) fluorescent carboxylate-modified microspheres were diluted in 98 μ l of ddH₂O. For several weeks, diluted microspheres may be kept at 4 °C. For 10 minutes, the finalized stock solution was sonicated. In 99 μ l of EtOH, 1 μ l of stock solution was diluted. 5 μ l of this solution was immediately put to a precleaned coverslip, spread out with the pipette tip, and allowed to air dry for at least 30 minutes. To ensure that on average, slightly less than one bead per field of view (256 x 256 pixels; field size of 20 x 20 mm with a pixel size of 80 nm) was achieved, the final concentrations 1:106 for green/red microspheres and 1:500 for blue/far-red microspheres were selected.

3.5.5.4 Bead-layer calibration slides

We sonicated 1 ml of undiluted 0.1- μ m fluorescent carboxylate-modified microspheres before transferring 1 μ l to an Eppendorf tube. Microspheres in the colors blue, green-yellow, red, and far-red were utilized in separate tubes. Each tube was filled with 5 μ l of EtOH absolute, followed adding all 6 μ l to the middle of a precleaned coverslip. We used the pipette tip to distribute the liquid from the middle as the EtOH evaporated without pipetting up and down. We allowed at least 20 minutes for the drying process. Spreading the microsphere droplet evenly over the coverslip is essential for creating flat beads patches rather than clusters.

3.5.5.5 Multicolor alignment bead slide

To achieve an equal dispersion of beads for image capture, 0.2- μ m-diameter TetraSpeck microspheres were diluted in ddH₂O 1:20 and vortexed for 1 minute. An Eppendorf tube was filled with 2 μ L of the bead solution. After adding 10 μ L of EtOH absolute, immediately afterward, 6 μ L of the suspension was pipetted gently into the center of a precleaned coverslip, and 6 μ L of the suspension was pipetted gently onto the middle of a precleaned slide. We gently streak out the bead suspension on the coverslip and slide surfaces using the pipette tip. The beads were left to dry for at least 20 minutes, under cover and away from dust sources.

3. Material and methods

3.5.5.6 Antibody labeling and image acquisition

Staining protocol for 25 μ m SIM-sections

Immunofluorescence staining of the different preparations was performed according to a uniform protocol. Prior to staining, sections were washed with 0.02 M glycine in phosphate buffered saline (PBS) for 30 min to quench free aldehyde autofluorescence, incubated and permeabilized in PBT 0,3 % for two hours, and blocked with blocking solution consisting of 1% bovine serum albumin (BSA) and 5% normal goat serum (NGS) in 0.3% PBT. The blocking solution was washed off, and the priming antibodies in 1% BSA, 5% normal goat serum (NGS) were added to 0.1% PBT (1:500). The primary antibodies remained on the sections overnight at four °C (36 hours). Samples were washed with blocking solution twice for 5 and twice for 20 min, followed by incubation with the second antibodies for 24 hours at room temperature. After repeated washing with PBS, the sections were kept in 1× PBS at 4 °C until imaging. For the SIM-imaging, the sections were mounted on silanized, beads-covered coverslips for the imaging.

Staining protocol for 25 μ m dSTORM-sections

The sections were washed with 0.02 M glycine in PBS for 2 hours, blocked overnight with a blocking solution of 1% BSA and 5% NGS in 0.3 percent PBT, then incubated at 4 °C for 36 hours with anti-Bassoon (Enzo Sap7F407, 1:500) antibodies. After washing with blocking solution twice for 5 minutes and twice for 20 minutes, the sections were incubated at 4 °C for 24 hours with Alexa 647 labelled goat anti-mouse Fab fragment (Invitrogen, 1:500). Identical washing procedures were then repeated, and the sections were maintained in PBS until mounted onto silanized, beads-covered coverslips, promptly dried, and stored in 1 PBS at 4 °C until dSTORM imaging.

3.5.5.7 Imaging

SIM imaging

SIM imaging was conducted using a commercial ELYRA S.1 structured illumination microscope (Zeiss AG). Four excitation lasers are used in this setup: a 405 nm diode (50 mW), a 488 nm OPAL (100 mW), a 561 nm OPAL (100 mW), and a 642 nm diode (150 mW). All SIM measurements were performed using a Plan-Apochromat 63x/1.40 immersion-oil objective (Zeiss AG).

The system may be controlled through the program 'Zen' (black edition, Zeiss AG), which includes procedures for customizing the setup, automating 3D imaging of selected ROIs, and performing image processing. The Zen software

3. Material and methods

was primarily used for color correction with a channel alignment tool and structured illuminations processing.

Acquisition of PSF/OTF sets

This calibration slide has a mixture of up to four distinct color PSF beads in optimum density to facilitate the acquisition of channel-specific PSF/OTF sets with the same immersion medium.

A part of the PSF slide containing isolated individual beads was identified, and a bead in the field of view was centered such that no other beads were visible. As its illumination focus was in the middle of the bead, the detector recorded its maximum count. The focus was gradually shifted deeper/shallower inside the bead (e.g., using z-steps of 0.1 μm) to find the optimum midsection. In wide-field mode, an 8- μm stack ($\pm 4 \mu\text{m}$ from the chosen bead center) was acquired with a 0.100- μm step size. We evaluated if the acquisition's dynamic range was as near to the camera's maximum bit depth as feasible (16-bit), without entering saturation, by examining the intensity histogram of this stack. We ensured that there was no saturation within a single acquisition frame and then acquired a second stack. Wide-field PSF was evaluated by scrolling over the z-stack and inspecting the orthogonal view for any variance, asymmetry, or astigmatism caused by the objective or air bubble(s) in the immersion medium. A series of OTFs were produced from a shiny bead utilizing various capture angles. SIMcheck's MMR and ZMV metrics were applied to provide a quantitative comparison of reconstruction quality. The reference imaging oil was used with a RI optimal for green/orange/red emission as needed. After determining the optimal RI for the center wavelength, a single-bead stack was obtained for OTF generation. This was done for all colors using immersion oil with the best trade-off in terms of channel asymmetry. Two OTF sets (multiple channel OTFs collected with the same RI immersion oil) were generated: one using the reference immersion oil optimized for the multicolor acquisition of blue and green fluorescence. The other used the optimal immersion medium for the orange/red channel. We adjusted for the orange/red channel since this is the preferred configuration for multicolor acquisitions, including the red and far-red channels.

Illumination pattern checks

Three slides exhibit monolayers of $\sim 100\text{-nm}$ (sub-diffraction)-diameter beads with various wavelengths that correspond to the system's operating range (in our SIM system 405 nm, 488 nm, 561/642 nm). Following the described procedure, these monolayers should be uniformly dispersed across the whole coverslip surface, with occasional patches of bead-free background areas with a few isolated beads remaining on the surface. It is recommended that these be used as reference slides for determining system parameters (line spacing, stripe rotation (k_0) angle), validating system alignment (phase and z-modulation; first- and

3. Material and methods

second-order beam position), and verifying system performance by quantifying the practically achievable resolution, reaffirming stability of system performance, and evaluating the quality of new parameter settings or new system OTFs.

A field comprising even bead monolayer patches with intermittent bead-free background regions and occasional single beads was detected on the bead-layer slide. To provide the correct clipping offset and to determine the sample's ZMV, empty regions were required. The acquisition settings were modified to match the camera's 16-bit depth while minimizing saturation. After checking the raw data for particularly dark areas, apparent aberrations, or extraneous patterns, a stack of 4 m (in structured illumination mode) of the bead field was acquired. The raw data set was opened in ImageJ/Fiji, and the SIMcheck tool "Channel Intensity Profiles" was applied. The intensity was adjusted to be about equal across phases (data point spacing) and between angles (the difference between rows of data points). Slight variation in intensity between angles is inevitable due to variables such as single-mode vs. multimode fiber-optic coupling or the transmittance/absorbance parameters of the dichroic mirror. SIMcheck was configured to use the "Raw Data" > "Fourier Projections" function. It was shown that the Fourier transform contains discrete first- and second-order spots. SIMcheck's 'Illumination Pattern Focus' calibration tool was used.

We ensured that the illumination's axial modulation was constant across all three angles.

Calibration data sets reconstruction and quality control

The raw data was reconstructed using commercial SIM reconstruction software utilizing the raw data obtained and the channel-specific OTFs collected. For multicolor acquisitions, we applied a set of channel-specific measured OTFs acquired with the same RI noil (or nsilicone) immersion media for all channels; for two- and three-color experiments, including the red channel, we optimized for the red channel.

The option in the reconstruction program that ignores negative unsigned values in the image was disabled for the calibration (as well as experimental) data sets. In Zeiss's Zen SIM reconstruction program, this option is referred to as "Baseline Cut."

dSTORM imaging

To facilitate reversible switching of single fluorophores during data acquisition, coverslips containing stained brain slices were placed in a custom-made holder and incubated in imaging buffer (see Recipe). The images were obtained using an inverted microscope mounted on a nosepiece-stage.

Excitation of Alexa Fluor 647 and Alexa Fluor 532 using 644 nm and 532 nm lasers, respectively, was employed. A clean-up filter and two dichroic mirrors were used to direct laser beams onto the sample. By employing a dichroic mirror

3. Material and methods

and a quadband filter, the emitted fluorescence was separated into two separate cameras. A long-pass filter or a bandpass filter for the red and green channels, respectively, were used to filter the fluorescence signals. The red channel had pixels with a size of 126 nm, and the green channel pixels with a size of 128 nm. RapidSTORM was used to locate single fluorophores and reconstruct high-resolution images (Wolter et al. 2012).

The quality of the color alignment is a critical aspect in the correctness of two-color data. We mostly use sequential measurements in which the signal from two fluorophores is divided spectrally across two cameras. Because of chromatic aberration and tiny variations in detection paths, spheres packed with fluorophores (ThermoFischer Tetraspecks) are detected on both cameras and utilized to calculate a registration matrix.

3D dSTORM images were captured using the same equipment mentioned before, including a Zeiss 63mm, NA 1.15 water immersion objective, a Piezo Z-stage, and a cylindrical lens in the emission path to acquire information about the fluorophore's three-dimensional location (B. Huang et al. 2008). We utilized multi-fluorescent beads that were adsorbed on a coverslip and then covered with water to calibrate the microscope's z-axis. The calibration sample was axially moved across the focal plane at a constant speed by the piezo, and the widths of the PSF in x and y were measured using rapidSTORM (Wolter et al. 2012). Using cubic B-splines, it is possible to interpolate the widths against the given z location, and this is exploited as a calibration table (Proppert et al. 2014). RapidSTORM was used to identify the axial location of localizations in samples, as disclosed previously (Proppert et al. 2014).

3.5.5.8 Data processing

Fiji

Fiji (also known as ImageJ) is an image processing application based on the open-source platform ImageJ that includes a number of features that aid in scientific image analysis. The tool is available and explained on (<https://imagej.net/software/fiji/>).

Imaris

Imaris is commercial software developed by Bitplane (Oxford Instruments) that provides visualization and processing tools for 3D microscopy data sets. It is employed in the rendering of 3D SIM datasets.

3. Material and methods

rapidSTORM

rapidSTORM is an open-source software that can be downloaded from the homepage of Prof. Dr. Markus Sauer's Biotechnology and Biophysics department at the University of Würzburg (<https://www.biozentrum.uni-wuerzburg.de/super-resolution/archiv/rapidstorm/>). rapidSTORM is now accessible in two versions: rapidSTORM 2 is the current stable branch, in which only notable bugs are fixed, and rapidSTORM 3 is the unstable development subcategory, which features an improved user interface and refined technical deployment. For the reconstruction of the SMLM raw data, the program rapidSTORM is utilized. Wolter et al. provide a comprehensive explanation of the underlying algorithm and work-flows (Wolter et al. 2012), as well as the rapidSTORM manual (Wolter, Proppert, and Aufmkolk, n.d.). rapidSTORM is a tool for detecting single fluorophores that emit sparsely in sequences of images. RapidSTORM, in a nutshell, determines the quantity and position of individual fluorophores' emission patterns. A two-dimensional Gaussian fitting algorithm is used to identify the most likely fluorophore site. The precision that can be achieved is largely determined by the signal's photonstatistic. This results in the creation of a list of localizations, which is then compiled into a reconstructed high-resolution image. rapidSTORM enables the implementation of a transformation matrix to rectify chromatic aberration in two-color data sets. Correction of linear drift is also attainable. Furthermore, the computation of individual fluorophore z-positions via analysis of shape changes in the point spread function allows three-dimensional imaging. It is possible to use both astigmatic and multi-layer methods.

4 Statistics and analysis

Statistical analyses were carried out using Sigma Plot 12 and 14 (Systat Software GmbH, Ekrath, Germany) and Prism 10, Version 9.2.0 (GraphPad Software, San Diego, California), with the non-parametric Mann–Whitney rank sum test or the non-parametric ANOVA for multiple comparisons. The significance level is indicated by an asterisk (* $p < 0.05$, ** $p < 0.01$, *** $p < 0.001$). Non-parametric data are presented as median \pm 25th and 75th percentiles unless otherwise noted, and parametric data are reported as mean \pm SD.

5 Results and Discussion

5.1 Super-resolving Microscopy of hippocampus mossy fiber active zones

Determining quantitative information on the molecular distribution and densities of synaptic proteins necessitates a method with the precision to resolve the spatial relationship between single synaptic proteins. The upcoming chapter will describe a workflow for multicolor structured illumination microscopy (SIM) as well as for 2D and 3D *d*STORM on two separate setups and discuss the findings using SIM and *d*STORM to image key AZ proteins after cLTP induction. The same experiment was carried out with two super-resolution imaging techniques in order to visualize the density and distribution of AZ's proteins in brain slices. All measurements were carried out as three-channel SIM or two-color *d*STORM in two dimensions using serial data capture, as described in the methods chapter. For two-color measurements, the possible resolution is dependent mainly on the photophysics of the specific fluorophore. This and the correctness of the channel alignment with Tetraspecks should be described in the examples beforehand. The advancement of super-resolution data analysis is one of the critical points of emphasis in this Chapter. It is critical to embed the sample in a chemical environment conducive to both methods. I will discuss possibilities to establish a compatible environment. Additionally, various possible methods for aligning the two data sets, which can be used in further investigations, will be reviewed.

5.2 Summarized setup workflow

In figure 14, the essential steps used in this work are demonstrated. Standard fluorescent labeling protocols are suitable and are primarily reliant on the target structure.

5. Results and Discussion

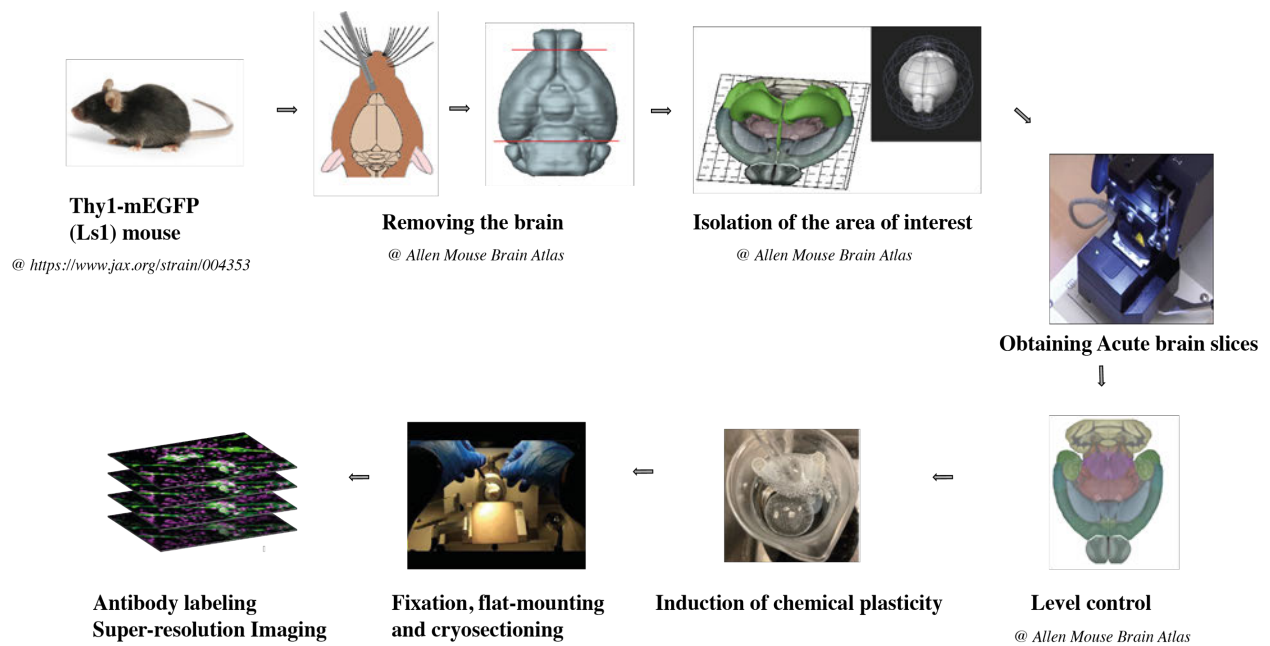


Figure 14. Schematic workflow overview for imaging of hippocampal mossy fiber synaptic contacts.

Male *Thy1mEGFP (Ls1)* mouse (Deguchi et al. 2011) were used for preparing the acute brain slices. 300 μm thin horizontal acute brain slices were made. Slices were chosen at definite hippocampal levels (1500 μm and 1800 μm from the ventral brain surface). We used images from a horizontal brain atlas stained by Nissl to align the cutting level between various animals on the identical hippocampal region (brainmaps.org) (Mikula et al. 2007). For the induction of cLTP, slices were exposed to ACSF with 50 μM forskolin in 0,5 % DMSO for 30 minutes at room temperature. The control slices were exposed to the same concentration of DMSO in ACSF for the same duration. Prior to fixation, the slices were moved into separate maintenance chambers containing carbogenated ACSF and allowed to sit at room temperature for 30 minutes before being fixed. Each slice was fixed with 1 ml of ice cold 4 % paraformaldehyde solution. Following the fixation step, 25 μm thin cryotome slices were cut at the defined level of the dorsal hippocampal, with the maximum height difference of 150 μm . The prepared brain slices were stained with antibodies (mouse monoclonal anti-Bassoon and rabbit anti-Munc-13-1 or rabbit anti-Tomosyn for SIM images and with mouse monoclonal anti-Bassoon for dSTORM images). Protein cluster size, number and density in selected *Thy1-EGFP(M)* / *Thy1mEGFP* positive boutons was measured and adjusted to the EGFP-positive area. See the method chapter for more detailed information

5.3 SIM

As previously mentioned, contemporary microscopy provides a variety of imaging modalities, each with its own set of benefits and drawbacks. High spatial

5. Results and Discussion

resolutions on the order of nanometers (e.g., single-molecule localization microscopy methods) are accomplished at the expense of speed (SMLM, for example, is characterized by protracted acquisitions involving hundreds of frames) and phototoxicity/bleaching (due to the high-power lasers required for each acquisition). The superb optical sectioning provided by confocal imaging is counterbalanced by the requirement for point-scanning, which significantly slows down acquisition time. Traditionally, the quick capture of large 3D volumes with little photobleaching and/or toxicity provided by light-sheet is counterbalanced by the numerical aperture (NA) constraints placed on objectives used to acquire pictures through orthogonal excitation. While substantial progress is being made to address the fundamental constraints of these methods, sophisticated light microscopy is not without trade-offs. Quantitative imaging experiment design is consequently significantly influenced by the question being asked and, as a result, which of the various imaging approaches available is most suited to answer that question in a given sample. Sample size, variability, and the time it takes to evaluate potentially vast volumes of data effectively and with slight bias are other vital concerns that are seldom highlighted.

SIM was selected because it can be easily applied to samples prepared for regular fluorescence microscopy without needing substantial extra sample preparation work. Furthermore, SR-SIM has multicolor capability, with up to four separate color channels routinely demonstrated and implemented. Image quality in SIM increases with more photostable dyes; however, several dye possibilities exist for different excitation wavelengths. We used the Zeiss Elyra S.1 (configuration Chapter methods) and with a 10x objective to detect distinct structures. After switching to the 63x oil objective, appropriate acquisition settings for each marker were selected. Image reconstruction was carried out on the Elyra S.1 with Zen software (black edition) and Imaris software.

5.3.1 Alignment accuracy in multi-color data

In multi-color data, the accuracy of the color alignment is a critical component in determining the reliability of the data. In SIM the pointillist data must be converted to a pixel or voxel grid. SIM reconstruction software, such as the commercial Zen Software (Zeiss), generates a pixel-based result, mostly a hyperstack including channel and z-layer values. These sets of data must be aligned and displayed in order to create a coherent picture. This requires a highly optimized read-out and robust graphics processing.

5. Results and Discussion

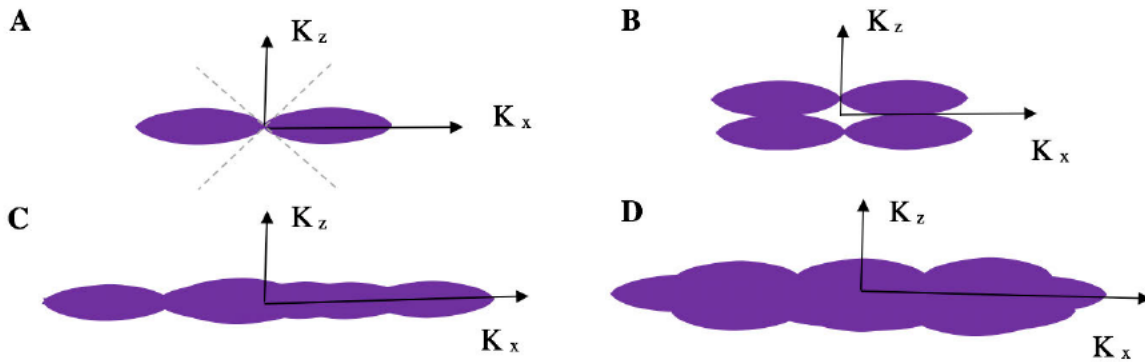


Figure 15. Functions of optical transfer (OTFs).

Under uniform illumination, the central k_x - k_z cross section of the zone of support for the detection OTF (A). This also holds to the OTF for zero component detection and, if the illumination is entirely coherent, to second component detection. The first-order detection OTF of three-beam SIM is illustrated in (B). Completed OTFs of reconstructed two-beam (C) and three-beam SIM (D) imaging (just one grating direction) with a grating vector somewhat lower than the narrowest achievable grating. Take note how several directions fill up the spaces along k_x in (D)

An ideal 3D-SIM setup acquires a sequence of SIM pictures for each focus location and steps the sample vertically across the focus in tiny increments. Due to the fact that the illumination structure generated by a three-beam SIM system also creates an axial intensity structure that shifts along Z concerning the sample coordinate framework as the focus changes, the axial components of the illumination structure become engrained on the detection point spread function. Only the first order (Figure 14 B), not the zero or second order (Figure 14 A), will seem to have an in-plane structured illumination but will really have a modified detection PSF created by multiplying a wide-field detection PSF by an axial sine wave. As a consequence, the matching first order OTF will be made up of two copies of a wide-field detection OTF, relocated once above ($+\Delta k_z$) and once below ($-\Delta k_z$) the lateral anchoring point along the axial direction (Figure 14 B). The z -sampling in the raw data, i.e. the separation between sequential slices, needs to be twice as fine as necessary for evenly illuminated wide-field data or two-beam SIM as a direct result of the optical transfer function's enlarged k_x range. This mandates the use of a distinct OTF for each lateral illumination sequence in the reconstruction framework. In reality, keeping the illumination phase in precise alignment with the optimal focus slice is often challenging. Significant

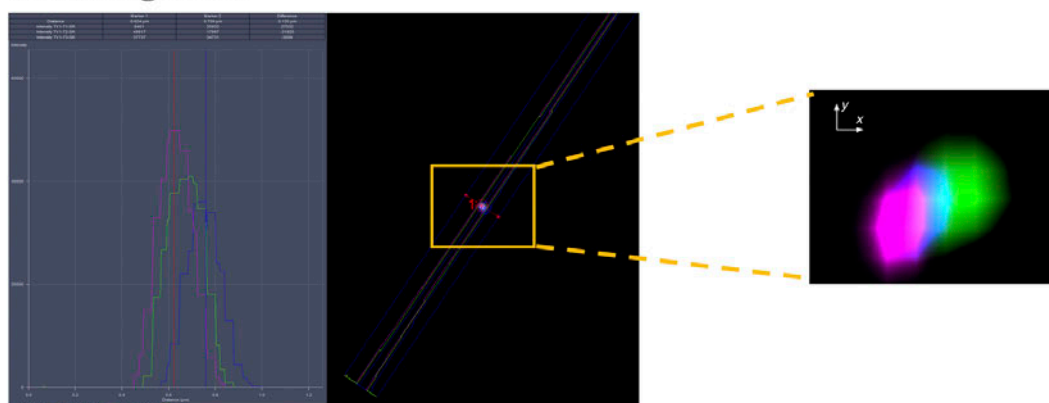
5. Results and Discussion

reconstruction artefacts may arise from such a z -shift of the woodpile intensity structure formed in the sample.

As a corollary, for the first component in the three-beam (five intensity components per direction) configuration, this impact must be adjusted by accordingly phase-modified OTF. This may also be achieved by employing a bead sample imaged under the same structured illumination and sample embedding circumstances to extract order-separated PSFs/OTFs (Mats G L Gustafsson et al. 2008).

In all images, each channel was processed using SIM algorithms available in the commercial software (for more details, see the method chapter). All channels were subsequently aligned based on the calculated transformation matrix (Figure 16).

Before alignment



After alignment

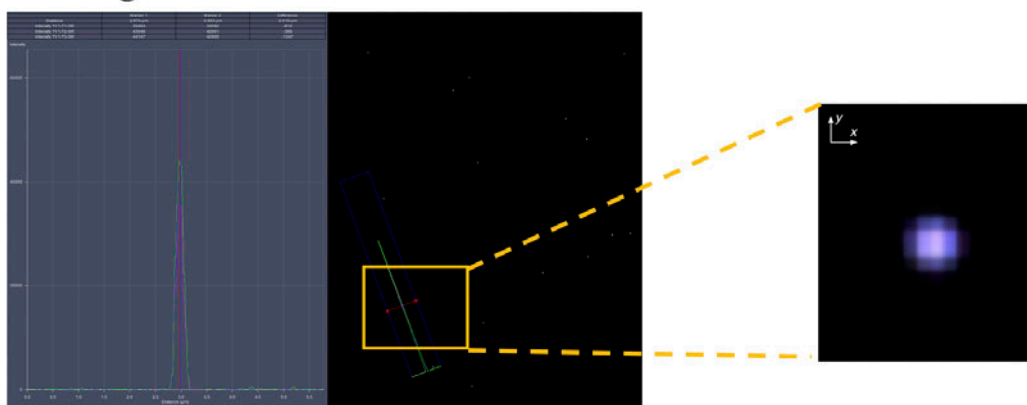


Figure 16. Calibration slide preparation.

PSF slides should have well-distributed single beads mounted to the coverslip surface that can be captured individually in a 256 256-pixel (px) frame. The expected result of a 3D multicolor alignment slide with a 200-nm TetraSpeck bead field demonstrated before and after alignment using image registration software.

5. Results and Discussion

Prior to the reconstruction and data analysis, the images were assessed for artifacts, background noise, and/or incomplete removal of grid lines. If artifacts are seen, the SIM processing algorithm parameters were readjusted, and the image was reprocessed.

5.3.2 Imaging synaptic contacts of hippocampal mossy fiber; Application of SIM to MFB

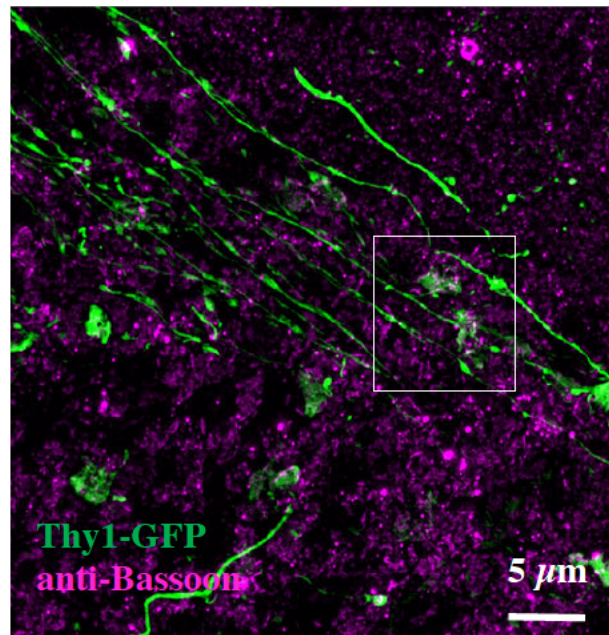


Figure 17. Bassoon immunofluorescence in normal tissue of Thy1EGFP (M) mice

Immunofluorescence staining of AZs in the hippocampus of Thy1EGFP(M) mice. An antibody against the AZ protein Bassoon was used as a marker for active zones. In the selected section from the mossy fiber tract with GFP-labelled MF axons, the clustering of the Bassoon signal into small groups is noticeable. In the two channels overlapped, individual groups can each be assigned to a bouton. Scale bar 5 μ m.

In visualizing active zones, it became clear that the diffraction limitation of conventional light microscopy is a crucial obstacle in determining numerous parameters such as number and size, and consequently in the assessment of synaptic plasticity.

In the past decade, different light microscopic techniques have been developed to bypass the diffraction limit. To visualize hippocampal mossy fiber synapses immunofluorescence staining was first performed on fixed CNS from Thy1-EGFP(M) (Figure 17). Immunofluorescence staining against the AZ protein Bassoon was thus established as a reference marker for AZ. In the cryosections of Thy1-mEGFP brains, sections of mossy fiber axons with large mossy fiber boutons could be clearly identified (Figure 18). Bassoon showed a clearly grouped

5. Results and Discussion

pattern in the mossy fiber tract. The clustering could be assigned to individual moss fiber boutons: A Bassoon group corresponded to the AZs of a bouton (Figure 19 and 20). A complete colocalization could not be expected, since not all granule cells are GFP-labeled in this animal line, so that numerous additional synapses can be expected between the labeled boutons in the image.

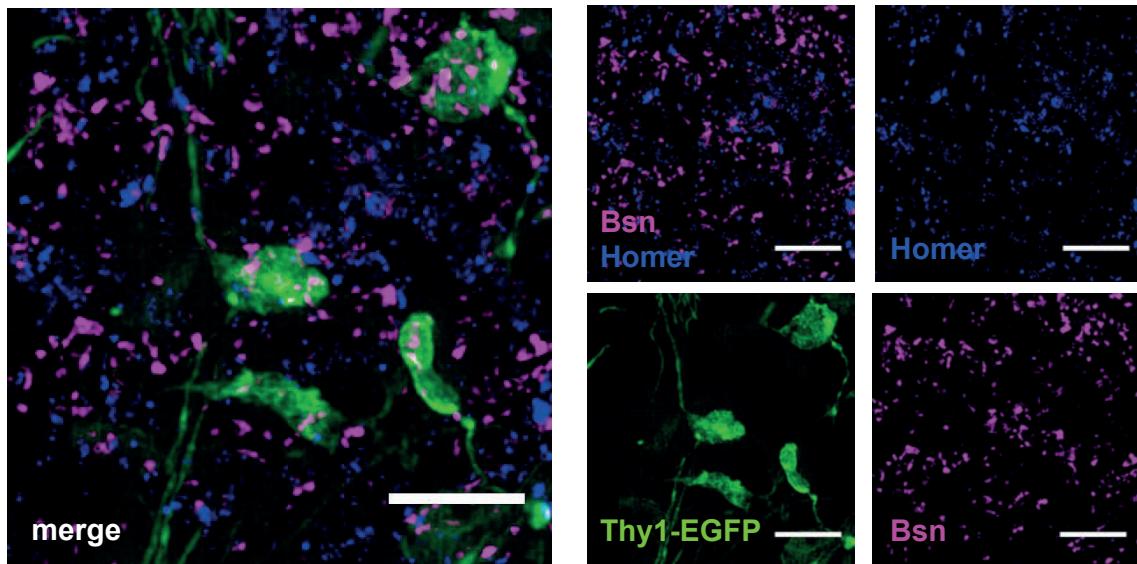


Figure 18. Immunofluorescence double staining of anti-homer and anti-bassoon in fixed mouse hippocampus.

Right: Three-channel SIM image of individual MFBs (green) and antibody-staining against Bsn (magenta) and the postsynaptic protein Homer (blue) in the CA3 region of Hippocampus Thy1-mEGFP mice. The anti-bassoon immunofluorescence shows a grouped pattern, with one group corresponding to a bouton. Clusters can be seen in the EGFP immunofluorescence images. In the overlay of both channels, a clear colocalisation of the EGFP and the anti-bassoon signal can be seen in the area of the clusters. Scale bar 5 μ m.

Individual MFB in the CA3 region of Thy1-mEGFP (Lsi1) mouse brain slice with expressing membrane bound EGFP in green. in three-channel SIM imaging could be identified (Figure 20).

5. Results and Discussion

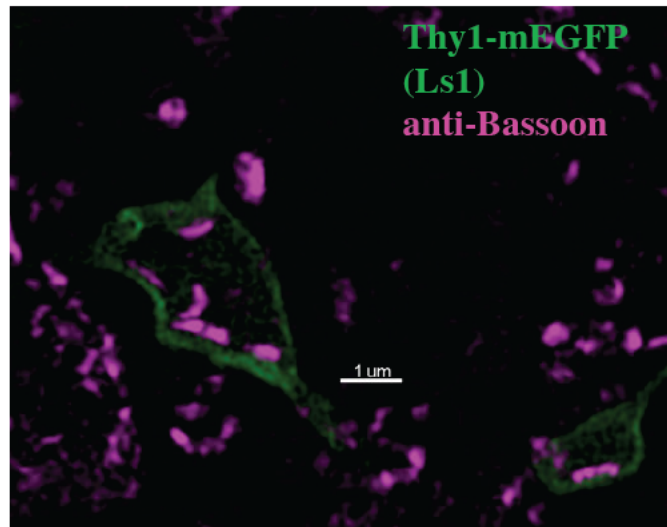


Figure 19. Representative SIM image of MFB in the CA3 region of a Thy1-mEGFP (Ls1) mouse brain slice (green) stained against Bsn (magenta).

Since individual bouton measurements are preferred, Thy1-mEGFP (Ls1) mice expressing membrane bound EGFP were used to visualize bouton surfaces. Large MFBs were clearly apparent in this preparation. The anti-GFP fluorescence MF boutons, filopodia, and axons are represented in a SIM image. Scale bar 1 μm .

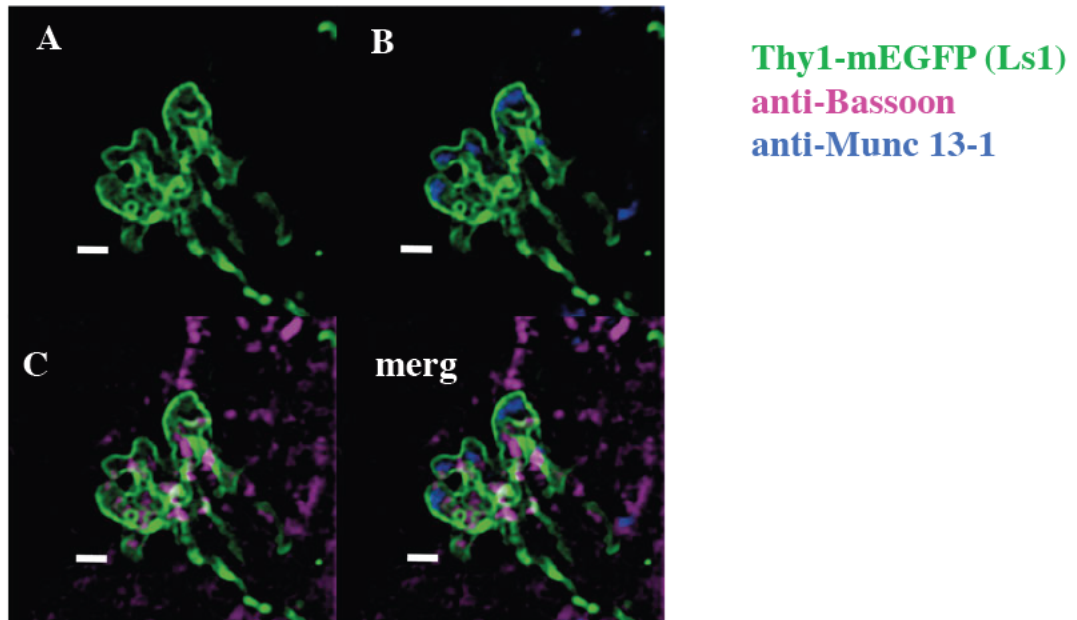


Figure 20. Three-channel SIM image of an individual MFB in the CA3 region of Thy1-mEGFP (Ls1) mouse brain slice

A) Representative of MFB in the CA3 region of hippocampus with expressing membrane bound EGFP in green. B) staining against Munc-13-1. C) The same MFB with the magenta staining against Bassoon (Bsn) protein. Merged image of the MFB with anti-Munc-13-1 and anti-Bsn staining. Scale bar 1 μm .

5.3.3 Surface analysis; Reconstruction of MF and AZ proteins in SIM images

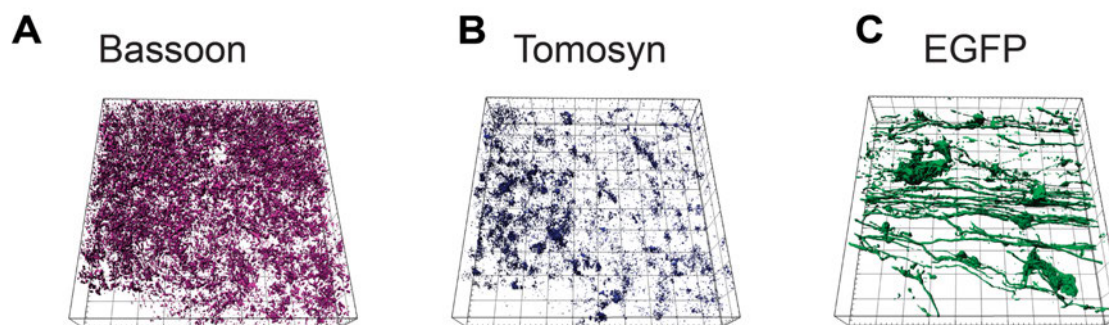


Figure 21. Representative 3D reconstruction of AZs proteins Bsn and Tomosyn in CA3.

3D SIM imaging in 25 μm thick Thy1-mEGFP (Lsi1) mouse brain tissue slices (A, B, C) 3D volume reconstruction in x y z-view, with Bsn and Tomosyn clusters. Grid size 5 μm .

Surfaces in Imaris are 3D models that are generated from 3D images via a series of pre-processing, segmentation, and linked component labeling processes (Figures 21 and 22). Surfaces are used to detect and depict key items within an image, as well as to get measurements of intriguing structures (Area, Volume, Intensity, Position, Ellipticity, and more). The Contour Surface enables users to extract a 3D item by manually sketching the outlines of the object on 2D slices while concentrating on key features. When automated surface segmentation fails to produce individual structures in a satisfactory manner, the Contour Surface technique is preferable (e.g., touching cells in confocal microscopy, complex tissue recorded by transmission microscopy).

5. Results and Discussion

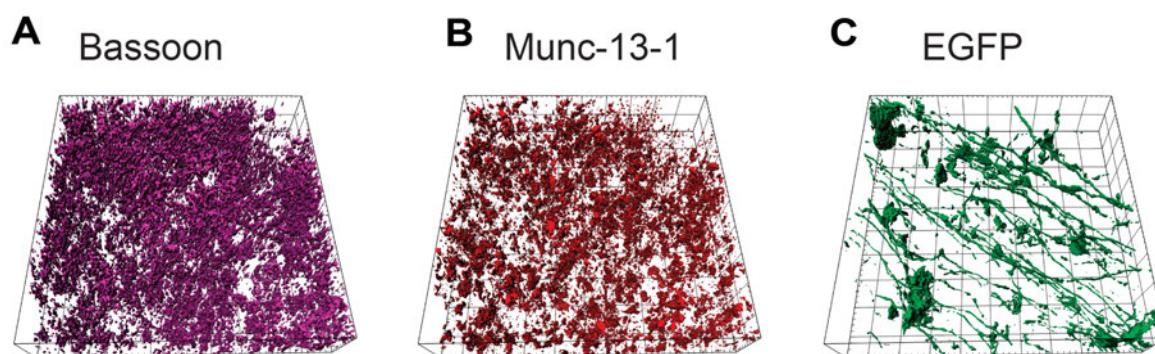


Figure 22. 3D reconstruction of AZs proteins Bsn and Munc-13-1 in CA3 region of Hippocampus.

3D SIM imaging in 25 μm thick Thy1-mEGFP (*Lsi1*) mouse brain tissue slices (A, B, C) 3D volume reconstruction in x y z-view, with Bsn and Munc-13-1 clusters. Grid size 5 μm .

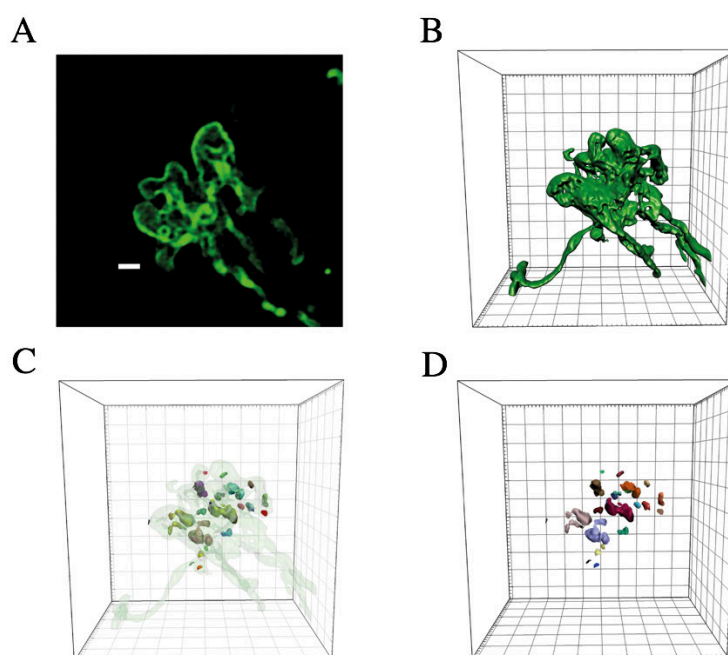


Figure 23. SIM; 3D reconstruction of MFB and Bsn clusters.

(A) Representative of MFB in the CA3 region of a Thy1-mEGFP (*Lsi1*) mouse brain slice (green) scale bar: 1 μm . (B) Reconstruction of the MFB in the CA3 region of a Thy1-mEGFP (*Lsi1*) mouse brain slice (green) with surface analysis of Imaris, grid size 1 μm . (C) 3D reconstruction image of MFB with Bsn staining. Grid size 1 μm . (D) Reconstruction of Bsn clusters in MFB, Grid size 1 μm .

5. Results and Discussion

After the alignment step, Imaris was used to view the image (Figure 23). The option "add new surfaces" initiates the surface planning process. After selecting a channel and deselecting the smoothing function, the same thresholding option for background removal was set for the images. Imaris is capable of generating a surface for each channel. Here, the sensitivity of the surface creation may be tweaked. Many thresholds were observed to prevent generating surfaces with excessive noise or fluorescence to determine the ideal signal-to-noise ratio. Imaris will have created the final surfaces for all the objects it has identified at this time. Finally, under the construct tab, we changed the region on the number of voxels histogram to eliminate any small undesired surfaces caused by noise or to eliminate a very big surface formed by background fluorescence or an unwanted structure.

5.3.4 Quantification of EGFP/MFB volume in SIM images

Six acute brain slices from the right brain hemisphere of three 16-week old male Thy1mEGFP (Lsi1) mice were used for this experiment. In total 20 images and 170 MFBs were analyzed.

Table 4. The number of MFBs per image. Animal 1-ACSF experiment, right hMFT: four 25 μ m sections; 2 images per section: 8 SIM images

| <i>Cryosection number</i> | <i>Proteins</i> | <i>Number of MFBs</i> |
|---------------------------|-------------------|-----------------------|
| 1 | Bsn and Munc 13-1 | 20 |
| | | 15 |
| 2 | Bsn and Tomosyn | 18 |
| | | 15 |
| 3 | Bsn and Munc 13-1 | 8 |
| | | 14 |
| 4 | Bsn and Tomosyn | 13 |
| | | 7 |

Table 5. The number of MBFs per SIM image. Animal 2-ACSF experiment, right hMFT, six 25 μ m sections; 1 image per section: 6 SIM images

| <i>Cryosection number</i> | <i>Proteins</i> | <i>Number of MFBs</i> |
|---------------------------|-------------------|-----------------------|
| 1 | Bsn and Munc 13-1 | 1 |
| 2 | Bsn and Tomosyn | 7 |
| 3 | Bsn and Tomosyn | 1 |
| 4 | Bsn and Munc 13-1 | 2 |
| 5 | Bsn and Munc 13-1 | 4 |
| 6 | Bsn and Munc 13-1 | 1 |

5. Results and Discussion

Table 6. The number of MBFs per SIM image. Animal 3-ACSF experiment, right hMFT, six 25 μm ; 1 image per section: 6 images

| <i>Cryosection number</i> | <i>Proteins</i> | <i>Number of MFBs</i> |
|---------------------------|-------------------|-----------------------|
| 1 | Bsn and Munc 13-1 | 7 |
| 2 | Bsn and Munc 13-1 | 5 |
| 3 | Bsn and Tomosyn | 9 |
| 4 | Bsn and Tomosyn | 4 |
| 5 | Bsn and Munc 13-1 | 8 |
| 6 | Bsn and Munc 13-1 | 11 |

Due to the resolution limit of SIM (Heintzmann and Cremer 1999; M G L Gustafsson 2000; M. G. Gustafsson, Agard, and Sedat 1999), we were unable to do a quantitative analysis of MFB-volume-related changes in our data. It was not possible to automate the process of establishing the start and end of a single bouton using Imaris software because the distance between MFBs in some brain sections was less than 100 nm.

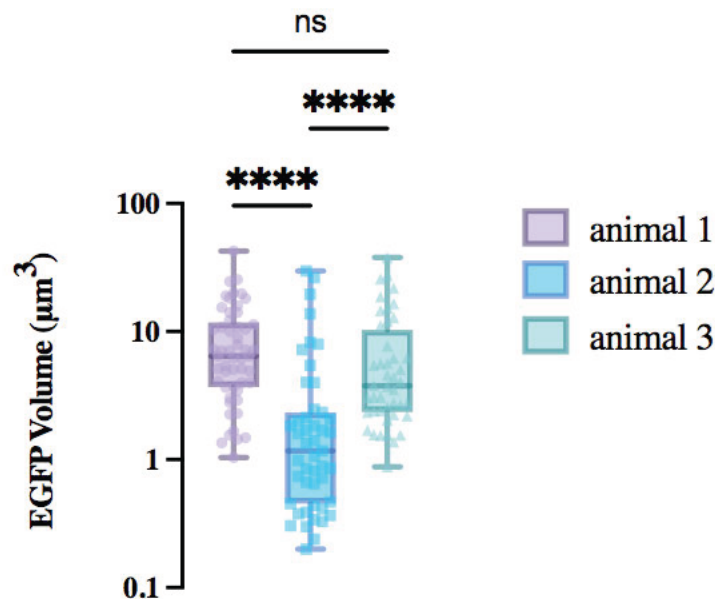


Figure 24. Quantification of MFB/EGFP volume in SIM images

We could observe a similarity between animals 1 and 3, whereas one out of three animals showed highly significant variation ($p < 0.001$) in volume of EGFP positive MFBs [median; animal 1: 3,931 (μm^3); animal 2: 0,9423 (μm^3); animal 3: 2,265 (μm^3).

Figure 24 shows the analysis of all the EGFP positive structures that the Imaris calculated starting from 0,1 μm^3 . Since the reported volume of MFBs is much larger than 0,1 μm^3 (8-17 μm^3) (Pauli et al. 2021; Wilke et al. 2013; Zhao et al.

5. Results and Discussion

2012), we filtered all data using a minimum size of size of $5 \mu\text{m}^3$. Figure 25 represents 170 MFBs positive (filtered data) from 3 three animals in 20 images.

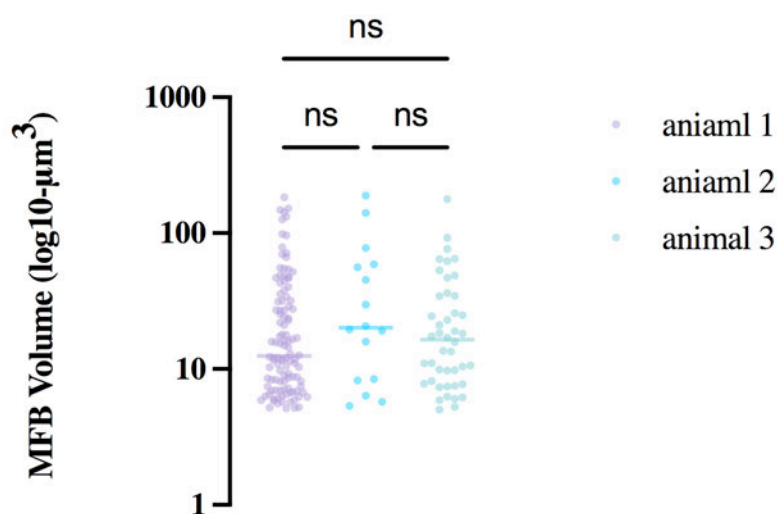


Figure 25. Quantification of MFBs in SIM images (filtered data).

After filtering the data and evaluating the MFBs that were larger than $5 \mu\text{m}^3$, the variability between individual animals was significantly decreased, line represents the median.

Table 7. Quantification of MFBs in SIM images (filtered data).

| | <i>animal 1</i> | <i>animal 2</i> | <i>animal 3</i> |
|--|-----------------|-----------------|-----------------|
| <i>Number of EGFP positive/MFBs</i> | 110 | 16 | 44 |
| <i>Minimum Volume</i> | 5,144 | 5,365 | 5,036 |
| <i>25% Percentile</i> | 7,391 | 8,293 | 7,862 |
| <i>Median</i> | 12,47 | 20,09 | 16,43 |
| <i>75% Percentile</i> | 32,41 | 58,45 | 34,57 |
| <i>Maximum Volume</i> | 183,4 | 188,8 | 178,0 |
| <i>Mean</i> | 28,14 | 44,18 | 27,23 |
| <i>Std. Deviation</i> | 35,18 | 52,58 | 31,70 |
| <i>Std. Error of Mean</i> | 3,354 | 13,14 | 4,779 |

5.3.5 Quantification of Bassoon, Munc 13-1 and Tomosyn protein intensity in SIM images

It is necessary to use consistent sectioning protocols when imaging in anatomically precise defined locations. Electrophysiological recordings are frequently performed on acute 300 μm slices. We chose a certain anatomical level of the hippocampus as our reference point. The Thy1mEGFP (Lsi1) mice, which have high levels of membrane-bound EGFP expression in MFs, were used to accurately position imaging windows (50 μm x 50 μm) in the center of the MF tract. Confocal microscopy was used to validate the location of the imaging windows in the MFs even more precisely. Horizontal sections with a thickness of 25 μm are appropriate for multicolor imaging with Alexa568 and ATTO 647 with SIM. We employed three-color 3D-SIM with antibodies directed against the presynaptic AZ proteins Bassoon, Munc 13-1 and Tomosyn.

Bassoon, Munc 13-1, and Tomosyn protein are well-characterized presynaptic proteins that are expressed in big mossy fiber boutons and CA3 pyramidal dendrites, and they are involved in synaptic transmission. The Bassoon is a multi-domain protein that interacts with other AZ components such as RBP, Piccolo, and other proteins via its various domains (Eckart D. Gundelfinger, Reissner, and Garner 2016; Dresbach et al. 2001; Torres and Inestrosa 2018; Tom Dieck et al. 1998; Davydova et al. 2014). Despite the fact that its orientation inside the AZ is uncertain, it seems to be connected in close proximity to the membrane according to its PxxP-motif interaction with RBP (Pauli et al. 2021).

Comparing individual animals, the intensity of Bassoon in the chosen EGFP positive boutons was substantially different in one of the three animals. In light of the fact that the size of Bassoon and the release of neurotransmitters are connected, the gradient found here between animal 1 and 2 and animal 2 and 3 are likely to contribute to the significant variability reported in recordings from MFBs. Furthermore, these discrepancies emphasize the need to accurately delineate areas of interest inside mouse brains with submillimeter accuracy.

Given the complex, partially folded structure of hippocampal MFBs, it is possible that surrounding Bassoon clusters are stacked in 2D imaging and hence appear larger than they are. With a lower z-range and higher resolution, the issue of overestimation becomes less problematic. 25 μm slices SIM imaging result in an overestimation of cluster size in MFT imaging. therefore, we only analyzed the sum of protein intensity and density per EGFP positive volume in SIM images. (see "Methods" Chapter).

5. Results and Discussion

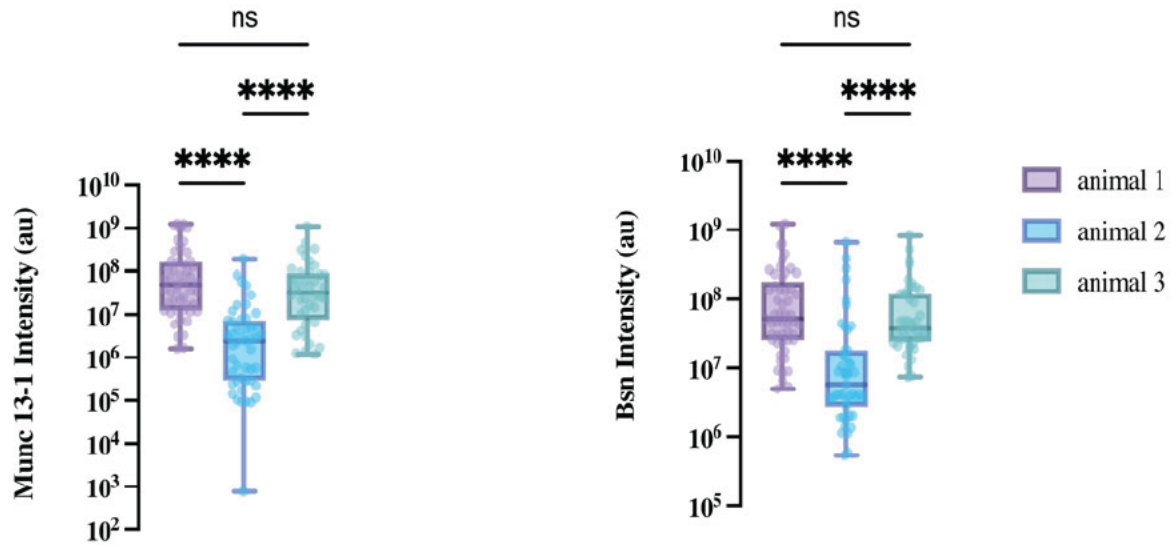


Figure 26. *Bsn and Munc 13-1 measures in scanning SIM of 25 μm cryosections of hippocampal mouse tissue.*

Bsn intensity sum in EGFP positive MFBs [median; Bsn animal 1: 32551950 (au); Bsn animal 2: 5028720 (au); Bsn animal 3: 20976400 (au)] and Munc 13-1-cluster intensity sum in EGFP positive MFBs [median; Munc 13-1 animal 1: 27120150 (au); Munc 13-1 animal 2: 1588880 (au); Munc 13-1 animal 3: 20494800 (au)]

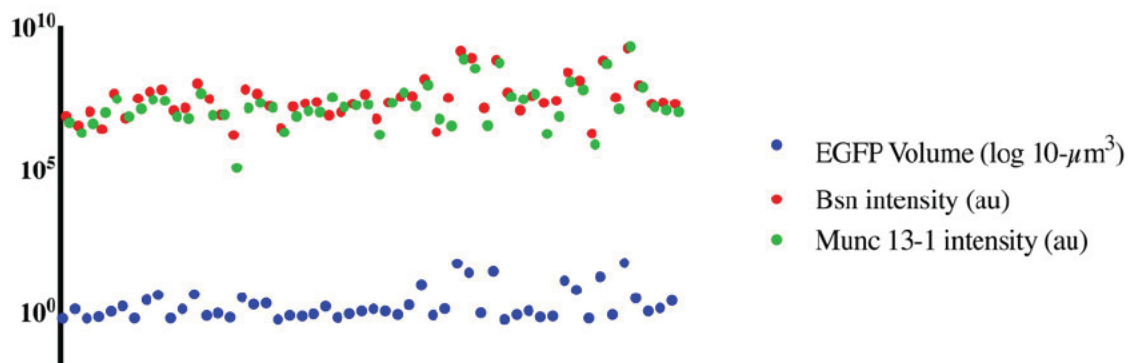


Figure 27. *Bsn and Munc 13-1 intensity and EGFP volume quantifications in a single SIM image of 25 μm cryosections of hippocampal MFT mouse tissue.*

Each point represents a single protein intensity measurement in the SIM image and its EGFP positive MFB. Due to the resolution limit of SIM, the EGFP positive Boutons or structures cannot be assigned to an individual MFB.

5. Results and Discussion

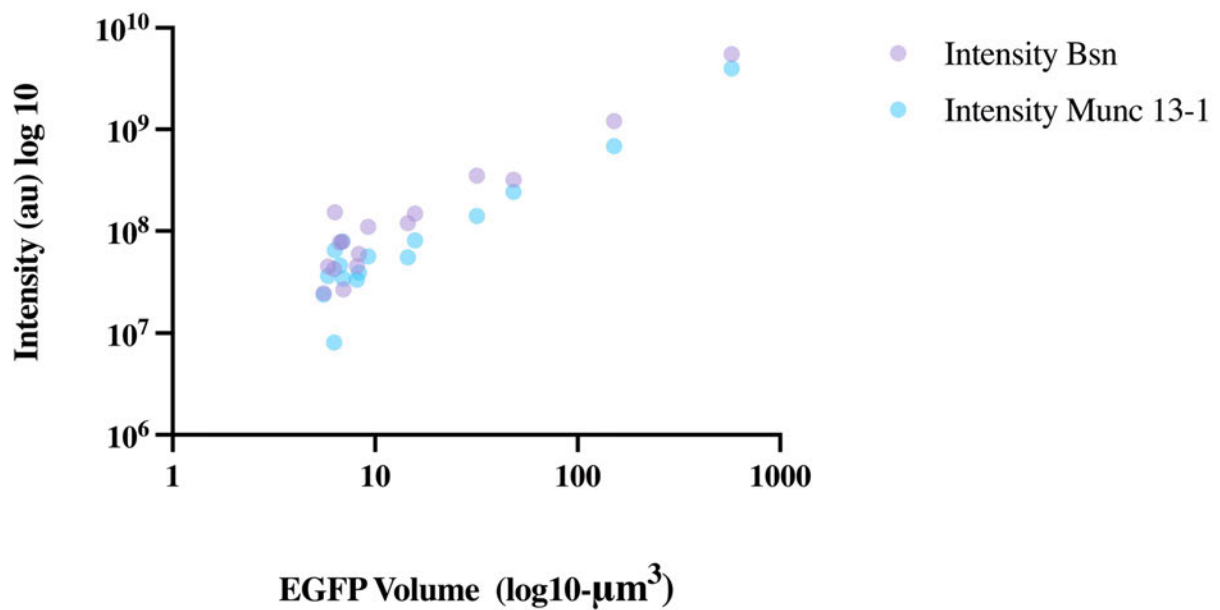


Figure 28. Bsn and Munc 13-1 intensity and EGFP volume measurements in a single SIM image of 25 μm cryosections of hippocampal MFT mouse tissue.

Here we can observe that the majority of the Bsn and Munc 13-1 are in small EGFP positive MFBs. Due to SIM resolution and the complex structure of the MFB, it is not sure whether each positive EGFP surface signal represents a single Bouton.

The data represented in Figures 26-28 are all nonfiltered data. We analyzed the data and excluded the EGFP positive values that were less than 5 μm^3 since, based on the known data (Pauli et al. 2021; Wilke et al. 2013; Zhao et al. 2012), the MFBs are likely to be bigger than five μm^3 . After filtering the data and analyzing the MFBs that were larger than 5 μm^3 , the findings of our analysis revealed a substantial level of uniformity in Bsn, Munc 13-1 and Tomosyn intensity across all animals (Figure 29, 30 and 31).

5. Results and Discussion

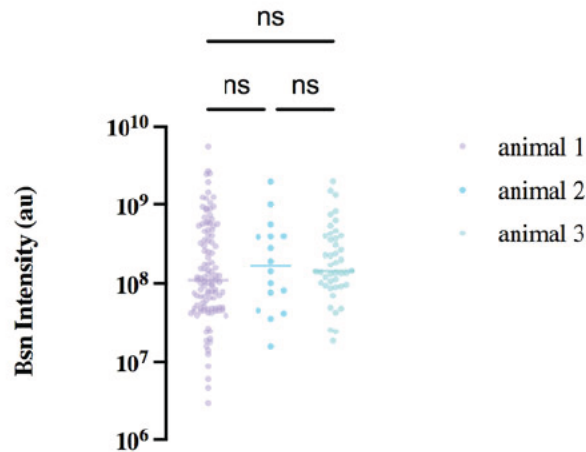


Figure 30. Bassoon sum intensity measures in scanning SIM of 25 μm cryosections obtained from 300 μm acute brain sections of hippocampal mouse tissue (filtered data).

The results of our analysis revealed that there was a significant degree of consistency in Bassoon intensity across all animals after filtering the data and analyzing the MFBs that were greater than 5 μm . Each point shows intensity in an EGFP positive MFB. The median is represented by a line.

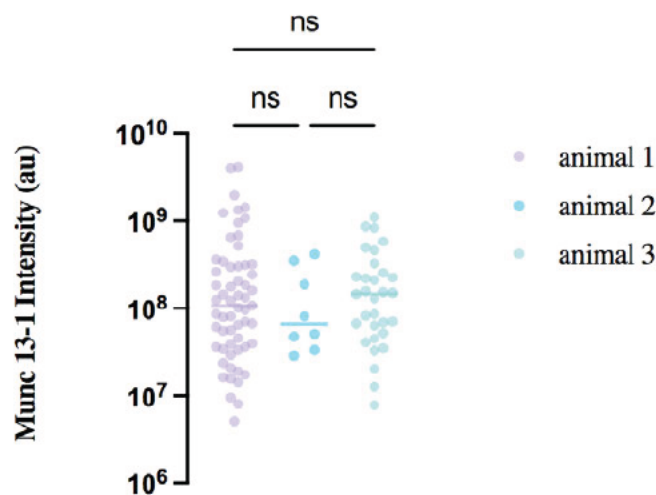


Figure 29. Munc 13-1 sum intensity measures in scanning SIM of 25 μm cryosections obtained from 300 μm acute brain sections of hippocampal mouse tissue (filtered data).

Results from our data analysis indicated that Munc 13-1 intensity was consistent across all animals after filtering the data and examining MFBs larger than 5 μm . Each dot represents the intensity of an EGFP positive MFB. A line is used to symbolize the median.

5. Results and Discussion

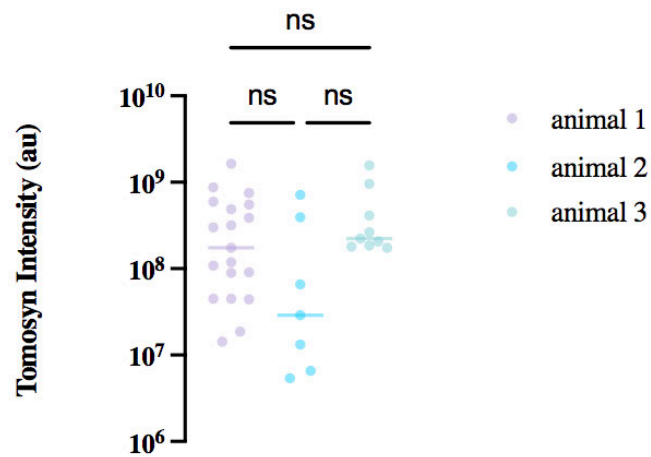


Figure 31. Tomosyn sum intensity measures in scanning SIM of 25 μm cryosections obtained from 300 μm acute brain sections of hippocampal mouse tissue (filtered data).

After filtering the data and analyzing the MFBs bigger than 5 m^3 , our findings suggest a substantial degree of consistency in Tomosyn intensity across all animals. The sum intensity of Tomosyn in an EGFP positive MFB is represented by each point. A line indicates the median.

5. Results and Discussion

5.3.6 Influence of Forskolin

Despite having similar molecular compositions, synapses may have very different functional transmitter release and plasticity characteristics. To investigate whether ultrastructural differences co-define functional heterogeneity following forskolin-induced plasticity, we compared functionally diverse alterations after induction of cLTP with forskolin.

5.3.6.1 Forskolin effect in hippocampal MFBs using SIM

The ultrastructural and functional correlates of chemical presynaptic potentiation and the molecular mechanisms how MFB synapses remodel to express and maintain long-term increase in neurotransmitter release have been studied by electron microscopy (Wilke et al. 2013; Vandael et al. 2020b). In this study SIM was used to study the changes in three selected AZ proteins in MFBs after induction of cLTP with forskolin. Bassoon intensity and density in MFT was measured in 25 μm cryosections obtained from 300 μm acute brain sections after stimulation with forskolin. Twenty-two acute hippocampal slices from three 16-week-old were prepared as described in (Hallermann et al. 2003).

SR microscopy is often used to provide structural information at scales ranging from 30 to 100 nm, depending on the modality (Y. Ma et al. 2021; Galbraith and Galbraith 2011b; Schermelleh, Heintzmann, and Leonhardt 2010). SR microscopy may also be used to investigate the nanoscale spatial relationships between proteins of interest by labeling them with diverse antibodies (Werner, Sauer, and Geis 2021). This is often accomplished by colocalization analysis, which measures spatial relationships on a scale larger than or equivalent to the imaging modality's resolution. For example, if we use a SIM implementation with an estimated resolution limit of 100 nm, colocalization analysis can tell us if two proteins interact at this scale but not whether they are separated at less than 100 nm. Colocalization analysis can be based on individual pixel correlation and overlap or spatial statistics estimated from the position of individual objects. We did not employ SIM images for protein colocalization analyses due to protein size and diffraction limitations. SMLM's pointillist character also lends itself to cluster analysis, a family of methods to quantify the spatial distribution of individual molecules. Ripley's K function and Pair Correlation may be used to identify whether the detections are randomly distributed or clustered. Individual clusters may then be segmented using techniques such as DBSCAN (density based spatial clustering of applications with noise), persistence-based clustering, or Voronoi tessellation straight from the point-cloud (Khater, Nabi, and Hamarneh 2020). This allows for quantifying factors such as cluster area, density, and the number of detections per cluster. We were unable to analyze the SIM data for distribution analysis since early data analysis indicated that the SIM imaging method was

5. Results and Discussion

insufficient for protein cluster localization evaluation in MFT. Finally, we decided to focus on protein intensity and density of the proteins in SIM images.

5.3.6.2 Analysis of protein intensity and density in hippocampal MFBs using SIM

Some essential aspects should be taken into consideration in order to produce reliable and quantifiable images for analysis. The general challenges of microscope alignment and sample preparation are covered in further depth in the method chapter.

To correctly quantify fluorescence intensity, the signal-to-noise ratio must be maximized while photobleaching is minimized. Image quality is greatly influenced by the alignment of the microscope, the objective lens, and the sample preparation. Proper alignment ensures that there is equal light over the whole field of view. To acquire the highest image intensity, an objective with a high numerical aperture (NA) should be used and it should be adjusted for optical aberrations at a magnification level acceptable for the sample. The sample should be fluorescently labeled in such a way that the ratiometric relationship between the fluorescent signal intensity and the amount of protein of interest is maintained throughout the experiment. Moreover, signal intensity loss owing to unintentional photobleaching during image acquisition should be minimized. The specifics of post-acquisition image analysis differ depending on the technique, but an accurate estimation of image intensity is crucial.

Fluorescence intensity of a two-dimensional image can be calculated using either the peak intensity of the spot (brightest pixel intensity) or the integrated intensity of the whole spot. Since SIM imaging of MFB does not imply a constant volume, we utilize integrated intensity to quantify the signal. When comparing numerous structures that vary in size and/or form, integrated intensity measurement will more precisely depict the intensity irrespective of fluorophore density. If a structure increases in size (decreasing fluorophore density), the brightest pixel measurements will indicate a lower signal intensity, which might lead to a deceptive estimate of the number of fluorophores. If the structure of interest is larger than the resolution limit in z , it may be required to combine intensity data from numerous z -planes. To completely depict the intensity of large structures, such as the MFB, it will be essential to employ the sum intensity of many z -planes. In the SIM images, the total intensity of three distinct proteins was used in this study. It is critical to compensate for background fluorescence in addition to utilizing integrated intensity measurements. This was accomplished by determining the background intensity value by measuring the total integrated intensity of the area of interest and a somewhat broader region. The intensity of the point of interest is then calculated by subtracting the background value.

5. Results and Discussion

5.3.6.3 Quantification of Bassoon intensity and density

The presynaptic protein Bassoon (encoded by the *Bsn* gene), which is involved in the orchestration of the active zone of neurotransmitter release, mediates a variety of functions, including proper synaptogenesis and structural development/maturation of the hippocampal *cornu ammonis* (CA)3 and dentate gyrus (DG) areas (Lanore et al. 2010; Annamneedi et al. 2018). Bassoon, in particular, interacts with other active zone components such as Piccolo, Rab3-interacting molecules (RIMs), RBPs, Munc13s, and ELKS/CAST proteins to regulate neurotransmitter release (Südhof 2012; Eckart D. Gundelfinger and Fejtova 2012; Eckart D. Gundelfinger, Reissner, and Garner 2016). Additionally, *Bsn*^{Δ_{Ex4/5}} mice exhibit significant electrophysiological changes, notably impaired synaptic fatigue during long-term depression (LTD) induction and long-term potentiation (LTP) at CA1 synapses (Altrock et al. 2003; Sgobio et al. 2010). Various observations suggest that the CAST complex, including Bassoon plays fundamental roles in setting the synaptic strength (see the introduction chapter). It is likely that Bassoon has a fundamental role in contribution to the synaptic plasticity in the central nervous system. This experiment questioned whether the induction of cLTP with forskolin could be modify Bassoon intensity and density in MFB.

The maximum intensity of the EGFP signal from each z-stacks of SIM image was analyzed in Imaris software using surface analysis. Sum Intensity for Bassoon was measured in EGFP positive boutons. Presynaptic terminals were identified as bouton-like swellings that colocalized with Bassoon. Presynaptic enrichment was calculated by dividing the background-subtracted intensity in presynaptic terminals by the background-subtracted intensity in the corresponding axons. All images were analyzed blinded to the condition (ACSF-sham, DMSO-control, forskolin-treatment). Sixty images were acquired in brain sections from six mice using a standardized protocol (for details see table 8-13). In two out of three animals, we found highly significant decrease ($p < 0.001$) in Bassoon intensity.

5. Results and Discussion

Table 8. The number of MFBs per image. Animal 1-FSK experiment, right hMFT, five 25 μ m cryo section; 2 image per section: 10 SIM images

| <i>Cryosection number</i> | <i>Proteins and experiment group</i> | <i>Number of MFBs</i> |
|---------------------------|--------------------------------------|-----------------------|
| 1 | FSK; Bsn and Munc | 5 |
| | | 8 |
| 2 | DMSO; Bsn and Tomosyn | 8 |
| | | 14 |
| 3 | DMSO; Bsn and Munc 13-1 | 13 |
| | | 21 |
| 4 | FSK; Bsn and Tomosyn | 13 |
| | | 15 |
| 5 | DMSO; Bsn and Munc 13-1 | 12 |
| | | 6 |

Table 9. The number of MFBs per image. Animal 2-FSK experiment, right hMFT; six 25 μ m cryo sections; 1-2 images per section: 11 SIM images

| <i>Cryosection number</i> | <i>Proteins and experiment group</i> | <i>Number of MFBs</i> |
|---------------------------|--------------------------------------|-----------------------|
| 1 | DMSO; Bsn and Munc 13-1 | 22 |
| | | 34 |
| 2 | FSK; Bsn and Tomosyn | 19 |
| | | 24 |
| 3 | FSK; Bsn and Munc 13-1 | 4 |
| | | 9 |
| 4 | DMSO; Bsn and Munc 13-1 | 14 |
| | | 20 |
| 5 | DMSO; Bsn and Tomosyn | 23 |
| | | 16 |
| 6 | DMSO; Bsn and Tomosy | 20 |

5. Results and Discussion

Table 10. The number of MFBs per image. Animal 3-FSK experiment, right hMFT, six 25 μ m cryo section; 1-2 image per section: 7 SIM images

| Cryosection number | Proteins and experiment group | Number of MFBs |
|---------------------------|--------------------------------------|-----------------------|
| 1 | FSK; Bsn and Munc 13-1 | 16 27 |
| 2 | FSK; Bsn and Tomosyn | 8 |
| 3 | DMSO; Bsn and Tomosyn | 2 |
| 4 | FSK; Bsn and Munc 13-1 | 16 |
| 5 | DMSO; Bsn and Munc 13-1 | 1 |
| 6 | FSK; Bsn and Tomosyn | 18 |

Table 11. The number of MFBs per image. Animal 4, right hMFT, five 25 μ m cryo sections; 1-2 images per section: 6 SIM images

| Cryosection number | Proteins and experiment group | Number of MFBs |
|---------------------------|--------------------------------------|-----------------------|
| 1 | DMSO; Bsn and Munc 13-1 | 0 1 |
| 2 | FSK; Bsn and Tomosyn | 4 |
| 3 | DMSO; Bsn and Tomosyn | 5 |
| 4 | FSK; Bsn and Munc | 12 |
| 5 | FSK; Bsn and Munc 13-1 | 27 |

5. Results and Discussion

Table 12. The number of MFBs per image. Animal 5, right hMFT, six 25 μ m cryo section; 1-2 image per section: 8 SIM images

| <i>Cryosection number</i> | <i>Proteins and experiment group</i> | <i>Number of MFBs</i> |
|----------------------------------|---|------------------------------|
| 1 | FSK; Bsn and Munc 13-1 | 10 |
| 2 | FSK; Bsn and Munc 13-1 | 3 |
| 3 | FSK; Bsn and Tomosyn | 5 |
| | | 12 |
| 4 | DMSO; Bsn and Munc 13-1 | 5 |
| | | 13 |
| 5 | DMSO; Bsn and Tomosyn | 5 |
| 6 | DMSO; Bsn and Tomosyn | 3 |

Table 13. The number of MFBs per image. Animal 6, right hMFT; six 25 μ m cryo sections; 1-2 images per section: 8 SIM images

| <i>Cryosection number</i> | <i>Proteins and experiment group</i> | <i>Number of MFBs</i> |
|----------------------------------|---|------------------------------|
| 1 | DMSO; Bsn and Munc 13-1 | 3 |
| 2 | DMSO; Bsn and Munc 13-1 | 5 |
| 3 | DMSO; Bsn and Tomosyn | 12 |
| | | 7 |
| 4 | FSK; Bsn and Munc 13-1 | 7 |
| | | 7 |
| 5 | FSK; Bsn and Tomosyn | 10 |
| 6 | FSK; Bsn and Tomosyn | 11 |

5. Results and Discussion

Table 14. Intensity of Bassoon in EGFP positive structures before and after Forskolin treatment in unfiltered images.

| <u>Animal 1 and 2 Bsn intensity</u> | DMSO-control | FSK-treatment |
|--|---------------------|----------------------|
| Number of EGFP positive structures | 739 | 828 |
| 25% Percentile | 5110730 | 1708965 |
| Median | 16121300 | 6193625 |
| 75% Percentile | 53601800 | 20880975 |
| Sum | 67378742644 | 49206311393 |
| Mean ranks | | |
| Kruskal-Wallis test | 227.4 | 155.6 |
| | | |
| <u>Animal 3 and 4 Bsn intensity</u> | DMSO-control | FSK-treatment |
| Number of EGFP positive structures | 151 | 808 |
| 25% Percentile | 443255 | 1928115 |
| Median | 852963 | 5207385 |
| 75% Percentile | 2186970 | 16979750 |
| Sum | 1379717229 | 28727354795 |
| Mean ranks | | |
| Kruskal-Wallis test | 74,67 | 204,9 |
| | | |
| <u>Animal 5 and 6 Bsn intensity</u> | DMSO-control | FSK-treatment |
| Number of EGFP positive structures | 125 | 497 |
| 25% Percentile | 13026650 | 741124 |
| Median | 29444900 | 3018230 |
| 75% Percentile | 132390500 | 13744350 |
| Sum | 19104206165 | 29784379192 |
| Mean ranks | | |
| Kruskal-Wallis test | 164,8 | 77,20 |

5. Results and Discussion

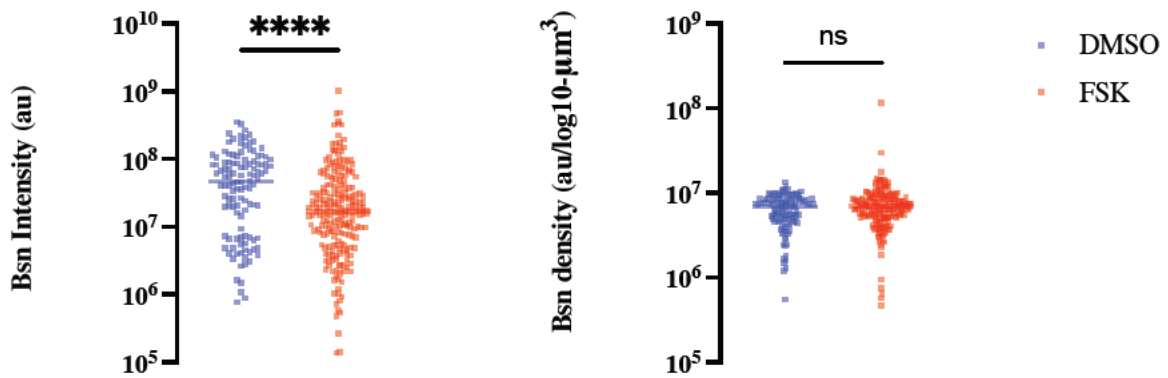


Figure 33. Intensity and density of Bassoon in EGFP positive structures before and after forskolin treatment in unfiltered images.

SIM images of 25 μm cryosections of hippocampus; control group treated with DMSO (blue); experimental group treated with forskolin (FSK) solution in DMSO (red). A significant decrease in Bassoon intensity was seen ($p < 0.001$) in Bassoon (Bsn)-cluster intensity in FSK-treated vs. DMSO treated brain slices (median; DMSO: 13709700 au, FSK: 5131240 au). $n=6$

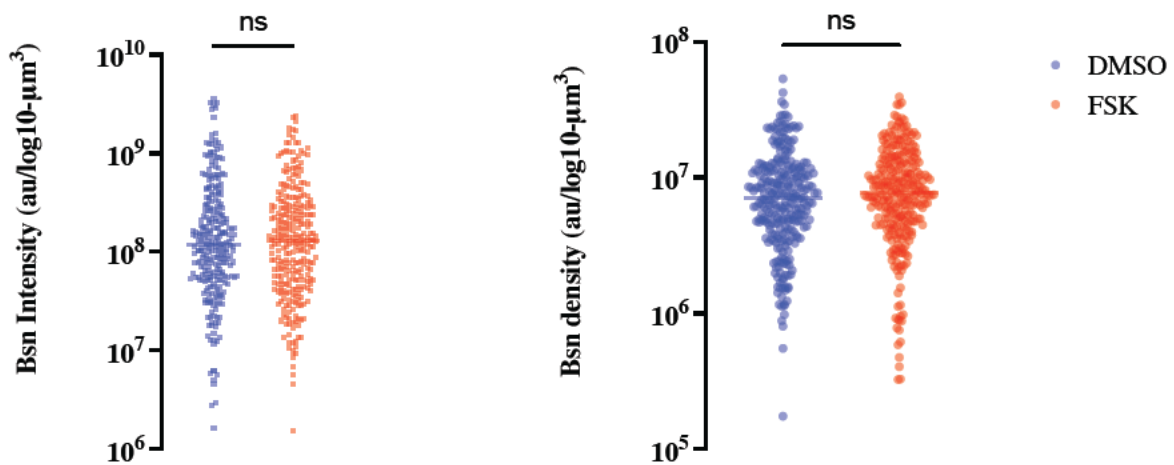


Figure 32. Intensity and density of Bassoon in MFBS before after forskolin treatment in filtered images, (MFBS > 5 μ^3).

Bsn Intensity and density measurements of 290 MFBS in forskolin condition (FSK: red) and 285 MFBS in control condition (DMSO: blue). The EGFP positive structures smaller than 5 μm are excluded in these figures. $n=6$

In unfiltered images Bassoon intensity significantly decreases after Forskolin treatment (Figure 32, Table 14) in spite of the rather high variability of the Bassoon fluorescence in brain sections from individual mice (Table 14).

5. Results and Discussion

However, no significant change was seen in Bassoon density in EGFP positive structures (Figure 32, Table 23). When EGFP positive structures smaller than five μm^3 were excluded, no differences between the treatments could be detected (Figure 33., Table 15 and 16)

Table 15. Intensity of Bassoon in MFBs before after Forskolin treatment in filtered images, (MFBs > 5 μm^3).

| <u>Filtered data Bsn-Intensity</u> | <i>DMSO-control</i> | <i>FSK-Treatment</i> |
|------------------------------------|---------------------|----------------------|
| <i>Number of MFBs</i> | 285 | 290 |
| <i>Minimum</i> | 1552160 | 1657770 |
| <i>25% Percentile</i> | 50497050 | 55321400 |
| <i>Median</i> | 130401000 | 119959000 |
| <i>75% Percentile</i> | 295591504 | 291193752 |
| <i>Maximum</i> | 2395579904 | 3604549888 |
| <i>Mean</i> | 271656237 | 304584981 |
| <i>Std. Deviation</i> | 388293907 | 530172903 |
| <i>Std. Error of Mean</i> | 23000546 | 31132825 |
| <i>Mean ranks</i> | | |
| <i>Mann-Whitney test</i> | 288,1 | 287,9 |

Table 16. Density of Bassoon in MFBs before after Forskolin treatment in filtered images, (MFBs > 5 μm^3).

| <u>Filtered data Bsn-Density</u> | <i>DMSO-control</i> | <i>FSK-Treatment</i> |
|----------------------------------|---------------------|----------------------|
| <i>Number of MFBs</i> | 285 | 290 |
| <i>Minimum</i> | 175504 | 325958 |
| <i>25% Percentile</i> | 4187757 | 4755157 |
| <i>Median</i> | 7067318 | 7707423 |
| <i>75% Percentile</i> | 11391848 | 12704877 |
| <i>Maximum</i> | 53316610 | 39153980 |
| <i>Mean</i> | 9015911 | 9529204 |
| <i>Std. Deviation</i> | 7376484 | 6839125 |
| <i>Std. Error of Mean</i> | 436945 | 401607 |
| <i>Mean ranks</i> | | |
| <i>Mann-Whitney test</i> | 277,2 | 298,6 |

5. Results and Discussion

These data would imply that the forskolin-induced decrease in Bassoon intensity was seen primarily in small *en-passant* or filopodial synaptic contacts rather than in large MFBs. Even if forskolin is known to induce LTP in inhibitory MF to interneuron synapses (Alle, Jonas, and Geiger 2001); This is surprising since forskolin is known to induce cLTP in large MFB to CA3 pyramidal cell synaptic contacts (Yan You Huang, Li, and Kandel 1994; Maccaferri, Tóth, and McBain 1998). In agreement with the present data, a recent investigation (Maus et al. 2020), using stimulated emission depletion (STED) microscopy and ultrastructural analyses, did not report massive changes in AZ number or size after forskolin treatment. Interestingly, a recent study employing TIRF microscopy demonstrated rapid (few milliseconds) and extremely localized changes in Ca^{2+} within MFBs after forskolin treatment (Fukaya et al. 2021). Our data could not show clear evidence for MFB-volume changes after the forskolin treatment (the volume of EGFP-positive structures in forskolin and DMSO treated brain slices in filtered images: median \pm range; DMSO: $13.57 \mu m^3 \pm 157.8 \mu m^3$, forskolin $12.16 \mu m^3 \pm 106.0 \mu m^3$ and unfiltered images: median \pm range DMSO: $14.27 \mu m^3 \pm 157.8 \mu m^3$, forskolin: $13.14 \mu m^3 \pm 106.0 \mu m^3$. Moreover, Bassoon density associated with EGFP-positive structures did not change after forskolin treatment. Nevertheless, structural changes after forskolin may be very transitory (Fukaya et al. 2021) or only slight alterations in AZ morphology without a dramatic change in the size or number (Orlando et al. 2021). The heterogeneity of synaptic targets and their functional state cannot be ruled out as possible causes for the observed diversity of forskolin-induced alterations.

5.3.6.4 Quantification of Munc13-1 intensity and density

Munc13-1, -2, -3, and -4 are the four Munc13 family members described for the CNS (Brose et al. 1995; Koch, Hofmann, and Brose 2000). At hippocampal synapses, two different isoforms of Munc13 (Munc13-1 and bMunc13-2) mediate opposing types of short-term presynaptic plasticity (STP) and so influence neural network properties differently (Rosenmund, Rettig, and Brose 2003; Rosenmund et al. 2002). The presynaptic protein Munc13-1 was discovered to form the core of distinct quantal SV release sites using a stochastic optical reconstruction microscopy method, with around six such self-assemblies per AZ. The number of Munc13-1 nanoassemblies corresponded to the estimated number of release-ready SVs (Sakamoto et al. 2018).

For the image interpretation, the same method that was employed for Bassoon quantification was used. Each z-stack of the SIM picture was analyzed using the Imaris program to determine the maximum intensity of the EGFP signal. Munc 13-1 Sum Intensity was quantified in EGFP positive boutons. Bouton-like swellings that colocalized with Bassoon and Munc 13-1 were determined to represent a presynaptic terminal. Presynaptic enrichment was estimated by dividing the intensity in presynaptic terminals by the intensity in the

5. Results and Discussion

corresponding axons after subtracting the background intensity. All of the images were evaluated with no awareness of the condition. The images were obtained in six separate mice, and we had a minimum of three images per condition.

In unfiltered images the sum Munc 13-1 intensity and density significantly decreased in forskolin treated as compared to DMSO treated brain slices (Figure 34). The response to forskolin was, however, variable in brain slices from individual mice (Table 17 and 24). After filtering the MFBs size and excluding the smaller EGFP positive structures (smaller than $5 \mu\text{m}^3$) no clear evidence of intensity or density alteration were visible (Figure 35, Table 18 and 19). A recent study utilizing gSTED microscopy revealed no evidence of a change upon forskolin application in the spatial distance between Ca^{2+} channel clusters and the putative release site marker Munc13-1 (Sakamoto et al. 2018; Rebola et al. 2019), as determined by peak-to-peak analysis (Fukaya et al. 2021). Additionally, no changes in the size or quantity of Munc13-1 clusters around Ca^{2+} channels were observed within the settings (Fukaya et al. 2021).

5. Results and Discussion

Table 17. Intensity of Munc13-1 in EGFP positive structures before and after Forskolin treatment in unfiltered images.

Animal 1 and 2 Munc 13-1

intensity

| | DMSO-control | FSK-treatment |
|------------------------------------|--------------|---------------|
| Number of EGFP positive structures | 477 | 355 |
| 25% Percentile | 7484075 | 1566880 |
| Median | 20914300 | 3644170 |
| 75% Percentile | 68749000 | 9974450 |
| Sum | 50048531464 | 11930186263 |
| Mean ranks | | |
| Kruskal-Wallis test | 236,9 | 113,0 |

Animal 3 and 4 Munc 13-1

intensity

| | DMSO-control | FSK-treatment |
|------------------------------------|--------------|---------------|
| Number of EGFP positive structures | 132 | 547 |
| 25% Percentile | 517034 | 2778060 |
| Median | 1837585 | 7369160 |
| 75% Percentile | 4891325 | 25207800 |
| Sum | 1480376968 | 26279848951 |
| Mean ranks | | |
| Kruskal-Wallis test | 95,80 | 209,1 |

Animal 5 and 6 Munc 13-1

intensity

| | DMSO-control | FSK-treatment |
|------------------------------------|--------------|---------------|
| Number of EGFP positive structures | 58 | 247 |
| 25% Percentile | 11447700 | 652235 |
| Median | 62839650 | 3085430 |
| 75% Percentile | 175378244 | 10966600 |
| Sum | 6864767117 | 16172875134 |
| Mean ranks | | |
| Kruskal-Wallis test | 164,3 | 79,44 |

5. Results and Discussion

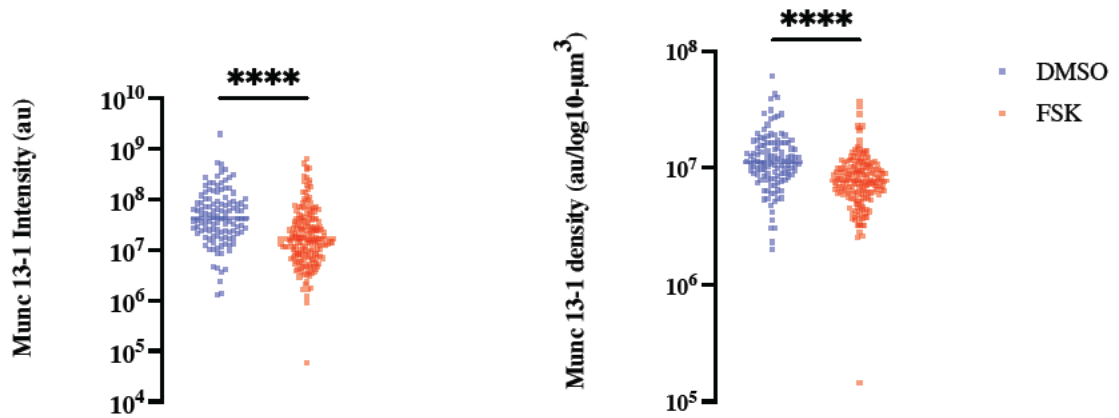


Figure 34. Intensity and density of Munc13-1 in EGFP positive structures before and after forskolin treatment in unfiltered images.

SIM images of 25 μm cryosections of hippocampus; control group treated with DMSO (blue); experimental group treated with forskolin (FSK) in DMSO (red).

A significant decrease in Munc 13-1 intensity was seen in pooled data and four animals ($p < 0.001$) in Munc 13-1 intensity (median; animal 1 and 2, DMSO: 20914300 au, FSK: 3644170 au; animal 5 and 6, DMSO: 62839650 au, FSK: 3085430 au). $n=6$

5. Results and Discussion

Table 18. Intensity of Munc 13-1 in MFBs before and after Forskolin treatment in filtered images, (MFBs > 5 μ 3).

| <u>Filtered data Munc 13-1</u> <u>Intensity</u> | <i>DMSO-control</i> | <i>FSK-Treatment</i> |
|--|---------------------|----------------------|
| <i>Number of MFBs</i> | 170 | 151 |
| <i>Minimum</i> | 2585420 | 10504900 |
| <i>25% Percentile</i> | 57126950 | 61115900 |
| <i>Median</i> | 143277496 | 113220000 |
| <i>75% Percentile</i> | 332596256 | 284183008 |
| <i>Maximum</i> | 3044189952 | 3041619968 |
| <i>Mean</i> | 286999305 | 299278079 |
| <i>Std. Deviation</i> | 430698385 | 480484530 |
| <i>Std. Error of Mean</i> | 33033058 | 39101277 |
| <i>Mean ranks</i> | | |
| <i>Mann-Whitney test</i> | 162.2 | 159.6 |

Table 19. Density of Munc 13-1 in MFBs before and after Forskolin treatment in filtered images, (MFBs > 5 μ 3).

| <u>Filtered data Munc 13-1</u> <u>density</u> | <i>DMSO-control</i> | <i>FSK-Treatment</i> |
|--|---------------------|----------------------|
| <i>Number of MFBs</i> | 170 | 151 |
| <i>Minimum</i> | 171686 | 1425562 |
| <i>25% Percentile</i> | 3851557 | 4369019 |
| <i>Median</i> | 7874046 | 7405227 |
| <i>75% Percentile</i> | 13920969 | 12189179 |
| <i>Maximum</i> | 48093597 | 38414021 |
| <i>Mean</i> | 10133701 | 9227323 |
| <i>Std. Deviation</i> | 8468298 | 6654413 |
| <i>Std. Error of Mean</i> | 649489 | 541528 |
| <i>Mean ranks</i> | | |
| <i>Mann-Whitney test</i> | 162.3 | 159.5 |

5. Results and Discussion

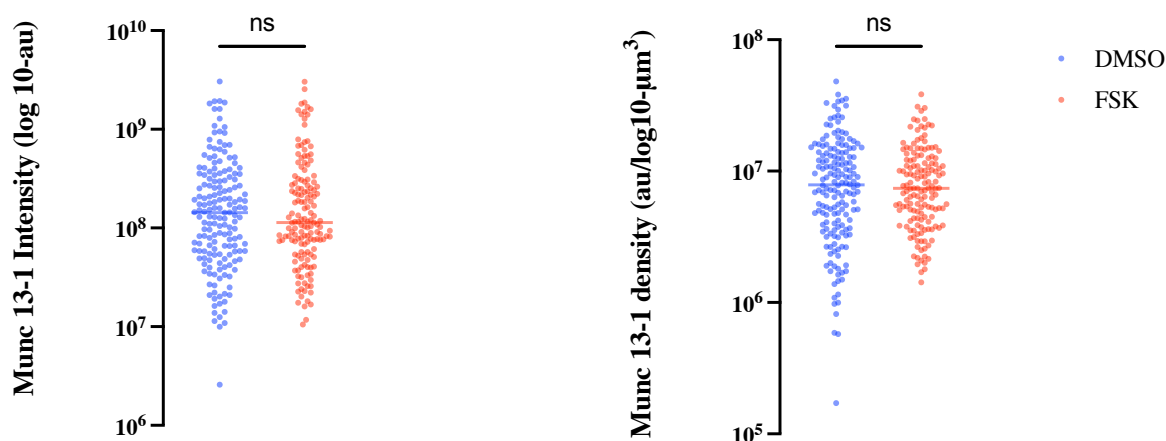


Figure 35. Intensity and density of Munc 13-1 in MFBs before and after forskolin treatment in filtered images, (MFBs $> 5\mu\text{m}$).

Munc 13-1 Intensity and density measurements of 151 MFBs in forskolin treatment (FSK: red) and 170 MFBs in control condition (DMSO: blue). The EGFP positive structures smaller than $5\mu\text{m}$ are excluded in these figures. $n=6$

Synaptic contact structure-function characteristics will alter as a result of synaptic plasticity, as was previously stated. When a large number of synaptic contacts of a particular kind are randomly selected, some may be in a baseline state, while others may be in an activity-modified state. If both findings can be unambiguously assigned to the same synapse type, the range of variability within that synapse type and the range of heterogeneity across synapse types will be enhanced. Ideally, the variability and heterogeneity of the basal state and the plasticity effects should be determined without the "contaminating" impact of non-wished plasticity mechanisms. Is there, on the other hand, such a phenomenon as a basic state of a synapse? One could consider a newly generated synapse that has been provided with all necessary components and is ready and capable of transmitting the information. The synapse may then receive stochastic patterns of action potentials, leading to possible occasional neurotransmitter release. This can be referred to as the basal state of the synapse in this context, and it could be hypothesized that a significant proportion of synapses exists in this state. The synapses can undergo many forms of plasticity in response to changes in the levels and patterns of activity (Wichmann and Kuner 2022). In a given synapse type, the variability of the baseline state seen may mainly be due to a stochastic process, while plasticity-induced alterations are driven by unique patterns of activity and follow a set of principles. The heterogeneity of various synapse types in their baseline state may be driven by the diverse physiological requirements that each synapse must meet, and plasticity-induced alterations are "added" to this heterogeneity by a synapse type-dependent reaction in response to distinct patterns of activity.

5. Results and Discussion

5.3.6.5 Quantification of Tomosyn intensity and density

Tomosyn is a protein that reduces synaptic transmission and vesicle release probability and is required for neuronal synaptic transmission modulation (Ashery 2009). Therefore, the effect of forskolin on Tomosyn intensity and density was investigated. The data are mainly based on measurements from brain sections of four animals. Due to technical problems in the third and fourth animal, just one or two images per condition were evaluated (Table 20 and 25). Tomosyn intensity significantly decreased and Tomosyn density significantly increased in all EGFP-positive structures in forskolin treated as compared to DMSO treated brain slices (Figure 36, Table 20 and 25). In filtered images both Tomosyn intensity and density were decreased after forskolin treatment as compared to DMSO (Figure 37, Table 21 and 22).

Table 20. Intensity of Tomosyn in EGFP positive structures before and after forskolin treatment in unfiltered images.

| <u>Animal 1 and 2 Tomosyn intensity</u> | DMSO-control | FSK-treatment |
|--|---------------------|----------------------|
| Number of EGFP positive structures | 262 | 473 |
| 25% Percentile | 4642505 | 3254765 |
| Median | 29011600 | 10262300 |
| 75% Percentile | 126172250 | 33260200 |
| Sum | 56656925632 | 46348619460 |
| Mean ranks | | |
| Kruskal-Wallis test | 207,0 | 152,2 |

| <u>Animal 3 and 4 Tomosyn intensity</u> | DMSO-control | FSK-treatment |
|--|---------------------|----------------------|
| Number of EGFP positive structures | 19 | 261 |
| 25% Percentile | 894445 | 1590325 |
| Median | 4105130 | 5895980 |
| 75% Percentile | 50958100 | 18682700 |
| Sum | 634248696 | 10645800870 |
| Mean ranks | | |
| Kruskal-Wallis test | 68,83 | 61,77 |

| <u>Animal 5 and 6 Tomosyn intensity</u> | DMSO-control | FSK-treatment |
|--|---------------------|----------------------|
| Number of EGFP positive structures | 67 | 250 |
| 25% Percentile | 12277300 | 710721 |
| Median | 32004700 | 2936790 |
| 75% Percentile | 110435000 | 11249325 |
| Sum | 13495091630 | 12601779147 |
| Mean ranks | | |
| Kruskal-Wallis test | 115,3 | 64,14 |

5. Results and Discussion

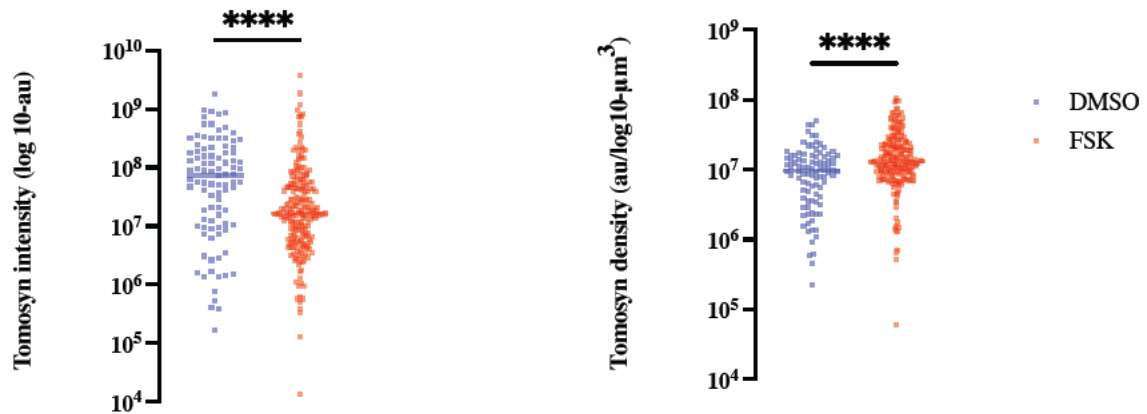


Figure 36. Intensity and density of Tomosyn in EGFP positive structures before and after forskolin treatment in unfiltered images.

SIM images of 25 μm cryosections of hippocampus; control group treated with DMSO (blue); experimental group treated with forskolin (FSK) solution in DMSO (red). A significant decrease in Tomosyn intensity was seen in four animals ($p < 0.001$) in Tomosyn intensity (median; animal 1 and 2 DMSO: 29011600 au, FSK: 10262300 au; animal 5 and 6 DMSO: 32004700 au, FSK: 2936790 au).

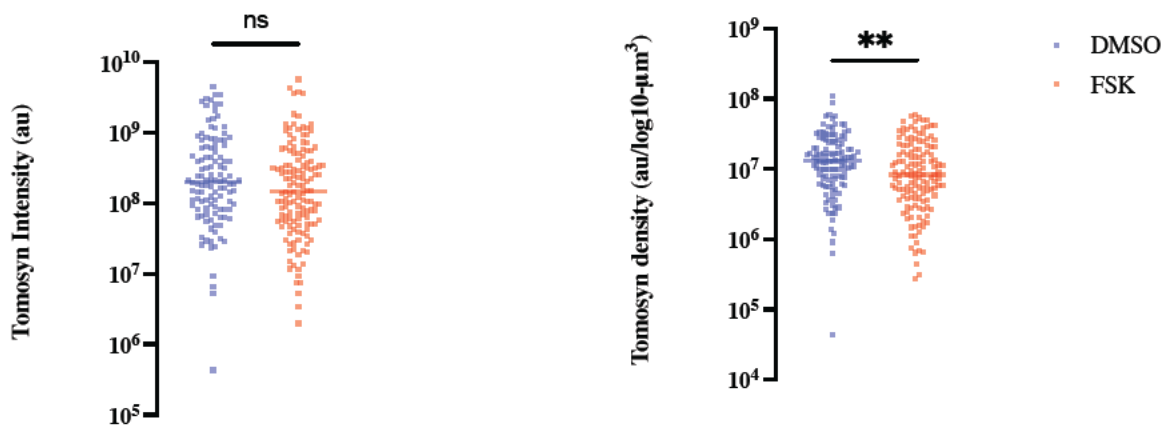


Figure 37. Intensity and density of Tomosyn in MFBs before and after forskolin treatment in filtered images, (MFBs $> 5\mu\text{m}^3$).

Munc 13-1 Intensity and density measurements of 151 MFBs in forskolin treatment (FSK: red) and 139 MFBs in control condition (DMSO: blue). The EGFP positive structures smaller than $5\mu\text{m}^3$ are excluded in these figures. $n=6$

5. Results and Discussion

Table 21. Intensity of Tomosyn in MFBs before and after Forskolin treatment in filtered images, (MFBs > 5 μ 3).

| <i>Filtered data Tomosyn Intensity</i> | <i>DMSO-control</i> | <i>FSK-Treatment</i> |
|---|----------------------------|-----------------------------|
| <i>Number of MFBs</i> | 115 | 139 |
| <i>Minimum</i> | 430214 | 1981250 |
| <i>25% Percentile</i> | 83025400 | 54680300 |
| <i>Median</i> | 203174000 | 146448992 |
| <i>75% Percentile</i> | 647076992 | 415964000 |
| <i>Maximum</i> | 4548530176 | 5736909824 |
| <i>Mean</i> | 557086024 | 441462010 |
| <i>Std. Deviation</i> | 857946269 | 835696195 |
| <i>Std. Error of Mean</i> | 80003902 | 70882826 |
| <i>Mean ranks</i> | | |
| <i>Mann-Whitney test</i> | 136,9 | 119,7 |

Table 22. Density of Tomosyn in MFBs before and after Forskolin treatment in filtered images, (MFBs > 5 μ 3).

| <i>Filtered data Tomosyn density</i> | <i>DMSO-control</i> | <i>FSK-Treatment</i> |
|---|----------------------------|-----------------------------|
| <i>Number of values</i> | 115 | 139 |
| <i>Minimum</i> | 43450 | 276947 |
| <i>25% Percentile</i> | 6956515 | 3729608 |
| <i>Median</i> | 12891990 | 8251475 |
| <i>75% Percentile</i> | 24260374 | 20543187 |
| <i>Maximum</i> | 111617257 | 59607826 |
| <i>Mean</i> | 17858125 | 13794990 |
| <i>Std. Deviation</i> | 17129933 | 13878234 |
| <i>Std. Error of Mean</i> | 1597374 | 1177136 |
| <i>Mean ranks</i> | | |
| <i>Mann-Whitney test</i> | 141,2 | 116,1 |

These data demonstrate that forskolin reduced the intensity of Bassoon, Munc 13-1 and Tomosyn largely in small synaptic contacts whereas no clear changes were detected in large mossy fiber boutons (MFBs). However, due to the high variability it cannot be ruled out that forskolin may differentially modify AZ protein composition depending on experimental circumstances such as age and gender of mice or the time point and duration of forskolin stimulation.

5. Results and Discussion

5.4 dSTORM data

5.4.1 Application of dSTORM to the brain slices

As SIM achieves only a resolution in 100-300 nm range (Heintzmann and Cremer 1999; M G L Gustafsson 2000), forskolin-induced changes in Bassoon expression were further examined with dSTORM. Important components of the visualization method are depicted in Figure 38. Notably, it defines the core steps for imaging active zones of complete giant presynaptic components with nanometer resolution in anatomically defined parts of the hippocampus with nanometer precision. This approach crucially relies on precise cutting, optimum and homogenous labeling, thick tissue blocks, and 3D scanning to limit the truncation of synapses.

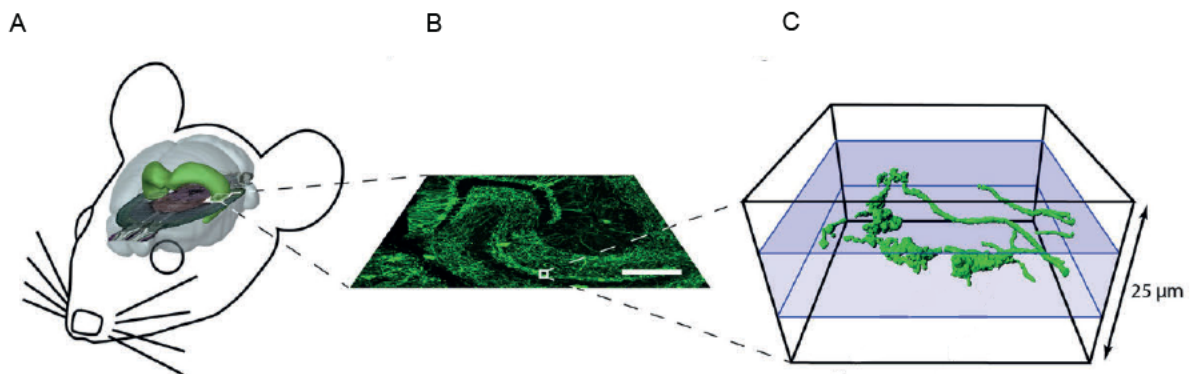


Figure 38. A schematic illustration of the method for visualizing the synaptic connections of hippocampus mossy fibers.

A) A virtualized mouse brain with the hippocampus formation's proportions highlighted in green and a horizontal cut from Allen's Mouse Brain Atlas (image credit: Allen Institute for Brain Science, available from: <http://mouse.brain-map.org/static/brainexplorer>). B) A confocal view of mossy fibers in a 25 μm thick hippocampus slice from a Thy1mEGFP (Lsi1) mouse. The white box indicates the area of interest (25 μm x 25 μm x 25 μm), which is enlarged in the next panel. scale bar 200 μm C) Three-dimensional (3D) volume reconstruction of mEGFP in xyz-view, demonstrating mossy fiber boutons (green), a typical bouton with filopodial extensions, and axons (Pauli et al. 2021).

It is preferred to utilize Alexa Fluor 647 since Ehmann et al. demonstrated that quantitative measurements with dSTORM are most reliably accomplished using this red-emitting carbocyanine dye or its homolog Cy5 (Ehmann et al. 2014). Utilizing Software rapidSTORM, the image is reassembled and the results are returned as a set of localization coordinates. Additional assessment is required for the 3D method (Franke, Sauer, and van de Linde 2017).

5. Results and Discussion

5.4.2 Surface analysis; Reconstruction of MF and AZ protein Bsn in *d*STORM images

MF boutons, filopodia, and axons are illustrated in a 3D *d*STORM reconstruction of the anti-GFP fluorescence (Fig. 39). For subsequent experiments, brain slices were placed on fluorescent bead-coated coverslips, allowing for the alignment of consecutive imaging and drift adjustment. We initially identified Bassoon with a monoclonal mouse anti-Bassoon antibody and secondary Alexa647-conjugated anti-mouse antibody. Following washing, the tissue was stained with anti-GFP nanobodies conjugated with Alexa647. Rapid axial scanning (ten times) over the ten μm area of interest in the center of the 25 μm brain slice revealed homogenous distributions of localization intensity and counts. Drift was minimized by initiating measurements remotely from outside the laboratory upon sample stabilization and through imaging beads at the start and end of each imaging acquisition, whereas the overall measurement time per experiment was approximately three hours.

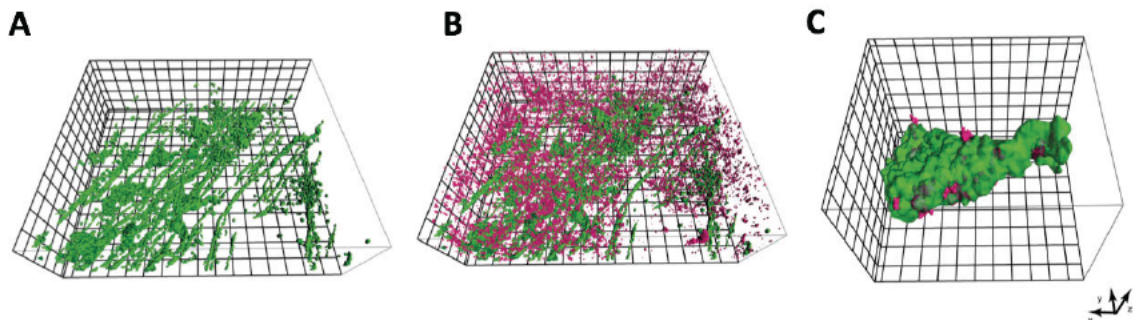


Figure 39. Sequential en bloc 3D imaging in 25 μm thick tissue slices of mEGFP (*Ls1*) mice showed Bassoon clusters in identified mossy fiber boutons.

A) 3D volume reconstruction of mEGFP in x y z-view, demonstrating axons and mossy fiber boutons (green) B) 3D reconstruction of Bassoon (magenta) and mEGFP (green) in large mossy fiber boutons C) Magnification of the two-channel dSTORM image of an individual MFB (green) and Bassoon clusters in B.

Sequential scanning enabled to assign Bassoon clusters to defined synaptic targets of individual MFBs and to quantify the size and density of Bassoon within individual MFBs at nanoscopic resolution.

5. Results and Discussion

5.4.3 Forskolin effect in hippocampal MFBs using *d*STORM

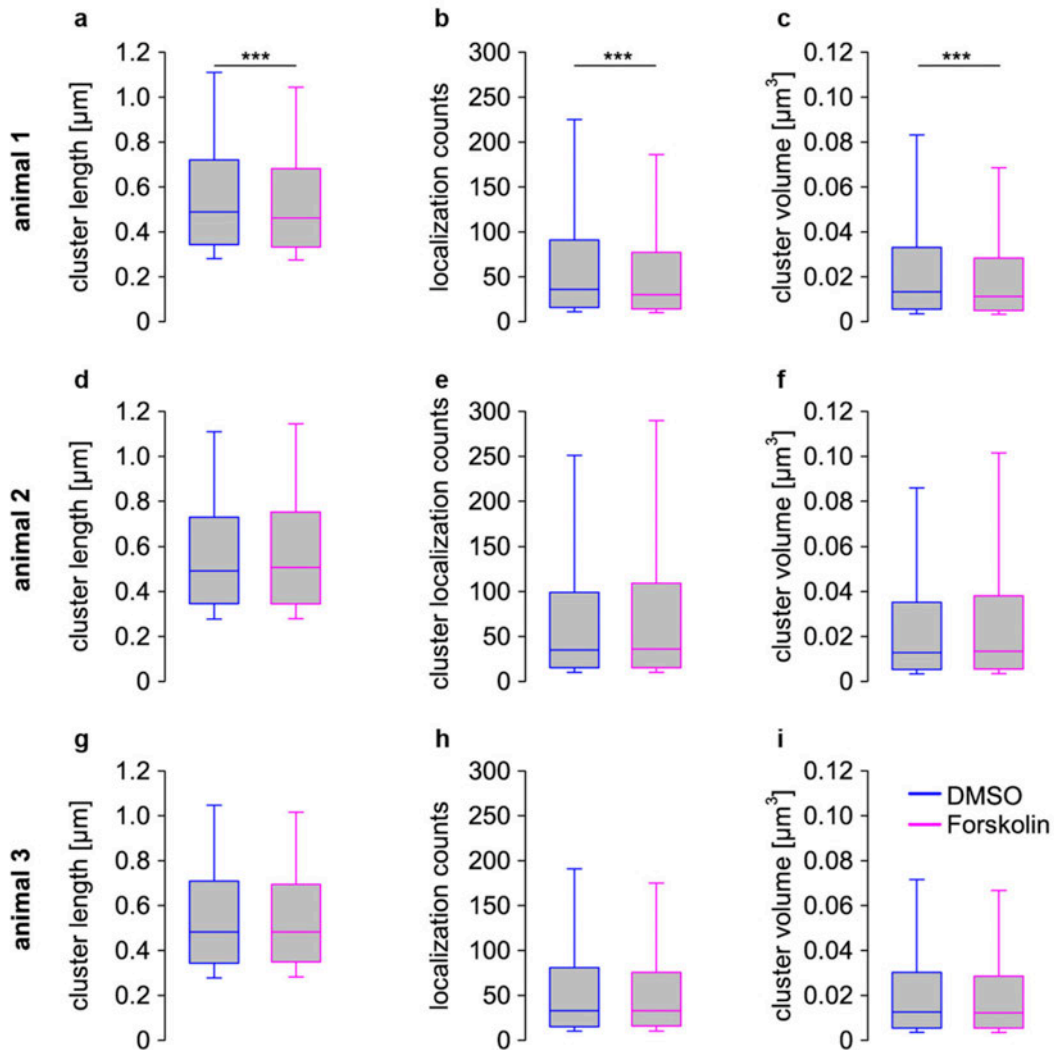


Figure 40. forskolin effect in *d*STORM images of MFB in three

*d*STORM scanning of 25 μm cryosections obtained from 300-micron acute brain slices of hippocampus mouse brain; control group treated with DMSO (blue); experimental group treated with forskolin solution in DMSO (magenta).

A highly substantial alteration was seen in one of the three animals ($p < 0.001$) in **a** Bassoon-cluster length (median ± 25th–75th percentile; DMSO: 0.490 ± 0.344 – 0.721 μm; forskolin: 0.462 ± 0.333 – 0.681 μm) **b** localization counts (DMSO: 36 ± 16 – 91 ; forskolin: 30 ± 14 – 77) and **c** volume (DMSO: 0.0132 ± 0.0056 – 0.0331 μm³; forskolin: 0.0112 ± 0.0050 – 0.0283 μm³); Animal 2: **d** length (DMSO: 0.482 ± 0.343 – 0.709 μm; forskolin: 0.482 ± 0.349 – 0.694 μm), **e** counts (DMSO: 33 ± 15 – 81 ; forskolin: 33 ± 16 – 75.5), **f** volume (DMSO: 0.0125 ± 0.00544 – 0.0302 μm³; forskolin: 0.0123 ± 0.00548 – 0.0285 μm³); Animal 3: **g** length (DMSO: 0.493 ± 0.345 – 0.729 μm; forskolin: 0.507 ± 0.345 – 0.752 μm), **h** counts (DMSO: 35 ± 15 – 99 ; forskolin: 36 ± 15 – 109), **i** volume (DMSO: 0.0127 ± 0.00526 – 0.0352 μm³; forskolin: 0.0134 ± 0.00541 – 0.0381 μm³).

5. Results and Discussion

Figure 40 is the observation from (Pauli et al. 2021), which were carried out together with my colleagues Dr. Martin Pauli and Prof. Dr. med. Anna-Leena Sirén.

Similar to the results obtained with SIM the high individual variability between animals in response to forskolin was also seen when Bassoon clusters were analyzed by in *d*STORM (Figure 40). Recent research utilizing stimulated emission depletion (STED) microscopy and ultrastructural analysis found that forskolin treatment did not lead to significant changes in AZ number or size (Maus et al. 2020). Furthermore, no alterations in the MF bouton area or the postsynaptic spine area were observed in this study. These data demonstrate that although the protocol does not result in significant structural changes as a result of increased network activity, it does enable us to identify subtle ultrastructural changes in the distribution of vesicles at AZs. Nevertheless, it cannot be ruled out that forskolin treatment may produce structural alterations in AZs under different experimental settings or at subsequent time periods. Both forskolin and DCG-IV did not affect docked or membrane-proximal SV and GV pools, while forskolin-treated MF synapses had more docked DCVs than control and DCG-IV-treated slices (Maus et al. 2020). Alternative interpretations include that the subtlety of the observed morphological alterations strengthens the idea that cAMP-mediated PKA activation impacts proteins of the SV fusion machinery at a post-docking/priming phase in order to enhance SV fusion, for example, by phosphorylation of complexins (Cho et al. 2015).

A recent report shed light on the structural and functional changes that occur during chemical pre-synaptic potentiation at hMFBS (Orlando et al. 2021). Taken together, the findings demonstrate that increasing the number of available release sites—rather than just the probability of release—is required for forskolin-induced MF presynaptic potentiation (Orlando et al. 2021). Presynaptic plasticity may entail structural changes (Ghelani and Sigrist 2018), as shown by the sustained increase in mossy fiber complexity observed in mice kept in enriched surroundings (Orlando et al. 2021; Nicholas P. Vyleta and Peter Jonas 2014).

The recruitment of novel release sites has been shown to contribute to chemically induced presynaptic potentiation (Orlando et al. 2021). Electrophysiological recordings of autaptic neurons (Tong, Malenka, and Nicoll 1996) and calcium imaging in cultured hippocampal slices (Emptage et al. 2003) have previously revealed this presynaptic unsilencing. According to recent EM and glutamate imaging analyses, an increase in AZ and release site number results in an increase in neurotransmission. The EM analysis of potentiated hMFBS demonstrated a rise in synaptic complexity, AZ density, and the RRP's morphological correlate (Orlando et al. 2021). Additionally, live 2-photon imaging of the glutamate sensor iGluu indicated an expansion of the presynaptic releasing area (Orlando et al. 2021). Nevertheless, under this experimental settings, structural alterations occurred after 15 minutes of Forskolin incubation. This suggests that structural rearrangements occur rapidly and, if sustained, may cement long-term synaptic strength alterations.

5. Results and Discussion

Our protocol, on the other hand, requires 30 minutes of incubation and 30 minutes of resting at room temperature. At *Drosophila* neuromuscular junctions, structural synaptic remodeling followed a similar time course: There, rapid AZ remodeling, which may include the insertion of AZ molecular scaffolds and the addition of new release sites, has been demonstrated to solidify presynaptic potentiation and to maintain long-term alterations in synaptic strength (Weyhersmüller et al. 2011; Böhme et al. 2019).

The increase in neurotransmitter release at potentiated hMFBs is also thought to be mediated by a reduction in the coupling distance between presynaptic calcium channels and release sites (Midorikawa and Sakaba 2017). This hypothesis was recently tested by using gSTED microscopy to determine the distance between the Cav2.1 and Munc13-1 signals (Orlando et al. 2021). They validated a somewhat loose coupling distance of around 65 nm between calcium source and release sites in mossy fibers, as earlier determined by electrophysiological recordings (Nicholas P. Vyleta and Peter Jonas 2014) and gSTED imaging (Brockmann et al. 2019). These values were equivalent in both control and potentiated synapses, suggesting that presynaptic potentiation is not mediated by a reduction in the distance between calcium source and release sites (Orlando et al. 2021).

Collectively, these new findings indicate that increasing cAMP in hMFBs enhances their morphological complexity, recruits more AZs, and prepares the release machinery for synchronous release from several release sites, despite the distance between calcium channels and release sites seeming to remain unchanged (Orlando et al. 2021). Rapid structural remodeling and higher release synchrony may thereby promote presynaptic LTP induction at MF synapses. Furthermore, activity-dependent ultrastructural alterations in hMFBs were characterized using flash- and-freeze electron microscopy (Borges-Merjane, Kim, and Jonas 2020; Imig et al. 2020). This methodological approach together with the novel optogenetic tool synptoPAC, which drives light-induced adenylyl cyclase activation (Oldani et al. 2021), may aid in unravelling the differential effects of chemically produced and action potential-evoked presynaptic potentiation at hMFBs.

5.5 Morphology of Bassoon protein in SIM and dSTORM imaging techniques

The study of active zone protein complexes has been revolutionized by super-resolution microscopy, which has shown striking patterning in the active zone. The big scaffold protein Bassoon is positioned in the vertebrate brain with its C-terminus (Wong et al. 2018) near the presynaptic plasma membrane and its N-terminus reaching tens of nanometers into the presynaptic cytoplasm (Dani et al. 2010).

5. Results and Discussion

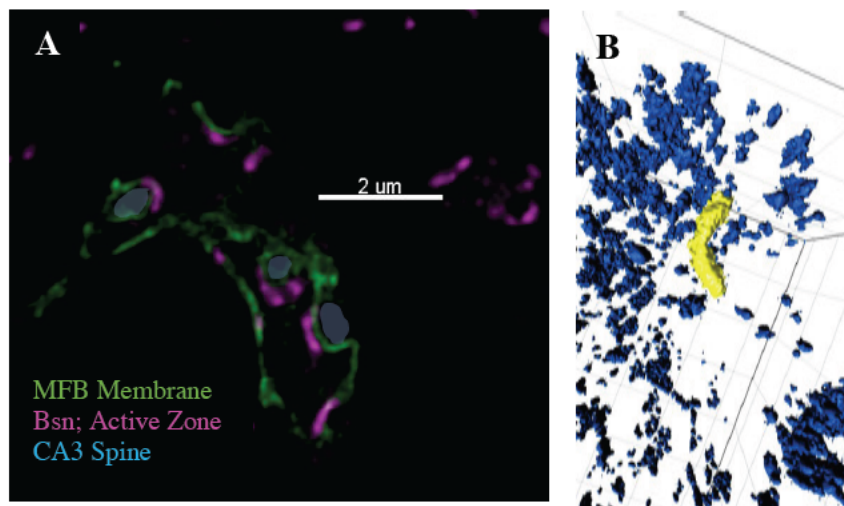


Figure 41. Bassoon protein morphology in SIM and dSTORM images

A) 2-D SIM image of an MFB and Bassoon in mEGFP (Ls1) mice. B) 3D-dSTORM image of Bsn in a similar mic. The Bsn Clusters were seen in the proximity of the presynaptic plasma membrane as banana-shaped structures.

Other active zone proteins are located between the Bassoon N- and C-termini, suggesting that they are all components of the same complex. Likewise, in the fly neuromuscular junction, where *Bruchpilot*, a partial homologue of ELKS, is orientated with its N-terminus near to the target membrane and the other presynaptic proteins are arranged around it (Liu et al. 2011; Fouquet et al. 2009). Morphological investigations reveal that the active zone is a highly structured structure composed of many proteins complexes whose compositions may vary within and between synapses.

Our SIM and dSTORM data observation showed that the Bassoon clusters could be found as banana-shaped structures near the presynaptic plasma membrane.

6 Conclusion and outlook

A chemical synapse is a sophisticated system made up of thousands of proteins that interact together to facilitate neurotransmitter-based inter-neuron signaling. Mechanistic and structural discoveries into the brain's fundamental functional unit are expected to have far-reaching implications for comprehending normal and abnormal neuronal circuits. Given the small size of the synaptic ultrastructure, electron microscopy (EM) has been used mainly to characterize it. While EM provides excellent spatial resolution, its application in 3D multicolor visualization of molecular components has been restricted.

In this work, a super-resolution fluorescence imaging method was used for determining the AZ proteins in mouse hippocampal MFBs. With the nanoscopic resolution provided by *d*STORM, along with the multicolor SIM imaging capabilities, we were able to image proteins in the presynaptic AZ. Using SIM imaging along with cLTP induction with forskolin on acute brain slices, we determined the synaptic plasticity changes of the key AZ proteins Bassoon, Munc 13-1 and Tomosyn. Due to the SIM limitations (Heintzmann and Cremer 1999; M G L Gustafsson 2000), we could not investigate the intensity and density of these proteins, but the single molecular quantification with the SIM technique was not feasible. The *d*STORM data demonstrated feasibility to perform single molecule 3D imaging of presynaptic active zones in distinct sub-compartments of the intact hippocampus. Our methods allowed quantitative mapping of molecular changes in AZ proteins after induction of plasticity.

Both *d*STORM and SIM microscopy have unique benefits as well as drawbacks. However, unlike EM, they do not allow intrinsic contrast of membranes, which is extremely important in distinguishing structures such as the synaptic cleft, vesicles, and other organelles located near the synaptic active zone. In order to capture the rapid dynamics at the molecular level, SIM may be used with SMLM to improve its spatial resolution. Furthermore, it is essential to miniaturize SIM systems to make them more portable, accessible, and low-cost for users across a wide range of disciplines. These imaging approaches may now be used to identify potential differences in functional molecular rearrangements of synaptic proteins in healthy and diseased brain (e.g. after induction of traumatic brain injury).

7 References

- Abbe, E. 1873. "Beiträge Zur Theorie Des Mikroskops Und Der Mikroskopischen Wahrnehmung." *Archiv Für Mikroskopische Anatomie* 9 (1): 413–68. <https://doi.org/10.1007/BF02956173>.
- Abel, T, P V Nguyen, M Barad, T A Deuel, E R Kandel, and R Bourtchouladze. 1997. "Genetic Demonstration of a Role for PKA in the Late Phase of LTP and in Hippocampus-Based Long-Term Memory." *Cell* 88 (5): 615–26. [https://doi.org/10.1016/s0092-8674\(00\)81904-2](https://doi.org/10.1016/s0092-8674(00)81904-2).
- Abraham, Wickliffe C., Owen D. Jones, and David L. Glanzman. 2019. "Is Plasticity of Synapses the Mechanism of Long-Term Memory Storage?" *Npj Science of Learning* 4 (1). <https://doi.org/10.1038/s41539-019-0048-y>.
- Abraham, Wickliffe C, Barbara Logan, Jeffrey M Greenwood, and Michael Dragunow. 2002. "Induction and Experience-Dependent Consolidation of Stable Long-Term Potentiation Lasting Months in the Hippocampus." *The Journal of Neuroscience : The Official Journal of the Society for Neuroscience* 22 (21): 9626–34. <https://doi.org/10.1523/JNEUROSCI.22-21-09626.2002>.
- Access, Open. 2021. "Recent Advances in Structured Illumination Microscopy."
- Ackermann, Frauke, Clarissa L Waites, and Craig C Garner. 2015. "Presynaptic Active Zones in Invertebrates and Vertebrates." *EMBO Reports* 16 (8): 923–38. <https://doi.org/10.15252/embr.201540434>.
- Acsády, László, and Szabolcs Káli. 2007. "Models, Structure, Function: The Transformation of Cortical Signals in the Dentate Gyrus." *Progress in Brain Research* 163: 577–99. [https://doi.org/10.1016/S0079-6123\(07\)63031-3](https://doi.org/10.1016/S0079-6123(07)63031-3).
- Acuna, Claudio, Xinran Liu, Aneysis Gonzalez, and Thomas C Südhof. 2015. "RIM-BPs Mediate Tight Coupling of Action Potentials to Ca(2+)-Triggered Neurotransmitter Release." *Neuron* 87 (6): 1234–47. <https://doi.org/10.1016/j.neuron.2015.08.027>.
- Agard, D A, Y Hiraoka, P Shaw, and J W Sedat. 1989. "Fluorescence Microscopy in Three Dimensions." *Methods in Cell Biology* 30: 353–77. [https://doi.org/10.1016/s0091-679x\(08\)60986-3](https://doi.org/10.1016/s0091-679x(08)60986-3).
- Agard, David A, and John W Sedat. 1983. "Three-Dimensional Architecture of a Polytene Nucleus." *Nature* 302 (5910): 676–81. <https://doi.org/10.1038/302676a0>.
- Alkadhi, Karim A. 2021. "NMDA Receptor-Independent LTP in Mammalian Nervous System." *Progress in Neurobiology* 200: 101986. <https://doi.org/https://doi.org/10.1016/j.pneurobio.2020.101986>.
- Alle, H., P. Jonas, and J. R. P. Geiger. 2001. "PTP and LTP at a Hippocampal Mossy Fiber-Interneuron Synapse." *Proceedings of the National Academy of Sciences* 98 (25): 14708–13. <https://doi.org/10.1073/pnas.251610898>.
- Altrock, Wilko D., Susanne Tom Dieck, Maxim Sokolov, Alexander C. Meyer, Albrecht Sigler, Cord Brakebusch, Reinhard Fässler, et al. 2003. "Functional Inactivation of a Fraction of Excitatory Synapses in Mice Deficient for the Active Zone Protein Bassoon." *Neuron* 37 (5): 787–800. [https://doi.org/10.1016/S0896-6273\(03\)00088-6](https://doi.org/10.1016/S0896-6273(03)00088-6).
- Amaral, D G, N Ishizuka, and B Claiborne. 1990. "Neurons, Numbers and the Hippocampal Network." *Progress in Brain Research* 83: 1–11. [https://doi.org/10.1016/s0079-6123\(08\)61237-6](https://doi.org/10.1016/s0079-6123(08)61237-6).
- Annamneedi, Anil, Gürsel Caliskan, Sabrina Müller, Dirk Montag, Eike Budinger, Frank Angenstein, Anna Fejtova, Wolfgang Tischmeyer, Eckart D Gundelfinger, and Oliver Stork. 2018. "Ablation of the Presynaptic Organizer Bassoon in Excitatory Neurons Retards Dentate Gyrus Maturation and Enhances Learning Performance." *Brain Structure & Function* 223 (7): 3423–45. <https://doi.org/10.1007/s00429-018-1692-3>.

7. References

- Aravamudan, B, T Fergestad, W S Davis, C K Rodesch, and K Broadie. 1999. "Drosophila UNC-13 Is Essential for Synaptic Transmission." *Nature Neuroscience* 2 (11): 965–71. <https://doi.org/10.1038/14764>.
- Ashery, U. 2009. "Friends and Foes in Synaptic Transmission." *Trends in Neurosciences* 32 (5): 275–82. <https://doi.org/10.1016/j.tins.2009.01.004>. Friends.
- Augustin, I, C Rosenmund, T C Südhof, and N Brose. 1999. "Munc13-1 Is Essential for Fusion Competence of Glutamatergic Synaptic Vesicles." *Nature* 400 (6743): 457–61. <https://doi.org/10.1038/22768>.
- Axelrod, Daniel. 2001. "Total Internal Reflection Fluorescence Microscopy in Cell Biology." *Traffic* 2 (11): 764–74. <https://doi.org/https://doi.org/10.1034/j.1600-0854.2001.21104.x>.
- Baba, Takeshi, Toshiaki Sakisaka, Sumiko Mochida, and Yoshimi Takai. 2005. "PKA-Catalyzed Phosphorylation of Tomosyn and Its Implication in Ca²⁺-Dependent Exocytosis of Neurotransmitter." *Journal of Cell Biology* 170 (7): 1113–25. <https://doi.org/10.1083/jcb.200504055>.
- Bailey, Craig H., Dusan Bartsch, and Eric R. Kandel. 1996. "Toward a Molecular Definition of Long-Term Memory Storage." *Proceedings of the National Academy of Sciences of the United States of America* 93 (24): 13445–52. <https://doi.org/10.1073/pnas.93.24.13445>.
- Banke, T G, D Bowie, H.-K. Lee, R L Haganir, A Schousboe, and S F Traynelis. 2000. "Control of GluR1 AMPA Receptor Function by CAMP-Dependent Protein Kinase." *The Journal of Neuroscience* 20 (1): 89 LP – 102. <https://doi.org/10.1523/JNEUROSCI.20-01-00089.2000>.
- Barad, M, R Bourtchouladze, D G Winder, H Golan, and E Kandel. 1998. "Rolipram, a Type IV-Specific Phosphodiesterase Inhibitor, Facilitates the Establishment of Long-Lasting Long-Term Potentiation and Improves Memory." *Proceedings of the National Academy of Sciences of the United States of America* 95 (25): 15020–25. <https://doi.org/10.1073/pnas.95.25.15020>.
- Barak, Boaz, Antionette Williams, Noa Bielopolski, Irit Gottfried, Eitan Okun, Meghan A. Brown, Ulf Matti, Jens Rettig, Edward L. Stuenkel, and Uri Ashery. 2010. "Tomosyn Expression Pattern in the Mouse Hippocampus Suggests Both Presynaptic and Postsynaptic Functions." *Frontiers in Neuroanatomy* 4 (DEC): 1–11. <https://doi.org/10.3389/fnana.2010.00149>.
- Basu, Jayeeta, Nan Shen, Irina Dulubova, Jun Lu, Rong Guan, Oleg Guryev, Nick V Grishin, Christian Rosenmund, and Josep Rizo. 2005. "A Minimal Domain Responsible for Munc13 Activity." *Nature Structural & Molecular Biology* 12 (11): 1017–18. <https://doi.org/10.1038/nsmb1001>.
- Bates, Mark, Timothy R Blosser, and Xiaowei Zhuang. 2005. "Short-Range Spectroscopic Ruler Based on a Single-Molecule Optical Switch." *Physical Review Letters* 94 (10): 108101. <https://doi.org/10.1103/PhysRevLett.94.108101>.
- Bates, Mark, Bo Huang, Graham T Dempsey, and Xiaowei Zhuang. 2007. "Multicolor Super-Resolution Imaging with Photo-Switchable Fluorescent Probes." *Science* 317 (5845): 1749 LP – 1753. <https://doi.org/10.1126/science.1146598>.
- Batten, S R, S Whiteheart, G Gerhardt, and J Slevin. 2016. "Neurotransmitter Function Presynaptic Neurotransmission: Alterations in Exocytotic/Secretory Machinery and Glutamate Signaling in Kindling." In .
- Baudry, Michel, and Gary Lynch. 2001. "Remembrance of Arguments Past: How Well Is the Glutamate Receptor Hypothesis of LTP Holding Up after 20 Years?" *Neurobiology of Learning and Memory* 76 (3): 284–97. <https://doi.org/https://doi.org/10.1006/nlme.2001.4023>.
- Bear, M F, and R C Malenka. 1994. "Synaptic Plasticity: LTP and LTD." *Current Opinion in Neurobiology* 4 (3): 389–99. [https://doi.org/10.1016/0959-4388\(94\)90101-5](https://doi.org/10.1016/0959-4388(94)90101-5).
- Bednarek, Ewa, and Pico Caroni. 2011. "β-Adducin Is Required for Stable Assembly of New

7. References

- Synapses and Improved Memory upon Environmental Enrichment.” *Neuron* 69 (6): 1132–46. <https://doi.org/10.1016/j.neuron.2011.02.034>.
- Ben-Simon, Yoav, Alma Rodenas-Ruano, Karina Alviña, Alice D. Lam, Edward L. Stuenkel, Pablo E. Castillo, and Uri Ashery. 2015. “A Combined Optogenetic-Knockdown Strategy Reveals a Major Role of Tomosyn in Mossy Fiber Synaptic Plasticity.” *Cell Reports* 12 (3): 396–404. <https://doi.org/10.1016/j.celrep.2015.06.037>.
- Bennett, Max R. 1999. “The Early History of the Synapse: From Plato to Sherrington.” *Brain Research Bulletin* 50 (2): 95–118. [https://doi.org/10.1016/S0361-9230\(99\)00094-5](https://doi.org/10.1016/S0361-9230(99)00094-5).
- Betz, Andrea, Pratima Thakur, Harald J. Junge, Uri Ashery, Jeong-Seop Seop Rhee, Volker Scheuss, Christian Rosenmund, Jens Rettig, and Nils Brose. 2001. “Functional Interaction of the Active Zone Proteins Munc13-1 and RIM1 in Synaptic Vesicle Priming.” *Neuron* 30 (1): 183–96. [https://doi.org/https://doi.org/10.1016/S0896-6273\(01\)00272-0](https://doi.org/https://doi.org/10.1016/S0896-6273(01)00272-0).
- Betzig, E, G H Patterson, R Sougrat, O W Lindwasser, S Olenych, J S Bonifacino, M W Davidson, J Lippincott-Schwartz, and H F Hess. 2006. “Imaging Intracellular Fluorescent Proteins at Nanometer Resolution.” *Science* 313: 1642.
- Betzig, Eric, and Jay K Trautman. 1992. “Near-Field Optics: Microscopy, Spectroscopy, and Surface Modification Beyond the Diffraction Limit.” *Science* 257 (5067): 189 LP – 195. <https://doi.org/10.1126/science.257.5067.189>.
- Bielopolski, Noa, Alice D Lam, Dana Bar-On, Markus Sauer, Edward L Stuenkel, and Uri Ashery. 2014. “Differential Interaction of Tomosyn with Syntaxin and SNAP25 Depends on Domains in the WD40 β -Propeller Core and Determines Its Inhibitory Activity.” *The Journal of Biological Chemistry* 289 (24): 17087–99. <https://doi.org/10.1074/jbc.M113.515296>.
- Birks, R., H. E. Huxley, and B. Katz. 1960. “The Fine Structure of the Neuromuscular Junction of the Frog.” *The Journal of Physiology* 150 (1): 134–44. <https://doi.org/10.1113/jphysiol.1960.sp006378>.
- Bliss, T V, and G L Collingridge. 1993. “A Synaptic Model of Memory: Long-Term Potentiation in the Hippocampus.” *Nature* 361 (6407): 31–39. <https://doi.org/10.1038/361031a0>.
- Bliss, T V, and A R Gardner-Medwin. 1973. “Long-Lasting Potentiation of Synaptic Transmission in the Dentate Area of the Unanaesthetized Rabbit Following Stimulation of the Perforant Path.” *The Journal of Physiology* 232 (2): 357–74. <https://doi.org/10.1113/jphysiol.1973.sp010274>.
- Bliss, T V, and T Lomo. 1973. “Long-Lasting Potentiation of Synaptic Transmission in the Dentate Area of the Anaesthetized Rabbit Following Stimulation of the Perforant Path.” *The Journal of Physiology* 232 (2): 331–56. <https://doi.org/10.1113/jphysiol.1973.sp010273>.
- Bloom, Floyd E., and George K Aghajanian. 1968. “Fine Structural and Cytochemical Analysis of the Staining of Synaptic Junctions with Phosphotungstic Acid.” *Journal of Ultrastructure Research* 22 (5–6): 361–75. [https://doi.org/10.1016/S0022-5320\(68\)90027-0](https://doi.org/10.1016/S0022-5320(68)90027-0).
- Bock, H, C Geisler, C A Wurm, C von Middendorff, S Jakobs, A Schönle, A Egner, S W Hell, and C Eggeling. 2007. “Two-Color Far-Field Fluorescence Nanoscopy Based on Photoswitchable Emitters.” *Applied Physics B* 88 (2): 161–65. <https://doi.org/10.1007/s00340-007-2729-0>.
- Böhme, Mathias A., Anthony W. McCarthy, Andreas T. Grasskamp, Christine B. Beuschel, Pragma Goel, Meida Jusyte, Desiree Laber, et al. 2019. “Rapid Active Zone Remodeling Consolidates Presynaptic Potentiation.” *Nature Communications* 10 (1): 1–16. <https://doi.org/10.1038/s41467-019-08977-6>.
- Bon, Pierre, Jeanne Linarès-Loyez, Maxime Feyeux, Kevin Alessandri, Brahim Lounis, Pierre Nassoy, and Laurent Cognet. 2018. “Self-Interference 3D Super-Resolution Microscopy

7. References

- for Deep Tissue Investigations.” *Nature Methods* 15 (6): 449–54. <https://doi.org/10.1038/s41592-018-0005-3>.
- Borges-Merjane, Carolina, Olena Kim, and Peter Jonas. 2020. “Functional Electron Microscopy, ‘Flash and Freeze,’ of Identified Cortical Synapses in Acute Brain Slices.” *Neuron* 105 (6): 992–1006.e6. <https://doi.org/10.1016/j.neuron.2019.12.022>.
- Bortolotto, Zuner A., and Graham L. Collingridge. 1993. “Characterisation of LTP Induced by the Activation of Glutamate Metabotropic Receptors in Area CA1 of the Hippocampus.” *Neuropharmacology* 32 (1): 1–9. [https://doi.org/10.1016/0028-3908\(93\)90123-K](https://doi.org/10.1016/0028-3908(93)90123-K).
- Brakemann, Tanja, Andre C Stiel, Gert Weber, Martin Andresen, Ilaria Testa, Tim Grotjohann, Marcel Leutenegger, et al. 2011. “A Reversibly Photoswitchable GFP-like Protein with Fluorescence Excitation Decoupled from Switching.” *Nature Biotechnology* 29 (10): 942–47. <https://doi.org/10.1038/nbt.1952>.
- Brakenhoff, G J, H T M van der Voort, E A van Spronsen, W A M Linnemans, and N Nanninga. 1985. “Three-Dimensional Chromatin Distribution in Neuroblastoma Nuclei Shown by Confocal Scanning Laser Microscopy.” *Nature* 317 (6039): 748–49. <https://doi.org/10.1038/317748a0>.
- Brockmann, Marisa M., Marta Maglione, Claudia G. Willmes, Alexander Stumpf, Boris A. Bouazza, Laura M. Velasquez, M. Katharina Grauel, et al. 2019. “RIM-BP2 Primes Synaptic Vesicles via Recruitment of Munc13-1 at Hippocampal Mossy Fiber Synapses.” *ELife* 8: 1–22. <https://doi.org/10.7554/eLife.43243>.
- Brodin, Lennart, and Oleg Shupliakov. 2006. “Giant Reticulospinal Synapse in Lamprey: Molecular Links between Active and Periaxonal Zones.” *Cell and Tissue Research* 326 (2): 301–10. <https://doi.org/10.1007/s00441-006-0216-2>.
- Brose, N, K Hofmann, Y Hata, and T C Südhof. 1995. “Mammalian Homologues of *Caenorhabditis Elegans* Unc-13 Gene Define Novel Family of C2-Domain Proteins.” *The Journal of Biological Chemistry* 270 (42): 25273–80. <https://doi.org/10.1074/jbc.270.42.25273>.
- Brown, Peter T, Rory Kruithoff, Gregory J Seedorf, and Douglas P Shepherd. 2020. “Multicolor Structured Illumination Microscopy and Quantitative Control of Coherent Light with a Digital Mirror Device.” *BioRxiv*, January, 2020.07.27.223941. <https://doi.org/10.1101/2020.07.27.223941>.
- Bruckner, Joseph J., Scott J. Gratz, Jessica K. Slind, Richard R. Geske, Alexander M. Cummings, Samantha E. Galindo, Laura K. Donohue, and Kate M. O’Connor-Giles. 2012. “Fife, a *Drosophila* Piccolo-RIM Homolog, Promotes Active Zone Organization and Neurotransmitter Release.” *Journal of Neuroscience* 32 (48): 17048–58. <https://doi.org/10.1523/JNEUROSCI.3267-12.2012>.
- Cajal, Santiago Ramon Y. 1894. “The Croonian Lecture: La Fine Structure Des Centres Nerveux.” *Proceedings of the Royal Society of London Series I* 55: 444–68.
- Cajal, SR. 1888. “Sobre Las Fibras Nerviosas de La Capa Molecular Del Cerebelo.” *Rev Trim Histol Norm Patol*, no. 1: 33–49.
- Cartmell, Jayne, John A. Kemp, Stephen P.H. Alexander, Haruhiko Shinozaki, and David A. Kendall. 1994. “Modulation of Cyclic AMP Formation by Putative Metabotropic Receptor Agonists.” *British Journal of Pharmacology* 111 (1): 364–69. <https://doi.org/10.1111/j.1476-5381.1994.tb14069.x>.
- Cases-Langhoff, C, B Voss, A M Garner, U Appeltauer, K Takei, S Kindler, R W Veh, P De Camilli, E D Gundelfinger, and C C Garner. 1996. “Piccolo, a Novel 420 KDa Protein Associated with the Presynaptic Cytomatrix.” *European Journal of Cell Biology* 69 (3): 214–223. <http://europepmc.org/abstract/MED/8900486>.
- Chen, Jie, Sara E Billings, and Hiroshi Nishimune. 2011. “Calcium Channels Link the Muscle-Derived Synapse Organizer Laminin B2 to Bassoon and CAST/Erc2 to Organize Presynaptic Active Zones.” *The Journal of Neuroscience: The Official Journal of the*

7. References

- Society for Neuroscience* 31 (2): 512–25. <https://doi.org/10.1523/JNEUROSCI.3771-10.2011>.
- Chicurel, Marina E., and Kristen M. Harris. 1992. “Three-dimensional Analysis of the Structure and Composition of CA3 Branched Dendritic Spines and Their Synaptic Relationships with Mossy Fiber Boutons in the Rat Hippocampus.” *Journal of Comparative Neurology* 325 (2): 169–82. <https://doi.org/10.1002/cne.903250204>.
- Cho, Richard W., Lauren K. Buhl, Dina Volfson, Adrienne Tran, Feng Li, Yulia Akbergenova, and J. Troy Littleton. 2015. “Phosphorylation of Complexin by PKA Regulates Activity-Dependent Spontaneous Neurotransmitter Release and Structural Synaptic Plasticity.” *Neuron* 88 (4): 749–61. <https://doi.org/10.1016/j.neuron.2015.10.011>.
- Citri, Ami, and Robert C. Malenka. 2008. “Synaptic Plasticity: Multiple Forms, Functions, and Mechanisms.” *Neuropsychopharmacology* 33 (1): 18–41. <https://doi.org/10.1038/sj.npp.1301559>.
- Claiborne, B J, D G Amaral, and W M Cowan. 1986. “A Light and Electron Microscopic Analysis of the Mossy Fibers of the Rat Dentate Gyrus.” *The Journal of Comparative Neurology* 246 (4): 435–58. <https://doi.org/10.1002/cne.902460403>.
- Clarke, Gwenaëlle L., Jie Chen, and Hiroshi Nishimune. 2012. “Presynaptic Active Zone Density during Development and Synaptic Plasticity.” *Frontiers in Molecular Neuroscience* 5 (JANUARY 2012): 1–12. <https://doi.org/10.3389/fnmol.2012.00012>.
- Conchello, José-Angel, and Jeff W Lichtman. 2005. “Optical Sectioning Microscopy.” *Nature Methods* 2 (12): 920–31. <https://doi.org/10.1038/nmeth815>.
- Couteaux, R., and Pecot-Dechavassine, M. 1970. “Synaptic Vesicles and Pouches at the Level of " Active Zones" of the Neuromuscular Junction. Comptes Rendus Hebdomadaires Des Seances de l'Academie Des Sciences.” *Serie D: Sciences Naturelles* 271(25): 2346–49.
- Cremer, C, and T Cremer. 1978. “Considerations on a Laser-Scanning-Microscope with High Resolution and Depth of Field.” *Microscopica Acta* 81 (1): 31–44.
- Dani, Adish, Bo Huang, Joseph Bergan, Catherine Dulac, and Xiaowei Zhuang. 2010. “Superresolution Imaging of Chemical Synapses in the Brain.” *Neuron* 68 (5): 843–56. <https://doi.org/10.1016/j.neuron.2010.11.021>.
- Daumas, Stéphanie, Johnatan Ceccom, Hélène Halley, Bernard Francés, and Jean-Michel Lassalle. 2009. “Activation of Metabotropic Glutamate Receptor Type 2/3 Supports the Involvement of the Hippocampal Mossy Fiber Pathway on Contextual Fear Memory Consolidation.” *Learning & Memory (Cold Spring Harbor, N.Y.)* 16 (8): 504–7. <https://doi.org/10.1101/lm.1418309>.
- Davydova, Daria, Claudia Marini, Claire King, Julia Klueva, Ferdinand Bischof, Stefano Romorini, Carolina Montenegro-Venegas, et al. 2014. “Bassoon Specifically Controls Presynaptic P/Q-Type Ca²⁺ Channels via RIM-Binding Protein.” *Neuron* 82 (1): 181–94. <https://doi.org/10.1016/j.neuron.2014.02.012>.
- Deguchi, Yuichi, Flavio Donato, Ivan Galimberti, Erik Cabuy, and Pico Caroni. 2011. “Temporally Matched Subpopulations of Selectively Interconnected Principal Neurons in the Hippocampus.” *Nature Neuroscience* 14 (4): 495–504. <https://doi.org/10.1038/nn.2768>.
- Demmerle, Justin, Cassandravictoria Innocent, Alison J North, Graeme Ball, Marcel Müller, Ezequiel Miron, Atsushi Matsuda, Ian M Dobbie, Yolanda Markaki, and Lothar Schermelleh. 2017. “Strategic and Practical Guidelines for Successful Structured Illumination Microscopy.” *Nature Protocols* 12 (5): 988–1010. <https://doi.org/10.1038/nprot.2017.019>.
- Dempsey, Graham T, Joshua C Vaughan, Kok Hao Chen, Mark Bates, and Xiaowei Zhuang. 2011. “Evaluation of Fluorophores for Optimal Performance in Localization-Based Super-Resolution Imaging.” *Nature Methods* 8 (12): 1027–36. <https://doi.org/10.1038/nmeth.1768>.

7. References

- Deng, Lunbin, Pascal S. Kaeser, Wei Xu, and Thomas C. Südhof. 2011. “RIM Proteins Activate Vesicle Priming by Reversing Autoinhibitory Homodimerization of Munc13.” *Neuron* 69 (2): 317–31. <https://doi.org/10.1016/j.neuron.2011.01.005>.
- Derkach, Victor, Andres Barria, and Thomas R Soderling. 1999. “Ca²⁺/Calmodulin-Kinase II Enhances Channel Conductance of α -Amino-3-Hydroxy-5-Methyl-4-Isloxazolepropionate Type Glutamate Receptors.” *Proceedings of the National Academy of Sciences* 96 (6): 3269 LP – 3274. <https://doi.org/10.1073/pnas.96.6.3269>.
- Diamond, D M, T V Dunwiddie, and G M Rose. 1988. “Characteristics of Hippocampal Primed Burst Potentiation in Vitro and in the Awake Rat.” *The Journal of Neuroscience : The Official Journal of the Society for Neuroscience* 8 (11): 4079–88. <https://doi.org/10.1523/JNEUROSCI.08-11-04079.1988>.
- Dittman, Jeremy, and Timothy A Ryan. 2009. “Molecular Circuitry of Endocytosis at Nerve Terminals.” *Annual Review of Cell and Developmental Biology* 25: 133–60. <https://doi.org/10.1146/annurev.cellbio.042308.113302>.
- Dondzillo, Anna, Kurt Sätzler, Heinz Horstmann, Wilko D Altmann, Eckart D Gundelfinger, and Thomas Kuner. 2010. “Targeted Three-Dimensional Immunohistochemistry Reveals Localization of Presynaptic Proteins Bassoon and Piccolo in the Rat Calyx of Held before and after the Onset of Hearing.” *The Journal of Comparative Neurology* 518 (7): 1008–29. <https://doi.org/10.1002/cne.22260>.
- Dong, Zhifang, Huili Han, Hongjie Li, Yanrui Bai, Wei Wang, Man Tu, Yan Peng, et al. 2015. “Long-Term Potentiation Decay and Memory Loss Are Mediated by AMPAR Endocytosis.” *The Journal of Clinical Investigation* 125 (1): 234–47. <https://doi.org/10.1172/JCI77888>.
- Donnert, Gerald, Jan Keller, Rebecca Medda, M Alexandra Andrei, Silvio O Rizzoli, Reinhard Lührmann, Reinhard Jahn, Christian Eggeling, and Stefan W Hell. 2006. “Macromolecular-Scale Resolution in Biological Fluorescence Microscopy.” *Proceedings of the National Academy of Sciences* 103 (31): 11440 LP – 11445. <https://doi.org/10.1073/pnas.0604965103>.
- Dossani, Rimal Hanif, Symeon Missios, and Anil Nanda. 2015. “The Legacy of Henry Molaison (1926-2008) and the Impact of His Bilateral Mesial Temporal Lobe Surgery on the Study of Human Memory.” *World Neurosurgery* 84 (4): 1127–35. <https://doi.org/10.1016/j.wneu.2015.04.031>.
- Dresbach, T., B. Qualmann, M. M. Kessels, C. C. Garner, and E. D. Gundelfinger. 2001. “The Presynaptic Cytomatrix of Brain Synapses.” *Cellular and Molecular Life Sciences* 58 (1): 94–116. <https://doi.org/10.1007/PL00000781>.
- Dulubova, Irina, Mikhail Khvotchev, Siqi Liu, Iryna Huryeva, Thomas C. Südhof, and Josep Rizo. 2007. “Munc18-1 Binds Directly to the Neuronal SNARE Complex.” *Proceedings of the National Academy of Sciences of the United States of America* 104 (8): 2697–2702. <https://doi.org/10.1073/pnas.0611318104>.
- Dulubova, Irina, Xuelin Lou, Jun Lu, Iryna Huryeva, Amer Alam, Ralf Schneggenburger, Thomas C. Südhof, and Josep Rizo. 2005. “A Munc13/RIM/Rab3 Tripartite Complex: From Priming to Plasticity?” *EMBO Journal* 24 (16): 2839–50. <https://doi.org/10.1038/sj.emboj.7600753>.
- Dulubova, Irina, Shuzo Sugita, Sandra Hill, Masahiro Hosaka, Imma Fernandez, Thomas C. Südhof, and Josep Rizo. 1999. “A Conformational Switch in Syntaxin during Exocytosis: Role of Munc18.” *EMBO Journal*. <https://doi.org/10.1093/emboj/18.16.4372>.
- Edwards, F A, A Konnerth, B Sakmann, and T Takahashi. 1989. “A Thin Slice Preparation for Patch Clamp Recordings from Neurones of the Mammalian Central Nervous System.” *Pflügers Archiv* 414 (5): 600–612. <https://doi.org/10.1007/BF00580998>.
- Egner, Alexander, Claudia Geisler, Claas von Middendorff, Hannes Bock, Dirk Wenzel,

7. References

- Rebecca Medda, Martin Andresen, et al. 2007. "Fluorescence Nanoscopy in Whole Cells by Asynchronous Localization of Photoswitching Emitters." *Biophysical Journal* 93 (9): 3285–90. <https://doi.org/10.1529/biophysj.107.112201>.
- Egner, Alexander, and Stefan W Hell. 2005. "Fluorescence Microscopy with Super-Resolved Optical Sections." *Trends in Cell Biology* 15 (4): 207–15. <https://doi.org/10.1016/j.tcb.2005.02.003>.
- Ehmann, Nadine, Sebastian van de Linde, Amit Alon, Dmitrij Ljaschenko, Xi Zhen Keung, Thorger Holm, Annika Rings, et al. 2014. "Quantitative Super-Resolution Imaging of Bruchpilot Distinguishes Active Zone States." *Nature Communications* 5 (1): 4650. <https://doi.org/10.1038/ncomms5650>.
- Ehmann, Nadine, David Oswald, and Robert J. Kittel. 2017. "Drosophila Active Zones: From Molecules to Behaviour." *Neuroscience Research*. <https://doi.org/10.1016/j.neures.2017.11.015>.
- Emptage, Nigel J., Christopher A. Reid, Alan Fine, and Timothy V.P. Bliss. 2003. "Optical Quantal Analysis Reveals a Presynaptic Component of LTP at Hippocampal Schaffer-Associational Synapses." *Neuron* 38 (5): 797–804. [https://doi.org/10.1016/S0896-6273\(03\)00325-8](https://doi.org/10.1016/S0896-6273(03)00325-8).
- Enoki, Ryosuke, Yi-Ling Hu, David Hamilton, and Alan Fine. 2009. "Expression of Long-Term Plasticity at Individual Synapses in Hippocampus Is Graded, Bidirectional, and Mainly Presynaptic: Optical Quantal Analysis." *Neuron* 62 (2): 242–53. <https://doi.org/10.1016/j.neuron.2009.02.026>.
- Evstratova, Alesya, and Katalin Tóth. 2014. "Information Processing and Synaptic Plasticity at Hippocampal Mossy Fiber Terminals." *Frontiers in Cellular Neuroscience* 8 (February): 7–12. <https://doi.org/10.3389/fncel.2014.00028>.
- Feder, Robert, and James B Ranck. 1973. "Studies on Single Neurons in Dorsal Hippocampal Formation and Septum in Unrestrained Rats: Part II. Hippocampal Slow Waves and Theta Cell Firing during Bar Pressing and Other Behaviors." *Experimental Neurology* 41 (2): 532–55. [https://doi.org/https://doi.org/10.1016/0014-4886\(73\)90291-4](https://doi.org/https://doi.org/10.1016/0014-4886(73)90291-4).
- Fejtova, Anna, Daria Davydova, Ferdinand Bischof, Vesna Lazarevic, Wilko D. Altmann, Stefano Romorini, Cornelia Schöne, et al. 2009. "Dynein Light Chain Regulates Axonal Trafficking and Synaptic Levels of Bassoon." *Journal of Cell Biology* 185 (2): 341–55. <https://doi.org/10.1083/jcb.200807155>.
- Fejtova, Anna, Hartmut Schmidt, Annika Weyhersmüller, R. Angus Silver, Eckart D. Gundelfinger, and Jens Eilers. 2010. "Bassoon Speeds Vesicle Reloading at a Central Excitatory Synapse." *Neuron* 68 (4): 710–23. <https://doi.org/10.1016/j.neuron.2010.10.026>.
- Fenster, Steven D., Wook Joon Chung, Rong Zhai, Claudia Cases-Langhoff, Britta Voss, Abigail M. Garner, Udo Kaempfer, Stefan Kindler, Eckart D. Gundelfinger, and Craig C. Garner. 2000. "Piccolo, a Presynaptic Zinc Finger Protein Structurally Related to Bassoon." *Neuron* 25 (1): 203–14. [https://doi.org/10.1016/S0896-6273\(00\)80883-1](https://doi.org/10.1016/S0896-6273(00)80883-1).
- Fernández-Busnadiego, Rubén, Shoh Asano, Ana-Maria Oprisoreanu, Eri Sakata, Michael Doengi, Zdravko Kochovski, Magdalena Zürner, et al. 2013. "Cryo-Electron Tomography Reveals a Critical Role of RIM1 α in Synaptic Vesicle Tethering." *Journal of Cell Biology* 201 (5): 725–40. <https://doi.org/10.1083/jcb.201206063>.
- Filippo, Massimiliano Di, Alessandro Tozzi, Cinzia Costa, Vincenzo Belcastro, Michela Tantucci, Barbara Picconi, and Paolo Calabresi. 2008. "Plasticity and Repair in the Post-Ischemic Brain." *Neuropharmacology* 55 (3): 353–62. <https://doi.org/10.1016/j.neuropharm.2008.01.012>.
- Fiolka, Reto, Lin Shao, E Hesper Rego, Michael W Davidson, and Mats G L Gustafsson. 2012. "Time-Lapse Two-Color 3D Imaging of Live Cells with Doubled Resolution Using Structured Illumination." *Proceedings of the National Academy of Sciences* 109 (14): 5311

7. References

- LP – 5315. <https://doi.org/10.1073/pnas.1119262109>.
- Fölling, Jonas, Mariano Bossi, Hannes Bock, Rebecca Medda, Christian A Wurm, Birka Hein, Stefan Jakobs, Christian Eggeling, and Stefan W Hell. 2008. “Fluorescence Nanoscopy by Ground-State Depletion and Single-Molecule Return.” *Nature Methods* 5 (11): 943–45. <https://doi.org/10.1038/nmeth.1257>.
- Fouquet, Wernher, David Oswald, Carolin Wichmann, Sara Mertel, Harald Depner, Marcus Dyba, Stefan Hallermann, Robert J. Kittel, Stefan Eimer, and Stephan J. Sigrist. 2009. “Maturation of Active Zone Assembly by *Drosophila* Bruchpilot.” *Journal of Cell Biology* 186 (1): 129–45. <https://doi.org/10.1083/jcb.200812150>.
- Frank, Thomas, Mark A. Rutherford, Nicola Strenzke, Andreas Neef, Tina Pangršič, Darina Khimich, Anna Fetjova, et al. 2010. “Bassoon and the Synaptic Ribbon Organize Ca²⁺ Channels and Vesicles to Add Release Sites and Promote Refilling.” *Neuron* 68 (4): 724–38. <https://doi.org/10.1016/j.neuron.2010.10.027>.
- Franke, Christian, Markus Sauer, and Sebastian van de Linde. 2017. “Photometry Unlocks 3D Information from 2D Localization Microscopy Data.” *Nature Methods* 14 (1): 41–44. <https://doi.org/10.1038/nmeth.4073>.
- Frotscher, Michael, Peter Jonas, and Robert S. Sloviter. 2006. “Synapses Formed by Normal and Abnormal Hippocampal Mossy Fibers.” *Cell and Tissue Research* 326 (2): 361–67. <https://doi.org/10.1007/s00441-006-0269-2>.
- Fujita, Yasuyuki, Hiromichi Shirataki, Toshiaki Sakisaka, Takeshi Asakura, Takeshi Ohya, Hirokazu Kotani, Shigekazu Yokoyama, et al. 1998. “Tomosyn: A Syntaxin-1-Binding Protein That Forms a Novel Complex in the Neurotransmitter Release Process.” *Neuron* 20 (5): 905–15. [https://doi.org/10.1016/S0896-6273\(00\)80472-9](https://doi.org/10.1016/S0896-6273(00)80472-9).
- Fukaya, Ryota, Marta Maglione, Stephan J. Sigrist, and Takeshi Sakaba. 2021. “Rapid Ca²⁺ Channel Accumulation Contributes to CaMKII-Mediated Increase in Transmission at Hippocampal Mossy Fiber Synapses.” *Proceedings of the National Academy of Sciences of the United States of America* 118 (9): 1–11. <https://doi.org/10.1073/pnas.2016754118>.
- Galbraith, Catherine G., and James A. Galbraith. 2011a. “Super-Resolution Microscopy at a Glance.” *Journal of Cell Science* 124 (10): 1607–11. <https://doi.org/10.1242/jcs.080085>.
- Galbraith, Catherine G., and James A Galbraith. 2011b. “Super-Resolution Microscopy at a Glance.” *Journal of Cell Science* 124 (Pt 10): 1607–11. <https://doi.org/10.1242/jcs.080085>.
- García-Junco-Clemente, P., P. Linares-Clemente, and R. Fernández-Chacón. 2005. “Active Zones for Presynaptic Plasticity in the Brain.” *Molecular Psychiatry* 10 (2): 185–200. <https://doi.org/10.1038/sj.mp.4001628>.
- Garner, Craig C., Stefan Kindler, and Eckart D. Gundelfinger. 2000. “Molecular Determinants of Presynaptic Active Zones.” *Current Opinion in Neurobiology* 10 (3): 321–27. [https://doi.org/10.1016/S0959-4388\(00\)00093-3](https://doi.org/10.1016/S0959-4388(00)00093-3).
- Geerts, Cornelia J., Roberta Mancini, Ning Chen, Frank T.W. Koopmans, Ka Wan Li, August B. Smit, Jan R.T. Van Weering, Matthijs Verhage, and Alexander J.A. Groffen. 2017. “Tomosyn Associates with Secretory Vesicles in Neurons through Its N- and C-Terminal Domains.” *PLoS ONE* 12 (7): 1–23. <https://doi.org/10.1371/journal.pone.0180912>.
- Ghelani, Tina, and Stephan J. Sigrist. 2018. “Coupling the Structural and Functional Assembly of Synaptic Release Sites.” *Frontiers in Neuroanatomy* 12 (October): 1–20. <https://doi.org/10.3389/fnana.2018.00081>.
- Göttfert, Fabian, Christian A Wurm, Veronika Mueller, Sebastian Berning, Volker C Cordes, Alf Honigsmann, and Stefan W Hell. 2013. “Coaligned Dual-Channel STED Nanoscopy and Molecular Diffusion Analysis at 20 Nm Resolution.” *Biophysical Journal*. <https://doi.org/10.1016/j.bpj.2013.05.029>.
- Goussakov, Ivan V., Klaus Fink, Christian E. Elger, and Heinz Beck. 2000. “Metaplasticity of Mossy Fiber Synaptic Transmission Involves Altered Release Probability.” *Journal of*

7. References

- Neuroscience* 20 (9): 3434–41. <https://doi.org/10.1523/jneurosci.20-09-03434.2000>.
- Govind, C. K., Patricia A. Quigley, and Joanne Pearce. 2001. “Synaptic Differentiation between Two Phasic Motoneurons to a Crayfish Fast Muscle.” *Invertebrate Neuroscience* 4 (2): 77–84. <https://doi.org/10.1007/s101580100009>.
- Gracheva, Elena O., Anna O. Burdina, Andrea M. Holgado, Martine Berthelot-Grosjean, Brian D. Ackley, Gayla Hadwiger, Michael L. Nonet, Robby M. Weimer, and Janet E. Richmond. 2006. “Tomosyn Inhibits Synaptic Vesicle Priming in *Caenorhabditis Elegans*.” *PLoS Biology* 4 (8): 1426–37. <https://doi.org/10.1371/journal.pbio.0040261>.
- Gracheva, Elena O., Gayla Hadwiger, Michael L. Nonet, and Janet E. Richmond. 2008. “Direct Interactions between *C. Elegans* RAB-3 and Rim Provide a Mechanism to Target Vesicles to the Presynaptic Density.” *Neuroscience Letters*. <https://doi.org/10.1016/j.neulet.2008.08.026>.
- Graf, E. R., V. Valakh, C. M. Wright, C. Wu, Z. Liu, Y. Q. Zhang, and A. DiAntonio. 2012. “RIM Promotes Calcium Channel Accumulation at Active Zones of the *Drosophila* Neuromuscular Junction.” *Journal of Neuroscience* 32 (47): 16586–96. <https://doi.org/10.1523/JNEUROSCI.0965-12.2012>.
- Gray, E G. 1963. “Electron Microscopy of Presynaptic Organelles of the Spinal Cord.” *Journal of Anatomy* 97 (Pt 1): 101–6. <http://www.ncbi.nlm.nih.gov/pubmed/13949972> <http://www.pubmedcentral.nih.gov/articlerender.fcgi?artid=PMC1244260> <http://www.pubmedcentral.nih.gov/articlerender.fcgi?artid=1244260&tool=pmcentrez&rendertype=abstract>.
- Groffen, Alexander J.A., Linda Jacobsen, Désirée Schut, and Matthijs Verhage. 2005. “Two Distinct Genes Drive Expression of Seven Tomosyn Isoforms in the Mammalian Brain, Sharing a Conserved Structure with a Unique Variable Domain.” *Journal of Neurochemistry* 92 (3): 554–68. <https://doi.org/10.1111/j.1471-4159.2004.02890.x>.
- Grotjohann, Tim, Ilaria Testa, Marcel Leutenegger, Hannes Bock, Nicolai T Urban, Flavie Lavoie-Cardinal, Katrin I Willig, Christian Eggeling, Stefan Jakobs, and Stefan W Hell. 2011. “Diffraction-Unlimited All-Optical Imaging and Writing with a Photochromic GFP.” *Nature* 478 (7368): 204–8. <https://doi.org/10.1038/nature10497>.
- Gundelfinger, E D, and S tom Dieck. 2000. “Molecular Organization of Excitatory Chemical Synapses in the Mammalian Brain.” *Die Naturwissenschaften* 87 (12): 513–23. <https://doi.org/10.1007/s001140050770>.
- Gundelfinger, Eckart D., and Anna Fejtova. 2012. “Molecular Organization and Plasticity of the Cytomatrix at the Active Zone.” *Current Opinion in Neurobiology* 22 (3): 423–30. <https://doi.org/10.1016/j.conb.2011.10.005>.
- Gundelfinger, Eckart D., Carsten Reissner, and Craig C. Garner. 2016. “Role of Bassoon and Piccolo in Assembly and Molecular Organization of the Active Zone.” *Frontiers in Synaptic Neuroscience* 7 (January). <https://doi.org/10.3389/fnsyn.2015.00019>.
- Gustafsson, M G, D A Agard, and J W Sedat. 1999. “i5M: 3D Widefield Light Microscopy with Better than 100 Nm Axial Resolution.” *Journal of Microscopy* 195 (Pt 1): 10–16. <https://doi.org/10.1046/j.1365-2818.1999.00576.x>.
- Gustafsson, M G L. 2000. “Surpassing the Lateral Resolution Limit by a Factor of Two Using Structured Illumination Microscopy.” *Journal of Microscopy* 198 (2): 82–87. <https://doi.org/https://doi.org/10.1046/j.1365-2818.2000.00710.x>.
- Gustafsson, Mats G L, Lin Shao, Peter M Carlton, C J Rachel Wang, Inna N Golubovskaya, W Zacheus Cande, David A Agard, and John W Sedat. 2008. “Three-Dimensional Resolution Doubling in Wide-Field Fluorescence Microscopy by Structured Illumination.” *Biophysical Journal* 94 (12): 4957–70. <https://doi.org/10.1529/biophysj.107.120345>.
- Hagena, Hardy, and Denise Manahan-Vaughan. 2011. “Learning-Facilitated Synaptic Plasticity at CA3 Mossy Fiber and Commissural-Associational Synapses Reveals Different Roles in Information Processing.” *Cerebral Cortex (New York, N.Y. : 1991)* 21 (11): 2442–49.

7. References

- <https://doi.org/10.1093/cercor/bhq271>.
- Hallam, Steven J., Alexandr Goncharov, Jason McEwen, Renee Baran, and Yishi Jin. 2002. "SYD-1, a Presynaptic Protein with PDZ, C2 and RhoGAP-like Domains, Specifies Axon Identity in *C. Elegans*." *Nature Neuroscience* 5 (11): 1137–46. <https://doi.org/10.1038/nn959>.
- Hallermann, Stefan, Christian Pawlu, Peter Jonas, and Manfred Heckmann. 2003. "A Large Pool of Releasable Vesicles in a Cortical Glutamatergic Synapse." *Proceedings of the National Academy of Sciences of the United States of America* 100 (15): 8975–80. <https://doi.org/10.1073/pnas.1432836100>.
- Hamada, Shun, and Toshihisa Ohtsuka. 2017. "CAST: Its Molecular Structure and Phosphorylation-Dependent Regulation of Presynaptic Plasticity." *Neuroscience Research*. <https://doi.org/10.1016/j.neures.2017.12.005>.
- Han, Yunyun, Pascal S. Kaeser, Thomas C. Südhof, and Ralf Schneggenburger. 2011. "RIM Determines Ca²⁺ Channel Density and Vesicle Docking at the Presynaptic Active Zone." *Neuron* 69 (2): 304–16. <https://doi.org/10.1016/j.neuron.2010.12.014>.
- Harlow, Mark L., David Ress, Arne Stoschek, Robert M. Marshall, and Uel J. McMahan. 2001. "The Architecture of Active Zone Material at the Frog's Neuromuscular Junction." *Nature* 409 (6819): 479–84. <https://doi.org/10.1038/35054000>.
- Harris, K.m., and P Sultan. 1995. "Variation in the Number, Location and Size of Synaptic Vesicles Provides an Anatomical Basis for the Nonuniform Probability of Release at Hippocampal CA1 Synapses." *Neuropharmacology* 34 (11): 1387–95. [https://doi.org/https://doi.org/10.1016/0028-3908\(95\)00142-S](https://doi.org/https://doi.org/10.1016/0028-3908(95)00142-S).
- Harris, Kristen M. 2020. "Structural LTP: From Synaptogenesis to Regulated Synapse Enlargement and Clustering." *Current Opinion in Neurobiology* 63: 189–97. <https://doi.org/10.1016/j.conb.2020.04.009>.
- Hata, Yutaka, Clive A. Slaughter, and Thomas C. Südhof. 1993. "Synaptic Vesicle Fusion Complex Contains Unc-18 Homologue Bound to Syntaxin." *Nature*. <https://doi.org/10.1038/366347a0>.
- Hatsuzawa, Kiyotaka, Thorsten Lang, Dirk Fasshauer, Dieter Bruns, and Reinhard Jahn. 2003. "The R-SNARE Motif of Tomosyn Forms SNARE Core Complexes with Syntaxin 1 and SNAP-25 and down-Regulates Exocytosis." *The Journal of Biological Chemistry* 278 (33): 31159–66. <https://doi.org/10.1074/jbc.M305500200>.
- Hebb DO. 1949. "The Organization of Behavior: A Neuropsychological Theory." *John Wiley*. https://pure.mpg.de/rest/items/item_2346268_3/component/file_2346267/content.
- Heilemann, Mike, Sebastian van de Linde, Mark Schüttpelz, Robert Kasper, Britta Seefeldt, Anindita Mukherjee, Philip Tinnefeld, and Markus Sauer. 2008. "Subdiffraction-Resolution Fluorescence Imaging with Conventional Fluorescent Probes." *Angewandte Chemie (International Ed. in English)* 47 (33): 6172–76. <https://doi.org/10.1002/anie.200802376>.
- Heilemann, Mike, Emmanuel Margeat, Robert Kasper, Markus Sauer, and Philip Tinnefeld. 2005. "Carbocyanine Dyes as Efficient Reversible Single-Molecule Optical Switch." *Journal of the American Chemical Society* 127 (11): 3801–6. <https://doi.org/10.1021/ja044686x>.
- Heilemann, Mike, Sebastian van de Linde, Anindita Mukherjee, and Markus Sauer. 2009. "Super-Resolution Imaging with Small Organic Fluorophores." *Angewandte Chemie International Edition* 48 (37): 6903–8. <https://doi.org/https://doi.org/10.1002/anie.200902073>.
- Heintzmann, Rainer. 2007. "Estimating Missing Information by Maximum Likelihood Deconvolution." *Micron (Oxford, England: 1993)* 38 (2): 136–44. <https://doi.org/10.1016/j.micron.2006.07.009>.
- Heintzmann, Rainer, and Christoph G Cremer. 1999. "Laterally Modulated Excitation

7. References

- Microscopy: Improvement of Resolution by Using a Diffraction Grating.” In *Optical Biopsies and Microscopic Techniques III*, edited by Irving J Bigio, Herbert Schneckenburger, Jan Slavik, Katarina Svanberg M.D., and Pierre M Viallet, 3568:185–96. SPIE. <https://doi.org/10.1117/12.336833>.
- Heintzmann, Rainer, and Thomas Huser. 2017. “Super-Resolution Structured Illumination Microscopy.” *Chemical Reviews* 117 (23): 13890–908. <https://doi.org/10.1021/acs.chemrev.7b00218>.
- Hell, S W, and J Wichmann. 1994. “Breaking the Diffraction Resolution Limit by Stimulated Emission: Stimulated-Emission-Depletion Fluorescence Microscopy.” *Optics Letters* 19 (11): 780–82. <https://doi.org/10.1364/ol.19.000780>.
- Hell, Stefan W. 2007. “Far-Field Optical Nanoscopy.” *Science* 316 (5828): 1153 LP – 1158. <https://doi.org/10.1126/science.1137395>.
- Hess, Samuel T, Thanu P K Girirajan, and Michael D Mason. 2006. “Ultra-High Resolution Imaging by Fluorescence Photoactivation Localization Microscopy.” *Biophysical Journal* 91 (11): 4258–72. <https://doi.org/10.1529/biophysj.106.091116>.
- Heuser, J. E., and T. S. Reese. 1973. “Evidence for Recycling of Synaptic Vesicle Membrane during Transmitter Release at the Frog Neuromuscular Junction.” *Journal of Cell Biology* 57 (2): 315–44. <https://doi.org/10.1083/jcb.57.2.315>.
- Heuser, J. E., T. S. Reese, M. J. Dennis, Y. Jan, L. Jan, and L. Evans. 1979. “Synaptic Vesicle Exocytosis Captured by Quick Freezing and Correlated with Quantal Transmitter Release.” *Journal of Cell Biology* 81 (2): 275–300. <https://doi.org/10.1083/jcb.81.2.275>.
- Hibino, H, R Pironkova, O Onwumere, M Vologodskaja, A J Hudspeth, and F Lesage. 2002. “RIM Binding Proteins (RBPs) Couple Rab3-Interacting Molecules (RIMs) to Voltage-Gated Ca(2+) Channels.” *Neuron* 34 (3): 411–23. [https://doi.org/10.1016/s0896-6273\(02\)00667-0](https://doi.org/10.1016/s0896-6273(02)00667-0).
- Hida, Yamato, and Toshihisa Ohtsuka. 2010. “CAST and ELKS Proteins: Structural and Functional Determinants of the Presynaptic Active Zone.” *Journal of Biochemistry* 148 (2): 131–37. <https://doi.org/10.1093/jb/mvq065>.
- Ho, N, J A Liauw, F Blaeser, F Wei, S Hanissian, L M Muglia, D F Wozniak, et al. 2000. “Impaired Synaptic Plasticity and cAMP Response Element-Binding Protein Activation in Ca²⁺/Calmodulin-Dependent Protein Kinase Type IV/Gr-Deficient Mice.” *The Journal of Neuroscience : The Official Journal of the Society for Neuroscience* 20 (17): 6459–72. <https://doi.org/10.1523/JNEUROSCI.20-17-06459.2000>.
- Hofmann, Michael, Christian Eggeling, Stefan Jakobs, and Stefan W Hell. 2005. “Breaking the Diffraction Barrier in Fluorescence Microscopy at Low Light Intensities by Using Reversibly Photoswitchable Proteins.” *Proceedings of the National Academy of Sciences of the United States of America* 102 (49): 17565 LP – 17569. <https://doi.org/10.1073/pnas.0506010102>.
- Holahan, Matthew R, Jerome L Rekart, Jimena Sandoval, and Aryeh Routtenberg. 2006. “Spatial Learning Induces Presynaptic Structural Remodeling in the Hippocampal Mossy Fiber System of Two Rat Strains.” *Hippocampus* 16 (6): 560–70. <https://doi.org/10.1002/hipo.20185>.
- Höpener, C, J P Siebrasse, R Peters, U Kubitscheck, and A Naber. 2005. “High-Resolution Near-Field Optical Imaging of Single Nuclear Pore Complexes under Physiological Conditions.” *Biophysical Journal* 88 (5): 3681–88. <https://doi.org/10.1529/biophysj.104.051458>.
- Huang, Bo, Sara A Jones, Boerries Brandenburg, and Xiaowei Zhuang. 2008. “Whole-Cell 3D STORM Reveals Interactions between Cellular Structures with Nanometer-Scale Resolution.” *Nature Methods* 5 (12): 1047–52. <https://doi.org/10.1038/nmeth.1274>.
- Huang, Y Y, and E R Kandel. 1994. “Recruitment of Long-Lasting and Protein Kinase A-Dependent Long-Term Potentiation in the CA1 Region of Hippocampus Requires

7. References

- Repeated Tetanization.” *Learning & Memory (Cold Spring Harbor, N.Y.)* 1 (1): 74–82.
- Huang, Yan You, Xiao Ching Li, and Eric R. Kandel. 1994. “CAMP Contributes to Mossy Fiber LTP by Initiating Both a Covalently Mediated Early Phase and Macromolecular Synthesis-Dependent Late Phase.” *Cell* 79 (1): 69–79. [https://doi.org/10.1016/0092-8674\(94\)90401-4](https://doi.org/10.1016/0092-8674(94)90401-4).
- Huerta, P T, and J E Lisman. 1995. “Bidirectional Synaptic Plasticity Induced by a Single Burst during Cholinergic Theta Oscillation in CA1 in Vitro.” *Neuron* 15 (5): 1053–63. [https://doi.org/10.1016/0896-6273\(95\)90094-2](https://doi.org/10.1016/0896-6273(95)90094-2).
- Ibrahim, Mohammad Zaki Bin, Amrita Benoy, and Sreedharan Sajikumar. 2021. “Long-term Plasticity in the Hippocampus: Maintaining within and ‘Tagging’ between Synapses.” *The FEBS Journal*, 1–26. <https://doi.org/10.1111/febs.16065>.
- Imig, Cordelia, Francisco José López-Murcia, Lydia Maus, Inés Hojas García-Plaza, Lena Sünke Mortensen, Manuela Schwark, Valentin Schwarze, et al. 2020. “Ultrastructural Imaging of Activity-Dependent Synaptic Membrane-Trafficking Events in Cultured Brain Slices.” *Neuron* 108 (5): 843-860.e8. <https://doi.org/10.1016/j.neuron.2020.09.004>.
- Ivanova, Daniela, Anika Dirks, Carolina Montenegro-Venegas, Cornelia Schöne, Wilko D Altrock, Claudia Marini, Renato Frischknecht, et al. 2015. “Synaptic Activity Controls Localization and Function of Ct BP 1 via Binding to Bassoon and P Iccolo .” *The EMBO Journal* 34 (8): 1056–77. <https://doi.org/10.15252/embj.201488796>.
- Jahn, Reinhard, and Dirk Fasshauer. 2012. “Molecular Machines Governing Exocytosis of Synaptic Vesicles.” *Nature* 490 (7419): 201–7. <https://doi.org/10.1038/nature11320>.
- Jiao, Wei, Sergej Masich, Oscar Franzén, and Oleg Shupliakov. 2010. “Two Pools of Vesicles Associated with the Presynaptic Cytosolic Projection in Drosophila Neuromuscular Junctions.” *Journal of Structural Biology* 172 (3): 389–94. <https://doi.org/10.1016/j.jsb.2010.07.007>.
- Jin, Yishi. 2005. “Synaptogenesis.” *WormBook : The Online Review of C. Elegans Biology*, December, 1–11. <https://doi.org/10.1895/wormbook.1.44.1>.
- Jing, Zhizi, Mark A. Rutherford, Hideki Takago, Thomas Frank, Anna Fejtova, Darina Khimich, Tobias Moser, and Nicola Strenzke. 2013. “Disruption of the Presynaptic Cytomatrix Protein Bassoon Degrades Ribbon Anchorage, Multiquantal Release, and Sound Encoding at the Hair Cell Afferent Synapse.” *Journal of Neuroscience* 33 (10): 4456–67. <https://doi.org/10.1523/JNEUROSCI.3491-12.2013>.
- Junge, Harald J., Jeong Seop Rhee, Olaf Jahn, Frederique Varoqueaux, Joachim Spiess, M. Neal Waxham, Christian Rosenmund, and Nils Brose. 2004. “Calmodulin and Munc13 Form a Ca²⁺ Sensor/Effector Complex That Controls Short-Term Synaptic Plasticity.” *Cell* 118 (3): 389–401. <https://doi.org/10.1016/j.cell.2004.06.029>.
- Kaesler, Pascal S., Lunbin Deng, Mingming Fan, and Thomas C. Südhof. 2012. “RIM Genes Differentially Contribute to Organizing Presynaptic Release Sites.” *Proceedings of the National Academy of Sciences of the United States of America*. <https://doi.org/10.1073/pnas.1209318109>.
- Kaesler, Pascal S., Lunbin Deng, Yun Wang, Irina Dulubova, Xinran Liu, Josep Rizo, and Thomas C. Südhof. 2011. “RIM Proteins Tether Ca²⁺ Channels to Presynaptic Active Zones via a Direct PDZ-Domain Interaction.” *Cell* 144 (2): 282–95. <https://doi.org/10.1016/j.cell.2010.12.029>.
- Kaesler, Pascal S., and Wade G. Regehr. 2014. “Molecular Mechanisms for Synchronous, Asynchronous, and Spontaneous Neurotransmitter Release.” *Annual Review of Physiology* 76 (1): 333–63. <https://doi.org/10.1146/annurev-physiol-021113-170338>.
- Kandel, E R. 2001. “The Molecular Biology of Memory Storage: A Dialogue between Genes and Synapses.” *Science (New York, N.Y.)* 294 (5544): 1030–38. <https://doi.org/10.1126/science.1067020>.
- KANDEL, E R, and W A SPENCER. 1961. “Electrophysiology of Hippocampal Neurons. II.

7. References

- After-Potentials and Repetitive Firing.” *Journal of Neurophysiology* 24 (May): 243–59. <https://doi.org/10.1152/jn.1961.24.3.243>.
- KANDEL, E R, W A SPENCER, and F J Jr BRINLEY. 1961. “Electrophysiology of Hippocampal Neurons. I. Sequential Invasion and Synaptic Organization.” *Journal of Neurophysiology* 24 (May): 225–42. <https://doi.org/10.1152/jn.1961.24.3.225>.
- Kandel, Eric R. 1976. *Cellular Basis of Behavior: An Introduction to Behavioral Neurobiology*. Edited by San Fransisco. W.H. Freeman.
- Katz, B. 1969. *Release of Neural Transmitter Substances*. Liverpool Univ Press, Liverpool, U.K.
- Kemp, M, P Roberts, P Pook, D Jane, A Jones, P Jones, D Sunter, P Udvarhelyi, and J Watkins. 1994. “Antagonism of Presynaptically Mediated Depressant Responses and Cyclic AMP-Coupled Metabotropic Glutamate Receptors.” *European Journal of Pharmacology* 266 (2): 187–92. [https://doi.org/10.1016/0922-4106\(94\)90109-0](https://doi.org/10.1016/0922-4106(94)90109-0).
- Khater, Ismail M., Ivan Robert Nabi, and Ghassan Hamarneh. 2020. “A Review of Super-Resolution Single-Molecule Localization Microscopy Cluster Analysis and Quantification Methods.” *Patterns* 1 (3): 100038. <https://doi.org/10.1016/j.patter.2020.100038>.
- Khimich, Darina, Régis Nouvian, Rémy Pujol, Susanne tom Dieck, Alexander Egner, Eckart D Gundelfinger, and Tobias Moser. 2005. “Hair Cell Synaptic Ribbons Are Essential for Synchronous Auditory Signalling.” *Nature* 434 (7035): 889–94. <https://doi.org/10.1038/nature03418>.
- Kirkwood, Alfredo, Marika G Rioult, and Mark F Bear. 1996. “Experience-Dependent Modification of Synaptic Plasticity in Visual Cortex.” *Nature* 381 (6582): 526–28. <https://doi.org/10.1038/381526a0>.
- Kittel, Robert J., and Manfred Heckmann. 2016. “Synaptic Vesicle Proteins and Active Zone Plasticity.” *Frontiers in Synaptic Neuroscience* 8 (APR): 1–8. <https://doi.org/10.3389/fnsyn.2016.00008>.
- Kiyonaka, Shigeki, Minoru Wakamori, Takafumi Miki, Yoshitsugu Uriu, Mio Nonaka, Haruhiko Bito, Aaron M. Beedle, et al. 2007. “RIM1 Confers Sustained Activity and Neurotransmitter Vesicle Anchoring to Presynaptic Ca²⁺ Channels.” *Nature Neuroscience* 10 (6): 691–701. <https://doi.org/10.1038/nn1904>.
- Klar, T A, S Jakobs, M Dyba, A Egner, and S W Hell. 2000. “Fluorescence Microscopy with Diffraction Resolution Barrier Broken by Stimulated Emission.” *Proceedings of the National Academy of Sciences of the United States of America* 97 (15): 8206–10. <https://doi.org/10.1073/pnas.97.15.8206>.
- Kner, Peter, Bryant B Chhun, Eric R Griffis, Lukman Winoto, and Mats G L Gustafsson. 2009. “Super-Resolution Video Microscopy of Live Cells by Structured Illumination.” *Nature Methods* 6 (5): 339–42. <https://doi.org/10.1038/nmeth.1324>.
- Ko, Jaewon, Moonseok Na, Seho Kim, Jae Ran Lee, and Eunjoon Kim. 2003. “Interaction of the ERC Family of RIM-Binding Proteins with the Liprin- α Family of Multidomain Proteins.” *Journal of Biological Chemistry* 278 (43): 42377–85. <https://doi.org/10.1074/jbc.M307561200>.
- Koch, Henriette, Kay Hofmann, and Nils Brose. 2000. “Definition of Munc13-Homology-Domains and Characterization of a Novel Ubiquitously Expressed Munc13 Isoform.” *Biochemical Journal* 349 (1): 247–53. <https://doi.org/10.1042/0264-6021:3490247>.
- Koster, Abraham J, and Judith Klumperman. 2003. “Electron Microscopy in Cell Biology: Integrating Structure and Function.” *Nature Reviews. Molecular Cell Biology Suppl* (September): SS6-10.
- Koushika, Sandhya P., Janet E. Richmond, Gayla Hadwiger, Robby M. Weimer, Erik M. Jorgensen, and Michael L. Nonet. 2001. “A Post-Docking Role for Active Zone Protein Rim.” *Nature Neuroscience*. <https://doi.org/10.1038/nn732>.
- Kusch, Valentin, Grit Bornschein, Desiree Loreth, Julia Bank, Johannes Jordan, David Baur,

7. References

- Masahiko Watanabe, et al. 2018. “Munc13-3 Is Required for the Developmental Localization of Ca²⁺ Channels to Active Zones and the Nanopositioning of Cav2.1 Near Release Sensors.” *Cell Reports* 22 (8): 1965–73. <https://doi.org/https://doi.org/10.1016/j.celrep.2018.02.010>.
- Lange, F de, A Cambi, R Huijbens, B de Bakker, W Rensen, M Garcia-Parajo, N van Hulst, and C G Figdor. 2001. “Cell Biology beyond the Diffraction Limit: Near-Field Scanning Optical Microscopy.” *Journal of Cell Science* 114 (Pt 23): 4153–60.
- Langnaese, Kristina, Constanze Seidenbecher, Heike Wex, Bert Seidel, Kathrin Hartung, Ute Appeltauer, Abigail Garner, et al. 1996. “Protein Components of a Rat Brain Synaptic Junctional Protein Preparation.” *Molecular Brain Research* 42 (1): 118–22. [https://doi.org/https://doi.org/10.1016/S0169-328X\(96\)00147-7](https://doi.org/https://doi.org/10.1016/S0169-328X(96)00147-7).
- Lanore, Frederic, Christophe Blanchet, Anna Fejtova, Paulo Pinheiro, Karin Richter, Detlef Balschun, Eckart Gundelfinger, and Christophe Mulle. 2010. “Impaired Development of Hippocampal Mossy Fibre Synapses in Mouse Mutants for the Presynaptic Scaffold Protein Bassoon.” *The Journal of Physiology* 588 (12): 2133–45. <https://doi.org/https://doi.org/10.1113/jphysiol.2009.184929>.
- Lassalle, J M, T Bataille, and H Halley. 2000. “Reversible Inactivation of the Hippocampal Mossy Fiber Synapses in Mice Impairs Spatial Learning, but Neither Consolidation nor Memory Retrieval, in the Morris Navigation Task.” *Neurobiology of Learning and Memory* 73 (3): 243–57. <https://doi.org/10.1006/nlme.1999.3931>.
- Lewis, Aaron, Hesham Taha, Alina Strinkovski, Alexandra Manevitch, Artium Khatchatourians, Rima Dekhter, and Erich Ammann. 2003. “Near-Field Optics: From Subwavelength Illumination to Nanometric Shadowing.” *Nature Biotechnology* 21 (11): 1378–86. <https://doi.org/10.1038/nbt898>.
- Lichtman, Jeff W, and José-Angel Conchello. 2005. “Fluorescence Microscopy.” *Nature Methods* 2 (12): 910–19. <https://doi.org/10.1038/nmeth817>.
- Lichtman, Jeff W, and Winfried Denk. 2011. “The Big and the Small: Challenges of Imaging the Brain’s Circuits.” *Science* 334 (6056): 618 LP – 623. <https://doi.org/10.1126/science.1209168>.
- Limbach, Christoph, Michael M. Laue, Xiaolu Wang, Bin Hu, Nadine Thiede, Greta Hultqvist, and Manfred W. Kilimann. 2011. “Molecular in Situ Topology of Aczonin/Piccolo and Associated Proteins at the Mammalian Neurotransmitter Release Site.” *Proceedings of the National Academy of Sciences* 108 (31): E392–401. <https://doi.org/10.1073/pnas.1101707108>.
- Linde, Sebastian van de, Anna Löschberger, Teresa Klein, Meike Heidbreder, Steve Wolter, Mike Heilemann, and Markus Sauer. 2011. “Direct Stochastic Optical Reconstruction Microscopy with Standard Fluorescent Probes.” *Nature Protocols* 6 (7): 991–1009. <https://doi.org/10.1038/nprot.2011.336>.
- Lisman, John. 2003. “Long-Term Potentiation: Outstanding Questions and Attempted Synthesis.” *Philosophical Transactions of the Royal Society of London. Series B, Biological Sciences* 358 (1432): 829–42. <https://doi.org/10.1098/rstb.2002.1242>.
- Lisman, John, Ryohei Yasuda, and Sridhar Raghavachari. 2012. “Mechanisms of CaMKII Action in Long-Term Potentiation.” *Nature Reviews. Neuroscience* 13 (3): 169–82. <https://doi.org/10.1038/nrn3192>.
- Liu, Karen S Y, Matthias Siebert, Sara Mertel, Elena Knoche, Stephanie Wegener, Carolin Wichmann, Tanja Matkovic, et al. 2011. “RIM-Binding Protein, a Central Part of the Active Zone, Is Essential for Neurotransmitter Release.” *Science (New York, N.Y.)* 334 (6062): 1565–69. <https://doi.org/10.1126/science.1212991>.
- Llinás, R., I. Z. Steinberg, and K. Walton. 1981. “Relationship between Presynaptic Calcium Current and Postsynaptic Potential in Squid Giant Synapse.” *Biophysical Journal* 33 (3): 323–51. [https://doi.org/10.1016/S0006-3495\(81\)84899-0](https://doi.org/10.1016/S0006-3495(81)84899-0).

7. References

- Loewi, O. 1921. "Über Humorale Übertragbarkeit Der Herznervenwirkung: Vorläufige Mitteilung." *Pflüger's Archiv Für Die Gesamte Physiologie Des Menschen Und Der Tiere* 207 (1): 1–7. <https://doi.org/10.1007/BF01740326>.
- Ma, Cong, Wei Li, Yibin Xu, and Josep Rizo. 2011. "Munc13 Mediates the Transition from the Closed Syntaxin-Munc18 Complex to the SNARE Complex." *Nature Structural & Molecular Biology* 18 (5): 542–49. <https://doi.org/10.1038/nsmb.2047>.
- Ma, Cong, Lijing Su, Alpay B Seven, Yibin Xu, and Josep Rizo. 2013. "Reconstitution of the Vital Functions of Munc18 and Munc13 in Neurotransmitter Release." *Science (New York, N.Y.)* 339 (6118): 421–25. <https://doi.org/10.1126/science.1230473>.
- Ma, Ying, Kai Wen, Min Liu, Juanjuan Zheng, Kaiqin Chu, Zachary J. Smith, Lixin Liu, and Peng Gao. 2021. "Recent Advances in Structured Illumination Microscopy." *JPhys Photonics* 3 (2). <https://doi.org/10.1088/2515-7647/abdb04>.
- Maccaferri, Gianmaria, Katalin Tóth, and Chris J McBain. 1998. "Target-Specific Expression of Presynaptic Mossy Fiber Plasticity." *Science* 279 (5355): 1368 LP – 1371. <https://doi.org/10.1126/science.279.5355.1368>.
- Malenka, Robert C., and Mark F. Bear. 2004. "LTP and LTD: An Embarrassment of Riches." *Neuron* 44 (1): 5–21. <https://doi.org/10.1016/j.neuron.2004.09.012>.
- Martin, S J, P D Grimwood, and R G Morris. 2000. "Synaptic Plasticity and Memory: An Evaluation of the Hypothesis." *Annual Review of Neuroscience* 23: 649–711. <https://doi.org/10.1146/annurev.neuro.23.1.649>.
- Maus, Lydia, ChoongKu Ku Lee, Bekir Altas, Sinem M. Sertel, Kirsten Weyand, Silvio O. Rizzoli, JeongSeop Seop Rhee, Nils Brose, Cordelia Imig, and Benjamin H. Cooper. 2020. "Ultrastructural Correlates of Presynaptic Functional Heterogeneity in Hippocampal Synapses." *Cell Reports* 30 (11): 3632–3643.e8. <https://doi.org/10.1016/j.celrep.2020.02.083>.
- Meador, Kimford J. 2007. "The Basic Science of Memory as It Applies to Epilepsy." *Epilepsia* 48 (SUPPL. 9): 23–25. <https://doi.org/10.1111/j.1528-1167.2007.01396.x>.
- Meinertzhagen, I. A., C. K. Govind, B. A. Stewart, J. M. Carter, and H. L. Atwood. 1998. "Regulated Spacing of Synapses and Presynaptic Active Zones at Larval Neuromuscular Junctions in Different Genotypes of the Flies *Drosophila* and *Sarcophaga*." *Journal of Comparative Neurology* 393 (4): 482–92. [https://doi.org/10.1002/\(SICI\)1096-9861\(19980420\)393:4<482::AID-CNE7>3.0.CO;2-X](https://doi.org/10.1002/(SICI)1096-9861(19980420)393:4<482::AID-CNE7>3.0.CO;2-X).
- Mendoza Schulz, Alejandro, Zhizi Jing, Juan María Sánchez Caro, Friederike Wetzel, Thomas Dresbach, Nicola Strenzke, Carolin Wichmann, and Tobias Moser. 2014. "Bassoon-Disruption Slows Vesicle Replenishment and Induces Homeostatic Plasticity at a CNS Synapse." *EMBO Journal* 33 (5): 512–27. <https://doi.org/10.1002/emboj.201385887>.
- Michel, Katrin, Johannes Alexander Müller, Ana Maria Opreașoreanu, and Susanne Schoch. 2015. "The Presynaptic Active Zone: A Dynamic Scaffold That Regulates Synaptic Efficacy." *Experimental Cell Research* 335 (2): 157–64. <https://doi.org/10.1016/j.yexcr.2015.02.011>.
- Midorikawa, Mitsuharu, and Takeshi Sakaba. 2017. "Kinetics of Releasable Synaptic Vesicles and Their Plastic Changes at Hippocampal Mossy Fiber Synapses." *Neuron* 96 (5): 1033–1040.e3. <https://doi.org/10.1016/j.neuron.2017.10.016>.
- Mikula, Shawn, Issac Trotts, James M Stone, and Edward G Jones. 2007. "Internet-Enabled High-Resolution Brain Mapping and Virtual Microscopy." *NeuroImage* 35 (1): 9–15. <https://doi.org/10.1016/j.neuroimage.2006.11.053>.
- Misura, Kira M.S., Richard H. Scheller, and William I. Weis. 2000. "Three-Dimensional Structure of the Neuronal-Sec1-Syntaxin 1a Complex." *Nature*. <https://doi.org/10.1038/35006120>.
- Mlodzianoski, Michael J, Paul J Cheng-Hathaway, Shane M Bemiller, Tyler J McCray, Sheng Liu, David A Miller, Bruce T Lamb, Gary E Landreth, and Fang Huang. 2018. "Active

7. References

- PSF Shaping and Adaptive Optics Enable Volumetric Localization Microscopy through Brain Sections.” *Nature Methods* 15 (8): 583–86. <https://doi.org/10.1038/s41592-018-0053-8>.
- Moore, C I, M D Browning, and G M Rose. 1993. “Hippocampal Plasticity Induced by Primed Burst, but Not Long-Term Potentiation, Stimulation Is Impaired in Area CA1 of Aged Fischer 344 Rats.” *Hippocampus* 3 (1): 57–66. <https://doi.org/10.1002/hipo.450030106>.
- Morris, R G. 1989. “Synaptic Plasticity and Learning: Selective Impairment of Learning Rats and Blockade of Long-Term Potentiation in Vivo by the N-Methyl-D-Aspartate Receptor Antagonist AP5.” *The Journal of Neuroscience : The Official Journal of the Society for Neuroscience* 9 (9): 3040–57. <https://doi.org/10.1523/JNEUROSCI.09-09-03040.1989>.
- Morris, Richard G M. 2013. “NMDA Receptors and Memory Encoding.” *Neuropharmacology* 74 (November): 32–40. <https://doi.org/10.1016/j.neuropharm.2013.04.014>.
- Müller, Claus B, and Jörg Enderlein. 2010. “Image Scanning Microscopy.” *Physical Review Letters* 104 (19): 198101. <https://doi.org/10.1103/PhysRevLett.104.198101>.
- Nägerl, U Valentin, Katrin I Willig, Birka Hein, Stefan W Hell, and Tobias Bonhoeffer. 2008. “Live-Cell Imaging of Dendritic Spines by STED Microscopy.” *Proceedings of the National Academy of Sciences* 105 (48): 18982 LP – 18987. <https://doi.org/10.1073/pnas.0810028105>.
- Nagwaney, Sharuna, Mark Lee Harlow, Jae Hoon Jung, Joseph A. Szule, David Ress, Jing Xu, Robert M. Marshall, and Uel Jackson McMahan. 2009. “Macromolecular Connections of Active Zone Material to Docked Synaptic Vesicles and Presynaptic Membrane at Neuromuscular Junctions of Mouse.” *Journal of Comparative Neurology* 513 (5): 457–68. <https://doi.org/10.1002/cne.21975>.
- Nakashiba, Toshiaki, Jesse D Cushman, Kenneth A Pelkey, Sophie Renaudineau, Derek L Buhl, Thomas J McHugh, Vanessa Rodriguez Barrera, et al. 2012. “Young Dentate Granule Cells Mediate Pattern Separation, Whereas Old Granule Cells Facilitate Pattern Completion.” *Cell* 149 (1): 188–201. <https://doi.org/10.1016/j.cell.2012.01.046>.
- Navakkode, Sheeja, Sreedharan Sajikumar, and Julietta Uta Frey. 2007. “Synergistic Requirements for the Induction of Dopaminergic D1/D5-Receptor-Mediated LTP in Hippocampal Slices of Rat CA1 in Vitro.” *Neuropharmacology* 52 (7): 1547–54. <https://doi.org/10.1016/j.neuropharm.2007.02.010>.
- Navakkode, Sheeja, Sreedharan Sajikumar, Martin Korte, and Tuck Wah Soong. 2012. “Dopamine Induces LTP Differentially in Apical and Basal Dendrites through BDNF and Voltage-Dependent Calcium Channels.” *Learning & Memory (Cold Spring Harbor, N.Y.)* 19 (7): 294–99. <https://doi.org/10.1101/lm.026203.112>.
- Navakkode, Sheeja, Sreedharan Sajikumar, Todd Charlton Sacktor, and Julietta U Frey. 2010. “Protein Kinase Mzeta Is Essential for the Induction and Maintenance of Dopamine-Induced Long-Term Potentiation in Apical CA1 Dendrites.” *Learning & Memory (Cold Spring Harbor, N.Y.)* 17 (12): 605–11. <https://doi.org/10.1101/lm.1991910>.
- Nicholas P. Vyleta and Peter Jonas. 2014. “Loose Coupling Between Ca²⁺ Channels and Release Sensors at a Plastic Hippocampal Synapse Nicholas.” *Science* 343 (February): 665–70.
- Nicoll, R A, and R C Malenka. 1999. “Expression Mechanisms Underlying NMDA Receptor-Dependent Long-Term Potentiation.” *Annals of the New York Academy of Sciences* 868 (April): 515–25. <https://doi.org/10.1111/j.1749-6632.1999.tb11320.x>.
- Nicoll, Roger A., and Dietmar Schmitz. 2005. “Synaptic Plasticity at Hippocampal Mossy Fibre Synapses.” *Nature Reviews Neuroscience* 6 (11): 863–76. <https://doi.org/10.1038/nrn1786>.
- Nishimune, Hiroshi, Yomna Badawi, Shuuichi Mori, and Kazuhiro Shigemoto. 2016. “Dual-Color STED Microscopy Reveals a Sandwich Structure of Bassoon and Piccolo in Active Zones of Adult and Aged Mice.” *Scientific Reports* 6 (1): 27935.

7. References

- <https://doi.org/10.1038/srep27935>.
- Nishimune, Hiroshi, Joshua R Sanes, and Steven S Carlson. 2004. "A Synaptic Laminin-Calcium Channel Interaction Organizes Active Zones in Motor Nerve Terminals." *Nature* 432 (7017): 580–87. <https://doi.org/10.1038/nature03112>.
- "Nobel Prizes for Super-Resolution Imaging." 2014. *ACS Nano* 8 (10): 9689–90. <https://doi.org/10.1021/nn505967q>.
- Nosov, Georgii, Martin Kahms, and Jurgen Klingauf. 2020. "The Decade of Super-Resolution Microscopy of the Presynapse." *Frontiers in Synaptic Neuroscience* 12 (August): 1–17. <https://doi.org/10.3389/fnsyn.2020.00032>.
- Ohtsuka, Toshihisa, Etsuko Takao-Rikitsu, Eiji Inoue, Marie Inoue, Masakazu Takeuchi, Kaho Matsubara, Maki Deguchi-Tawarada, et al. 2002. "CAST: A Novel Protein of the Cytomatrix at the Active Zone of Synapses That Forms a Ternary Complex with RIM1 and Munc13-1." *Journal of Cell Biology* 158 (3): 577–90. <https://doi.org/10.1083/jcb.200202083>.
- Oldani, Silvia, Laura Moreno-Velasquez, Lukas Faiss, Alexander Stumpf, Christian Rosenmund, Dietmar Schmitz, and Benjamin R. Rost. 2021. "SynaptoPAC, an Optogenetic Tool for Induction of Presynaptic Plasticity." *Journal of Neurochemistry* 156 (3): 324–36. <https://doi.org/10.1111/jnc.15210>.
- Orlando, Marta, Anton Dvorzhak, Felicitas Bruentgens, Marta Maglione, Benjamin R. Rost, Stephan J. Sigrist, Jörg Breustedt, and Dietmar Schmitz. 2021. "Recruitment of Release Sites Underlies Chemical Presynaptic Potentiation at Hippocampal Mossy Fiber Boutons." *PLOS Biology* 19 (6): e3001149. <https://doi.org/10.1371/journal.pbio.3001149>.
- Otmakhov, N. 2004. "Forskolin-Induced LTP in the CA1 Hippocampal Region Is NMDA Receptor Dependent." *Journal of Neurophysiology* 91 (5): 1955–62. <https://doi.org/10.1152/jn.00941.2003>.
- Otto, C, Y Kovalchuk, D P Wolfer, P Gass, M Martin, W Zuschratter, H J Gröne, et al. 2001. "Impairment of Mossy Fiber Long-Term Potentiation and Associative Learning in Pituitary Adenylate Cyclase Activating Polypeptide Type I Receptor-Deficient Mice." *The Journal of Neuroscience : The Official Journal of the Society for Neuroscience* 21 (15): 5520–27. <https://doi.org/10.1523/JNEUROSCI.21-15-05520.2001>.
- Owald, David, Wernher Fouquet, Manuela Schmidt, Carolin Wichmann, Sara Mertel, Harald Depner, Frauke Christiansen, et al. 2010. "A Syd-1 Homologue Regulates Pre- and Postsynaptic Maturation in Drosophila." *Journal of Cell Biology* 188 (4): 565–79. <https://doi.org/10.1083/jcb.200908055>.
- Palay, Sanford L, and Victoria Chan-Palay. 2012. *Cerebellar Cortex: Cytology and Organization*. Springer Science & Business Media.
- Palmer, M. J., A. J. Irving, G. R. Seabrook, D. E. Jane, and G. L. Collingridge. 1997. "The Group I mGlu Receptor Agonist DHPG Induces a Novel Form of LTD in the CA1 Region of the Hippocampus." *Neuropharmacology* 36 (11–12): 1517–32. [https://doi.org/10.1016/S0028-3908\(97\)00181-0](https://doi.org/10.1016/S0028-3908(97)00181-0).
- Papouin, Thomas, and Philip Haydon. 2018. "Obtaining Acute Brain Slices." *Bio-Protocol* 8 (2): 1–12. <https://doi.org/10.21769/bioprotoc.2699>.
- Park, Pojeong, Heather Kang, Thomas M Sanderson, Zuner A Bortolotto, John Georgiou, Min Zhuo, Bong-Kiun Kaang, and Graham L Collingridge. 2019. "On the Role of Calcium-Permeable AMPARs in Long-Term Potentiation and Synaptic Tagging in the Rodent Hippocampus." *Frontiers in Synaptic Neuroscience*. <https://www.frontiersin.org/article/10.3389/fnsyn.2019.00004>.
- Pauli, Martin, Mila M. Paul, Sven Proppert, Achmed Mrestani, Marzieh Sharifi, Felix Repp, Lydia Kürzinger, et al. 2021. "Targeted Volumetric Single-Molecule Localization Microscopy of Defined Presynaptic Structures in Brain Sections." *Communications Biology* 4 (1): 1–13. <https://doi.org/10.1038/s42003-021-01939-z>.

7. References

- Pavlidis, C, Y J Greenstein, M Grudman, and J Winson. 1988. “Long-Term Potentiation in the Dentate Gyrus Is Induced Preferentially on the Positive Phase of Theta-Rhythm.” *Brain Research* 439 (1–2): 383–87. [https://doi.org/10.1016/0006-8993\(88\)91499-0](https://doi.org/10.1016/0006-8993(88)91499-0).
- Pfenninger, K., K. Akert, H. Moor, and C. Sandri. 1972. “The Fine Structure of Freeze-Fractured Presynaptic Membranes.” *Journal of Neurocytology* 149: 129–49. <https://doi.org/10.1007/BF01099180>.
- Phillips, Greg R., Jeffrey K. Huang, Yun Wang, Hidekazu Tanaka, Lawrence Shapiro, Wandong Zhang, Wei-song Song Shan, et al. 2001. “The Presynaptic Particle Web: Ultrastructure, Composition, Dissolution, and Reconstitution.” *Neuron* 32 (1): 63–77. [https://doi.org/10.1016/S0896-6273\(01\)00450-0](https://doi.org/10.1016/S0896-6273(01)00450-0).
- Pin, Jean-Philippe, and Francine Acher. 2002. “The Metabotropic Glutamate Receptors: Structure, Activation Mechanism and Pharmacology.” *Current Drug Targets. CNS and Neurological Disorders* 1 (3): 297–317. <https://doi.org/10.2174/1568007023339328>.
- Proppert, Sven, Steve Wolter, Thorge Holm, Teresa Klein, Sebastian van de Linde, and Markus Sauer. 2014. “Cubic B-Spline Calibration for 3D Super-Resolution Measurements Using Astigmatic Imaging.” *Optics Express* 22 (9): 10304. <https://doi.org/10.1364/OE.22.010304>.
- Pulido, Camila, and Alain Marty. 2017. “Quantal Fluctuations in Central Mammalian Synapses: Functional Role of Vesicular Docking Sites.” *Physiological Reviews* 97 (4): 1403–30. <https://doi.org/10.1152/physrev.00032.2016>.
- Ramon y Cajal, Santiago. 1894. “The Croonian Lecture.—La Fine Structure Des Centres Nerveux.” *Proceedings of the Royal Society of London* 55 (331–335): 444–68. <https://doi.org/10.1098/rspl.1894.0063>.
- Ramón y Cajal, Santiago. 1909. *Histologie Du Système Nerveux de l'homme & Des Vertébrés*. . Ed. frança. Vol. v. 1. Paris : Maloine,. <https://www.biodiversitylibrary.org/item/103261>.
- Rayleigh, Lord. 1903. “On the Theory of Optical Images, with Special Reference to the Microscope.” *Journal of the Royal Microscopical Society* 23 (4): 474–82. <https://doi.org/https://doi.org/10.1111/j.1365-2818.1903.tb04831.x>.
- Rebola, Nelson, Mario Carta, and Christophe Mulle. 2017. “Operation and Plasticity of Hippocampal CA3 Circuits: Implications for Memory Encoding.” *Nature Reviews Neuroscience* 18 (4): 209–21. <https://doi.org/10.1038/nrn.2017.10>.
- Rebola, Nelson, Maria Reva, Tekla Kirizs, Miklos Szoboszlai, Andrea Lőrincz, Gael Moneron, Zoltan Nusser, and David A. DiGregorio. 2019. “Distinct Nanoscale Calcium Channel and Synaptic Vesicle Topographies Contribute to the Diversity of Synaptic Function.” *Neuron* 104 (4): 693–710.e9. <https://doi.org/10.1016/j.neuron.2019.08.014>.
- Regus-Leidig, Hanna, Susanne tom Dieck, and Johann Helmut Brandstätter. 2010. “Absence of Functional Active Zone Protein Bassoon Affects Assembly and Transport of Ribbon Precursors during Early Steps of Photoreceptor Synaptogenesis.” *European Journal of Cell Biology* 89 (6): 468–75. <https://doi.org/https://doi.org/10.1016/j.ejcb.2009.12.006>.
- Reimer, Richard J., Katharina Schneider, Sergio Leal-Ortiz, Carolina Montenegro-Venegas, Sally A. Kim, Loren C. Garner, Eckart D. Gundelfinger, Richard J. Reimer, and Craig C. Garner. 2017. “Bassoon Controls Presynaptic Autophagy through Atg5.” *Neuron* 93 (4): 897–913.e7. <https://doi.org/10.1016/j.neuron.2017.01.026>.
- Ribrault, Claire, Ken Sekimoto, and Antoine Triller. 2011. “From the Stochasticity of Molecular Processes to the Variability of Synaptic Transmission.” *Nature Reviews Neuroscience* 12 (7): 375–87. <https://doi.org/10.1038/nrn3025>.
- Richmond, J. E., R. M. Weimer, and E. M. Jorgensen. 2001. “An Open Form of Syntaxin Bypasses the Requirement for UNC-13 in Vesicle Priming.” *Nature* 412 (6844): 338–41. <https://doi.org/10.1038/35085583>.
- Richmond, J E, W S Davis, and E M Jorgensen. 1999. “UNC-13 Is Required for Synaptic Vesicle Fusion in *C. Elegans*.” *Nature Neuroscience* 2 (11): 959–64.

7. References

- <https://doi.org/10.1038/14755>.
- Rollenhagen, A., K. Satzler, E. P. Rodriguez, P. Jonas, M. Frotscher, and J. H. R. Lübke. 2007. "Structural Determinants of Transmission at Large Hippocampal Mossy Fiber Synapses." *Journal of Neuroscience* 27 (39): 10434–44. <https://doi.org/10.1523/JNEUROSCI.1946-07.2007>.
- Rollenhagen, Astrid, and Joachim H R Lübke. 2010. "The Mossy Fiber Bouton: The 'Common' or the 'Unique' Synapse?" *Frontiers in Synaptic Neuroscience* 2 (MAR): 1–9. <https://doi.org/10.3389/fnsyn.2010.00002>.
- Rose, G M, and T V Dunwiddie. 1986. "Induction of Hippocampal Long-Term Potentiation Using Physiologically Patterned Stimulation." *Neuroscience Letters* 69 (3): 244–48. [https://doi.org/10.1016/0304-3940\(86\)90487-8](https://doi.org/10.1016/0304-3940(86)90487-8).
- Rosenmund, Christian, Jens Rettig, and Nils Brose. 2003. "Molecular Mechanisms of Active Zone Function." *Current Opinion in Neurobiology* 13 (5): 509–19. <https://doi.org/10.1016/j.conb.2003.09.011>.
- Rosenmund, Christian, Albrecht Sigler, Iris Augustin, Kerstin Reim, Nils Brose, and Jeong Seop Rhee. 2002. "Differential Control of Vesicle Priming and Short-Term Plasticity by Munc13 Isoforms." *Neuron* 33 (3): 411–24. [https://doi.org/10.1016/s0896-6273\(02\)00568-8](https://doi.org/10.1016/s0896-6273(02)00568-8).
- Routtenberg, Aryeh. 2010. "Adult Learning and Remodeling of Hippocampal Mossy Fibers: Unheralded Participant in Circuitry for Long-Lasting Spatial Memory." *Hippocampus* 20 (1): 44–45. <https://doi.org/10.1002/hipo.20664>.
- Ruediger, Sarah, Claudia Vittori, Ewa Bednarek, Christel Genoud, Piergiorgio Strata, Benedetto Sacchetti, and Pico Caroni. 2011. "Learning-Related Feedforward Inhibitory Connectivity Growth Required for Memory Precision." *Nature* 473 (7348): 514–18. <https://doi.org/10.1038/nature09946>.
- Rust, Michael J, Mark Bates, and Xiaowei Zhuang. 2006. "Sub-Diffraction-Limit Imaging by Stochastic Optical Reconstruction Microscopy (STORM)." *Nature Methods* 3 (10): 793–96. <https://doi.org/10.1038/nmeth929>.
- Ryan, Joel, Abby R Gerhold, Vincent Boudreau, Lydia Smith, and Paul S Maddox. 2017. "Introduction to Modern Methods in Light Microscopy." *Methods in Molecular Biology (Clifton, N.J.)* 1563: 1–15. https://doi.org/10.1007/978-1-4939-6810-7_1.
- Sacktor, T C, P Osten, H Valsamis, X Jiang, M U Naik, and E Sublette. 1993. "Persistent Activation of the Zeta Isoform of Protein Kinase C in the Maintenance of Long-Term Potentiation." *Proceedings of the National Academy of Sciences of the United States of America* 90 (18): 8342–46. <https://doi.org/10.1073/pnas.90.18.8342>.
- Sajikumar, Sreedharan, and Martin Korte. 2011. "Metaplasticity Governs Compartmentalization of Synaptic Tagging and Capture through Brain-Derived Neurotrophic Factor (BDNF) and Protein Kinase Mζ (PKMζ)." *Proceedings of the National Academy of Sciences* 108 (6): 2551 LP – 2556. <https://doi.org/10.1073/pnas.1016849108>.
- Sakamoto, Hirokazu, Tetsuroh Ariyoshi, Naoya Kimpara, Kohtaroh Sugao, Isamu Taiko, Kenji Takikawa, Daisuke Asanuma, Shigeyuki Namiki, and Kenzo Hirose. 2018. "Synaptic Weight Set by Munc13-1 Supramolecular Assemblies." *Nature Neuroscience* 21 (1): 41–49. <https://doi.org/10.1038/s41593-017-0041-9>.
- Salin, P A, M Scanziani, Robert C. Malenka, Roger A. Nicoll, Christoph Schmidt-hieber, Peter Jonas, Josef Bischofberger, et al. 1996. "Distinct Short-Term Plasticity at Two Excitatory Synapses in the Hippocampus." *Proceedings of the National Academy of Sciences of the United States of America* 93 (23): 13304–9. <https://doi.org/10.1073/pnas.93.23.13304>.
- Sätzler, Kurt, Leander F. Söhl, Johann H. Bollmann, J. Gerard G. Borst, Michael Frotscher, Bert Sakmann, and Joachim H.R. Lübke. 2002. "Three-Dimensional Reconstruction of a Calyx of Held and Its Postsynaptic Principal Neuron in the Medial Nucleus of the

7. References

- Trapezoid Body.” *Journal of Neuroscience* 22 (24): 10567–79. <https://doi.org/10.1523/jneurosci.22-24-10567.2002>.
- Sauer, Markus. 2013. “Localization Microscopy Coming of Age: From Concepts to Biological Impact.” *Journal of Cell Science* 126 (16): 3505–13. <https://doi.org/10.1242/jcs.123612>.
- Sauer, Markus, and Mike Heilemann. 2017. “Single-Molecule Localization Microscopy in Eukaryotes.” *Chemical Reviews* 117 (11): 7478–7509. <https://doi.org/10.1021/acs.chemrev.6b00667>.
- Scannevin, R H, and R L Haganir. 2000. “Postsynaptic Organization and Regulation of Excitatory Synapses.” *Nature Reviews. Neuroscience* 1 (2): 133–41. <https://doi.org/10.1038/35039075>.
- Schermelleh, Lothar, Peter M Carlton, Sebastian Haase, Lin Shao, Lukman Winoto, Peter Kner, Brian Burke, et al. 2008. “Subdiffraction Multicolor Imaging of the Nuclear Periphery with 3D Structured Illumination Microscopy.” *Science* 320 (5881): 1332 LP – 1336. <https://doi.org/10.1126/science.1156947>.
- Schermelleh, Lothar, Alexia Ferrand, Thomas Huser, Christian Eggeling, Markus Sauer, Oliver Biehlmaier, and Gregor P C Drummen. 2019. “Super-Resolution Microscopy Demystified.” *Nature Cell Biology* 21 (1): 72–84. <https://doi.org/10.1038/s41556-018-0251-8>.
- Schermelleh, Lothar, Rainer Heintzmann, and Heinrich Leonhardt. 2010. “A Guide to Super-Resolution Fluorescence Microscopy.” *Journal of Cell Biology* 190 (2): 165–75. <https://doi.org/10.1083/jcb.201002018>.
- Schikorski, T, and C F Stevens. 1997. “Quantitative Ultrastructural Analysis of Hippocampal Excitatory Synapses.” *The Journal of Neuroscience : The Official Journal of the Society for Neuroscience* 17 (15): 5858–67. <https://doi.org/10.1523/JNEUROSCI.17-15-05858.1997>.
- Schneggenburger, Ralf, and Erwin Neher. 2005. “Presynaptic Calcium and Control of Vesicle Fusion.” *Current Opinion in Neurobiology* 15 (3): 266–74. <https://doi.org/10.1016/j.conb.2005.05.006>.
- Schoch, Susanne, Pablo E. Castillo, Tobias Jo, Konark Mukherjee, Martin Geppert, Yun Wang, Frank Schmitz, Robert C. Malenka, and Thomas C. Südhof. 2002. “RIM1 α Forms a Protein Scaffold for Regulating Neurotransmitter Release at the Active Zone.” *Nature*. <https://doi.org/10.1038/415321a>.
- Schoch, Susanne, and Eckart D. Gundelfinger. 2006. “Molecular Organization of the Presynaptic Active Zone.” *Cell and Tissue Research* 326 (2): 379–91. <https://doi.org/10.1007/s00441-006-0244-y>.
- Schulz, Olaf, Christoph Pieper, Michaela Clever, Janine Pfaff, Aike Ruhlandt, Ralph H Kehlenbach, Fred S Wouters, Jörg Großhans, Gertrude Bunt, and Jörg Enderlein. 2013. “Resolution Doubling in Fluorescence Microscopy with Confocal Spinning-Disk Image Scanning Microscopy.” *Proceedings of the National Academy of Sciences* 110 (52): 21000 LP – 21005. <https://doi.org/10.1073/pnas.1315858110>.
- Seress, L, and M Frotscher. 1990. “Morphological Variability Is a Characteristic Feature of Granule Cells in the Primate Fascia Dentata: A Combined Golgi/Electron Microscope Study.” *The Journal of Comparative Neurology* 293 (2): 253–67. <https://doi.org/10.1002/cne.902930208>.
- Sgobio, Carmelo, Veronica Ghiglieri, Cinzia Costa, Vincenza Bagetta, Sabrina Siliquini, Ilaria Barone, Massimiliano Di Filippo, et al. 2010. “Hippocampal Synaptic Plasticity, Memory, and Epilepsy: Effects of Long-Term Valproic Acid Treatment.” *Biological Psychiatry* 67 (6): 567–74. <https://doi.org/10.1016/j.biopsych.2009.11.008>.
- Shao, Lin, Peter Kner, E Hesper Rego, and Mats G L Gustafsson. 2011. “Super-Resolution 3D Microscopy of Live Whole Cells Using Structured Illumination.” *Nature Methods* 8 (12): 1044–46. <https://doi.org/10.1038/nmeth.1734>.

7. References

- Shapira, Mika, R. Grace Zhai, Thomas Dresbach, Tal Bresler, Viviana I. Torres, Eckart D. Gundelfinger, Noam E. Ziv, and Craig C. Garner. 2003. "Unitary Assembly of Presynaptic Active Zones from Piccolo-Bassoon Transport Vesicles." *Neuron* 38 (2): 237–52. [https://doi.org/10.1016/S0896-6273\(03\)00207-1](https://doi.org/10.1016/S0896-6273(03)00207-1).
- Shepherd, Jason D, Gavin Rumbaugh, Jing Wu, Shoaib Chowdhury, Niels Plath, Dietmar Kuhl, Richard L Huganir, and Paul F Worley. 2006. "Arc/Arg3.1 Mediates Homeostatic Synaptic Scaling of AMPA Receptors." *Neuron* 52 (3): 475–84. <https://doi.org/10.1016/j.neuron.2006.08.034>.
- Sheppard, C J, and T Wilson. 1981. "The Theory of the Direct-View Confocal Microscope." *Journal of Microscopy* 124 (Pt 2): 107–17. <https://doi.org/10.1111/j.1365-2818.1981.tb00304.x>.
- Sheppard, Colin J R, Shalin B Mehta, and Rainer Heintzmann. 2013. "Superresolution by Image Scanning Microscopy Using Pixel Reassignment." *Optics Letters* 38 (15): 2889–92. <https://doi.org/10.1364/OL.38.002889>.
- Shetty, Mahesh Shivarama, and Sreedharan Sajikumar. 2017. "Differential Involvement of Ca(2+)/Calmodulin-Dependent Protein Kinases and Mitogen-Activated Protein Kinases in the Dopamine D1/D5 Receptor-Mediated Potentiation in Hippocampal CA1 Pyramidal Neurons." *Neurobiology of Learning and Memory* 138 (February): 111–20. <https://doi.org/10.1016/j.nlm.2016.07.020>.
- Shohami, Esther, and Anat Biegon. 2014. "Novel Approach to the Role of NMDA Receptors in Traumatic Brain Injury." *CNS & Neurological Disorders Drug Targets* 13 (4): 567–73. <https://doi.org/10.2174/18715273113126660196>.
- Sigrist, Stephan J, and Dietmar Schmitz. 2011. "Structural and Functional Plasticity of the Cytoplasmic Active Zone." *Current Opinion in Neurobiology* 21 (1): 144–50. <https://doi.org/10.1016/j.conb.2010.08.012>.
- Silva, A J, C F Stevens, S Tonegawa, and Y Wang. 1992. "Deficient Hippocampal Long-Term Potentiation in Alpha-Calcium-Calmodulin Kinase II Mutant Mice." *Science (New York, N.Y.)* 257 (5067): 201–6. <https://doi.org/10.1126/science.1378648>.
- Smolen, Paul, Douglas A Baxter, and John H Byrne. 2020. "Comparing Theories for the Maintenance of Late LTP and Long-Term Memory: Computational Analysis of the Roles of Kinase Feedback Pathways and Synaptic Reactivation." *Frontiers in Computational Neuroscience* 14 (December): 569349. <https://doi.org/10.3389/fncom.2020.569349>.
- Söllner, Thomas, Mark K. Bennett, Sidney W. Whiteheart, Richard H. Scheller, and James E. Rothman. 1993. "A Protein Assembly-Disassembly Pathway in Vitro That May Correspond to Sequential Steps of Synaptic Vesicle Docking, Activation, and Fusion." *Cell*. [https://doi.org/10.1016/0092-8674\(93\)90376-2](https://doi.org/10.1016/0092-8674(93)90376-2).
- Squire, L R. 1992. "Memory and the Hippocampus: A Synthesis from Findings with Rats, Monkeys, and Humans." *Psychological Review* 99 (2): 195–231. <https://doi.org/10.1037/0033-295x.99.2.195>.
- Squire, L R, B Knowlton, and G Musen. 1993. "The Structure and Organization of Memory." *Annual Review of Psychology* 44: 453–95. <https://doi.org/10.1146/annurev.ps.44.020193.002321>.
- Staubli, U, and G Lynch. 1987. "Stable Hippocampal Long-Term Potentiation Elicited by 'theta' Pattern Stimulation." *Brain Research* 435 (1–2): 227–34. [https://doi.org/10.1016/0006-8993\(87\)91605-2](https://doi.org/10.1016/0006-8993(87)91605-2).
- Stelzer. 1998. "Contrast, Resolution, Pixelation, Dynamic Range and Signal-to-Noise Ratio: Fundamental Limits to Resolution in Fluorescence Light Microscopy." *Journal of Microscopy* 189 (1): 15–24. <https://doi.org/https://doi.org/10.1046/j.1365-2818.1998.00290.x>.
- Stuart, G J, H U Dodt, and B Sakmann. 1993. "Patch-Clamp Recordings from the Soma and Dendrites of Neurons in Brain Slices Using Infrared Video Microscopy." *Pflugers*

7. References

- Archiv : European Journal of Physiology* 423 (5–6): 511–18. <https://doi.org/10.1007/BF00374949>.
- Südhof, Thomas C. 2012. “The Presynaptic Active Zone.” *Neuron*. <https://doi.org/10.1016/j.neuron.2012.06.012>.
- . 2013. “Neurotransmitter Release: The Last Millisecond in the Life of a Synaptic Vesicle.” *Neuron* 80 (3): 675–90. <https://doi.org/10.1016/j.neuron.2013.10.022>.
- Südhof, Thomas C., and James E. Rothman. 2009. “Membrane Fusion: Grappling with SNARE and SM Proteins.” *Science* 323 (5913): 474–77. <https://doi.org/10.1126/science.1161748>.
- Südhof, Thomas C., and Josep Rizo. 2011. “Synaptic Vesicle Exocytosis.” *Cold Spring Harbor Perspectives in Biology* 3 (12). <https://doi.org/10.1101/cshperspect.a005637>.
- Szule, Joseph A, Jae Hoon Jung, and Uel J McMahan. 2015. “The Structure and Function of ‘Active Zone Material’ at Synapses.” *Philosophical Transactions of the Royal Society B: Biological Sciences* 370 (1672): 20140189. <https://doi.org/10.1098/rstb.2014.0189>.
- Takamori, Shigeo, Matthew Holt, Katinka Stenius, Edward A Lemke, Mads Grønborg, Dietmar Riedel, Henning Urlaub, et al. 2006. “Molecular Anatomy of a Trafficking Organelle.” *Cell* 127 (4): 831–46. <https://doi.org/10.1016/j.cell.2006.10.030>.
- Takao-Rikitsu, Etsuko, Sumiko Mochida, Eiji Inoue, Maki Deguchi-Tawarada, Marie Inoue, Toshihisa Ohtsuka, and Yoshimi Takai. 2004. “Physical and Functional Interaction of the Active Zone Proteins, CAST, RIM1, and Bassoon, in Neurotransmitter Release.” *Journal of Cell Biology* 164 (2): 301–11. <https://doi.org/10.1083/jcb.200307101>.
- Tang, Ai-Hui Hui, Haiwen Chen, Tuo P. Li, Sarah R. Metzbower, Harold D. MacGillavry, Thomas A. Blanpied, E Betzig, et al. 2016. “A Trans-Synaptic Nanocolumn Aligns Neurotransmitter Release to Receptors.” *Nature* 536 (7615): 210–14. <https://doi.org/10.1038/nature19058>.
- Tom Dieck, Susanne, Lydia Sanmartí-Vila, Kristina Langnaese, Karin Richter, Stefan Kindler, Antje Soyke, Heike Wex, et al. 1998. “Bassoon, a Novel Zinc-Finger CAG/Glutamine-Repeat Protein Selectively Localized at the Active Zone of Presynaptic Nerve Terminals.” *Journal of Cell Biology* 142 (2): 499–509. <https://doi.org/10.1083/jcb.142.2.499>.
- Tong, Gang, Robert C. Malenka, and Roger A. Nicoll. 1996. “Long-Term Potentiation in Cultures of Single Hippocampal Granule Cells: A Presynaptic Form of Plasticity.” *Neuron* 16 (6): 1147–57. [https://doi.org/10.1016/S0896-6273\(00\)80141-5](https://doi.org/10.1016/S0896-6273(00)80141-5).
- Tønnesen, Jan, Gergely Katona, Balázs Rózsa, and U Valentin Nägerl. 2014. “Spine Neck Plasticity Regulates Compartmentalization of Synapses.” *Nature Neuroscience* 17 (5): 678–85. <https://doi.org/10.1038/nn.3682>.
- Tønnesen, Jan, and U Valentin Nägerl. 2013. “Superresolution Imaging for Neuroscience.” *Experimental Neurology* 242 (April): 33–40. <https://doi.org/10.1016/j.expneurol.2012.10.004>.
- Torres, Viviana I., and Nivaldo C. Inestrosa. 2017. “Vertebrate Presynaptic Active Zone Assembly: A Role Accomplished by Diverse Molecular and Cellular Mechanisms.” *Molecular Neurobiology*, 1–16. <https://doi.org/10.1007/s12035-017-0661-9>.
- Torres, Viviana I, and Nivaldo C Inestrosa. 2018. “Vertebrate Presynaptic Active Zone Assembly: A Role Accomplished by Diverse Molecular and Cellular Mechanisms.” *Molecular Neurobiology*. <https://doi.org/10.1007/s12035-017-0661-9>.
- Tsanov, Marian, and Shane M. O’Mara. 2015. “Decoding Signal Processing in Thalamo-Hippocampal Circuitry: Implications for Theories of Memory and Spatial Processing.” *Brain Research* 1621: 368–79. <https://doi.org/10.1016/j.brainres.2014.12.003>.
- Tsuji, Shigeru. 2006. “René Couteaux (1909-1999) and the Morphological Identification of Synapses.” *Biology of the Cell / under the Auspices of the European Cell Biology Organization* 98 (8): 503–9. <https://doi.org/10.1042/BC20050036>.
- Uriu, Yoshitsugu, Shigeki Kiyonaka, Takafumi Miki, Masakuni Yagi, Satoshi Akiyama, Emiko Mori, Akito Nakao, et al. 2010. “Rab3-Interacting Molecule Gamma Isoforms Lacking the

7. References

- Rab3-Binding Domain Induce Long Lasting Currents but Block Neurotransmitter Vesicle Anchoring in Voltage-Dependent P/Q-Type Ca²⁺ Channels.” *The Journal of Biological Chemistry* 285 (28): 21750–67. <https://doi.org/10.1074/jbc.M110.101311>.
- Vandael, David, Carolina Borges-Merjane, Xiaomin Zhang, and Peter Jonas. 2020a. “Short-Term Plasticity at Hippocampal Mossy Fiber Synapses Is Induced by Natural Activity Patterns and Associated with Vesicle Pool Engram Formation.” *Neuron* 107 (3): 509-521.e7. <https://doi.org/https://doi.org/10.1016/j.neuron.2020.05.013>.
- . 2020b. “Short-Term Plasticity at Hippocampal Mossy Fiber Synapses Is Induced by Natural Activity Patterns and Associated with Vesicle Pool Engram Formation.” *Neuron* 107 (3): 509-521.e7. <https://doi.org/10.1016/j.neuron.2020.05.013>.
- Vangindertael, J., R. Camacho, W. Sempels, H. Mizuno, P. Dedecker, and K. P.F. F Janssen. 2018. “An Introduction to Optical Super-Resolution Microscopy for the Adventurous Biologist.” *Methods and Applications in Fluorescence* 6 (2): 22003. <https://doi.org/10.1088/2050-6120/aaae0c>.
- Varoqueaux, Frederique, Albrecht Sigler, Jeong-Seop Rhee, Nils Brose, Carsten Enk, Kerstin Reim, and Christian Rosenmund. 2002. “Total Arrest of Spontaneous and Evoked Synaptic Transmission but Normal Synaptogenesis in the Absence of Munc13-Mediated Vesicle Priming.” *Proceedings of the National Academy of Sciences* 99 (13): 9037 LP – 9042. <https://doi.org/10.1073/pnas.122623799>.
- Venkataramani, Varun, Markus Kardorff, Frank Herrmannsdörfer, Ralph Wieneke, Alina Klein, Robert Tampé, Mike Heilemann, and Thomas Kuner. 2018. “Enhanced Labeling Density and Whole-Cell 3D DSTORM Imaging by Repetitive Labeling of Target Proteins.” *Scientific Reports* 8 (1): 5507. <https://doi.org/10.1038/s41598-018-23818-0>.
- Vitureira, Nathalia, and Yukiko Goda. 2013. “Cell Biology in Neuroscience: The Interplay between Hebbian and Homeostatic Synaptic Plasticity.” *The Journal of Cell Biology* 203 (2): 175–86. <https://doi.org/10.1083/jcb.201306030>.
- Vose, Linnea R, and Patric K Stanton. 2017. “Synaptic Plasticity, Metaplasticity and Depression.” *Current Neuropharmacology* 15 (1): 71–86. <https://doi.org/10.2174/1570159x14666160202121111>.
- Wagh, Dhananjay A., Tobias M. Rasse, Esther Asan, Alois Hofbauer, Isabell Schwenkert, Heike Dürrbeck, Sigrid Buchner, et al. 2006. “Bruchpilot, a Protein with Homology to ELKS/CAST, Is Required for Structural Integrity and Function of Synaptic Active Zones in *Drosophila*.” *Neuron* 49 (6): 833–44. <https://doi.org/10.1016/j.neuron.2006.02.008>.
- Waites, Clarissa L., Sergio A. Leal-Ortiz, Nathan Okerlund, Hannah Dalke, Anna Fejtova, Wilko D. Altroock, Eckart D. Gundelfinger, and Craig C. Garner. 2013. “Bassoon and Piccolo Maintain Synapse Integrity by Regulating Protein Ubiquitination and Degradation.” *EMBO Journal* 32 (7): 954–69. <https://doi.org/10.1038/emboj.2013.27>.
- Wallace, W, L H Schaefer, and J R Swedlow. 2001. “A Workingperson’s Guide to Deconvolution in Light Microscopy.” *BioTechniques* 31 (5): 1076–78, 1080, 1082 passim. <https://doi.org/10.2144/01315bi01>.
- Walter, Alexander M., Mathias A. Böhme, and Stephan J. Sigrist. 2018. “Vesicle Release Site Organization at Synaptic Active Zones.” *Neuroscience Research*. <https://doi.org/10.1016/j.neures.2017.12.006>.
- Wang, X, M Kibschull, M M Laue, B Lichte, E Petrasch-Parwez, and M W Kilimann. 1999. “Aczonin, a 550-KD Putative Scaffolding Protein of Presynaptic Active Zones, Shares Homology Regions with Rim and Bassoon and Binds Profilin.” *The Journal of Cell Biology* 147 (1): 151–62. <https://doi.org/10.1083/jcb.147.1.151>.
- Wang, Xiaolu, Bin Hu, Agata Zieba, Nicole G Neumann, Monika Kasper-Sonnenberg, Annegret Honsbein, Greta Hultqvist, et al. 2009. “A Protein Interaction Node at the Neurotransmitter Release Site: Domains of Aczonin/Piccolo, Bassoon, CAST, and Rim Converge on the N-Terminal Domain of Munc13-1.” *The Journal of Neuroscience* 29 (40):

7. References

- 12584 LP – 12596. <https://doi.org/10.1523/JNEUROSCI.1255-09.2009>.
- Wang, Yun, Masaya Okamoto, Frank Schmitz, Kay Hofmann, and Thomas C. Südhof. 1997. “Rim Is a Putative Rab3 Effector in Regulating Synaptic-Vesicle Fusion.” *Nature* 388 (6642): 593–98. <https://doi.org/10.1038/41580>.
- Wang, Yun, and Thomas C Südhof. 2003. “Genomic Definition of RIM Proteins: Evolutionary Amplification of a Family of Synaptic Regulatory Proteins.” *Genomics* 81 (2): 126–37. [https://doi.org/10.1016/s0888-7543\(02\)00024-1](https://doi.org/10.1016/s0888-7543(02)00024-1).
- Weingarten, Jens, Melanie Laßek, Benjamin F. Mueller, Marion Rohmer, Ilaria Lunger, Dominic Baeumlisberger, Simone Dudek, Patricia Gogesch, Michael Karas, and Walter Volkandt. 2014. “The Proteome of the Presynaptic Active Zone from Mouse Brain.” *Molecular and Cellular Neuroscience* 59: 106–18. <https://doi.org/10.1016/j.mcn.2014.02.003>.
- Werner, Christian, Markus Sauer, and Christian Geis. 2021. “Super-Resolving Microscopy in Neuroscience.” *Chemical Reviews*. <https://doi.org/10.1021/acs.chemrev.0c01174>.
- Westphal, Volker, Silvio O Rizzoli, Marcel A Lauterbach, Dirk Kamin, Reinhard Jahn, and Stefan W Hell. 2008. “Video-Rate Far-Field Optical Nanoscopy Dissects Synaptic Vesicle Movement.” *Science* 320 (5873): 246 LP – 249. <https://doi.org/10.1126/science.1154228>.
- Weyhersmüller, Annika, Stefan Hallermann, Nicole Wagner, and Jens Eilers. 2011. “Rapid Active Zone Remodeling during Synaptic Plasticity.” *The Journal of Neuroscience* 31 (16): 6041 LP – 6052. <https://doi.org/10.1523/JNEUROSCI.6698-10.2011>.
- Wichmann, C.Sigrist, S.J. 2010. “The Active Zone T-Bar – a Plasticity Module? *J. Neurogenet.*” *J Neurogenet* 24 (3): 133–145.
- Wichmann, Carolin, and Thomas Kuner. 2022. “Heterogeneity of Glutamatergic Synapses: Cellular Mechanisms and Network Consequences.” *Physiological Reviews* 102 (1): 269–318. <https://doi.org/10.1152/physrev.00039.2020>.
- Wienisch, Martin, and Jurgen Klingauf. 2006. “Vesicular Proteins Exocytosed and Subsequently Retrieved by Compensatory Endocytosis Are Nonidentical.” *Nature Neuroscience* 9 (8): 1019–27. <https://doi.org/10.1038/nn1739>.
- Wiera, Grzegorz, and Jerzy W. Mozrzymas. 2015. “Extracellular Proteolysis in Structural and Functional Plasticity of Mossy Fiber Synapses in Hippocampus.” *Frontiers in Cellular Neuroscience* 9 (November): 1–21. <https://doi.org/10.3389/fncel.2015.00427>.
- Wilke, Scott A., Joseph K. Antonios, Eric A. Bushong, Ali Badkoobehi, Elmar Malek, Minju Hwang, Masako Terada, Mark H. Ellisman, and Anirvan Ghosh. 2013. “Deconstructing Complexity: Serial Block-Face Electron Microscopic Analysis of the Hippocampal Mossy Fiber Synapse.” *Journal of Neuroscience* 33 (2): 507–22. <https://doi.org/10.1523/JNEUROSCI.1600-12.2013>.
- Willig, Katrin I, Silvio O Rizzoli, Volker Westphal, Reinhard Jahn, and Stefan W Hell. 2006. “STED Microscopy Reveals That Synaptotagmin Remains Clustered after Synaptic Vesicle Exocytosis.” *Nature* 440 (7086): 935–39. <https://doi.org/10.1038/nature04592>.
- Wojcik, Sonja M, and Nils Brose. 2007. “Regulation of Membrane Fusion in Synaptic Excitation-Secretion Coupling: Speed and Accuracy Matter.” *Neuron* 55 (1): 11–24. <https://doi.org/10.1016/j.neuron.2007.06.013>.
- Wolter, Steve, Anna Löscherberger, Thorge Holm, Sarah Aufmkolk, Marie-Christine Dabauvalle, Sebastian van de Linde, and Markus Sauer. 2012. “RapidSTORM: Accurate, Fast Open-Source Software for Localization Microscopy.” *Nature Methods* 9 (11): 1040–41. <https://doi.org/10.1038/nmeth.2224>.
- Wolter, Steve, Sven Proppert, and Sarah Aufmkolk. n.d. “Rapid STORM Manual.”
- Wong, Man Yan, Changliang Liu, Shan Shan H. Wang, Aram C.F. Roquas, Stephen C. Fowler, and Pascal S. Kaeser. 2018. “Liprin-A3 Controls Vesicle Docking and Exocytosis at the Active Zone of Hippocampal Synapses.” *Proceedings of the National Academy of Sciences of the United States of America* 115 (9): 2234–39.

7. References

- <https://doi.org/10.1073/pnas.1719012115>.
- Wu, Yicong, and Hari Shroff. 2018. “Faster, Sharper, and Deeper: Structured Illumination Microscopy for Biological Imaging.” *Nature Methods* 15 (12): 1011–19. <https://doi.org/10.1038/s41592-018-0211-z>.
- Yizhar, Ofer, Ulf Matti, Rely Melamed, Yamit Hagalili, Dieter Bruns, Jens Rettig, and Uri Ashery. 2004. “Tomosyn Inhibits Priming of Large Dense-Core Vesicles in a Calcium-Dependent Manner.” *Proceedings of the National Academy of Sciences of the United States of America* 101 (8): 2578–83. <https://doi.org/10.1073/pnas.0308700100>.
- Yokoyama, Shigekazu, Hiromichi Shirataki, Toshiaki Sakisaka, and Yoshimi Takai. 1999. “Three Splicing Variants of Tomosyn and Identification of Their Syntaxin-Binding Region.” *Biochemical and Biophysical Research Communications* 256 (1): 218–22. <https://doi.org/https://doi.org/10.1006/bbrc.1999.0300>.
- York, Andrew G, Panagiotis Chandris, Damian Dalle Nogare, Jeffrey Head, Peter Wawrzusin, Robert S Fischer, Ajay Chitnis, and Hari Shroff. 2013. “Instant Super-Resolution Imaging in Live Cells and Embryos via Analog Image Processing.” *Nature Methods* 10 (11): 1122–26. <https://doi.org/10.1038/nmeth.2687>.
- York, Andrew G, Sapun H Parekh, Damian Dalle Nogare, Robert S Fischer, Kelsey Temprine, Marina Mione, Ajay B Chitnis, Christian A Combs, and Hari Shroff. 2012. “Resolution Doubling in Live, Multicellular Organisms via Multifocal Structured Illumination Microscopy.” *Nature Methods* 9 (7): 749–54. <https://doi.org/10.1038/nmeth.2025>.
- Zalutsky, R A, and R A Nicoll. 1990. “Comparison of Two Forms of Long-Term Potentiation in Single Hippocampal Neurons.” *Science (New York, N.Y.)* 248 (4963): 1619–24. <https://doi.org/10.1126/science.2114039>.
- Zanten, Thomas S van, Alessandra Cambi, Marjolein Koopman, Ben Joosten, Carl G Figdor, and Maria F Garcia-Parajo. 2009. “Hotspots of GPI-Anchored Proteins and Integrin Nanoclusters Function as Nucleation Sites for Cell Adhesion.” *Proceedings of the National Academy of Sciences of the United States of America* 106 (44): 18557–62. <https://doi.org/10.1073/pnas.0905217106>.
- Zhai, R. Grace, and Hugo J. Bellen. 2004. “The Architecture of the Active Zone in the Presynaptic Nerve Terminal.” *Physiology* 19 (5): 262–70. <https://doi.org/10.1152/physiol.00014.2004>.
- Zhao, Shanting, Daniel Studer, Xuejun Chai, Werner Graber, Nils Brose, Sigrun Nestel, Christina Young, E. Patricia Rodriguez, Kurt Saetzler, and Michael Frotscher. 2012. “Structural Plasticity of Hippocampal Mossy Fiber Synapses as Revealed by High-Pressure Freezing.” *Journal of Comparative Neurology* 520 (11): 2340–51. <https://doi.org/10.1002/cne.23040>.
- Zimmermann, M. 2001. “Pathobiology of Neuropathic Pain.” *European Journal of Pharmacology* 429 (1–3): 23–37. [https://doi.org/10.1016/s0014-2999\(01\)01303-6](https://doi.org/10.1016/s0014-2999(01)01303-6).
- Ziv, Noam E, and Craig C Garner. 2004. “Cellular and Molecular Mechanisms of Presynaptic Assembly.” *Nature Reviews. Neuroscience* 5 (5): 385–99. <https://doi.org/10.1038/nrn1370>.
- Zucker, Robert S., and Wade G. Regehr. 2002. “Short-Term Synaptic Plasticity.” *Annual Review of Physiology* 64: 355–405. <https://doi.org/10.1146/annurev.physiol.64.092501.114547>.

8 Abbreviation

2D = two dimensional

3D = three dimensional

ACSF = Stock artificial cerebrospinal fluid

AMPA = α -amino-3-hydroxy-5-methyl-4-isoxazolepro- pionic acid

APD = avalanche photodiode detector

Au = Arbitrary unit

AZ = active zone

BRP = Bruchpilot

Ca²⁺ = calcium

CaCl₂ = calcium chloride

CaM = Ca²⁺ calmodulin

CaMKII = Ca²⁺/calmodulin-dependent protein kinase II

cAMP = Cyclic AMP

CAST = CAZ-associated structural protein

Cav channels = voltage-dependent calcium channel

CAZ = cytomatrix associated with the AZ/cytomatrix at the active zone

CC = coiled-coil

CLSM =confocal laser scanning microscopy

cLTP = Chemically induced LTP

cm = centimeter

CNS = central nervous system

DAG = diacyl-glycerol

DBSCAN = density based spatial clustering of applications with noise

DG = dentate gyrus

DMSO = dimethyl sulfoxide

dSTORM = direct stochastic optical reconstruction microscopy

dSTORM = direct STORM

e.g. = for example, *exempli gratia*

ELKS = glutamic acid (E), leucine (L), lysine (K), and serine (S)-rich protein

ELKS = protein rich in the amino acids E, L, K, and S

EM = electron microscopy

EPSPs = excitatory postsynaptic potentials

FSK = Forskolin

GFP = green fluorescent protein

GluR = glutamate receptor

GTP = guanosine triphosphate

H₂O = water

HCl = hydrogen chloride

HFS = High-frequency stimulation

i.e. = that is, *id est*

KCl = potassium chloride

8. Abbreviation

kDa = kilo Dalton
LTD = long-term depression
LTP = long-term potentiation
MF = mossy fiber
MFB = mossy fiber bouton
MFT = mossy fiber tract
MgCl₂ = magnesium chloride
mm = millimeter
mM = millimolar; M = molar
MUN = Munc homology domain
Munc13 = mammalian homologue of the nematode *C. elegans* Unc13 (uncoordinated) protein]
NA = numerical aperture
NaCl = Sodium chloride
NaH₂PO₄ = Sodium di-hydrogen phosphate/ Sodium phosphate monobasic anhydrous
NaHCO₃ = Sodium bicarbonate
NaOH = sodium hydroxide
NGS = normal goat serum
nm = nanometer
NMDA = N-Methyl-D-aspartate
NMDAR = N-methyl-D-aspartate receptor
NMDARs = N-methyl-D-aspartate glutamate receptors
NMJ = neuromuscular junction
Nrx = neurexin
NSF = N-ethylmaleimide-sensitive factor
NSOM = near-field scanning optical microscopy
NTs = neurotransmitters
PALM = photo-activated localization microscopy
PB = Primed burst
PBS = phosphate buffered saline
PFA = paraformaldehyde
PH = pleckstrin homology
PKA = Protein kinase A
PMT = Photomultiplier tube
PS = Population spike
PSD = Postsynaptic density
PSF = Point-spread function
pvr = Release probability
RBP= RIM-binding protein
RESOLFT = Reversible saturable/switchable optical linear (fluorescence) transitions
RIM = Rab3-interacting molecule
RIM-BP = RIM-binding protein

8. Abbreviation

RRP = Readily releasable pool
s.d. = Standard deviation
SIM = Structured illumination microscopy
SM = Sec1/Munc18-like
SMLM = Single-molecule localization microscopy
SNAP = Synaptosomal-associated protein
SNAPs = Soluble NSF attachment proteins
SNARE = Soluble N-ethylmaleimide-sensitive factor attachment receptor
SNOM, NSOM = Near-field scanning optical microscopy
SR = Super-resolution
SR-SIM = super-resolution structured illumination microscopy
SRM = super-resolution microscopy
STED = Stimulated emission depletion
SV = Synaptic vesicle
SYD-1 = Synapse defective-1
Syd-2 = Synapse-defective 2
Syt 1 = Synaptotagmin 1
TBS = Theta-burst stimulation
TIRF = Total internal reflection microscopy
TIRF-SIM = Total internal reflection fluorescence SIM
TIRFM = TIRF microscopy
Unc13 = Uncoordination mutant 13
VGCC = Voltage-gated calcium channel
WF = Wide-field
Zn = Zinc
ZnF = Zinc finger
 β -PE = β -phorbol esters
 μm = Micrometer (10^{-6} meter)

9 List of figures

| | |
|--|----|
| Figure 1. Spinal cord synapses with dense projections in presynaptic processes. [modified from (Gray 1963)] | 4 |
| Figure 2. AZ ultrastructures. (A-J) Schematics of AZ structures in different organisms Modified from (Zhai and Bellen 2004). | 6 |
| Figure 3 Molecular Model of main players at the presynaptic AZ. An SV (grey) is shown schematically with the numerous active zone proteins and their interconnections. | 7 |
| Figure 4. Schematic diagram illustrates how the CAZ proteins interact to form a network that regulates the active zone. for abbreviations, see Abbreviation Table) (Eckart D. Gundelfinger and Fejtova 2012) | 12 |
| Figure 5. Domain structure of CAZ protein Munc13s and Bassoon. [modified from (Schoch and Gundelfinger 2006)] | 14 |
| Figure 6. Schematic model of the presynaptic bouton and the composition of the active zone proteins. | 15 |
| Figure 7. Henry Molaison in Hartford, Connecticut, USA, in 1975. (Photograph courtesy of Dr. Suzanne Corkin (Dossani, Missios, and Nanda 2015) | 22 |
| Figure 8. Anatomical component drawings of a hippocampus A, B (Ramón y Cajal), microscopic illustration of mossy fibers and their postsynaptic target cells. | 23 |
| Figure 9. characterization of hippocampal mossy fibre synapses using Golgi impregnation and electron microscopy (Frotscher, Jonas, and Sloviter 2006). | 24 |
| Figure 10. Illustration of pivotal synaptic components and the optical resolution limit imposed by the diffraction limit in light microscopy. | 28 |
| Figure 11. Fundamental principles of super-resolution microscopy. | 33 |
| Figure 12. Nest beaker. For incubating acute brain slices both before and after recovery, modified from (Papouin and Haydon 2018). | 49 |
| Figure 13. Treatment design for SIM experiments | 55 |
| Figure 14. Schematic workflow overview for imaging of hippocampal mossy fiber synaptic contacts. | 65 |
| Figure 15. Functions of optical transfer (OTFs). | 67 |
| Figure 16. Calibration slide preparation. | 68 |
| Figure 17. Bassoon immunofluorescence in normal tissue of Thy1EGFP (M) mice | 69 |
| Figure 18. Immunofluorescence double staining of anti-homer and anti-bassoon in fixed mouse hippocampus. | 70 |
| Figure 19. Representative SIM image of MFB in the CA3 region of a Thy1-mEGFP (Lsi1) mouse brain slice (green) stained against Bsn (magenta). | 71 |
| Figure 20. Three-channel SIM image of an individual MFB in the CA3 region of Thy1-mEGFP (Lsi1) mouse brain slice | 71 |
| Figure 21. Representative 3D reconstruction of AZs proteins Bsn and Tomosyn in CA3. | 72 |
| Figure 22. 3D reconstruction of AZs proteins Bsn and Munc-13-1 in CA3 region of Hippocampus. | 73 |
| Figure 23. SIM; 3D reconstruction of MFB and Bsn clusters. | 73 |
| Figure 24. Quantification of MFB/EGFP volume in SIM images | 75 |
| Figure 25. Quantification of MFBs in SIM images (filtered data). | 76 |
| Figure 26. Bsn and Munc 13-1 measures in scanning SIM of 25 μm cryosections of hippocampal mouse tissue. | 78 |
| Figure 27. Bsn and Munc 13-1 intensity and EGFP volume quantifications in a single SIM image of 25 μm cryosections of hippocampal MFT mouse tissue. | 78 |
| Figure 28. Bsn and Munc 13-1 intensity and EGFP volume measurements in a single SIM image of 25 μm cryosections of hippocampal MFT mouse tissue. | 79 |
| Figure 29. Bassoon sum intensity measures in scanning SIM of 25 μm cryosections obtained from 300 μm acute brain sections of hippocampal mouse tissue (filtered data). | 80 |
| Figure 30. Munc 13-1 sum intensity measures in scanning SIM of 25 μm cryosections obtained from 300 μm acute brain sections of hippocampal mouse tissue (filtered data). | 80 |
| Figure 31. Tomosyn sum intensity measures in scanning SIM of 25 μm cryosections obtained from 300 μm acute brain sections of hippocampal mouse tissue (filtered data). | 81 |
| Figure 33. Intensity and density of Bassoon in MFBs before after Forskolin treatment in filtered images, (MFBs > 5 μm^3). | 89 |
| Figure 32. Intensity and density of Bassoon in EGFP positive structures before and after Forskolin treatment in unfiltered images. | 89 |
| Figure 34. Intensity and density of Munc13-1 in EGFP positive structures before and after Forskolin treatment in unfiltered images. | 94 |
| Figure 35. Intensity and density of Munc 13-1 in MFBs before and after Forskolin treatment in filtered images, (MFBs > 5 μm^3). | 96 |
| Figure 36. Intensity and density of Tomosyn in EGFP positive structures before and after Forskolin treatment in unfiltered images. | 98 |

9. List of figures

| | |
|--|-----|
| <i>Figure 37. Intensity and density of Tomosyn in MFBs before and after Forskolin treatment in filtered images, (MFBs > 5μm³).</i> | 98 |
| <i>Figure 38. A schematic illustration of the method for visualizing the synaptic connections of hippocampus mossy fibers.</i> | 100 |
| <i>Figure 39. Sequential en bloc 3D imaging in 25 μm thick tissue slices of mEGFP (Ls1) mice showed Bassoon clusters in identified mossy fiber boutons.</i> | 101 |
| <i>Figure 40. Forskolin effect in dSTORM images of MFB in three</i> | 102 |
| <i>Figure 41. Bassoon protein morphology in SIM and dSTORM images</i> | 105 |

10 List of Tables

| | |
|--|-----|
| <i>Table 1. The principal roles of some vertebrate active zone protein</i> | 10 |
| <i>Table 2. Links between DG–CA3 synaptic plasticity and memory</i> | 25 |
| <i>Table 3. Treatment design using acute hippocampal (HC) slices.</i> | 56 |
| <i>Table 4. The number of MFBs per image. Animal 1-ACSF experiment, right hMFT; four 25 μm sections; 2 images per section: 8 SIM images</i> | 74 |
| <i>Table 5. The number of MFBs per SIM image. Animal 2-ACSF experiment, right hMFT, six 25 μm sections; 1 image per section: 6 SIM images</i> | 74 |
| <i>Table 6. The number of MFBs per SIM image. Animal 3-ACSF experiment, right hMFT, six 25 μm; 1 image per section: 6 images</i> | 75 |
| <i>Table 7. Quantification of MFBs in SIM images (filtered data).</i> | 76 |
| <i>Table 8. The number of MFBs per image. Animal 1-FSK experiment, right hMFT, five 25 μm cryo section; 2 image per section: 10 SIM images</i> | 85 |
| <i>Table 9. The number of MFBs per image. Animal 2-FSK experiment, right hMFT; six 25 μm cryo sections; 1-2 images per section: 11 SIM images</i> | 85 |
| <i>Table 10. The number of MFBs per image. Animal 3-FSK experiment, right hMFT, six 25 μm cryo section; 1-2 image per section: 7 SIM images</i> | 86 |
| <i>Table 11. The number of MFBs per image. Animal 4, right hMFT, five 25 μm cryo sections; 1-2 images per section: 6 SIM images</i> | 86 |
| <i>Table 12. The number of MFBs per image. Animal 5, right hMFT, six 25 μm cryo section; 1-2 image per section: 8 SIM images</i> | 87 |
| <i>Table 13. The number of MFBs per image. Animal 6, right hMFT; six 25 μm cryo sections; 1-2 images per section: 8 SIM images</i> | 87 |
| <i>Table 14. Intensity of Bassoon in EGFP positive structures before and after Forskolin treatment in unfiltered images.</i> | 88 |
| <i>Table 15. Intensity of Bassoon in MFBs before after Forskolin treatment in filtered images, (MFBs > 5μm³).</i> | 90 |
| <i>Table 16. Density of Bassoon in MFBs before after Forskolin treatment in filtered images, (MFBs > 5μm³).</i> | 90 |
| <i>Table 17. Intensity of Munc13-1 in EGFP positive structures before and after Forskolin treatment in unfiltered images.</i> | 93 |
| <i>Table 18. Intensity of Munc 13-1 in MFBs before and after Forskolin treatment in filtered images, (MFBs > 5μm³).</i> | 95 |
| <i>Table 19. Density of Munc 13-1 in MFBs before and after Forskolin treatment in filtered images, (MFBs > 5μm³).</i> | 95 |
| <i>Table 20. Intensity of Tomosyn in EGFP positive structures before and after forskolin treatment in unfiltered images.</i> | 97 |
| <i>Table 21. Intensity of Tomosyn in MFBs before and after Forskolin treatment in filtered images, (MFBs > 5μm³).</i> | 99 |
| <i>Table 22. Density of Tomosyn in MFBs before and after Forskolin treatment in filtered images, (MFBs > 5μm³).</i> | 99 |
| <i>Table 23. Statistical analysis of Bassoon density in unfiltered SIM images</i> | 138 |
| <i>Table 24. Statistical analysis of Munc13-1 density in unfiltered SIM images</i> | 139 |
| <i>Table 25. Statistical analysis of Tomosyn density measurements in unfiltered SIM images</i> | 140 |

11. Appendix

Table 23. Statistical analysis of Bassoon density in unfiltered SIM images

| <u>Animal 1 and 2 Bsn density</u> | DMSO-control | FSK-treatment |
|--|---------------------|----------------------|
| Number of EGFP positive structures | 739 | 828 |
| 25% Percentile | 2791187 | 3515976 |
| Median | 5393938 | 7333985 |
| 75% Percentile | 9462184 | 12387866 |
| Sum | 5347120060 | 7801468569 |
| Mean ranks | | |
| Kruskal-Wallis test | 140,4 | 209,9 |

| <u>Animal 3 and 4 Bsn density</u> | DMSO-control | FSK-treatment |
|--|---------------------|----------------------|
| Number of EGFP positive structures | 151 | 808 |
| 25% Percentile | 443255 | 1928115 |
| Median | 852963 | 5207385 |
| 75% Percentile | 2186970 | 16979750 |
| Sum | 1379717229 | 28727354795 |
| Mean ranks | | |
| Kruskal-Wallis test | 74,67 | 204,9 |

| <u>Animal 5 and 6 Bsn density</u> | DMSO-control | FSK-treatment |
|--|---------------------|----------------------|
| Number of EGFP positive structures | 125 | 593 |
| 25% Percentile | 5920422 | 1916831 |
| Median | 10022687 | 4176040 |
| 75% Percentile | 15347884 | 8000276 |
| Sum | 1516485092 | 4973887249 |
| Mean ranks | | |
| Kruskal-Wallis test | 227,4 | 155,6 |

Table 24. Statistical analysis of Munc13-1 density in unfiltered SIM images

| <u>Animal 1 and 2 Munc13-1 density</u> | DMSO-control | FSK-treatment |
|---|---------------------|----------------------|
| Number of EGFP positive structures | 477 | 355 |
| 25% Percentile | 2878850 | 2943123 |
| Median | 6925207 | 6093237 |
| 75% Percentile | 13840112 | 12244297 |
| Sum | 4876352958 | 3372136680 |
| Mean ranks | | |
| Kruskal-Wallis test | 188,0 | 151,7 |
| | | |
| <u>Animal 3 and 4 Munc13-1 density</u> | DMSO-control | FSK-treatment |
| Number of EGFP positive structures | 132 | 547 |
| 25% Percentile | 4211635 | 2903438 |
| Median | 11832103 | 5349732 |
| 75% Percentile | 24721446 | 10123090 |
| Sum | 2727792335 | 4172288494 |
| Mean ranks | | |
| Kruskal-Wallis test | 201,0 | 155,4 |
| | | |
| <u>Animal 5 and 6 Munc13-1 density</u> | DMSO-control | FSK-treatment |
| Number of EGFP positive structures | 58 | 247 |
| 25% Percentile | 5252887 | 2597652 |
| Median | 8368048 | 5614286 |
| 75% Percentile | 15341369 | 10595127 |
| Sum | 764250339 | 2180656970 |
| Mean ranks | | |
| Kruskal-Wallis test | 141,8 | 91,21 |

11. Appendix

Table 25. Statistical analysis of Tomosyn density measurements in unfiltered SIM images

| <u>Animal 1 and 2 Tomosyn density</u> | DMSO-control | FSK-treatment |
|--|---------------------|----------------------|
| Number of EGFP positive structures | 262 | 473 |
| 25% Percentile | 2881007 | 3585354 |
| Median | 9144542 | 9682535 |
| 75% Percentile | 19689223 | 20759408 |
| Sum | 3866605260 | 7534464805 |
| Mean ranks | 140,6 | 192,5 |

| <u>Animal 3 and 4 Tomosyn density</u> | DMSO-control | FSK-treatment |
|--|---------------------|----------------------|
| Number of EGFP positive structures | 19 | 261 |
| 25% Percentile | 1232384 | 3136755 |
| Median | 2841708 | 9896502 |
| 75% Percentile | 8070508 | 21594020 |
| Sum | 89438125 | 4455524152 |
| Mean ranks | | |
| Kruskal-Wallis test | 23,83 | 71,97 |

| <u>Animal 5 and 6 Tomosyn density</u> | DMSO-control | FSK-treatment |
|--|---------------------|----------------------|
| Number of EGFP positive structures | 67 | 250 |
| 25% Percentile | 6045017 | 1271848 |
| Median | 11024009 | 3470433 |
| 75% Percentile | 16530895 | 7850003 |
| Maximum | 51584133 | 48701396 |
| Sum | 873048426 | 1477436857 |
| Mean ranks | | |
| Kruskal-Wallis test | 118,2 | 67,21 |

11 Curriculum vitae

